Reactively Sputtered Nano-Structured Multilayer Coatings on Architectural Glazing for Active Solar Energy Façades

THÈSE N^O 6485 (2015)

PRÉSENTÉE LE 27 MARS 2015

À LA FACULTÉ DE L'ENVIRONNEMENT NATUREL, ARCHITECTURAL ET CONSTRUIT

LABORATOIRE D'ÉNERGIE SOLAIRE ET PHYSIQUE DU BÂTIMENT

PROGRAMME DOCTORAL EN ENVIRONNEMENT

ÉCOLE POLYTECHNIQUE FÉDÉRALE DE LAUSANNE

POUR L'OBTENTION DU GRADE DE DOCTEUR ÈS SCIENCES

PAR

Stefan MERTIN

acceptée sur proposition du jury:

Prof. K. Beyer, présidente du jury
Prof. J.-L. Scartezzini, Prof. P. Muralt, directeurs de thèse
Dr V. Hody-Le Caër, rapporteuse
Dr A. Romanyuk, rapporteur
Dr R. Sanjines, rapporteur

ÉCOLE POLYTECHNIQUE
FÉDÉRALE DE LAUSANNE

Suisse
2015

We all know that light travels faster than sound. That's why certain people appear bright until you hear them speak.

<div style="text-align: right">Albert Einstein</div>

Abstract

Improving the aesthetic of solar thermal collectors would grant architects a huge potential for a perfect integration of solar panels into building façades: this can be achieved by coloured interference coatings on the cover glass. These coatings also open the possibility to match the colours of the collectors to those of other architectural components and design elements. An important boundary condition for the coloured filter production is however, to provide a sufficiently high solar transmittance. To deal with the latter, sophisticated numerical simulations are needed to improve the colour-filter design. In addition, a large variety of coating materials is important, ideally with huge differences in their refractive indices, while the absorption of all materials needs to be close to zero.

This doctoral thesis focuses on the optical film design and the deposition of new coloured thin-film multilayers with an optimised energetic performance and an only little varying coloured reflection at different viewing angles. To access more directly the correlation between solar transmittance, light spectra and visual and energetic performance of the coatings, a thin-film simulation framework has been developed on the basis of Mathematica$^{\text{TM}}$. New coating designs have reduced the number of parameters necessary to be adjusted and tuned during the coating-development process: this could help to shorten the prototype-development phase on industrial coaters significantly as well as the whole coating-development cycle. Based on the new developed colour-filter designs, multilayer stacks were deposited via reactive magnetron sputtering. The deposited coatings exhibit a solar transmittance $T_{\text{sol}} > 87\%$. For greenish colour hues even a T_{sol} up to 91% was reached, which corresponds to less than 1% loss in T_{sol} (respectively solar energy performance) in comparison to the uncoated glass substrate.

Furthermore, the research deals with the deposition of low-refractive magnesium fluoride (MgF_2) and MgF_2 containing composites. Hereby, a novel deposition process

by reactive magnetron sputtering was developed for MgF_2 using a metallic magnesium target and a reactive gas mixture of oxygen (O_2) and carbon tetrafluoride (CF_4) diluted with argon. The obtained MgF_2 films exhibit a very-low refractive index of $n = 1.382$ at $550\,nm$, which is congruent with the polycrystalline bulk, and only a very weak absorption in the whole solar spectral range (300–2500 nm). In addition, a novel approach to deposit $Mg-F-Si-O$ composite materials by magnetron co-sputtering from compound MgF_2 and silicon dioxide (SiO_2) targets was performed. The obtained films show a two-phase system with nanocrystals of MgF_2 embedded in a SiO_2-rich amorphous matrix. The lowest achieved refractive index amounts to $n = 1.424$ at $550\,nm$ combined with a negligible extinction coefficient ($k < 10^{-9}$).

The investigated sputtered low-index materials open-up manifold possibilities for coloured filters. For instance, by adding a supplementary MgF_2 inter-layer, a colour-invariant solar transmittance of $T_{sol} = 85$–85.7% could be achieved, as shown by numerical simulations. With this novel optical filter design it will be feasible to offer a whole colour palette for solar thermal collectors exhibiting all the same solar thermal energy performance.

Zusammenfassung

Eine verbesserte Ästhetik von Solarkollektoren würde Architekten ein Vielfalt von Möglichkeiten eröffnen diese in Gebäudefassaden zu integrieren. Dies kann durch farbige Interferenzbeschichtungen auf den Abdeckgläsern erreicht werden und würde zudem die Möglichkeit einer farblichen Anpassung der Kollektoren an Gebäude- und Designelemente ermöglichen. Eine wichtige Randbedingung für diese Farbfilter ist jedoch, dass sie einen ausreichend hohen solarer Transmissionsgrad aufweisen müssen. Um letzteres zu gewährleisten, sind umfangreiche und anspruchsvolle numerische Simulationen bezüglich deren Optimierung nötig. Hierbei ist eine Vielfalt an Beschichtungsmaterialien mit großen Unterschieden in den jeweiligen Brechzahlen bei gleichzeitig geringer bis nahe zu keiner Absorption von großer Bedeutung.

Die vorliegende Doktorarbeit beschäftigt sich mit der Entwicklung und Abscheidung von neuen farbigen Dünnfilm-Mehrschichtsystemen, welche einen optimierten Energieeintrag sowie eine winkelstabile Reflexionsfarbe aufweisen. Um einen direkten Zugriff auf den Zusammenhang zwischen solarem Transmissionsgrad, Lichtspektren und visueller und energetischer Leistung zu bekommen, wurde eine neue Simulationsumgebung in Mathematica$^{\text{TM}}$ entwickelt. Mittels neuer Schichtdesigns konnte die Anzahl der freien Parameter, welche zum Anpassen und Justieren der Schichten notwendig ist, reduziert werden. Hierdurch kann die Entwicklungszeit für Prototypen auf Industriebeschichtungsanlagen deutlich reduziert werden, sowie der gesamte Schichtentwicklungszyklus. Basierend auf den neuen Schichtdesigns wurden Mehrschichtsysteme mittels reaktivem Magnetronsputtering abgeschieden. Diese Beschichtungen weisen einen solaren Transmissionsgrad $T_{\text{sol}} > 87\%$ auf. Für grünliche Schichten konnte sogar ein T_{sol} von bis zu 91% erreicht werden. Dies entspricht einem Verlust von 1% an solarem Energieeintrag im Vergleich zu einem unbeschichteten Glassubstrat.

Des Weiteren beschäftigt sich diese Forschungsarbeit mit der Schichtherstellung von niedrigbrechenden Magnesiumfluorid (MgF_2) und MgF_2 enthaltenden Kompo-

sitschichten. Dabei wurde ein neuartiger Beschichtungsprozess mittels reaktivem Magnetronsputtering entwickelt, bei dem ein metallisches Magnesiumtarget und ein mit Argon verdünntes Reaktivgasgemisch aus Sauerstoff (O_2) und Tetrafluorkohlenstoff (CF_4) verwendet werden. Die produzierten MgF_2-Schichten weisen einen niedrigen Brechungsindex von $n = 1.382$ bei $550\,\mathrm{nm}$ auf, was übereinstimmend mit dem von polykristallinem Material ist, und sind dabei im gesamten solaren Wellenlängenbereich (300–2500 nm) nur schwach absorbierend. Zusätzlich wurden eine neuartige Beschichtungsmethode zur Herstellung von $Mg-F-Si-O$-Kompositmaterialien mittels Magnetron-Co-Sputtering von MgF_2- und SiO_2-Targets untersucht. Die so hergestellten Filme bestehen aus MgF_2-haltigen Nanokristallen, welche in einer SiO_2-haltigen amorphen Matrix eingebettet sind. Der niedrigste erzielte Brechungsindex beträgt $n = 1.424$ bei $550\,\mathrm{nm}$, bei einem gleichzeitig vernachlässigbaren Absorptionskoeffizienten ($k < 10^{-9}$).

Diese neuartigen Materialen mit niedrigem Brechungsindex eröffnen vielfältige neue Möglichkeiten für die Farbfilterentwicklung. Zum Beispiel, durch Hinzufügen einer MgF_2-Zwischenschicht kann, wie mittels numerischen Simulationen gezeigt wurde, ein farbunabhängiger solarer Transmissionsgrad T_{sol} von 85–85.7% erreicht werden. Diese neuartige Beschichtung ermöglicht es eine komplette Farbpalette für thermische Sonnenkollektoren anzubieten, welche die gleiche solarthermische Leistung aufweisen.

Stichwörter: *farbige Sonnenkollektoren, solare Dünnschichten auf Glas, Mehrschicht-Dünnfilmfilter, reaktives Magnetronsputtering, Magnesiumfluorid, niedriger Brechungsindex, nanokristalline Mikrostruktur, Nano-Komposite, spektroskopische Ellipsometrie, Spektrophotometrie, Photoelektronspektroskopie, solarer Transmissionsgrad, Fassadenintegration*

Résumé

Améliorer l'esthétique de capteurs solaires thermiques accorderait aux architectes un potentiel énorme pour une parfaite intégration des panneaux solaires dans les façades des bâtiments : cela peut être réalisé par des couches d'interférence de couleur sur la protection en verre. Ces revêtements offrent également la possibilité de faire correspondre les couleurs des capteurs à celles d'autres éléments architecturaux ou de conception. Une condition importante pour la production des filtres colorés est de fournir une transmission solaire suffisamment élevée. Pour répondre à cette dernière, des simulations numériques sophistiquées sont nécessaires pour améliorer la conception des filtres colorés. De plus, il est important que les matériaux constituant les couches minces soient variés, de préférence avec de grandes différences dans leurs indices de réfraction, tandis que leur absorption doit être proche de zéro.

Cette thèse doctorale porte sur la conception de films optiques et le dépôts de nouvelles couches minces de couleur ayant une performance énergétique optimisée ainsi qu'un faible changement de couleur de réflexion lors d'une variation de l'angle de vision. Pour corréler plus directement la transmission solaire, les spectres lumineux et la performance visuelle et énergique de ces revêtements, un cadre de simulation de couches minces a été développé sur la base de Mathematica$^{\mathrm{TM}}$. Les nouvelles conceptions de revêtements ont réduit le nombre de paramètres nécessaires à ajuster et à régler au cours du développement du processus : cela pourrait aider à raccourcir de manière significative la phase de développement du prototype sur les équipements industriels pour revêtement, ainsi que l'ensemble du cycle de développement. Basé sur les nouvelles conceptions des filtres colorés, des multi-couches ont été déposées par pulvérisation cathodique réactive. Les revêtements ainsi déposés présentent un facteur de transmission solaire $T_{\mathrm{sol}} > 87\%$. Les nuances de couleur verdâtre présentent même un T_{sol} allant jusqu'à 91%, ce qui correspond à une perte de moins de 1% en T_{sol} (respectivement du rendement de l'énergie solaire) par rapport au substrat de

verre non revêtu.

En outre, la recherche porte sur le dépôt de fluorure de magnésium (MgF_2) avec un faible indice de réfraction et sur le dépôt des composites contenant de MgF_2. Par la présente, un nouveau procédé de dépôt par pulvérisation magnétron réactive a été développé pour le MgF_2 à partir d'une cible métallique de magnésium et un mélange des gaz réactifs d'oxygène (O_2) et de tétrafluorure de carbone (CF_4), dilué avec de l'argon. Les couches de MgF_2 obtenues présentent un très faible indice de réfraction $n = 1,382$ à $550\,nm$, qui est congruent avec la structure polycristalline, et seulement une très faible absorption dans toute la gamme solaire (300–2500 nm). En plus de cela, une nouvelle approche pour déposer les matériaux composites $Mg-F-Si-O$ par pulvérisation co-cathodique a été réalisée, à partir des cibles MgF_2 et dioxyde de silicium (SiO_2). Les films obtenus montrent un système à deux phases avec des nanocristaux de MgF_2 noyées dans une matrice amorphe riche en SiO_2. L'indice de réfraction le plus bas obtenu est $n = 1,424$ à $550\,nm$ associé à un coefficient d'extinction négligeable ($k < 10^{-9}$).

Les matériaux pulvérisés étudiés possédant un faible indice de réfraction ouvrent des possibilités multiples pour les filtres colorés. Par exemple, en ajoutant une couche intermédiaire de MgF_2, une transmission solaire, invariante selon les couleurs, de T_{sol} = 85 à 85,7% pourrait être atteinte, comme montré par les simulations numériques. Avec cette nouvelle conception de filtres optiques, il sera possible d'offrir toute une palette de couleurs pour les capteurs solaires thermiques, présentant tous la même performance thermique de l'énergie solaire.

Mots clefs : *capteurs solaires colorés, revêtement solaire sur verre, filtres minces en multi-couches, pulvérisation cathodique magnétron, fluorure de magnésium, faible indice de réfraction, microstructure nanocristalline, composite nano, ellipsométrie spectroscopique, spectrophotométrie, spectroscopie de photoélectrons, transmission solaire, intégration dans les façades*

Contents

List of Publications

The results of this thesis research are based on the following journal papers:

Paper 1 Stefan Mertin, Virginie Hody-Le Caër, Martin Joly, Iris Mack, Peter Oelhafen, Jean-Louis Scartezzini, and Andreas Schüler. Reactively Sputtered Coatings on Architectural Glazing for Coloured Active Solar Thermal Façades. *Energy and Buildings*, 68 (2014) 764–770

Paper 2 Stefan Mertin, Laurent Marot, Cosmin S. Sandu, Roland Steiner, Jean-Louis Scartezzini, and Paul Muralt. Nanocrystalline Low-Refractive Magnesium Fluoride Films Deposited by Reactive Magnetron Sputtering: Optical and Structural Properties. Submitted manuscript.

Paper 3 Stefan Mertin, Paul Muralt, and Jean-Louis Scartezzini. Advanced Coloured Coating Designs with Colour-Invariant Solar Transmittance by Means of a Magnesium Fluoride Inter-Layer. Submitted manuscript.

Paper 4 Stefan Mertin, Tony Länzlinger, Cosmin S. Sandu, Jean-Louis Scartezzini, and Paul Muralt. Combinatorial Study of Low-Refractive $Mg-F-Si-O$ Nano-Composites Deposited by Magnetron Co-Sputtering from Compound Targets. Preliminary version of manuscript.

Other relevant publications and conference proceedings co-authored by the author:

- Virginie Hody-Le Caër, Estelle De Chambrier, **Stefan Mertin**, Martin Joly, Michel Schaer, Jean-Louis Scartezzini, and Andreas Schüler. Optical and Morphological Characterisation of Low Refractive Index Materials for Coatings on Solar Collector Glazing. *Renewable Energy,* Volume 53, May 2013, Pages 27-34

- **Stefan Mertin**, Virginie Hody-Le Caër, Martin Joly, Jean-Louis Scartezzini, and Andreas Schüler. Coloured Coatings for Glazing of Active Solar Thermal

Façades by Reactive Magnetron Sputtering. *CISBAT 2011, Cleantech for Sustainable Buildings - From Nano to Urban Scale, EPFL, Lausanne, September 2011*

- Iris Mack, **Stefan Mertin**, Virginie Hody-Le Caër, Yves Ducommun, and Andreas Schüler. Air Cooling Powered by Façade Integrated Coloured Opaque Solar Thermal Panels. *CISBAT 2011, Cleantech for Sustainable Buildings - From Nano to Urban Scale, EPFL, Lausanne, September 2011*

- Ségolène Pélisset, Martin Joly, Valentin Chapuis, Andreas Schüler, **Stefan Mertin**, Virginie Hody-Le Caër, Christophe Ballif, and Laure-Emmanuelle Perret-Aebi. Efficiency of Silicon Thin-Film Photovoltaic Modules with a Front Coloured Glass. *CISBAT 2011, Cleantech for Sustainable Buildings - From Nano to Urban Scale, EPFL, Lausanne, September 2011*

Related project reports co-authored by the author:

- Christian Roecker, Maria Cristina Munari Probst, Marja Edelman, Andreas Schüler, **Stefan Mertin**, Virginie Hody-Le Caër. Capteurs Solaires en Couleur; Phase 3: Intégration architecturale - Rapport final. *Swiss Federal Office of Energy,* Project: 100506 - Capteurs solaires en couleur; Publication Number: 290365; Date: 17.01.2011

Nomenclature

Acronyms

AFM atomic force microscopy

AR antireflection

CIE International Commission on Illumination (Commission Internationale de l´Eclairage)

CIELAB CIE $L^* a^* b^*$ colour system

CIME Interdisciplinary Centre for Electron Microscopy, EPFL

CMF colour-matching function

CMi Center for MicroNanoTechnology, EPFL

CTL colour-tuning layer

D$_{65}$ CIE illuminant D$_{65}$, natural daylight

DC direct current

DHW domestic hot water

EDX electron dispersive X-ray spectroscopy

EPFL École Polytechnique Fédérale de Lausanne

ESCA electron spectroscopy for chemical analysis

EU European Union

HV high vacuum

IPCC Intergovernmental Panel on Climate Change

IR infrared wavelength range

ITO indium tin oxide

LC Ceramics Laboratory, EPFL

LESO-PB Solar Energy and Building Physics Laboratory, EPFL

LMOM Laboratory of Macromolecular and Organic Materials, EPFL

Low-E low-emissivity

LP Polymers Laboratory, EPFL

MF mid frequency

NIR near-infrared wavelength range

PDF powder diffraction file

PES photoelectron spectroscopy

PIAD plasma ion-assisted deposition

PIPS$^{\text{TM}}$ precision ion polishing system

PV photovoltaic

PVD physical vapour deposition

QQR quarter quarter-wave reflector

QQR+ quarter quarter-wave reflector plus outer-layer

QQRAR quarter quarter-wave reflector plus anti-reflector

QW quarter-wave

RF radio frequency

RMSE root mean square error

R&D research and development

SAED selected area electron diffraction

sccm standard cubic centimetres per minute

SEM scanning electron microscopy

SPG sun protection glass

TEM transmission electron microscopy

UHV ultra-high vacuum

UV ultraviolet wavelength range

VIS visible wavelength range

XPS X-ray photoelectron spectroscopy

XRD X-ray diffraction

Physical quantities

$A(\lambda)$	absorptance
a^*	colour value a^* (CIELAB)
η	optical admittance
A_{sol}	solar absorptance
A_{vis}	visible absorptance
b^*	colour value b^* (CIELAB)
Δ	ellipsometric parameter
$\delta(\lambda)$	phase factor
ΔE	colour difference
Δ_{sol}	energetic solar loss
$\Delta_{\mathrm{sol,hh}}$	bi-hemispherical energetic solar loss
E_{b}	binding energy
$E(\lambda)$	electric field component
E_{k}	kinetic energy
ε	thermal emissivity
$H(\lambda)$	magnetic field component
$I_0(\lambda)$	incident radiation
$I_{\mathrm{R}}(\lambda)$	reflected radiation
$I_{\mathrm{T}}(\lambda)$	transmitted radiation
$k(\lambda)$	extinction coefficient
L^*	lightness value L^* (CIELAB)
λ	wavelength
λ_{ref}	reference wavelength
M	figure of merit
$n(\lambda)$	refractive index
$N(\lambda)$	complex refractive index
OPD	optical path difference
$\mathrm{P}_{\mathrm{CF}_4}$	partial pressure of CF_4
$\mathrm{P}_{\mathrm{O}_2}$	partial pressure of O_2
ψ	ellipsometric parameter
$R(\lambda)$	reflectance

$R(\lambda, \vartheta)$	angular-dependent reflectance
R_{sol}	solar reflectance
R_{vis}	visible reflectance
$T(\lambda)$	transmittance
$T(\lambda, \vartheta)$	angular-dependent transmittance
T_{sol}	solar transmittance
$T_{\text{sol,hh}}$	bi-hemispherical solar transmittance
T_{vis}	visible transmittance
ϑ	angle of light incidence
$V(\lambda)$	photopic luminous efficiency function
$\bar{x}(\lambda), \bar{y}(\lambda), \bar{z}(\lambda)$	colour-matching functions

Chemical formulas

Al	aluminium
Al_2O_3	aluminium oxide
Ar	argon
Au	gold
C	carbon
CaF_2	calcium fluoride
CeF_3	cerium fluoride
CF_4	carbon tetrafluoride
CF_x	fluorocarbons
CO	carbon monoxide
CO_2	carbon dioxide
F_2	fluorine
He	helium
Mg	magnesium
$Mg-F-Si-O$	magnesium-fluoride-silicon-oxide composite
MgF_2	magnesium fluoride
N_2	nitrogen
Na_3AlF_6	cryolite
O_2	oxygen
Si	silicon
Si_3N_4	silicon nitride
SiO_2	silicon dioxide
Ta_2O_5	tantalum oxide
Ti	titanium
TiO	titanium monoxide
TiO_2	titanium dioxide
TiO_2-SiO_2	titania-silica composite
$Ti_xSi_{1-x}O_y$	titanium-silicon-oxide composite

1 Introduction

1.1 Motivation

The world-wide increasing energy demand – combined with the limitation of fossil energy resources, leading to continuously increasing costs – stresses the importance for the use of alternative and sustainable energy sources. In addition, with respect to the 5th climatic report from 2013 of the Intergovernmental Panel on Climate Change (IPCC) a significant reduction of carbon dioxide (CO_2) emission is planned by the European Union (EU). There is a natural, and almost infinite energy source, which delivers energy free of charge and CO_2 emission to almost every place on earth: our sun. The energy density of direct sunlight at sea level is around $1100\,\mathrm{W/m^2}$.[1] This gives a great potential of an almost infinite source of energy. The impinging solar energy on earth during a time period of 30 min would be enough to cover todays total worldwide energy demand of one year.[2] However, only a small part of the potential solar radiation can be used. The main reason is a still moderate efficiency of solar devices when converting the primary energy (electro-magnetic radiation) into electricity.[3] In addition, the hours of sunshine vary with weather, season and geographic location.

For heat production, however, solar radiation can be converted very efficiently into hot water, which should be noticed, since the energy consumption in most European countries for space heating in buildings amounts to around 40%.[4] The idea to use solar thermal heating for buildings is obvious. A variety of highly selective black absorbers are available on the market to convert solar radiation into hot water, leading to an overall collector efficiency of up to 70% for solar thermal systems.[5] Nowadays, the majority of thermal collectors is installed on rooftops to produce domestic hot water (DHW) or to heat swimming pools; on top of that they can be

integrated in the heating system. The critical point of those installations is that a
huge amount of hot water is produced in summer whereas the need in this period
is relatively moderate. Therefore, to avoid overheating and boiling water in the
collector-heat-exchanger system, it is often necessary to switch off the system by
emptying the liquid circuit of the collectors. On the other hand, from autumn to
spring, less heat is produced. This can be barely compensated by heat storage in
hot-water tanks. Those tanks can only buffer cloudy and overcast days, however not
extended periods of non-sufficient heat production.[6] This makes it very difficult to
dimension a solar heating system and to integrate it into building services.[1]

In our latitudes however, one solution – to overcome the overheating in summer
without decreasing the energy produced during the rest of the year – would be
to install the solar thermal collectors on the building's façade rather than on the
rooftop. The solar radiation per square metre on south facing roofs and façades
through the year is shown in Figure 1.1. Since the solar radiation is less on the
façade, a larger collector area is needed to meet the same energy production as with
inclined collectors on the roof. While the impinging radiation peaks for the roof in
July, and therefore the energy gain, it is nearly constant on the façade from March
to September. Moreover in spring and autumn, where more heat is needed than in
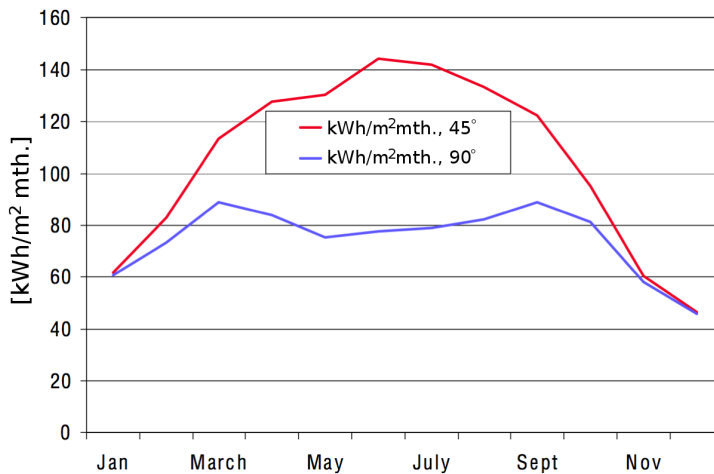

Figure 1.1: The solar radiation on south facing façade (90°) and roof (45°) mounted solar
thermal collectors. The advantage of the façade is the more regular and flatter profile of the
solar radiation.[7,8] Source: WEISS[7]

summer, a façade installation might be even favourable, since the sun remains low on its ecliptic. The overall reduced radiation on the façade could be easily compensated with a larger collector area, which is feasible since the total cost of a solar thermal installation does not scale linear with the area of solar panels. Increasing the active solar surface decreases the specific costs (costs/m^2) of solar collector systems.[5] In addition, on commercial buildings, there is often more surface available on the façade than on the rooftop.

However, there is a tradeoff which limits and often blocks the usage of solar thermal collectors. It is a pure aesthetic and architectural aspect. An architectural integration of common glazed or unglazed solar thermal collectors in a building is difficult to obtain, since perfect integration means that the collector becomes part of the building's envelope or an architectural design element and can therefore not be recognised immediately as solar collector.[7,8] The intense black or dark bluish colour of selective absorbers, which can be a flat plate, tubes, or a corrugated metal sheet with welding traces, is highly visible even through a standard cover glass. This gives collectors a very technical appearance, which often limits the acceptance of a solar thermal installation on highly visible building elements, such as the building's façade.[4,9] Mounting state-of-the-art solar thermal collectors on the façade changes its optic significantly. A harmonic and aesthetic integration with existing solutions can be only achieved by adapting the whole façade design to the collectors. Retrofits with standard collectors to old buildings without destroying their architectural appearance is not possible and often even not permitted due to protection of historic buildings. For all these reasons, conventional solar collectors are very rarely mounted on the façade of buildings.[7] In historic towns, in particular, standard solar panels or photovoltaic (PV) modules compared to orange-reddish roof tiles have a very high visual impact. Building and roof integration of PV modules, however, will not be further discussed, as they are topic of another doctoral thesis.[10]

Figure 1.2 shows modern buildings with façade mounted standard solar thermal collectors, as described in detail e.g. in DUFFIE AND BECKMANN.[1] The latter are integrated technically wise. However, they cannot be considered as fully architectural integrated. Since the ability of a good integration of solar collectors might have a greater impact on the solar collector market than price or technological improvement due to a higher acceptance, it is also important to focus on this aspect.[7] Associating

Figure 1.2: (a) Solar façade at the "centre d'entretien des routes nationales" (CERN) in Bursins, Switzerland. Credits: Energie Solaire SA. (b) Façade installation with glazed solar thermal collectors. Credits: Winkler Solar GmbH

the visible and exposed part of the collector with a colour, while hiding the technical installation (absorber, tubes, etc.) behind, would grant architects complete freedom to integrate them perfectly into the building's envelope. [8,11,12]

As part of the research presented in this thesis, coloured cover-glass panels for solar thermal collectors on the basis of coloured interference thin films are developed. Hereby, the work focuses on the different aspects of the development of new coloured coatings to improve their visual properties and at the same time to increase their energetic performance. Furthermore, only industrial-used deposition techniques are employed in order to facilitate the industrialisation of the proposed new coatings.

1.2 Structure of the presented research

The research on coloured coatings for solar collectors deals with following aspects: development of new thin-film multilayer stacks by numerical simulations and optical analysis, investigation of novel coating materials with low and tuneable refractive indices, and finally the deposition of those coating materials, including multilayer stacks of coloured filters. For the film deposition reactive magnetron sputtering is used – a wide-spread technology for optical coatings on glass.

This thesis is structured as follows:

Chapter 2 describes the state-of-the-art research prior to this work and defines the scientific goals of the presented research. Different approaches for coloured solar collectors are discussed and suitable materials for potential solar applica-

tions and their deposition in industrial production are reviewed. The chapter concludes with the definition of the scientific objectives of this thesis.

Chapter 3 deals with the design and development of optical coatings in general, and solar coatings in particular. The basic theory of thin-film optical filters is reviewed, as well as the principle of coloured solar interference and anti-reflective coatings. The used characterisation methods for optical properties are described in detail. The basic principle of coloured filters for solar thermal collectors is discussed and new coloured filter designs developed during this doctoral work are presented including a newly developed and very flexible advanced simulation framework for optical thin films on the basis of Wolfram Mathematica$^{\text{TM}}$.

Chapter 4 outlines the experimental work performed in the scope of this research. In particular, new developed and built scientific equipment and tools for film deposition, as well as in-situ and ex-situ film analysis is shown. In addition, new established deposition processes and methods are explained.

Chapter 5 presents and discusses the results and outcome of the thesis research. It is structured in four sections corresponding to four journal articles, where one of them is published, two are submitted, and one is in preparation:

- *Reactively Sputtered Coatings on Architectural Glazing for Coloured Active Solar Thermal Façades*, published in *Energy and Buildings* 68 (2014) 764–770.

- *Nanocrystalline Low-Refractive Magnesium Fluoride Films Deposited by Reactive Magnetron Sputtering: Optical and Structural Properties*, submitted manuscript.

- *Advanced Coloured Coating Designs with Colour-Invariant Solar Transmittance by Means of a Magnesium Fluoride Inter-Layer*, submitted manuscript.

- *Combinatorial Study of Low-Refractive $Mg-F-Si-O$ Nano-Composites Deposited by Magnetron Co-Sputtering from Compound Targets*, preliminary version of manuscript.

Chapter 6 summarises and concludes this research work. It combines the different aspects of research and reflects them in a global context. Finally, it gives an outlook and visionary view on future research, development and applications.

2 State-of-the-Art and Objectives

2.1 Coloured solar thermal collectors

One approach towards coloured solar thermal collectors is to change the colour of the principle collector element: the absorber. Tripanagnostopoulos et al.[13] propose to use, instead of a highly selective black absorber coating, a coloured moderate selective paint. They assume that the resulting reduced efficiency of the collector could be compensated by additional booster reflectors. Crnjak Orel et al.[14] replace partially the black pigments of the selective paint to generate a colour. They report a moderate selectivity of $A_{\mathrm{sol}} = 85\%$ (solar absorptance) and $\varepsilon = 25\%$ (thermal emissivity) for blueish and greenish colours and $A_{\mathrm{sol}} = 80\%$ and $\varepsilon = 30\%$ for yellowish colours in comparison to $A_{\mathrm{sol}} = 89\%$ and $\varepsilon = 15\%$ for their black absorber. Kalogirou et al.[12] investigate the efficiency of collectors with coloured selective paint ($A_{\mathrm{sol}} = 85\%$ and $\varepsilon = 10\%$) in comparison to black ($A_{\mathrm{sol}} = 95\%$ and $\varepsilon = 10\%$) selective absorbers. An acceptable decrease of collector efficiency by 7–18%, compared to the black absorbers, depending on the geographical location is reported.

Another approach is to embed coloured pigments in an alumina matrix by spray pyrolysis electroplating. A low thermal emissivity (5–7%) is reported, but at the same time the achieved solar absorptance is only 62–65%.[15] Since both, absorptance and emissivity increase with coating thickness, a compromise for thick and colour-intensive layers – having at the same time a low emissivity – needs to be found.[14] Zhu and Zhao[16] propose a coloured selective multilayer coating instead of a coloured paint on the absorber deposited by magnetron sputtering. For a green coloured coating they report a high performance with $A_{\mathrm{sol}} = 92\%$ and $\varepsilon = 8\%$. These coloured absorbers can be integrated into buildings with improved optical appearance and aesthetic, as can be seen on the photograph of a retrofitted building with reddish

Figure 2.1: Example for a building retrofit with a reddish coloured solar thermal installation in Göttingen, Germany. Credits: SOLARWALL[©]

Solarwall[©] collectors in Figure 2.1. However, there is a drawback of colouring the absorber: the technical structure, such as tubes, welding points, and corrugated metal sheets still give a very technical appearance.

In collaboration with the University of Basel researchers from the Solar Energy and Building Physics Laboratory (LESO-PB), EPFL, propose a different approach for coloured collectors: producing a coloured reflection by means of an optical interference film on the reverse side of the cover-glass panel of glazed solar collectors while the front side of the glass exhibits a light-diffusing surface finish by chemical etching.[11,17,18] Structural properties, such as welding points and corrugated metal sheets are no longer visible. Moreover, it opens the possibility to use every type of thermal absorber (flat plate or tubes) behind such a coloured glass panel. In addition, colouring the cover glass rather than the absorber separates the function of selective absorption and coloured appearance. This approach permits more freedom and flexibility for optimisation.[17] In addition, the same coloured glass panel could be used also with no absorber behind as a dummy design element. Ergo, with so-called active and passive solar façade elements a complete uniform building and façade integration could be achieved, which would grant architects complete freedom for a perfect architectural integration of solar collectors into the building's envelope.[8,11]

The physical principle and basic idea of the coloured thermal collectors is described by Schüler et al.[19] and Roecker et al.[20] report a first breakthrough. Sev-

eral design types for coloured interference filters on the basis of alternating high- and low-refractive-index materials with negligible optical absorptance are proposed. [17,19] The feasibility of coloured thermal collectors has been successfully demonstrated by sol–gel deposition technique and magnetron sputtering at LESO-PB and at the Department of Physics of the University of Basel, respectively. [21–23] In addition, three real-size prototypes (see Figure 2.2) were produced in collaboration with Glas Trösch AG, Switzerland. However, industrial in-line sputtering process and coating design were not yet well coordinated and tuned to produce the coloured coatings with an optimised energetic performance. Details of the industrial process are described in Section 2.2.2 and the principle of the coloured coatings is discussed in Section 3.1.2.
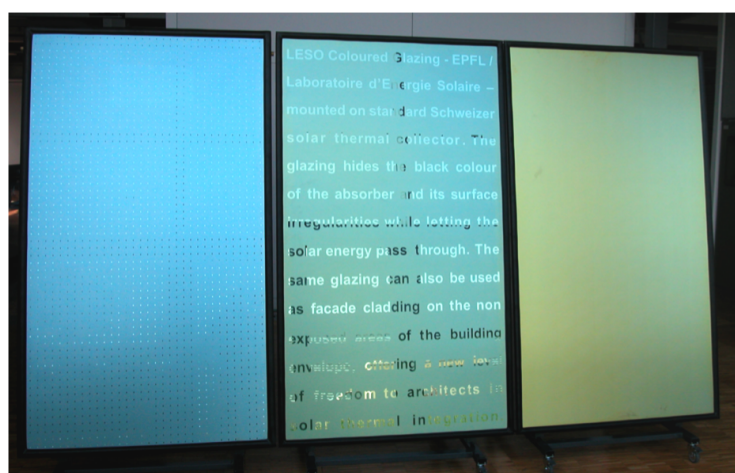

Figure 2.2: Photograph of the real-size coloured collector prototypes at LESO-PB, EPFL, with a coloured interference coating on the reverse side of the cover glass. The front side is a light-diffusing chemically etched surface: different patterning, even letters or individual logos are possible.

2.2 Solar coatings

2.2.1 Interference-filter materials

In general, one speaks about solar coatings when the optical film properties are adapted to the solar spectrum. The considered solar range may vary with application. A weak or near-zero absorptance is a requisite if only interference effects should occur inside the film. Interference thin films consist of alternating high- and low-refractive-

index materials. For optical interference coatings widely used high-index materials are titanium dioxide (TiO_2),[23–26] tantalum oxide (Ta_2O_5),[24,25,27–29] and silicon nitride (Si_3N_4):[25,26,30,31] they form hard and durable films. Magnesium fluoride (MgF_2) has a low refractive index ($n = 1.38$) which is the lowest known refractive index among inorganic compact and dense coating materials.[32,33] Therefore, MgF_2 is predestinated as low-index material. Fluorides in general are transparent over a wide range of electromagnetic radiation, from the ultraviolet (UV) to the infrared (IR) wavelength range. Other fluorides to be considered for optical coatings are e.g. calcium fluoride (CaF_2), cerium fluoride (CeF_3) and cryolite (Na_3AlF_6).[26,34,35]

For large-scale production in glass industry, such as in-line magnetron sputtering, silicon dioxide (SiO_2) is often used as low-refractive-index material ($n = 1.45$–1.5). It is used, although its refractive index is higher than the one of MgF_2, because there has been no known reliable sputtering process for MgF_2 yet.

Lately, nano-composite materials came in discussion due to the possibility to tune their refractive index over a wide range.[36–41] A summary of selected oxides and nitrides is given in Table 2.1, and of fluorides in Table 2.2. Figure 2.3 illustrates the transparency range of selected optical coating materials based on the graphic from Hass and Ritter.[42]

A huge variety of materials with different optical properties play a central role for more flexibility and freedom in designing optical thin-film filters, which is an important condition to be able to improve the film performance for a specific application.

Material	n at 550 nm	Used as high/low	Sputtering Mode	References
SiO_2	1.45-1.5	low	RF, r.p.DC, Twin	23–26
SiO_xN_y	1.5-2.0	low or high	r.p.DC	30,43
Al_3O_2	1.63-1.65	low or high	r.p.DC	23,24,27
TiO_2	2.2–2.7	high	r.p.DC, Twin	23–26
$Ti_xSi_{1-x}O_2$	1.5–2.4	low or high	RF, r.p.DC	18,44
Ta_2O_5	1.8–2.18	high	RF, Twin	24,25,27,29
Si_3N_4	1.8–2.05	high	RF, Twin	25,26,30,31
ZnO	2.00	high	Twin	25
SnO_2	2.00	high	RF, Twin	25,45

Table 2.1: Selected low- and high-refractive-index oxides and nitrides for sputtered dielectric coatings. The sputtering modes are RF (radio frequency at 13.56 MHz), r.p.DC (reactive pulsed direct current), and Twin (twin magnetron sputtering at 10–100 kHz).

Material	n at 193 nm	Transparency	Method	References
MgF_2	1.38–1.40	0.2–5 µm	sol–gel, IBS, evaporation	32,35,46,47
CaF_2	1.43	0.5–12 µm	sol–gel, ALD, evaporation	24,34,48,49
CeF_3	1.63	0.3–5 µm	evaporation	35,50
Na_3AlF_6	1.35	0.2–10 µm	evaporation	35,51

Table 2.2: Selected fluorides for optical coatings. Those fluorides exhibit a relative low refractive index and stand out for their large wavelength range of transparency down to the UV. The deposition methods are sol–gel, IBS (ion beam sputtering), ALD (atomic layer deposition), and physical vapour evaporation.
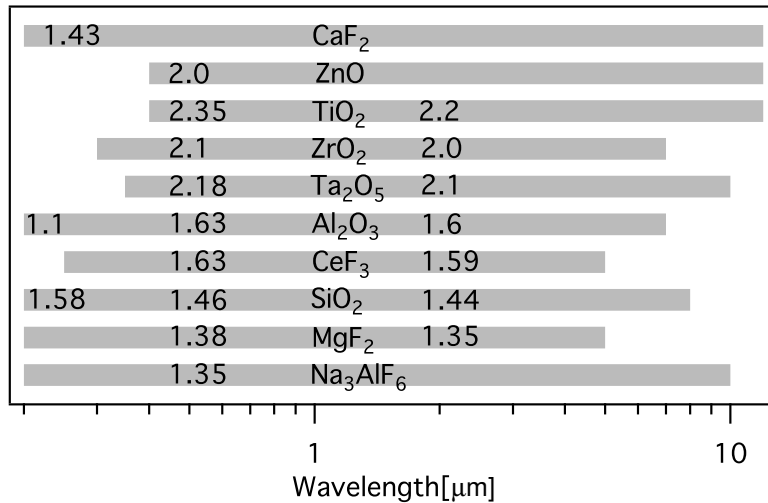

Figure 2.3: Transparency range of optical coatings (oxides and fluorides) including refractive indices at different wavelengths. [24,25,42]

2.2.2 Large-area optical coating deposition

Common techniques for thin-film deposition are physical vapour deposition (PVD), such as thermal evaporation, electron-beam evaporation, and magnetron sputtering, [52–54] chemical vapour deposition, [55] and dip-coating (sol–gel). [56] They are used for a wide range of optical coatings going from thin-film photovoltaic cells to high precision filters on glass. [26] However, for large-area coating magnetron sputtering is the dominant deposition technique, since it can be easily up-scaled to coat glass panes up to $3.2 \times 6\,m^2$ with a high reproducibility. [26,57] This is mandatory for architectural application where it is necessary to produce thousands of square metres of identical glass with an industrial in-line vacuum coater. Potential applications go
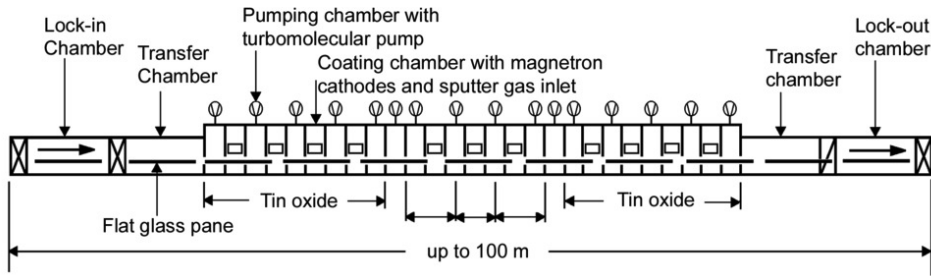
Figure 2.4: Schematic drawing of an industrial in-line plant for magnetron sputtering for architectural glazing. Source: GLÄSER[59]

from low-emissivity (Low-E) coatings, over more advanced sun-protection coatings on architectural glazing, to anti-reflective coatings, and conductive transparent ITO (indium tin oxide) coatings for displays and thin-film photovoltaics.[26,58]

The working principle of in-line sputtering plants is that glass panes move with constant speed underneath the sputtering sources – the magnetrons – which cover the whole width of the glass panes (see Figure 2.4 and 2.5). By adjusting glass transport speed and target power one can change the deposition rate and with it the film thickness. However, the constant displacement of the glass substrate leads to a particular characteristic of in-line sputtering plants: it is very difficult to deposit very thin layers from target materials exhibiting a high sputtering yield alternating with thick layers from targets with a low sputtering yield. This fact was also a limitation when producing the first coloured prototypes of LESO-PB (see Figure 2.2).

Most layers deposited in glass industry are dielectrics, such as SiO_2 and TiO_2. They can be sputtered in reactive mode from semiconductor (Si) or metallic targets (Ti), from partially oxidised targets (TiO), or from completely oxidised ceramic (TiO_2) and quartz glass targets (SiO_2) in non-reactive mode. An inert gas, such as argon (Ar), is used as sputtering gas and additional gases such as oxygen (O_2) and nitrogen (N_2) are added to the process in case of reactive sputtering. To stabilise the deposition process and to reduce the electric charges on the target during the reactive process, double or twin planar and rotary cathodes are used.

The principle of twin cathodes is shown in Figure 2.5. They are driven by mid-frequency power, as above a frequency of $10\,kHz$ arcing can be successfully suppressed.[61] Hereby, half of the cycle time each target acts as cathode, the other half cycle as anode: charges can be efficiently neutralised.[60] Using rotary targets min-
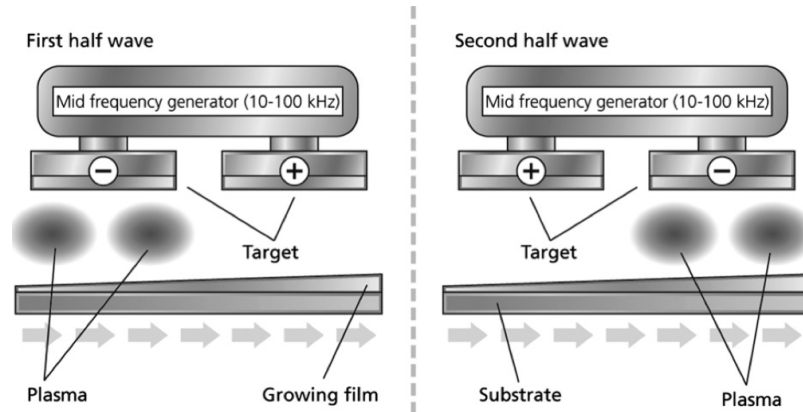
Figure 2.5: Principle of double planar cathodes driven by MF AC power at frequencies 10-100 kHz to reduce the charging potential. Each cathode acts alternatively as electrical cathode and anode. [60]

imise additionally the inhomogenously consumed surface of the target during reactive sputtering and therefore the areas where arcing can appear, which makes the plasma discharge more stable. [62] Figure 2.6a shows the principle of a rotary cathode. Water cooling and magnets are placed statically insight the tube, while the target material in cylindric form covers only the outside of the rotating body. Figure 2.6b illustrates the different areas of sputtering (plasma erosion or race track) of a planar cathode in comparison to a rotary cathode. For details about the sputtering processes used in this research see Section 4.1.
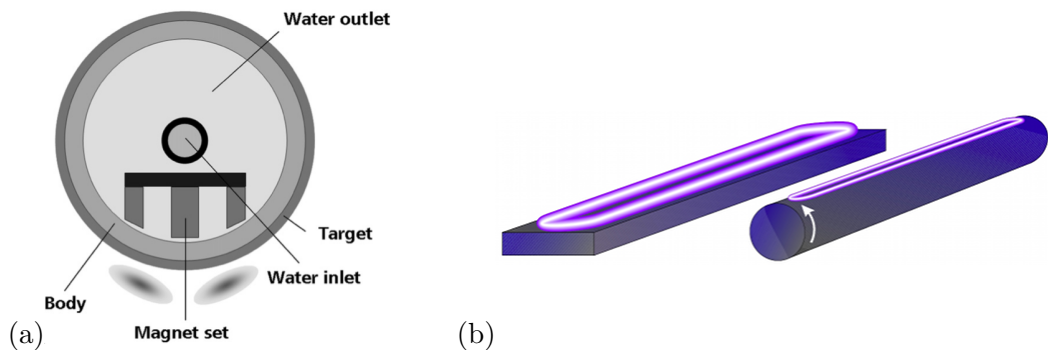

Figure 2.6: (a) Principle of a rotary cathode. Water cooling and magnets are placed inside a hollow cylinder. Due to the rotation the surface of the target material gets eroded homogeneously. (b) Differences in the plasma area (race-track) on planar and rotary cathodes. [60,62]

2.3   Scientific goals of thesis

The aim of this thesis research is to develop new coating designs for coloured solar collectors with an improved energetic and optical performance. As a requisite they should be suitable for up-scaling to industrial production. This defines also the boundary conditions for the usage of the deposition technique (magnetron sputtering) as well as the potential coating materials and the layer thicknesses. Since the research is close to application – building integration of solar thermal collectors – also a study to match the colours of the collectors to existing architectural glazing is performed. Furthermore, the objective is to investigate novel low-refractive-index coating materials to provide more flexibility in the multilayer design to be able to further improve the coloured filters. Therefore, novel sputtering processes need to be found, and their potential for up-scaling to industrial dimensions shall be evaluated. The individual scientific goals of the thesis are summarised below:

- Developing of new coloured interference filters with improved solar energy and visual performance.

- Colour matching of coloured collector glazing with commercial architectural glazing and building elements.

- Investigating novel sputtering processes for low-refractive-index materials on the basis of MgF_2 with a refractive index smaller than the one of SiO_2, which can provide more flexibility in the coloured coating designs.

- Developing of novel advanced optical filters on the basis of the researched low-refractive-index materials.

- Reducing the number of free and variable design and deposition parameters of the coloured filters with the aim to shorten the coating development cycle, when fine-tuning the coloured filters for e. g. colour matching.

- Industrial prototyping of coloured multilayers applying the optimised and advanced filters and the researched coating materials.

3 Theoretical Background and Coating-Design Engineering

The first two sections of this chapter describe the principle of non-absorbing solar coatings based on the examples of quarter-wave multilayer and antireflection stacks as well as the optical characterisation techniques, which are fundamental for coating development. The third and forth section deal with the basics of colour matching and the therefore applied coating development cycle. The following two sections give a description of existing and novel simulation tools and present coloured coating designs which were newly developed and optimised in this doctoral research.

3.1 Principle of non-absorbing solar coatings

3.1.1 Optics of thin-film filters

Optical thin-film filters describe in general coatings designed to influence, modify and enhance the optical properties of a substrate within the wavelength range of ultraviolet (UV, 100–400 nm), visible (VIS, 400–800 nm), and near infrared (NIR, 0.8–3 μm) electromagnetic radiation, further also noted as light.[63] Those filters are based on thin single-layer or multilayer coatings; hereby, a film is called optically thin when interference effects are dominating.

At each interface between two media an incoming beam is split into transmitted and reflected parts (see Figure 3.1). The phenomena of reflection and transmission can be explained when light is described as an electromagnetic wave. The relation between the electric and magnetic field vectors $\vec{E}$ and $\vec{H}$ is given through the Maxwell equations (see Appendix B.1). $\vec{E}$, $\vec{H}$ and the direction of propagation $\vec{x}$ describe a right-handed set (see Figure 3.2). At the interface between two media with the
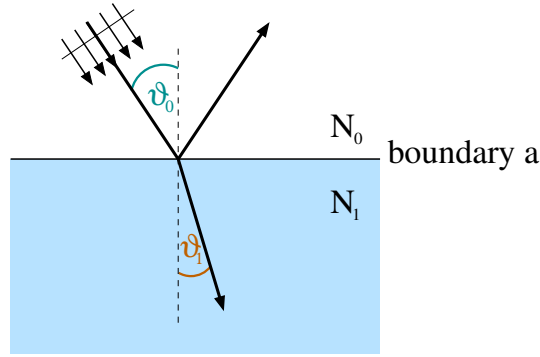
Figure 3.1: Schematic drawing of incident, reflected and transmitted beam on a plane interface with the boundary a. The incident angle ϑ_0 is linked to the refracted angle ϑ_1 through Snell's law. N_0 and N_1 are the complex refractive indices of the two media.

complex refractive indices $N_0 = (n_0 - ik_0)$ and $N_1 = (n_1 - ik_1)$ the field components of the wave change. The real part of the complex refractive index $N(\lambda)$ is called simply refractive index $n(\lambda)$ and the imaginary part extinction coefficient $k(\lambda)$.

For the reflected wave the direction of propagation perpendicular to the boundary is reversed, consequently the orientation of magnetic and electric field cannot remain both the same: the right-handed set must remain valid. By convention, the orientation of the electric field vector remains unchanged, while the orientation of the magnetic field vector changes.[64] In order to understand the optics of thin films the reflectance R and transmittance T need to be described as a function of the electromagnetic field components. It is useful to introduce the components H and E of the wave vectors $\vec{H}$ and $\vec{E}$, which are parallel to the boundary plane, and to define $\eta = \frac{H}{E}$ as the corresponding tilted optical admittance (arbitrary incident angle ϑ_0). For normal incidence at optical frequencies the optical admittance can be written as

$$\eta = N \cdot \mathcal{Y} \tag{3.1}$$

where $\mathcal{Y}$ is the optical admittance in free space. For the oblique case however, the incoming arbitrarily polarised electromagnetic wave splits into two components, $\vec{E}_{\mathrm{p}}$ parallel aligned to the plane boundary (p-polarised) and $\vec{E}_{\mathrm{s}}$ perpendicular (s-polarised) to the boundary. The orientation of the corresponding H-vectors follow the rule of the right-handed set and the optical admittance is given for p- and s-
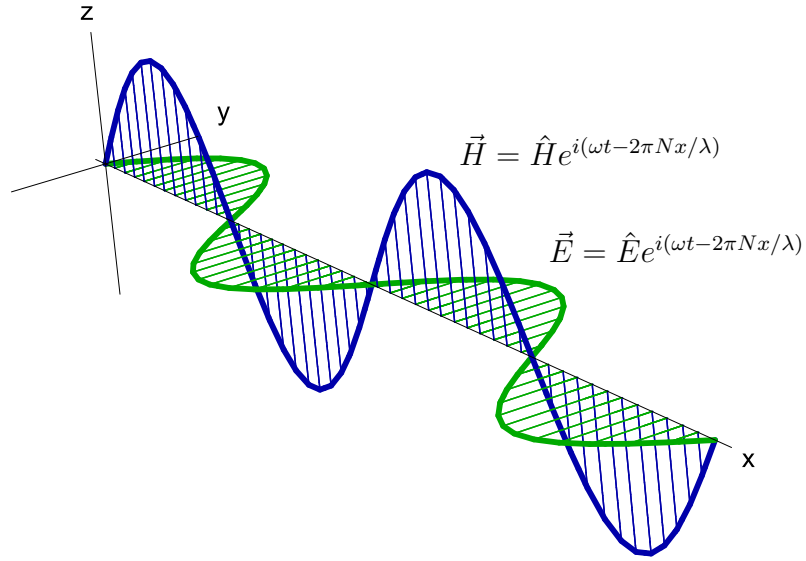
$$\vec{H} = \hat{H}e^{i(\omega t - 2\pi N x/\lambda)}$$

$$\vec{E} = \hat{E}e^{i(\omega t - 2\pi N x/\lambda)}$$

Figure 3.2: Plot of an electromagnetic wave. $\vec{E}$ and $\vec{H}$ are perpendicular, and both are normal to the propagation direction $\vec{x}$, forming an orthogonal right-handed set. $\hat{E}$ and $\hat{H}$ are the amplitudes and $N = (n - ik)$ is the complex refractive index.

polarised beams respectively by:

$$\eta_{\mathrm{p}} = \frac{N\mathcal{Y}}{\cos\vartheta} = \frac{(n - ik)\mathcal{Y}}{\cos\vartheta} \tag{3.2}$$

$$\eta_{\mathrm{s}} = N\mathcal{Y}\cos\vartheta = (n - ik)\mathcal{Y}\cos\vartheta \tag{3.3}$$

where N and ϑ are those appropriate to the corresponding medium (see Figure 3.1).[33] Using the optical admittance from Equation (3.2) and (3.3) the reflectance at a single interface is then given by

$$R = \left(\frac{\eta_0 - \eta_1}{\eta_0 + \eta_1}\right)\left(\frac{\eta_0 - \eta_1}{\eta_0 + \eta_1}\right)^{*} \tag{3.4}$$

and the corresponding transmittance by

$$T = \frac{4\eta_0 Re(\eta_1)}{(\eta_0 + \eta_1)(\eta_0 + \eta_1)^{*}} \tag{3.5}$$

where $*$ denotes complex conjugate; the indices in η_0 and η_1 refer to the incident and

exit medium, respectively. [33] Hereby, the reflected electromagnetic wave undergoes a phase shift of π for $n_1 > n_0$ whereas the transmitted wave remains in phase. For the incident medium – as it is in most cases air – zero absorption ($k = 0$) can be assumed. However, substrate and coating materials may have a non-negligible absorptance.

Single-layer thin films

Adding a layer to the system introduces an additional boundary for the electromagnetic wave when propagating from the incident medium to the substrate (see Figure 3.3). The beam reflected at the first boundary a and the beam reflected at the second boundary b undergo a constructive interference when the optical path difference (OPD) between the two is

$$OPD = m \cdot \lambda \tag{3.6}$$

where λ is the wavelength and m any natural number. The corresponding condition for destructive interference is:

$$OPD = \frac{2m - 1}{2} \cdot \lambda \tag{3.7}$$

Applying Snell's law $N_0 \sin \vartheta_0 = N_1 \sin \vartheta_1$ where ϑ_0 and ϑ_1 are the incident and refractive angle, and N_0 and N_1 the refractive indices of incident medium and film,
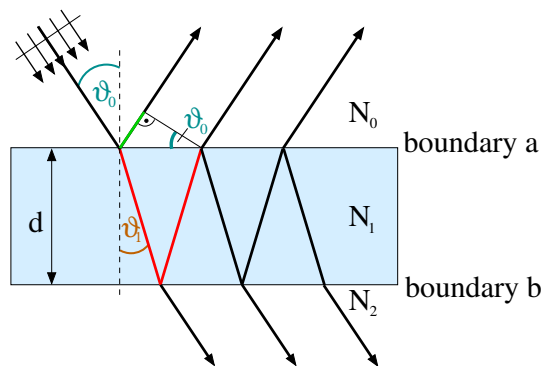

Figure 3.3: Schematic drawing of multiple reflections and transmissions between the two surfaces of a thin film. The incident angle ϑ_0 is connected with the refracted angle ϑ_1 by Snell's law. The optical path differences between light reflected at the front interface and at the back interface is marked in green and red, respectively.

respectively, the OPD of latter can be calculated using the geometrical relations given in Figure 3.3 as follows:

$$
\begin{aligned}
OPD &= \left(2\frac{N_1 d}{\cos \vartheta_1} - 2N_0 d \tan \vartheta_1 \sin \vartheta_0 \right) \\
&= \left(2\frac{N_1 d}{\cos \vartheta_1} - 2N_1 d \frac{\sin^2 \vartheta_1}{\cos \vartheta_1} \right) \\
OPD &= 2N_1 d \cos \vartheta_1
\end{aligned}
\tag{3.8}
$$

With Equation (3.8) an optical phase factor δ can be defined:

$$
\begin{aligned}
2\delta &= \frac{2\pi}{\lambda} OPD \\
&= \frac{2\pi}{\lambda} 2N_1 d \cos \vartheta_1 \\
\delta &= \frac{2\pi N_1 d \cos \vartheta_1}{\lambda}
\end{aligned}
\tag{3.9}
$$

The variation of E and H at the boundary a can be described by multiplying the characteristic matrix of the film with the field components at the boundary b through the fundamental equation

$$
\begin{bmatrix} E_a \\ H_a \end{bmatrix} = \begin{bmatrix} \cos(\delta) & \frac{i\sin(\delta)}{\eta_1} \\ i\eta_1 \sin(\delta) & \cos(\delta) \end{bmatrix} \cdot \begin{bmatrix} E_b \\ H_b \end{bmatrix}
\tag{3.10}
$$

where δ is the phase factor from Equation (3.9) with the physical layer thickness d. Hereby, $OPD = 2N_1 d \cos \vartheta_1$ has to be smaller then the coherence length of light,[33] which is fulfilled for thin films. The indices a and b represent the boundaries of the two interfaces of the single layer in Figure 3.3. $N_1 = (n_1 - ik_1)$ is the complex refractive index, while the angle ϑ_1 becomes complex for $k > 0$. Equation (3.10) can be re-written in normalised form as:

$$
\begin{bmatrix} E_a/E_b \\ H_a/E_b \end{bmatrix} = \begin{bmatrix} B \\ C \end{bmatrix} = \begin{bmatrix} \cos(\delta) & \frac{i\sin(\delta)}{\eta_1} \\ i\eta_1 \sin(\delta) & \cos(\delta) \end{bmatrix} \cdot \begin{bmatrix} 1 \\ \eta_2 \end{bmatrix}
\tag{3.11}
$$

$\begin{bmatrix} B \\ C \end{bmatrix}$ is called characteristic matrix of the assembly.

Multilayer thin films

Adding a second or more layers to the system introduces a new boundary for each layer. One speaks of a multilayer stack. Since every layer can be represented by its specific characteristic matrix, the whole stack consisting of q layers can be mathematically described as a product of those matrices:[33]

$$\prod_{r=1}^{q} M_r = \prod_{r=1}^{q} \begin{bmatrix} \cos(\delta_r) & \frac{i \sin(\delta_r)}{\eta_r} \\ i\eta_r \sin(\delta_r) & \cos(\delta_r) \end{bmatrix} \tag{3.12}$$

Hereby, the order of the layers needs to be respected. Figure 3.4 illustrates the multiple reflections in a multilayered thin film consisting of three layers. Combining Equation (3.11) and (3.12) describes the total assembly of q layers on the substrate:

$$\begin{bmatrix} B \\ C \end{bmatrix} = \prod_{r=1}^{q} M_r \cdot \begin{bmatrix} 1 \\ \eta_{\text{sub}} \end{bmatrix} \tag{3.13}$$

Analog to the titled optical admittance $\eta = \frac{H}{E}$, an optical admittance Y of the parallel field components at the first boundary E_a and H_a of a multilayer coating
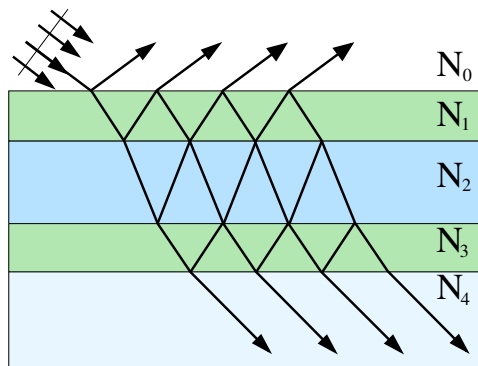

Figure 3.4: Schematic drawing of a planar wave incidenting on a multilayer thin film, which consists of three optically flat layers. N_0 is 1 (incident medium air) and N_4 corresponds to the complex refractive index of the substrate.

can be defined:

$$Y(\lambda) = \frac{H_a(\lambda)}{E_a(\lambda)} = \frac{C}{B} \tag{3.14}$$

By replacing η_1 in Equation (3.4) with Y, the spectral reflectance $R(\lambda)$ of the whole assembly can be written as

$$R(\lambda) = \left(\frac{\eta_0(\lambda) - Y(\lambda)}{\eta_0(\lambda) + Y(\lambda)}\right)\left(\frac{\eta_0(\lambda) - Y(\lambda)}{\eta_0(\lambda) + Y(\lambda)}\right)^* \tag{3.15}$$

and the spectral transmittance in Equation (3.5) becomes:

$$T(\lambda) = \frac{4\eta_0(\lambda)Re(Y(\lambda))}{(\eta_0(\lambda) + Y(\lambda))(\eta_0(\lambda) + Y(\lambda))^*} \tag{3.16}$$

The absorption can be simply derived by energy conservation

$$A(\lambda) = 1 - T(\lambda) - R(\lambda) \tag{3.17}$$

i.e., all light that is neither transmitted nor reflected is necessarily absorbed (assuming optical flat interfaces and no scattering). For non-absorbing films ($k = 0$) Equation (3.15), (3.16) and (3.17) simplify to

$$R(\lambda) = \left(\frac{\eta_0(\lambda) - Y(\lambda)}{\eta_0(\lambda) + Y(\lambda)}\right)^2 \tag{3.18}$$

$$T(\lambda) = \frac{4\eta_0(\lambda)Y(\lambda)}{(\eta_0(\lambda) + Y(\lambda))^2} \tag{3.19}$$

$$1 = T(\lambda) + R(\lambda) \tag{3.20}$$

3.1.2 Coloured solar interference coatings

The basic idea of coloured solar coatings is to give solar glass panels a coloured appearance while remaining highly transparent over most part of the solar spectral range – in other words: introducing an aesthetic aspect to solar thermal panels while preserving the energetic efficiency (see Chapter 2). The principle of coloured

solar coatings is based on optical interference filters producing ideally a narrowband reflection in the VIS, while the solar radiation of all other wavelengths should be transmitted, as shown in Figure 3.5. Three fundamental properties can be defined as requirements: [17,19,22,65]

- near-zero absorption in the whole solar spectral range

- narrowband coloured reflection peak with a significant visible reflectance R_{vis}

- high solar transmittance T_{sol} for the whole system (glass panel plus coating)

Dealing with solar thermal collectors the whole solar spectrum needs to be taken into account, since black selective absorbers are sensitive in the whole solar range. The wavelength range 300–2500 nm covers 99% of the total solar spectrum on sea level and is therefore well adapted for investigations of solar-thermal-collector coatings. Due to the first requirement – quasi-nil absorption – dielectric films turned out to be the most promising materials for such coatings, [17] as their extinction coefficient
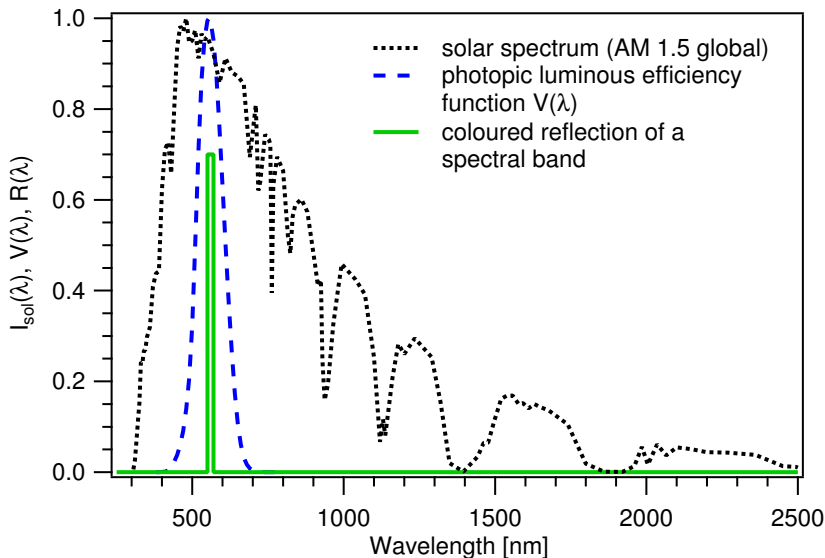

Figure 3.5: Principle of coloured coatings for solar collectors. [8,19] To illustrate the principle an idealised narrowband coloured reflection is plotted in the visible spectral range, with the human eye sensitivity (photopic luminous efficiency function $V(\lambda)$) and the solar spectrum.

$k(\lambda)$ is zero or nearly zero in the considered spectral range (see transparency range of dielectric coating materials in Figure 2.3).

The second requirement of a coloured reflection peak can be achieved by thin-film narrowband filters. Narrowband filters are in general made of two reflectors separated by a spacer layer.[33] The spacer layer is a half-wave layer of either a low (LL) or a high (HH) refractive-index material. Whereas the reflectors are made of a series of H and L layers having each an optical quarter-wave thickness. H and L denote hereby the thickness of a quarter-wave layer of high- or low-refractive-index materials, respectively. For a given number of layers the reflectance is maximised, if the outermost layer is an H layer.

This general setup for narrowband filters has been simplified by Schüler et al.[19] for the application of coloured solar collector glazing. Instead of using a spacer layer and two reflectors, they propose a quarter-wave multilayer stack with the design schemata glass$\|(HL)^m H\|$air (see Figure 3.6a), where m denotes a natural number. This design is further also denoted as quarter-wave (QW) design. The calculated reflectance and transmittance of the proposed design schemata for varying m are given in Figure 3.6b, showing that the peaks become more intense and more narrow when m is increased. This effect is more pronounced for small differences in the
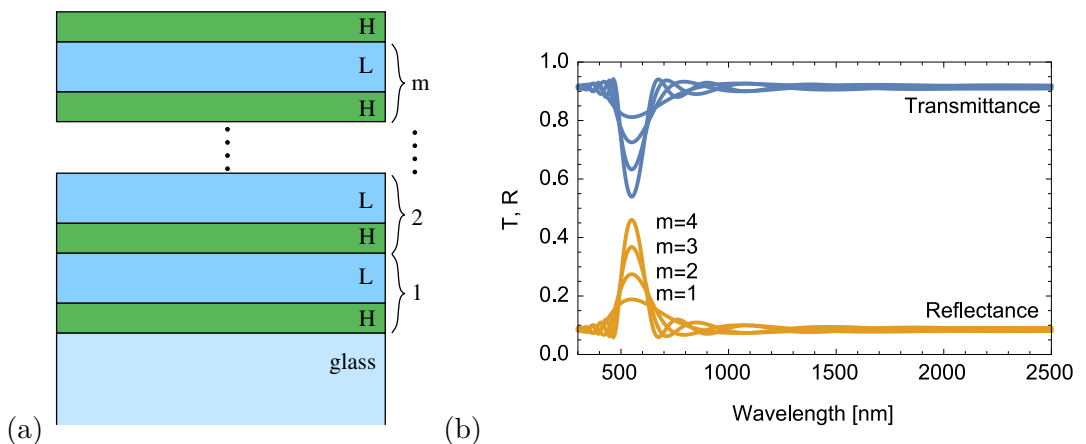

Figure 3.6: (a) Typical QW design type glass$\|(HL)^m H\|$air of the coloured filters, where H and L represent the corresponding quarter-wave thickness of the high-index and low-index material, respectively. (b) Calculated reflectance and transmittance for $1 \leq m \leq 4$ and $\lambda_{\mathrm{ref}} = 550\,\mathrm{nm}$. At greater m (more layers) the reflectance peak becomes more intense and more narrow.[19]

$n(\lambda)$ between the H- and L-layers. For the simulations, the H-index is $n = 1.63$ (aluminium oxide, Al_2O_3) and the L-index is $n = 1.45$ (SiO_2).

The a^*b^*-plane of the CIELAB diagram in Figure 3.7a illustrates the reflection colour depending on the design parameter m. It can be seen that increasing m leads to more saturated spectral colours. The CIELAB ($L^*a^*b^*$) colour space of the International Commision on Illumination (CIE)[1] describes and quantifies colours mathematically.[66] L^* is defined as the lightness of the colour, whereas the a^*-axis represents colours from red to green and the b^*-axis from yellow to blue. It is often used to describe colour differences as it represents well the colour vision of the human eye.[67] Another colour system is the CIE 1931. It describes all natural colours by the chromaticity diagram (xy-plane), where saturated spectral colours follow a horseshoe-like trajectory, and the relative luminance Y of a colour is directly linked to R_{vis}. For more details about the CIE colour systems see SCHANDA[66] and Appendix A.2.
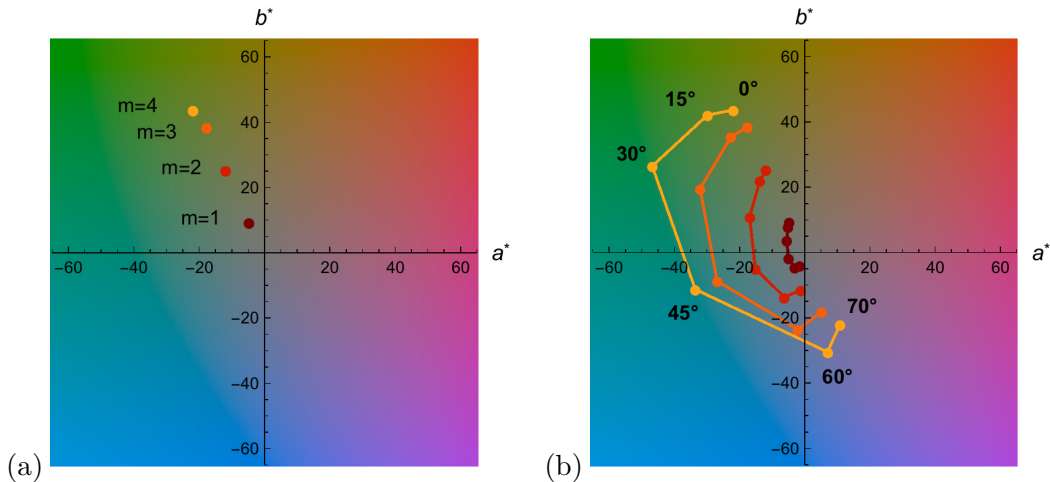

(a)   (b)

Figure 3.7: (a) Colour values for the quarter-wave designs for $1 \leq m \leq 4$ and $\lambda_{ref} = 550\,nm$. For increasing m the reflection colour gets more saturated (data points from dark red to yellow). (b) Variation of the colours for increasing angle of incident from $0°$ to $70°$.

Furthermore, the angular dependency of the coloured reflection for changing viewing angle from 0–$70°$ is shown in Figure 3.7b. It is a general property of coloured reflections based on a small spectral band that they shift towards smaller wavelengths

---

[1]The abbreviation CIE is derived from its French name *Commission Internationale de l´Eclairage*

for increasing angles of light incidence. The less pronounced this colour shift is, the more angular-stable appears the coloured reflection.

To quantify the defined third requirement, a high solar transmittance T_{sol}, combined with a still significant visible reflectance R_{vis}, a figure of merit M has been introduced.[17] It describes the ratio between R_{vis} and solar reflectance R_{sol}. The definition of these quantities is given in Appendix A.1. M can be expressed for the non- or weakly-absorbing case by T_{sol}:

$$M = \frac{R_{\text{vis}}}{R_{\text{sol}}} = \frac{R_{\text{vis}}}{1 - T_{\text{sol}}} \tag{3.21}$$

A greater M indicates that less solar radiation is reflected compared to the visible reflectance, which is equivalent to an increased solar transmittance. However, it is no absolute indication how much solar energy is transmitted. Moreover, M can be interpreted as an indicator for the relative energetic and visible performance of a coloured filter. Table 3.1 gives a summary of the simulated performance and of reflection colours for the quarter-wave stack for different m. Combining the results given in Table 3.1 and Figure 3.7b shows that one fundamental property of the QW design is the tradeoff: high-performance coating (great M) or angular-stable coloured reflection.
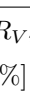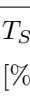
m	Colour coordinates			Colour		R_{Vis} [%]	T_{Sol} [%]	$M = \frac{R_{Vis}}{R_{Sol}}$
	L*	a*	b*					
1	47.7	-4.7	9.3	grey-green		16.6	88.6	1.45
2	54.1	-11.9	25.3	olive-green		22.0	87.7	1.79
3	59.0	-17.7	38.5	green		26.9	87.0	2.07
4	62.7	-21.8	43.7	bright green		31.1	86.3	2.27

Table 3.1: CIELAB colour values and performance of the QW design for coloured filters at the reference wavelength 550 nm, $n_L = 1.45$ and $n_H = 1.63$ for $1 \leq m \leq 4$.[19] With greater m the coloured peak becomes more narrow and the colour brighter and more saturated.

3.1.3 Quarter-wave antireflection principle

A coating is named anti-reflective, when the spectral reflection $R(\lambda)$ of the coated surface at a given wavelength λ is less then $R(\lambda)$ of the uncoated surface of the same substrate. Transferring the concept of antireflection to solar-energy applications, a coating is energetically anti-reflective, if the coated substrate reflects less solar radiation and therefore the solar device exhibits a greater energetic performance than the same device without anti-reflective coating.

The effect of antireflection can be produced by interference thin films. The condition for antireflection is a phase thickness of 90° at a given reference wavelength λ_{ref}, the so-called quarter-wave optical thickness.[33] An optical quarter-wave single-layer represents the simplest anti-reflective coating. The reflection for a coated surface is given by

$$R(\lambda) = \left(\frac{n_{\text{air}}(\lambda) - n_{\text{coating}}^2(\lambda)/n_{\text{substrate}}(\lambda)}{n_{\text{air}}(\lambda) + n_{\text{coating}}^2(\lambda)/n_{\text{substrate}}(\lambda)} \right)^2 \tag{3.22}$$

with the refractive index n of air, coating, and substrate, respectively. For complete antireflection (zero reflectance) the derivative of the reflectance becomes zero. For a given substrate this is the case, when:

$$n_{\text{coating}}(\lambda) = \sqrt{n_{\text{air}}(\lambda) \cdot n_{\text{substrate}}(\lambda)} \tag{3.23}$$

For a glass substrate ($n = 1.52$ at $\lambda = 550\,\text{nm}$), the ideal refractive index for the coating amounts to $n_{\text{coating}} = 1.23$ and the physical thickness d of the QW layer computes to $d = 550\,\text{nm}/(4 \cdot 1.23) = 112\,\text{nm}$.

Figure 3.8 shows the antireflection property of a quarter-wave coating on an infinite thick glass substrate for the given reference wavelength $\lambda_{\text{ref}} = 550\,\text{nm}$ for different refractive indices. Only the ideal refractive index $n = 1.23$ leads to zero reflection at the reference wavelength. The reflectance for quarter-wave films of MgF_2 ($n = 1.38$) and SiO_2 ($n = 1.45$) are included in the graph for comparison.

The concept of quarter-wave antireflection can be combined with the concept of coloured filters (see advanced colour solar filters with MgF_2 in Section 3.6.3).
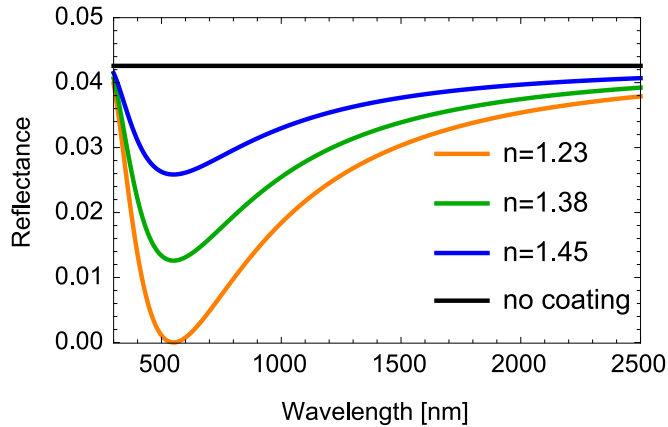
Figure 3.8: Quarter-wave antireflection for different n at $\lambda_{\mathrm{ref}} = 550\,\mathrm{nm}$. The glass substrate is assumed as infinite thick (no back reflection from the second surface).

3.2   Optical characterisation techniques

For optical coating design and development, it is essential to know the optical properties and performance of the films very precisely. Spectrophotometry and spectroscopic ellipsometry are well adapted and widely used techniques to determine transmittance $T(\lambda)$, reflectance $R(\lambda)$, absorptance $A(\lambda)$, refractive index $n(\lambda)$, and extinction coefficient $k(\lambda)$ of optical coatings.[17,18,21,22,68,69]

3.2.1   Spectrophotometry

A spectrophotometer is used to determine the transmittance, the reflectance and the absorptance versus the wavelength. It measures the ratio between incident radiation $I_0(\lambda)$ and transmitted radiation $I_{\mathrm{T}}(\lambda)$ or reflected radiation $I_{\mathrm{R}}(\lambda)$. Often, spectrophotometers are equipped with an Ulbricht sphere[2] which allows to measure in addition to the specular part of reflectance and the direct part of transmittance also their diffuse parts. Sum of diffuse and specular reflectance and sum of diffuse and direct transmittance are defined as total hemispherical reflectance $R(\lambda)$ and transmittance $T(\lambda)$, respectively. For the measurements of both, $T(\lambda)$ and $R(\lambda)$, the

---

[2]An Ulbricht sphere is a hollow sphere which is coated from the inside with PTFE (Poly Tetra Fluoro Ethylene, also known as Teflon). The PTFE surface reflects light nearly perfect diffusively.

coated side of the samples is facing the incoming light beam. The absorption can be determined by Equation (3.17).

Since the reflectance and transmittance spectra of a coating are sensitive to the thickness of each individual layer, those spectra can be used to monitor thickness changes. The VIS part of the spectral reflectance is directly linked to the visible colour of a sample. To describe colours of the coatings mathematically the CIELAB colour space can be used (see Appendix A.2).

The measurements were performed with the following instruments: at the LESO-PB a Multispec 77400 spectrometer from ORIEL was used for the VIS (375–850 nm) and for the NIR (850–2500 nm) an OL 730 detector combined with an OL 750-S monochromator from Optronic Laboratories. An Ulbricht sphere allowed also to characterise coloured samples with an etched reverse side. The measurements have been baseline and background corrected. However, reliable measurements with a sufficient signal-to-noise ratio were only possible above 400 nm. Since also the solar energy for $\lambda < 400$ nm has an influence on the solar performance, several glass samples were measured with a Varian Cary 5 spectrophotometer equipped with a 110-mm-diameter Ulbricht sphere in the spectral range 250–2500 nm at the Department of Physics of the University of Basel. The measurements have been baseline and background corrected. The reflectance has been additionally calibrated with a Spectralon diffuse reflectance standard SRS-99-020 for 250–2500 nm. In addition, measurements were performed with a double beam Brechbrühler V-670 spectrophotometer (187–2700 nm) equipped with a monochromator and two detectors for UV–VIS and NIR to determine the direct transmittance at the Laboratory of Macromolecular and Organic Materials (LMOM), EPFL. Furthermore, the direct reflectance was also measured with a FilMetrics F20-UV reflectometer (200–1100 nm) with a spot size of 1.5 mm at the Center for MicroNanoTechnology (CMi), EPFL.

The angle-dependent reflectance $R(\lambda, \vartheta)$ and transmittance $T(\lambda, \vartheta)$ of large samples and real-size glazing were measured with the Window Test Bench (see Figure 3.9). This equipment was developed by the University of Basel to characterise the optical and thermal properties of real-size insulating windows for different angles of light incidence.[70] In the framework of this doctoral thesis the equipment was moved from Basel to LESO-PB at EPFL. It consists of a 42-cm-large diffuse light source, producing a homogeneous and omnidirectional radiation, and a collimator
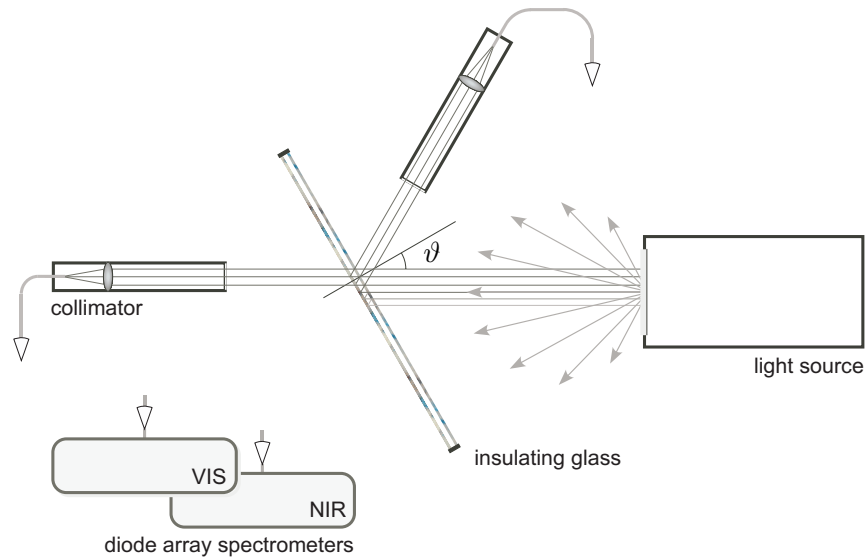
Figure 3.9: Schematic drawing of the Window Test Bench for angular-dependent transmittance and reflectance measurements of real-size glazing.[70] The measurement setup consist of a diffuse light source, two diode-array spectrometers for VIS and NIR with a collimator, and a rotatable support for the window under investigation.

at the detector side. The glazing is placed in the light path between the two. The selected radiation of one direction is transmitted through a quartz fibre to two diode-array Zeiss spectrometers (UV–VIS from 180–1000 nm and NIR from 880–2200 nm). In order to measure the angular dependency of the transmittance and reflectance, the angle of light incidence ϑ can be changed between 0° and 75° by turning the window. To measure $R(\lambda, \vartheta)$ the collimator needs to be displaced for each measurement to the corresponding viewing angle ϑ. A limiting factor for this measurement setup is that only specular reflectance and direct transmittance can be measured. Glazing having a diffuse surface, such as etched coloured panels, cannot be measured, since no stray light is captured by the collimator. For further details about the Window Test Bench see Appendix C.

3.2.2 Spectroscopic ellipsometry

Spectroscopic ellipsometry is used to determine the dielectric properties – refractive index $n(\lambda)$ and extinction coefficient $k(\lambda)$ – of thin films. However, they cannot be measured directly. With ellipsometry the ratio of parallel and perpendicular

polarised reflection $\tan \psi$, and the phase shift Δ between both, is measured. The wavelength-dependent optical constants $n(\lambda)$ and $k(\lambda)$ are then derived by means of minimising the root mean square error (RMSE) between the simulated curves using a suitable dispersion model (see Appendix B.2 and B.3) and the measured data, as described e. g. in RÖSELER.[71] The measurement principle is shown in Figure 3.10.
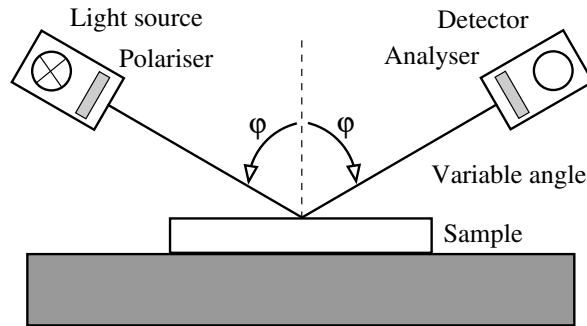

Figure 3.10: Measurement principle of spectroscopic ellipsometry. For various angle ellipsometry, the light source with polariser and the detector with analyser are rotated relative to the normal by the angle φ.

The ellipsometric parameters ψ and Δ were measured at various reflection angles from 55–75° with three different instruments: a Sentech SE 850 spectroscopic ellipsometer at the Department of Physics of the University of Basel in the spectral range 300–2300 nm, a Sopra GES 5E spectroscopic ellipsometer equipped with a spectrograph (CCD detector for 190–990 nm and linear detector for 990–1700 nm) at the CMi, or a Sopra GESP 5 spectroscopic ellipsometer at the Polymers Laboratory (LP) equipped with a monochromator and spectrometer (tube photomultiplier, for 190–990 nm and diode detector, 750–2000 nm) for high-resolution measurements.

The determination of the extinction coefficient $k(\lambda)$ of weak-absorbing coatings by only ellipsometry, however, is rather difficult.[69] Since the transmittance of thin films on transparent substrates is very sensitive to absorption in the film, spectrophotometry can be used in combination with spectral ellipsometry to determine n and k of weak-absorbing transparent films. Starting with the optical constants from ellipsometry, spectral transmittance and reflectance curves are fitted to the measured data by spectrophotometry using the matrix multiplication method for thin films, (see Section 3.1.1) refining the $n(\lambda)$ and $k(\lambda)$ values. The resulted dispersion rela-

tions for $n(\lambda)$ and $k(\lambda)$ are then used again as starting parameters for a new data fit of the ellipsometric data. This iterative process is repeated several times until both, $n(\lambda)$ and $k(\lambda)$ – determined by ellipsometry and by spectrophotometry – are in good agreement.

3.3   Colour matching

The CIE 1931 colour space defines colours by the colour-matching functions (CMFs)[3] $\bar{x}(\lambda)$, $\bar{y}(\lambda)$, and $\bar{z}(\lambda)$, which correspond to the sensitivity of the photoreceptors in the human eye. Any colour can be matched by adding the tristimulus values X, Y, and Z, which are derived from the CMFs. The CIE 1931 colour space represents all existing colours in the two-dimensional xyY-chromaticity diagram, where x, y are colour values and Y is the relative luminance of a specific colour.[66] For details about the CIE 1931 colour space and a xyY-chromaticity diagram see Appendix A.2.

The more recently introduced standard CIELAB ($L^*a^*b^*$ colour space), with D_{65} (natural daylight) as illuminant, is used to quantify the distance ΔE of two colours, as it represents better the human colour vision for colour differences.[67] Therefore, it has been chosen to characterise the reflection colours of the interference filters.

For matching the colour of one object with the colour of another, or to guarantee that the colour of the coloured samples is reproducible and stable in time, the distance between two different colours is determined by:[66]

$$\Delta E = \sqrt{(\Delta L^*)^2 + (\Delta a^*)^2 + (\Delta b^*)^2} \qquad (3.24)$$

ΔL^* is the difference of the colour lightness, whereas Δa^* and Δb^* correspond to the differences in the colour values a^* and b^* in the CIELAB a^*b^*-plane. Two different colours are in-distinguishable for the human eye, when ΔE becomes sufficiently small. Chou and Wu[72] indicate a threshold of $\Delta E > 3$ to distinguish one colour from another. Consequently, to match the reflection colour of thin-film filters to the coloured appearance of other objects, such as façade elements or windows, ΔE needs to be minimised ($\Delta E < 3$). For details about the CIELAB colour space and the determination of L^*, a^* and b^* of a reflection colour see Appendix A.2.

---

[3]In the CIE 1931 the CMFs of the CIE 2°-standard observer are used.

3.4 Coloured coating development cycle

By the nature of the architectural application for the coloured solar coatings, a precise reflection colour is tremendously important, especially when matching the reflection colour of the coatings to commercial products.[73] The transmittance $T(\lambda)$ and reflectance $R(\lambda)$ of the coloured filters depend on both, the optical constant $n(\lambda)$ and $k(\lambda)$ of each coating material, as well as on the thickness of each layer. In practice, however, $n(\lambda)$ and $k(\lambda)$ are usually pre-defined by the established deposition processes.[74,75] Therefore, in general, the thickness of the layers is adjusted to refine the spectra of the filters rather than the optical constants $n(\lambda)$ and $k(\lambda)$. Consequently, the coating development follows a so-called coating development cycle: starting with depositions of single layers to determine very precisely the optical constants of each layer under the given coater and deposition configuration, followed by simulation of the multilayer stack using the obtained optical constants from the single-layer deposition, and finally the deposition of the complete multilayer stack. Since the optical properties of thin-film filters are very sensitive to an accurate layer thickness, and the latter strongly depends on the deposition parameters, including the actual state of the sputtering targets and the underlaying layer, the multilayer stack usually needs be refined after it has been deposited for the first time.

For refinement, the $T(\lambda)$ and $R(\lambda)$ of the multilayered samples are measured by spectrophotometry, the absorption is determined by energy conservation, see Equation (3.17). Afterwards, the thickness of the deposited layers can be derived by minimising the RMSE between the theoretic thin-film model and the measured spectral data. In the following step the deposition parameters are adapted to fine-tune the interference multilayer stack and the coating is afterwards re-deposited. This procedure is repeated for several iterations, until the required coloured reflection combined with a sufficient high solar transmittance is achieved. The amount of free parameters can vary during the coating development, such as number of layers and different coating materials used. Many free parameters make this iterative process more complex, time consuming and cost-intensive. One research goal of the thesis is therefore, to reduce the number of design parameters during the filter designing phase. In Figure 3.11, the development cycle for coating optimisation and multilayer stack refinement is shown.
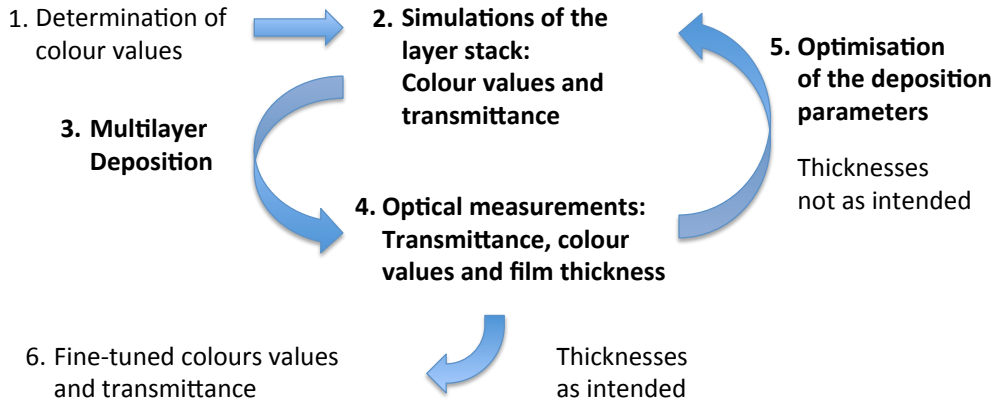
Figure 3.11: Coating development cycle for coloured solar coatings. The steps 2–5 need to be repeated until the required coloured reflection combined with a suitable high solar transmittance is achieved.

3.5 Development tools for numerical simulations

3.5.1 Commercial thin-film design software

The spectral transmittance $T(\lambda)$, reflectance $R(\lambda)$, and absorptance $A(\lambda)$ of optical multilayer coatings can be calculated by multiplication of the characteristic matrices for each optical thin film (see Section 3.1.1). Hereby, it is necessary to know the refractive index $n(\lambda)$ and the extinction coefficient $k(\lambda)$ of the different thin-film materials for all layers. There are several scientific software tools for thin-film calculations on the market with a huge functionality to simulate interference coatings and to fit calculated curves to optical data.

In this research project, mainly the thin-film software TFCalc$^{\text{TM}}$ from *Spectra Software* was used. It can handle multilayer stacks with up to five thousand single layers as well as various angles of light incidence. The software supports front and back layers i.e. two interfaces for transparent substrates, as well as it takes the absorption inside the substrate into account. Next to the spectral values, the colour values of reflection and transmission are calculated using the CIE 1931 or CIELAB colour system (see Appendix A.2). Furthermore, it is possible to optimise designs by computing the best fit to existing target data. These can be transmittance or

reflectance spectra as well as colour values. Possible applications are for example fine-tuning of multilayer stacks or colour matching.

For the analysis of spectroscopic ellipsometry measurements and of combined ellipsometry and spectrophotometry as described in Section 3.2.2, Film Wizard[TM] from *SCI Scientific Computing International* was used. With this software $n(\lambda)$ and $k(\lambda)$ can be determined by adjusting the parameters of the different dispersion models either to fit the ellipsometric angles ψ and Δ or the transmittance and reflectance spectra. Hereby Film Wizard[TM] can handle up to 1000 layers. Furthermore, effective media approximations (EMA), such as Maxwell-Garnett, Bruggeman or Ping Sheng, are implemented. [76,77] This allows to determine the material ratio inside a composite material, such as titania-silica composite (TiO_2-SiO_2), which makes it a powerful tool for ellipsometric analysis of EMA materials. Nevertheless, there is one limitation for thin films on glass only one-side-coated substrates can be modelled.

3.5.2   New Mathematica framework for thin-film simulations

To understand the performance of a coloured solar coating, a direct access to the resulting T_{sol} and R_{vis} of the numerical computed transmittance and reflectance spectra is fundamental. For an efficient performance improvement of the coloured filters, all relevant quantities should be taken into account during the numerical simulation. This sounds trivial, but practice has shown it is not. Most software packages for thin-film simulations (including the above mentioned TFCalc[TM] and Film Wizard[TM]) are only designed to compute optical spectra as well as the colour coordinates of spectra. However, relevant integrated quantities, such as T_{sol} and R_{vis} for solar applications (see Section 3.1.2) are not implemented. Nevertheless, without these quantities, especially T_{sol}, it is rather difficult to optimise a coating design, since for an energetic improvement, it is necessary to increase the figure of merit $M = R_{vis}/(1 - T_{sol})$, while having a sufficient strong and saturated enough visible reflection.

For this purpose, a new thin-film simulation framework for optical solar coatings has been programmed in the scope of this thesis on the basis of Wolfram Mathematica[TM]. It implements the thin-film equations from Section 3.1.1, as well as the relevant solar and visible quantities from Appendix A.1, including the colorimetric values from Appendix A.2. The aim of this framework is to have a simulation

tool available, which is more adapted to the specific characteristics of coloured thin films for solar applications. The developed framework is very flexible and can be easily adapted to specific needs. It is structured and divided into three separated packages which are written from scratch, applying the basic principles of the Wolfram Language: lists and replacement rules. Functionality and functional range of the packages are described below:

thinFilm.m to compute $T(\lambda)$, $R(\lambda)$ and $A(\lambda)$ of thin film samples.

The package consists of two modules: the first one to calculate the thin film on a single surface, the second one to assemble the multilayer film with the substrate as whole sample (finite transparent substrate with two plane-parallel surfaces). The number of layers which can be handled is only limited by computational time. The package is designed to compute front-, reverse-, or both-side coated substrates:

$$\text{air}\|\text{film } or \text{ no film}\|\text{finite substrate}\|\text{film } or \text{ no film}\|\text{air} \qquad (3.25)$$

The calculations are based on the matrix multiplication method as described in Section 3.1.1. Equation (3.10) is implemented in its general form, with no additional physical assumptions or limitations. The optical constants n and k of the different layer materials can be supplied as n-k tables or directly as dispersion-relation functions. With the optical admittance η the angle of light incidence is respected and thus also the polarisation of the reflected and transmitted light. The optical spectra are finally calculated using Equation (3.15), (3.16) and (3.17).

$T(\lambda)$ and $R(\lambda)$ are calculated considering all multiple reflections occurring at the two substrate surfaces. The incident angle can vary between normal ($\vartheta_0 = 0°$) and near parallel ($\vartheta_0 = 89.9°$) to the sample surface. While the thin-film materials may possess a weak absorption, the substrate must not. This allowed to implement the multiple reflections mathematically as geometric series. Nevertheless, this is not a limitation for the coating optimisation, since non-absorbing substrates were used. Absorbing substrates can be implemented in future, if it becomes necessary.

solarQuantities.m to calculate the solar and visible quantities, such as solar trans-
mittance T_{sol}, reflectance R_{sol}, absorptance A_{sol} and visible transmittance T_{vis},
reflectance R_{vis}, absorptance A_{vis}, respectively, by numerical integration.

For calculating T_{sol}, R_{sol} and A_{sol} the solar irradiance AM 1.5 global[4] is used.
The CIE defines as natural daylight condition the illuminant CIE D_{65} as well as
the photopic luminous efficiency function $V(\lambda)$ to describe the light sensitivity
of the human eye, which are used to calculate T_{vis}, R_{vis} and A_{vis}. Details to
the definition and relationship between these solar and visible quantities are
given in Appendix A.1.

colourCoordinates.m to evaluate the colour values of spectral data in the CIE
1931 and CIELAB colour space.

This package consists of three principle modules. The first one calculates the
tristimulus values for $T(\lambda)$ or $R(\lambda)$ depending on the used colour space. The
other two modules compute the colour values. For determining the CIE 1931
colour values (xyY) a perfect white illuminant is used and the tristimulus values
calculated with the $2°$ colour-matching functions (CMFs). The CIELAB colour
values $(L^*a^*b^*)$ are calculated with the illuminant CIE D_{65} and the tristimulus
values using the $10°$ CMFs. For details about the calculations and the colour
spaces see Appendix A.2.

The design window has been developed as an user interface, by combining the three
packages into a graphical front end. It allows to change physical or optical thickness
of the layers, as well as the complete design of the multilayer stack. Using standard
Mathematica^{TM} commands, options can be easily adjusted. $T(\lambda)$, $R(\lambda)$, $A(\lambda)$ and
the colour values are plotted graphically. Hereby, the CIELAB or CIE 1931 colour
chart can be chosen. In addition, the colour values are given numerically, as well as
the physical thickness of the layers, T_{sol}, R_{vis} and the figure of merit M.

Figure 3.12 illustrates the design window configured for a three-layer coating
design on the reverse side of a glass substrate. The coating materials TiO_2 and SiO_2
with $n = 2.4$ and $n = 1.45$, respectively, and $k = 0$ have been used. Instead of
the physical thickness the optical thickness is selected. For the high-index layers,
it can be changed as a fraction x of the optical quarter-wave thickness (H/x). The
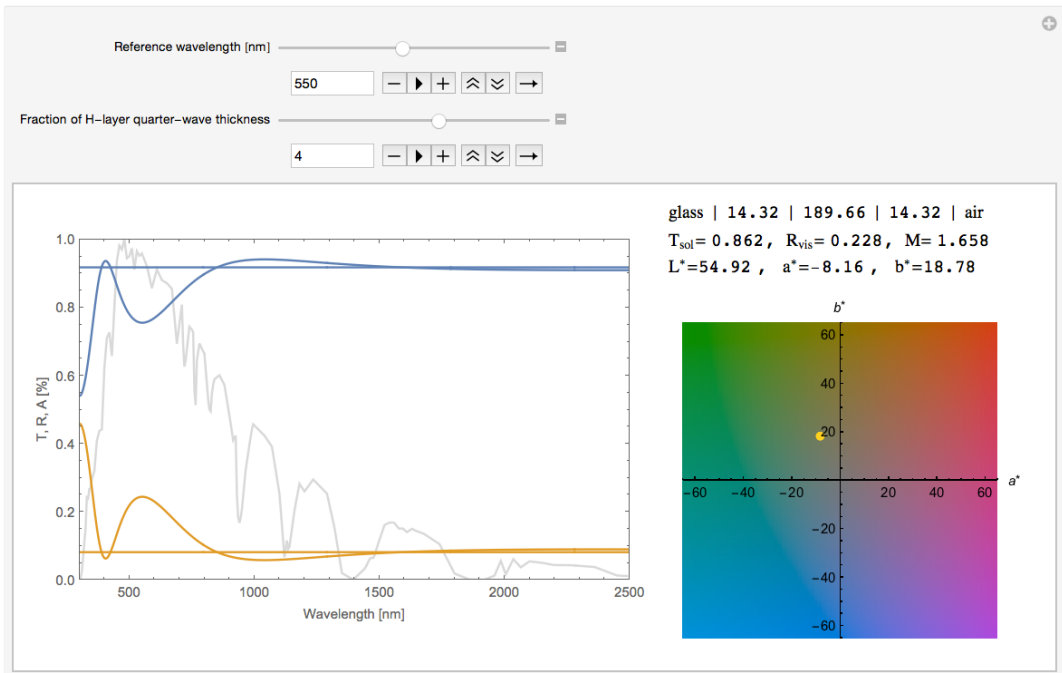
---

[4]direct and diffuse solar radiation at the air mass 1.5

Figure 3.12: Design window for coloured coating development programmed in Mathematica$^\text{TM}$. At the top of the window λ_ref and the fraction of the high-index QW layer (H) can be changed. In the simulation-result area $T(\lambda)$, $R(\lambda)$ and $A(\lambda)$ is plotted. The solar spectrum AM 1.5 global in included in the background. On the right-hand side the first line corresponds to the layer thicknesses, followed by T_sol, R_vis and M. Underneath the CIELAB colour values, including the a^*b^*-colour chart at a fix $L^* = 50$, are given.

complete design schemata is given by air$\|$glass$\|\frac{H}{x}LL\frac{H}{x}\|$air. As start parameters, the reference wavelength $\lambda_\text{ref} = 550\,\text{nm}$ and $x = 4$ have been pre-selected. The quarter-wave fraction x, as well as the reference wavelength λ_ref (sometimes also referred to as design wavelength) can be varied using the graphical interface. The spectra and the numerical values are re-calculated immediately. Thus, by *sliding* the bars in the design window i. e., changing λ_ref from 450–750\,nm or the fraction x from 1–6, the effective changes to the solar transmittance and the coloured reflection are directly graphically and numerically displayed. The configuration of the design window is performed with standard Wolfram language commands. It is therefore very flexible and can be adapted to the specific requirements.

Outside the design window all simulated results are accessible via standard commands in Mathematica$^\text{TM}$, which can be useful when combining it e. g. with other

software tools or to export the data. In addition, by defining a parameter list, a simulation task can be applied to the whole list, followed by the presentation of the results in table form, or as graphs. This feature is used in the following section for the energetic optimisation of the coloured interference filters.

3.6 Coating-design optimisation of coloured interference filters

New multilayer stacks were designed by numerical simulations with the aim to improve the energetic performance of the coloured filters and to simplify the coating development process in comparison to those described before. For these simulations at first the refractive indices $n(\lambda)$ were set constant to the literature values at $\lambda = 550\,\mathrm{nm}$ and the extinction coefficients to $k = 0$. In the second step, they were refined with real optical material data of sputtered single layers (from the results in Section 5.1 and 5.2). The interference stacks used are based on layers of alternating high- and low-refractive-index materials. Before starting the optimisation process it is substantial to give some thoughts to the relevant parameters, which should be considered:

1. **Energetic performance** means a high solar transmittance T_{sol} combined with a sufficient high visible reflectance R_{vis}. The figure of merit M can be hereby used as an indicator for the energetic performance of the coating (see Equation 3.21).

2. **Angular behaviour** describes how strong the coloured reflection of the interference filter varies for different angles of light incidence. It is however a general property of the coloured interference filters that for larger angles of incidence the coloured reflection shifts towards smaller wavelengths. In other words: for different viewing angles, a shorter trajectory in the a^*b^*-diagram and consequently a smaller colour difference ΔE corresponds to an increased angular stability of colours.

3. **Industrial large-scale production** is of great importance, since the typical size of solar collector glazing is in the order of square metres. To keep the industrialisation of the coloured filters feasible, the number of layers in the multilayer stack has to be kept as small as possible. In addition, the free

and variable design parameters, such as reference wavelength, layer thickness, number of materials, etc. should be kept as simple and also as few as possible. It is necessary to keep in mind that the whole idea of the coloured coating has an aesthetic aspect. Therefore, changing, adapting, and matching the coloured reflection is a repetitive task: in research and development (R&D) as well as in industrial production.

Taking the above criteria into account, different layer schemes have been investigated. The goal of the simulations was to find design types which are improved in at least one or all of the three above mentioned criteria. For the new proposed designs, the outermost layer is a reflector to maximise the intensity of the coloured reflection, as explained in Section 3.1.2. While the QW design glass$\|(HL)^m H\|$air has a good optical and energetic performance for small difference Δn of the refractive index and $m \geq 2$, which corresponds to five and more layers, the angular dependency of its coloured reflection is quite pronounced (see Figure 3.7). This means, two of the three optimisation criteria should stand in the focus for further improvements: fewer layers for industrial production and the angular behaviour of the coatings.

The three-layer coating design described by Schüler et al.[65] with a variable thickness for the outer reflector layer is a promising ansatz to reduce the number of layers from five to three while maintaining a good energetic performance. However, the design wavelength λ_{ref} of this coating design no longer corresponds to the maximum of the reflection peak. This is contradictory to the idea of a straight forward layer-thickness adaption to achieve a desired reflection colour with good energetic performance.

In Section 5.1 four energetically optimised filters with 2–4 layers are discussed. On the basis of these, coloured coatings were produced. The colours of the presented designs with blue and green reflection are sufficiently stable for different viewing angles, whereas the angular dependency for orange-reddish colours needs to be further reduced. Details about the elimination of free and variable design parameters as well as the angular behaviour of the coloured reflection is discussed in the following three subsections.

3.6.1   Reduction of variable design parameters

New design types are investigated to reduce the number of variable and free design parameters. In contrast to the design types described by Schüler et al. [19,65] in 2005, they contain an optical half-wave (LL) and not a quarter-wave (L) low-refractive layer. This means, the discussed development is not based on quarter-wave stacks or derivates, but on a more general view: the theory of standard narrowband-pass filters. [33] The coating designs proposed in this thesis consist of an optical half-wave spacer layer, which is denoted as (LL), and high-index reflectors, which are thinner than an optical quarter wave. Using the before described Mathematica$^{\text{TM}}$ framework, a generalised design model has been found by an extensive study of design parameters, which can be noted for three layers as glass$\|\frac{H}{x}LL\frac{H}{x}\|$air, with $x > 1$. Hereby, the parameter x is influenced by the refractive-index difference Δn of the used coating materials. To obtain the same intensity of reflection, if Δn is increased, it is necessary to increase x, which results in thinner reflector layers. Figure 3.13 plots simulations with the values $3 \leq x \leq 5$ and $2.15 \leq n \leq 2.66$ for the high-index reflectors. For the LL-spacer $n = 1.45$ (SiO$_2$) is chosen. All three simulations produce a coloured reflection with comparable intensity around the design reference
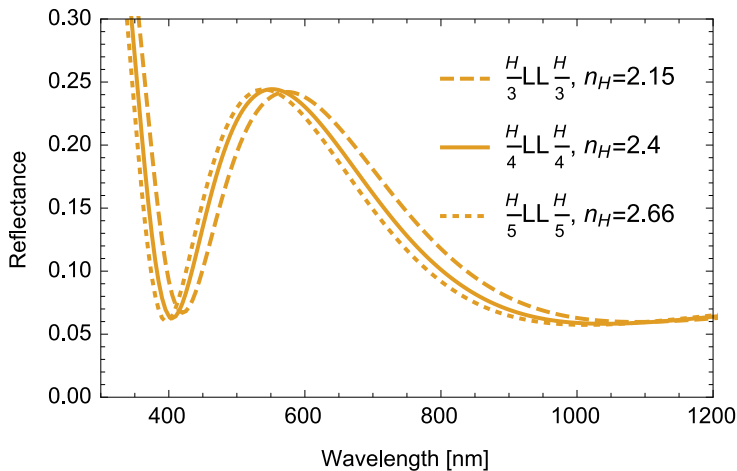

Figure 3.13:   Simulated reflectance curves with different design parameters x and n. To reproduce a comparable reflection peak with the centre around the design wavelength $\lambda_{\text{ref}} = 550\,\text{nm}$, the choice of a greater refractive index n is compensated with a greater value of x. For the L-material $n = 1.45$ is used.

wavelength $\lambda_{\text{ref}} = 550\,\text{nm}$.

Using TiO_2 ($n = 2.4$) for H/x-reflectors and SiO_2 ($n = 1.45$) for LL-spacer layer a quarter of a quarter wave ($x = 4$) turned out to be a suitable thickness for the reflectors. The coating design is therefore also referred to as quarter quarter-wave reflector (QQR) design. A comparison of the reflectance and transmittance spectra between the QQR and the quarter-wave (QW) design with $m = 2$ (described in Section 3.1.2) is shown in Figure 3.14. Both designs have the reflectance maximum at the same design wavelength λ_{ref}, in the graph at 550 nm. To visualise the effect of the filters on their solar performance, the solar spectrum is plotted in the background of the graph. The broader reflectance band of the QQR at around 800 nm in comparison to the QW design is compensated by an area of less reflection in the region around 1100 nm. The second order reflectance peak of the QQR at around 300 nm is positioned at the UV-border of the solar spectral range and has therefore only a minor effect on the solar transmittance T_{sol}. The performance and design parameters of the QQR design are discussed in the results in Section 5.3.

While this QQR design has a good performance for green and blue reflections, the performance decreases for yellowish and orange colours. This is due to the second
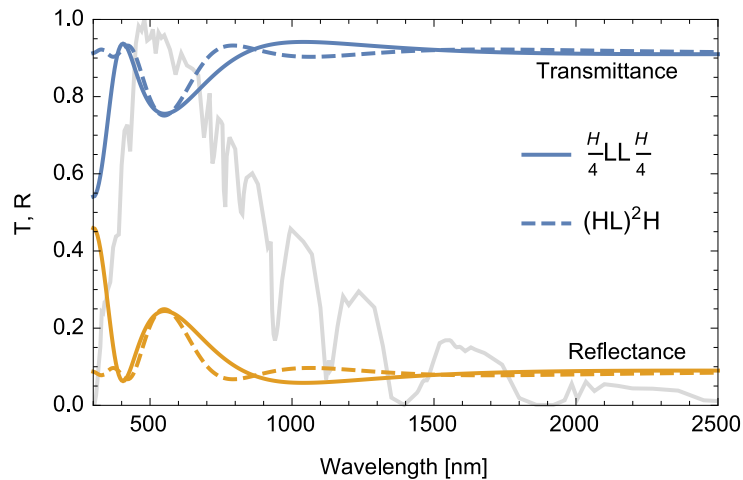

Figure 3.14: Comparison of $T(\lambda)$ and $R(\lambda)$ between the QW design type ($n_H = 1.63$, $n_L = 1.45$, $m = 2$) and the new QQR design ($n_H = 2.4$, $n_L = 1.45$, $x = 4$). In the background the solar spectrum is plotted. Both designs have the reflectance maximum at the same design reference wavelength λ_{ref}, here 550 nm. The area of higher reflection of the new design at around 800 nm is compensated by an area of antireflection at 1100 nm.

order maximum in the coloured reflection, which shifts to larger wavelengths, if the design wavelength is increased. This second order peak possesses two negative effects at the same time. At first, it directly reduces the solar transmittance, since it reflects in the UV and blue area. Secondly, this UV-blueish reflection is superposed to the reflection of the λ_{ref}-peak, which desaturates the colour[5]. Figure 3.15 plots the reflectance and transmittance curves for glass$\|\frac{H}{4}LL\frac{H}{4}\|$air for four different reference wavelengths $450 \leq \lambda_{ref} \leq 750\,\text{nm}$.
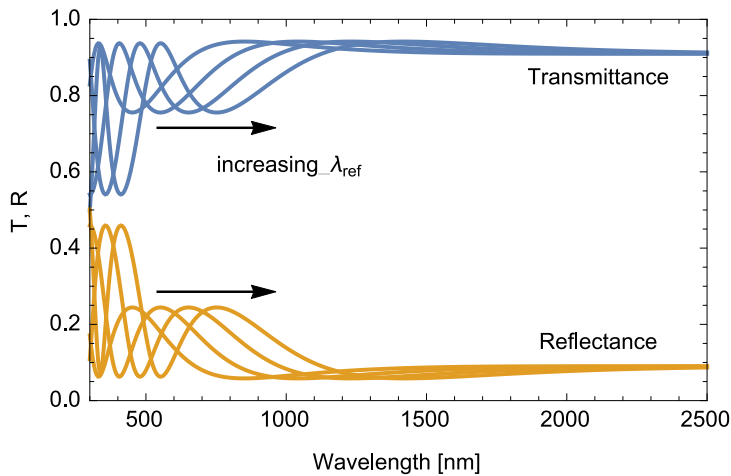

Figure 3.15: Simulated reflectance and transmittance curves of the QQR design for different design wavelengths λ_{ref} (450, 550, 650, 750 nm). With increasing λ_{ref} the spectral reflectance shifts to longer wavelengths. The maximum of the first order reflectance peak corresponds to the design wavelength λ_{ref}. For $\lambda_{ref} = 650\,\text{nm}$ and 750 nm the second order maximum enters significantly into the solar spectral range and reduces both, energetic and visual performance.

By adding a second spacer layer and another reflector the model can be expanded to a so-called double-cavity band-pass filter, [33] which can be written in generalised form as a multi-cavity band-pass filter glass$\|(\frac{H}{x}LL)^m\frac{H}{x}\|$air. However, only $m = 1$ and 2 are considered for the simulations due to the third optimisation criterion: a small number of layers for industrial production. Since multiple cavities reduce the second order reflection peak a double-cavity filter is considered for yellowish-orange colours.

---

[5]A white reflection can be produced by superposing only three spectral colours[66]

Another approach to simplify the designing phase is to further reduce the number of layers down to two. As discussed before, it is beneficial for the coloured reflection that the outermost layer is an reflector. This is no longer fulfilled for a two layer design where the outer layer is a *spacer* layer. Those design schemes (glass$\|\frac{H}{x}LL\|$air, with $1 \leq x \leq 4$) can nevertheless exhibit a strong effect of antireflection. A zero-loss coloured coating was realised for a greenish colour hue with a significant strong coloured reflection (see published results in Section 5.1).

3.6.2 Angular stability of reflection colours

The design scheme glass$\|\frac{H}{x}LL\frac{H}{x}\|$air was extensively studied with optical data from sputtered TiO_2 and SiO_2 single layers. For details about the used spectral refractive indices $n(\lambda)$ and extinction coefficients $k(\lambda)$ see Figure 5.3 in Section 5.1. The reflectance and transmittance curves ($x = 4$) are plotted for different reference wavelengths at normal incidence in Figure 3.16a and for various angles of light incidence at a constant $\lambda_{\mathrm{ref}} = 550$ in Figure 3.16b. With increasing incident angle the reflection peak shifts towards smaller wavelengths.

Figure 3.17a illustrates the CIELAB a^*b^*-chart of the QQR design at the reference wavelength $550\,\mathrm{nm}$ for different values of parameter $3 \leq x \leq 6$ and Figure 3.17b the colour trajectories of those designs when changing the angle of light incidence (0–70°). The lightness L^* of the colour chart is kept to 50 for suitable illustration. With different L^* values the a^*b^* colours values change slightly their colour hue. Therefore, the printed colour in Figure 3.17a corresponding to particular $L^*a^*b^*$ values cannot be represented precisely with a fixed L^*, but it remains close enough to give a good impression for the colour change (see Appendix A.2). When increasing the parameter $3 \leq x \leq 6$ (dark-red to yellow points, respectively), the colour of the filter gets desaturated but it remains greenish. For the former chosen value $x = 4$ a clear green reflection colour is obtained, which is suitable as cover glass for solar collectors. Increasing the incident angle, the coloured reflection shifts – as discussed before – to shorter wavelengths, which corresponds to the trajectory from greenish to more greenish-blue and finally to blueish colours in the colour chart (see Figure 3.17b). In comparison to the colour trajectories of the QW design at the same design wavelength $\lambda_{\mathrm{ref}} = 550\,\mathrm{nm}$ the trajectories of the QQR design in Figure 3.17b enclose a smaller area in the a^*b^*-plane. This is equal to a smaller
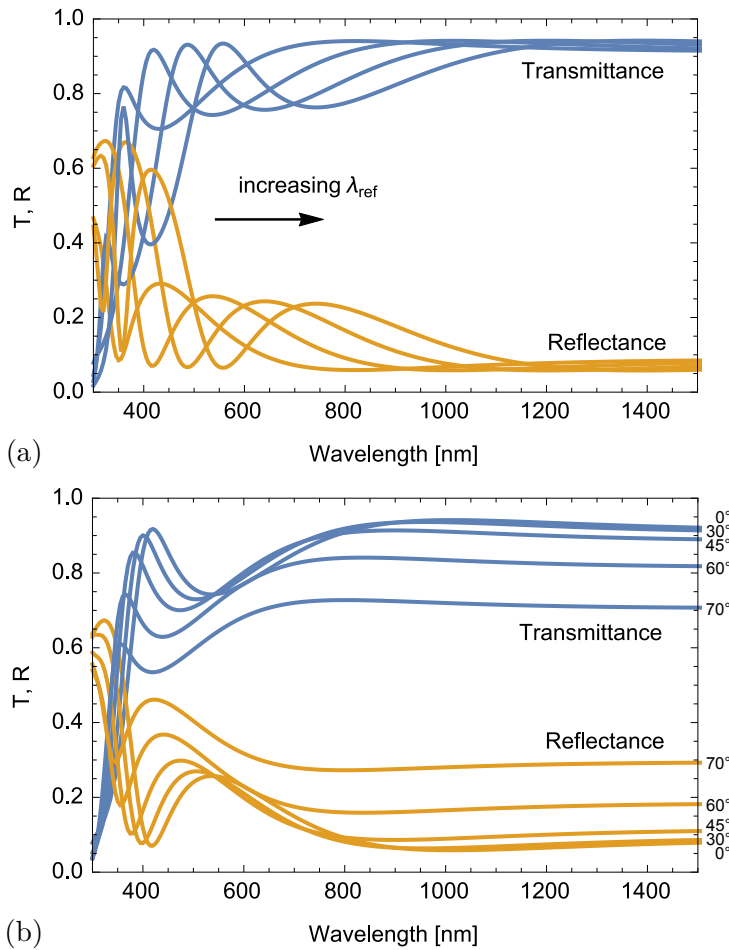
(a)

(b)

Figure 3.16: Simulated reflectance and transmittance curves of the QQR design based on the measured optical constants of TiO_2 and SiO_2. (a) At different design wavelengths λ_{ref} (450, 550, 650, and 750 nm). The spectra exhibit a weak absorptance in the UV in comparison to Figure 3.15. (b) At $\lambda_{ref} = 550$ nm for various angles of light incidence (0, 30, 45, 60, and 70°). With increasing angle the spectral reflectance shifts towards shorter wavelengths, and therefore the coloured reflection shifts from green-blue to blueish colours before it gets desaturated for oblique incidence greater 45°.

value of ΔE, see Equation (3.24), which is equivalent to a more angular-invariant colour. In other words, for changing viewing angles the reflection colour of the QQR design for $\lambda_{ref} = 550$ nm is less angular-dependent than the one of the QW design. This is a significant improvement towards the second optimisation criterion.
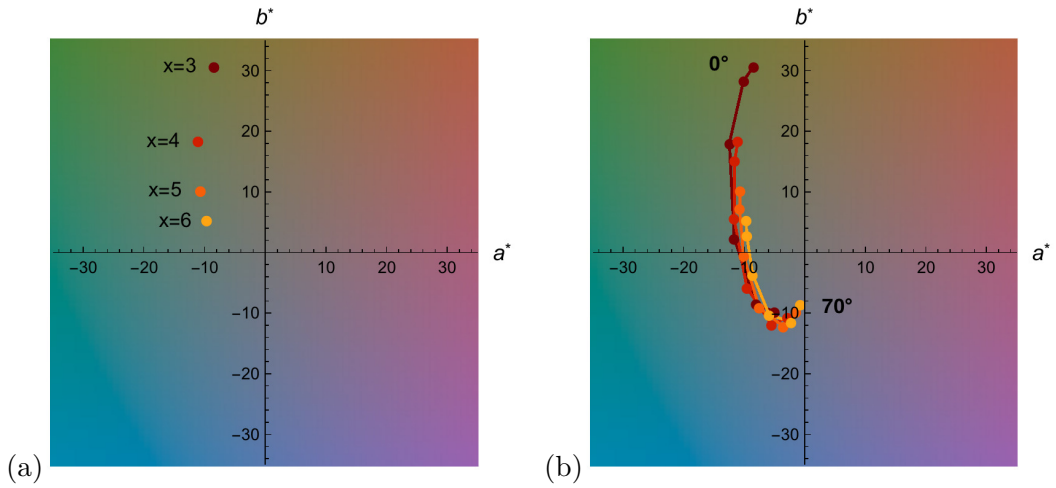
Figure 3.17: (a) Colour values for the glass$\|\frac{H}{x}LL\frac{H}{x}\|$air designs for $3 \leq x \leq 6$ and $\lambda_{\mathrm{ref}} = 550\,\mathrm{nm}$. (b) Colour trajectories when changing the angle of light incidence (0, 15, 30, 45, 60, and 70°) for these designs. The value of L^* was set to 50 in order to obtain a suitable graphical representation of the colours.

3.6.3 Advanced coloured solar filters with supplementary low-refractive-index materials

The aim of the coloured filters is to provide a narrowband reflection in the visible range (see Section 3.1.2) while remaining transparent to the rest of the solar radiation. Already the uncoated substrate reflects a significant amount of light (8.2% for an extra-white iron-free 1-mm-thick float glass). To increase the energetic performance of the coloured coatings, an anti-reflective layer could be added beyond the band-pass. The resulting antireflection part of the spectrum can then compensate the reduced light transmission due to the coloured reflection. Hereby, the overall energetic performance of the coloured filter will increase.

To achieve this, a second SiO_2 layer ($n = 1.45$) is added to the QQR coating design. However, the additional SiO_2 layer does not act as a second half-wave spacer layer between two TiO_2 reflectors. Moreover, it is added after the outermost reflector as an intermediate-refractive-index layer in between TiO_2 ($n = 2.4$) and air ($n = 1$). Therefore, the additional SiO_2 layer acts already as an antireflection (AR) layer in the area of 600–800 nm. This design is named quarter quarter-wave reflector plus outer-layer (QQR+). As second step an MgF_2 layer with $n = 1.382$ at 550 nm and

with a thickness of 56 nm is added on top of the SiO_2 layer. Linked to the AR property of the MgF_2 layer the design is named quarter quarter-wave reflector plus anti-reflector (QQRAR) design. Results on the optical properties of sputtered MgF_2, necessary for this coating design, are presented in Section 5.2.

Figure 3.18 shows the effect on $R(\lambda)$ of the supplementary second SiO_2 as well as the MgF_2 layer. The second SiO_2 layer diminishes a part of the reflection in the area around 900 nm, while the MgF_2 creates a zone of antireflection between the coloured peak and the UV (at around 400 nm). At the same time the NIR-reflection beyond 1200 nm is reduced as well (not shown in the graph). The regions with decreased reflection lead to an increased energetic performance combined with a greater M; in other words, T_{sol} increases, while R_{vis} produces an intensive and saturated colour.
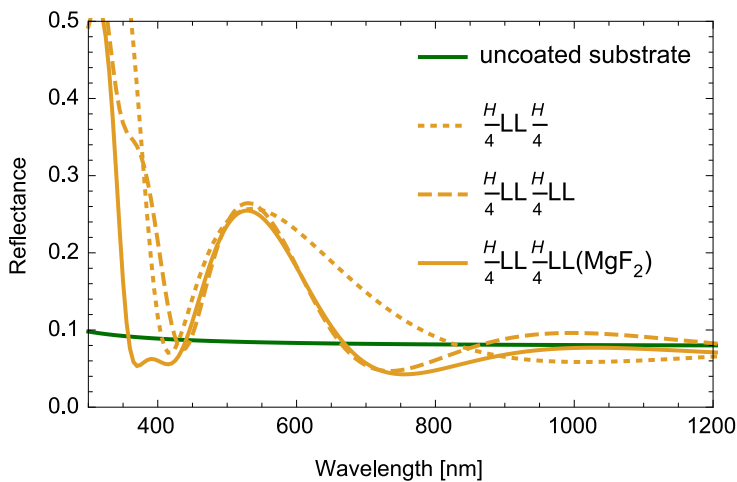

Figure 3.18: Simulated reflectance of the three design types QQR, QQR+ and QQRAR. In the legend the layer sequence is given, with the substrate on the left and air on the right side. The reference wavelength is $\lambda_{ref} = 550$ nm for QQR and QQR+, and for QQRAR $\lambda_{ref} = 490$ nm with an MgF_2 layer thickness of 56 nm.

Figure 3.19 depicts this saturation effect due to the added outer SiO_2 layer. The additional MgF_2 layer only changes the colour marginal, since the AR area at 400 nm and below is almost at the sensitivity limit of the human eye (see Appendix A.1 and A.2). With the supplementary MgF_2 layer the colour of the reflection does no longer correspond to the design wavelength $\lambda_{ref} = 550$ nm, but is several nanometres below the reflection maximum (new $\lambda_{ref} = 490$ nm). However, the angular stability of the
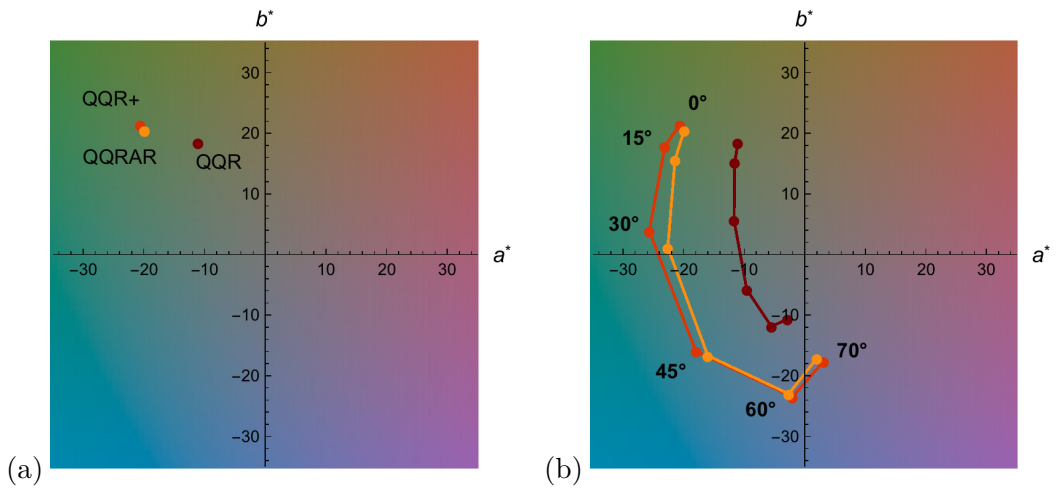
Figure 3.19: (a) CIELAB colour values of the three different filter designs QQR, QQR+ and QQRAR. The colour shift due to the added AR layer in the QQRAR is only marginal. (b) Colour trajectories for the three coating designs at changing viewing angles (0, 15, 30, 45, 60, and 70°). The value of L* was set to 50 in order to obtain a suitable graphical representation.

colours is slightly improved. Table 3.2 summarises the colour values, $T_{\rm sol}$, $R_{\rm vis}$ and the figure of merit M for the original QQR design type and the two modifications, the QQR+ design and the QQRAR design.

Another possibility is to insert an MgF$_2$ inter-layer in the QQR design between the spacer and the inner reflector, which is referred to as colour-tuning layer (CTL)

Design	Colour coordinates			Colour		R_{Vis} [%]	T_{Sol} [%]	$M = \frac{R_{Vis}}{R_{Sol}}$
	L*	a*	b*					
QQR	55.9	-11.1	18.4	greenish		23.7	84.7	1.60
QQR+	54.1	-20.6	21.4	green		22.0	86.6	1.72
QQRAR	53.6	-19.9	20.4	green		21.5	88.3	1.95

Table 3.2: Comparison of the colour values, as well as the energetic and optical performance of the QQR, QQR+ and QQRAR design types. For the first two designs the reference wavelength is $\lambda_{\rm ref} = 550\,{\rm nm}$, for the third $\lambda_{\rm ref} = 490\,{\rm nm}$ with an MgF$_2$ layer thickness of 56 nm.

design, see Figure 5.15 in Section 5.3. The advantage of this *sandwich* design is that the reflection colour can be tuned by only varying the thickness of the MgF_2 layer while the design wavelength λ_{ref} does not change i.e. the thickness of TiO_2 reflector and SiO_2 spacer layers remain fix. At the same time T_{sol} is nearly constant for all colour hues. Table 3.3 illustrates a possible colour palette of reflection colours for the configuration $\lambda_{ref} = 450$ nm and reflector thickness of $\frac{H}{4}$. The thickness of the MgF_2 layer varies in the range 0–100 nm, whereas 0 corresponds to the starting QQR design type. The solar transmittance amounts to around 88%. This colour-tuning design is discussed in detail in Section 5.3. The angular dependency of the coloured reflection of the CTL design is illustrated in Figure 3.20 in comparison to the QQR design for two different configurations of λ_{ref} and MgF_2 layer thickness. The design parameters for the blue-green reflection are $\lambda_{ref} = 505$ nm (dark red markers) for the QQR design and $\lambda_{ref} = 400$ nm with a 37 nm thick MgF_2 layer (bright red markers) for the CTL design. The reflector thickness in the CTL design is increased to $\frac{H}{3}$ in order to obtain a similar colour intensity as for the QQR design with $\frac{H}{4}$. For the green-yellow reflection, the design parameters are $\lambda_{ref} = 605$ nm (orange markers) and $\lambda_{ref} = 400$ nm with an MgF_2 layer thickness of 78 nm (yellow markers), for QQR and CTL respectively. The colour trajectories for oblique incidence are nearly identical, which is in agreement with the also very similar reflectance curves (see

MgF_2	Colour coordinates			Colour		R_{vis}	T_{sol}	$M =$
[nm]	L*	a*	b*			[%]	[%]	$\frac{R_{vis}}{R_{sol}}$
0	49.2	-7.0	-18.1	blue		17.8	87.0	1.43
20	49.9	-10.1	-4.1	blue-green		18.4	87.7	1.56
40	48.3	-9.9	12.9	green		17.0	88.1	1.50
60	44.6	-2.1	18.8	yellow-green		14.2	88.2	1.25
80	40.0	12.8	-0.9	violett		11.2	88.0	0.97
100	36.5	24.7	-25.2	purple		9.3	87.7	0.79

Table 3.3: Comparison of the colour values and the solar quantities for increasing thickness of the MgF_2 inter-layer (CTL design).

Figure 5.17 and 5.18 in Section 5.3). The colours of the CTL design, however, tend to be a little less variant.
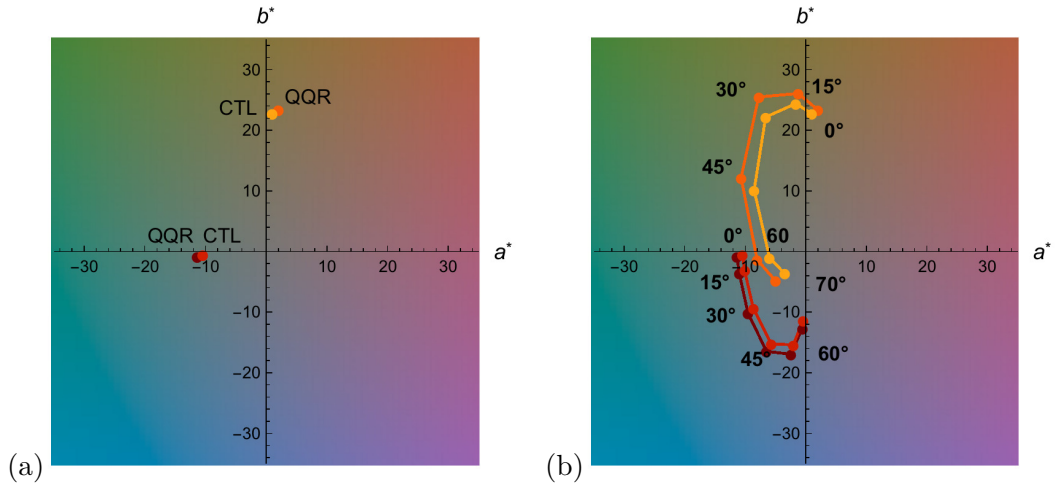
Figure 3.20: (a) Colour values for the QQR design glass$\|\frac{H}{4}LL\frac{H}{4}\|$air with $\lambda_{\mathrm{ref}} = 505\,\mathrm{nm}$ (dark red marker) and $\lambda_{\mathrm{ref}} = 605\,\mathrm{nm}$ (orange marker) and the CTL design glass$\|\frac{H}{3}(\mathrm{MgF_2})LL\frac{H}{3}\|$air with $\lambda_{\mathrm{ref}} = 400\,\mathrm{nm}$ and an $\mathrm{MgF_2}$ layer thickness of $37\,\mathrm{nm}$ (bright red marker) and $78\,\mathrm{nm}$ (yellow marker). (b) Colour trajectories for oblique light incidence of these designs for the angles (0, 15, 30, 45, 60, and 70°). The value of L^* was set to 50 in order to obtain a suitable graphical colour representation.

4 Deposition Methods and Tools

For the multilayer deposition of coloured thin-film filters magnetron sputtering is used in reactive and non-reactive mode. This technology is chosen, as magnetron sputtering is the dominant deposition technique for large-area coating on glass.[78] In addition, magnetron sputtering is also suitable for mixed materials, such as TiO_2-SiO_2, either by using two sputtering sources in parallel or composite targets. For R&D co-sputtering with two sources has the benefit that the mixing-ratio of the two coating materials can easily be changed by applying different target powers, instead of changing the whole composite target. Co-sputtering is already carried out in research since a long time.[79,80] It now also becomes of importance in industry to deposit advanced composite materials.[44,81] In this chapter, the basics of the magneton sputtering process are described, as well as the individual experimental setups and tools for the presented research.

4.1 Thin-film deposition

4.1.1 Sputtering process

Sputtering is a physical vapour deposition (PVD) technique. It is carried out in a vacuum chamber and is based on the kinetic ejection of atoms and particles from a target by bombardment with positive ions. For this purpose, the sputtering gas is ionised by electron collisions in an electric field which is applied between the target (cathode) and the grounded anode (shields and chamber walls). Figure 4.1 illustrates the basic sputtering principle. The partially ionised gas containing equally positive and negative charges, as well as un-ionised atoms and molecules is called plasma.[82] The particles inside the plasma are not in a thermodynamic equilibrium, the heavy ions are rather slow (at ambient temperature), hence it is a cold plasma.[83] The
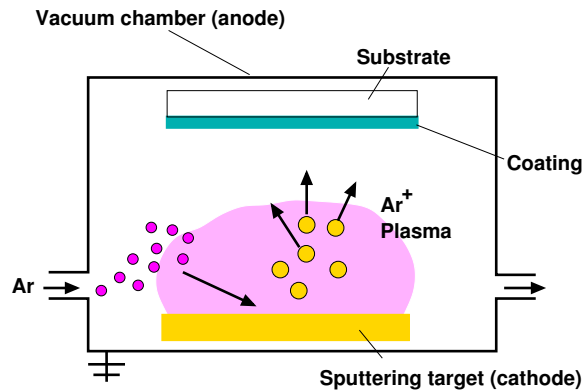
Figure 4.1: Schematic drawing of the sputtering principle: argon atoms are ionised by electrons in an electric field, and are then accelerated to the negative cathode. Hereby they can sputter material from the surface of the cathode which is then deposited on the substrate.

positive ions are accelerated onto the target at negative potential. At an incident energy in the range of 50–2000 eV the sputtering process for thin-film deposition can occur. During the sputtering process the following steps take place: the incident ions of the sputtering gas collide with surface atoms and break up chemical bonds of the target material, they transfer a part of their energy to the now mobile surface atoms, which are hence ejected at a typical energy of some eV.[84,85] Sputtering gases are typically nobel gases, such as neon, argon, krypton and xenon, since they do not react with the target material.[86] For thin-film deposition, however, mainly argon (Ar) is used as it has a reasonable sputtering yield and is easier available than krypton or xenon.[82] The relatively light neon is not used as sputtering gas, since it has a very low sputtering yield, especially for heavy target materials, such as gold or tantalum. The reason is that the sputtering yield (number of ejected atoms per impinging ion) depends on the atomic mass of the impinging ion and the surface atom.[82]

In the simple setup of diode sputtering, where only an electric discharge potential is used, the electron density is relatively low, and hence the ionisation rate as well. Therefore, relatively high pressures ($1 \cdot 10^{-1}$ mbar) must be applied to increase the sputtering yield, but the deposition rate does not increase significantly because of particle–ion collisions in the plasma discharge.[87,88] One possibility to increase the sputtering yield and with it the deposition rate is to integrate a magnetic field to trap the electrons, which is described in the following section. Other sources and further details to plasma discharge processes can be found e.g. in CHAPMAN.[82]

4.1.2   Magnetron sputtering

One of the most used sputtering sources nowadays are magnetrons. They are widespread in research (with sizes in the order of centimetres) as well as in industry (up to 3.6 m in length). In magnetron sputtering, a magnetic field enhances the sputtering yield and the deposition rate.[89] This fact gives also the sputtering source the name magnetron. The magnets are arranged in such a way that the magnetic field lines are perpendicular to the electric field (see Figure 4.2), which forces electrons to move on a helix-shaped trajectory close to the target (see Figure 4.3).
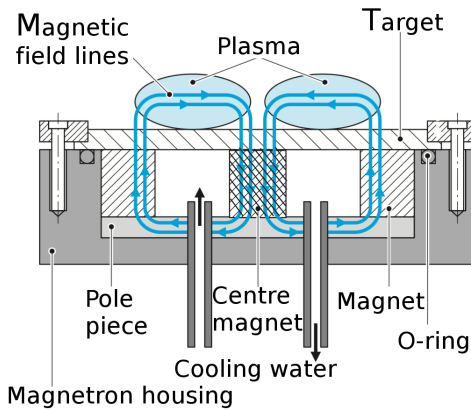
Figure 4.2: Schematic lateral view of a magnetron sputtering source. The magnetic field lines and the localised plasma are shown in blue. Source: Billard and Perry[89]
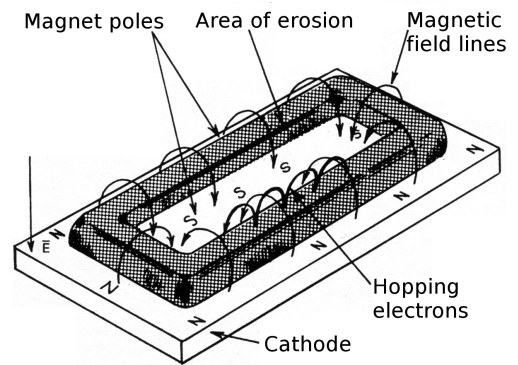
Figure 4.3: Magnetic and electric field configuration of a planar magnetron. The electrons stay *trapped* between the south and north poles of the magnets, where the plasma is then more intense. Source: Chapman[82]

Because of the spiral movement the electrons stay much longer inside the plasma close to the target, which increases the ionisation probability of argon atoms significantly.[82] The process pressure for magnetron sputtering is in the range of 0.5 to $3 \cdot 10^{-2}$ mbar which is much lower than for dipole sources (as consequence, less voltage is needed for a higher deposition rate). Due to the ion bombardment and the energy transfer the target and the magnets need to be water cooled.[90]

For laboratory size and in semiconductor industry, normally planar cathodes are used.[91] Figure 4.4 shows a planar source with ongoing plasma discharge during a co-sputtering process. The plasma discharge is not homogeneously distributed on the target surface, due to the applied magnetic field, which leads to different areas of more
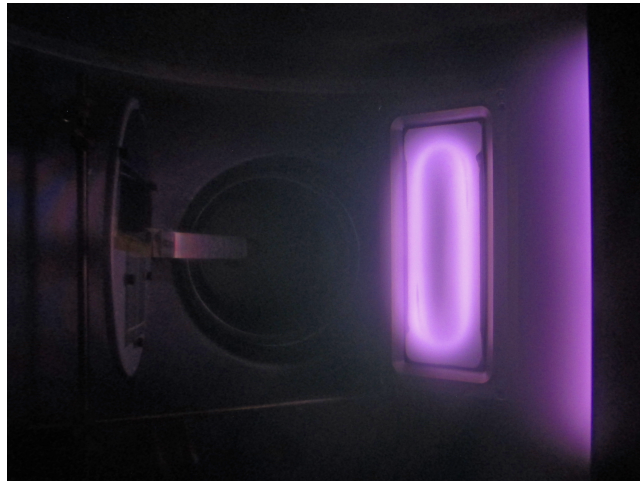
Figure 4.4: Photograph of an on-going co-sputtering process at the Ceramics Laboratory (LC), EPFL. On the target in the back (MgF_2) the sputtering race-track is clearly visible. From the target in front (SiO_2) only the plasma is visible. On the left side in the picture, the manipulator with substrate holder and sample is shown.

or less strong plasma erosion (area of sputtered material). Due to the arrangement of the magnets, the plasma is localised in a cycle or stadium-like closed loop. The zone of erosion is often also referred to as *race-track*. In industry also rotary cathodes are used, where the target is a hollow, rotating cylinder (see Figure 2.6). They have the advantage of smaller erosion areas since the rotation decreases the unused target material.[62] For details about industrial magnetron sputtering see Section 2.2.2.

4.1.3   Sputtering modes

For the deposition of insulating films, such as oxides and fluorides, there are two sputtering modes – reactive and non-reactive mode. In the non-reactive mode ceramic or compound targets and only the sputtering gas Ar are used. To assure a stoichiometric composition of the films, small amounts of other gases can be added, e. g. oxygen to compensate an oxygen loss during the deposition. The second mode is reactive sputtering, where the deposition is performed from a metallic, semiconductor, or under-stoichiometric target. One or more reactive gases are added to the sputtering gas, to form the chemical composition of the film by a chemical reaction during the deposition process.

Reactive sputtering mode

When using a metallic target or an under-stoichiometric composite target (e.g. a partially oxidised material, such as TiO) in reactive mode, the sputtering source can be driven by direct current (DC), pulsed DC, or radio frequency (RF) power. In the following, the example of reactively sputtered oxides is used. The O_2 of the process gas reacts with both, film on the substrate and target surface. Depending on the partial pressure of the reactive gas, and the target power, the target surface gets partially or fully oxidised. The latter is called *poisoned* state. In between the metallic and the poisoned state of the target is the transition state, where the target switches from metallic mode to reactive mode.[92] By changing the O_2 partial pressure, it is possible to switch between these states. This transition can be monitored by the target bias which follows the so-called hysteresis of reactive sputtering (see Figure 4.5). Since the sputtering yield of the oxide on the target surface is lower than that of the metal atoms due to chemical bonding, the deposition rates drops dramatically, when the O_2 partial pressure is increased. The optimal position in the hysteresis diagram for stable reactive sputtering conditions for stoichiometric films is on the plateau, just before the target voltage drops, when the O_2 pressure is decreased.
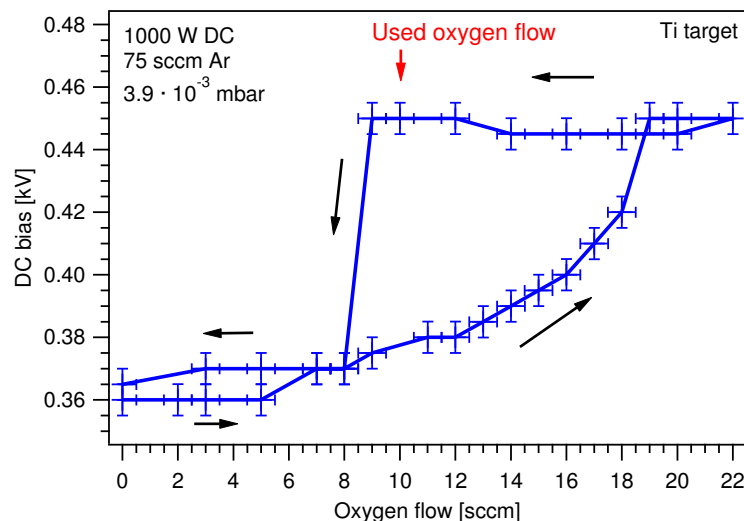

Figure 4.5: Measured hysteresis loop (target DC bias versus oxygen flow) of TiO_2 deposition reactively sputtered from Ti target on a Balzers BAS 450 sputtering system at CMi, EPFL.

When using higher power or larger targets and to avoid instabilities due to sparks in the plasma, accumulating positive charges on the oxidised area of the targets – especially next to the race-track – can by compensated by applying a short positive power pulse. During this positive pulse, the accumulated positive charges get neutralised by electron bombardment. This power mode is called pulsed DC. Hereby, the deposition rate can be optimised by changing pulse frequency and pulse width. Modern industrial coaters even include automatic arc-detection and pulse-generating accessories.[93] Furthermore, also RF power is possible. Depending on the desired film properties it might be of advantage to power the target either by pulsed DC or RF.[94] Details about RF sputtering are described below.

Non-reactive sputtering mode

When using insulating targets, such as oxides or ceramics, it is necessary to apply RF voltage to the target. RF power is typically a sinus wave with a frequency of 13.56 MHz changing the orientation of the electric field at the target. The charged particles in the plasma are oscillating with the same frequency. However, the heavy Ar^+ ions are too inert to follow the field oscillation, whereas the light electrons do. As a result the plasma during RF sputtering is the most positively charged area in the sputtering chamber. The electrons get accelerated strongly and collide with the walls of the chamber, including the target, before the electric field changes again. Due to the electron bombardment, the target gets charged with the so-called self-bias. It is this negative self-bias potential which accelerates the positive Ar^+ ions to the target for the resulting sputtering process. Since radio frequency is involved, the target including plasma acts like an antenna. Only when the connection between generator and antenna are matching the same impedance, energy can be transferred to the plasma. Therefore, in addition to the power generator, a matching network is needed, consisting of a match box and a control unit. This equipment is used to adjust the impedance and the load at the output of the generator to $50\,\Omega$. This makes RF sputtering more complex and cost intensive.

Compared to the reactive process, the deposition rate from ceramic or compound targets is lower. In addition, to achieve stoichiometric oxide films from oxide targets, it is sometimes necessary to add a small amount of O_2 to the process to compensate the oxygen losses during the deposition progress (e. g. for SiO_2 some oxygen is

added, for TiO_2 not necessarily). This decreases the deposition rate even further. If the deposition rate is of minor importance, like for very thin films ($<100\,nm$), the advantage of this process is that the deposition is often more stable than the corresponding reactive process, and easier to control. Another advantage is that it is easier to achieve fully oxidised films. For composite targets in industry double rotary cathodes are used, driven not with RF, but with alternating bi-polar mid frequency (MF) power, as described in Section 2.2.2 and illustrated in Figure 2.5 and Figure 2.6.

4.2 Experimental setups

To achieve the thesis objectives (see Section 2.3) different scientific equipments had to be built or adapted, which are described in detail in the following sections. To deposit coloured interference filters with a homogeneous coloured appearance, the sputtering tool of the Solar Energy and Building Physics Laboratory (LESO-PB), EPFL, has been designed to deposit layers on substrates up to $100\,mm$ in diameter with a relative thickness difference between centre and border of the substrate of only a few percent. For the research on low-refractive-index materials two different setups have been used: the ultra-high vacuum (UHV) deposition chamber of the Department of Physics of the University of Basel and the high vacuum (HV) sputtering tools of the Ceramics Laboratory (LC) at EPFL. The first one has been complemented by an in-situ mass spectrometer to analyse the chemical reactions during the reactive sputtering deposition of MgF_2; in addition, it is connected to an in-situ photoelectron spectrometer. The second one has been specially designed to deposit low-refractive composite films by magnetron co-sputtering with a spacial gradient of refractive index across the substrate.

4.2.1 Sputtered multilayer coatings for coloured solar collectors

For the deposition of the coloured collector coatings by reactive magnetron sputtering and for the development of new coloured coatings, a brand-new UHV deposition chamber was designed and built at the LESO-PB. The chamber consists of a custom built centre part produced by Pink, Germany, and standard lid and ground-plate flanges from AJA International, USA. On the ground plate four AJA magnetrons
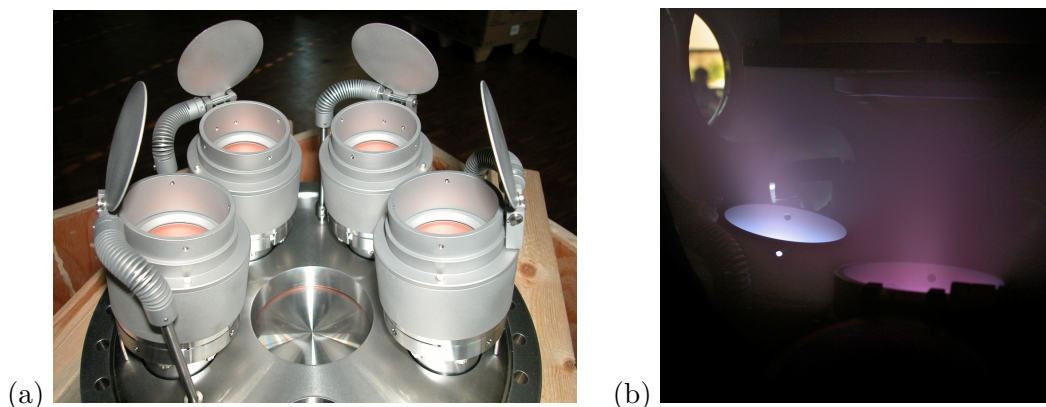
(a)   (b)

Figure 4.6: (a) Image of the ground plate of the modular UHV deposition chamber with the four magnetrons made by AJA International. (b) Photograph of an on-going co-sputtering process of TiO_2-SiO_2 at the LESO-PB, EPFL.

for 2-inch targets are installed (see Figure 4.6a). They can be driven by DC, pulsed DC, or RF with a power of maximum 500 W. Figure 4.6b shows an on-going co-sputtering deposition of TiO_2-SiO_2 using an Si target powered by RF and a TiO target by pulsed DC. The lid holds the rotatable sample holder, fixed on a vertical linear drive for changing the target–substrate distance. In addition, the substrate can be heated during deposition. For this purpose a standard HV substrate radiation heater has been modified and adapted to operate reliable under UHV conditions. The films in this study however, where without exception deposited at room temperature, a requisite for the later industrial production. Ar is used as sputtering gas which is introduced directly at the magnetrons into the chamber. The Ar gas line has been designed in such a way, that all four inlets exhibit the same gas pressure on the foreline. As reactive gas, oxygen and nitrogen can be used. They are pre-mixed and injected into the chamber through a ring with small openings around the substrate holder. Figure 4.7 sketches a schematic lateral cut of the chamber arrangement. The base pressure of the chamber is in the order of $2 \cdot 10^{-8}$ mbar without any bake-out. The process pressure is monitored with a Vacom Atmion pressure gauge. The process pressure can be set with MKS mass flow controllers and by throttling manually the process valve between chamber and pumping system. For the sputtering gas, a 100-sccm-mass-flow controller is used and the oxygen flow is regulated with a 10-sccm-mass-flow controller. The nitrogen line remains unused for the here described
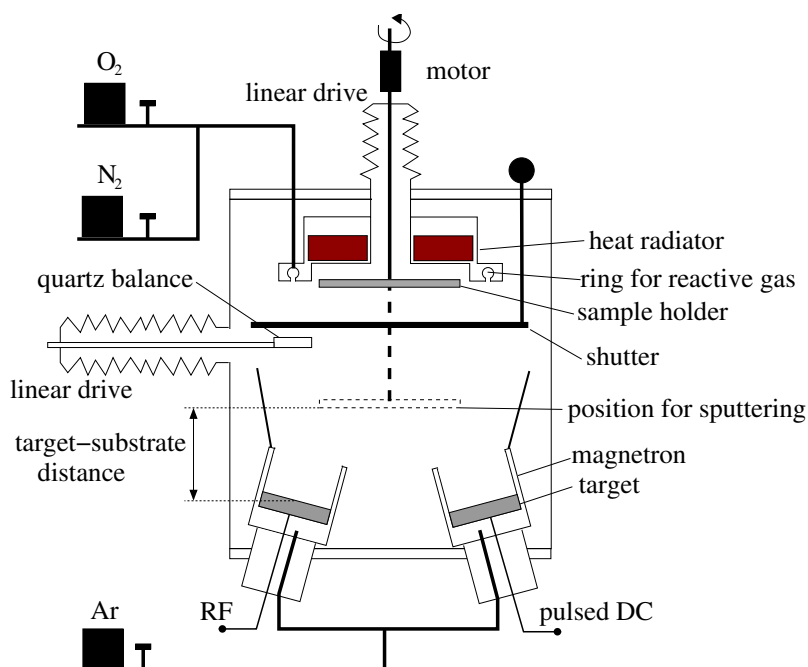
Figure 4.7: Schematic lateral cut of the UHV deposition chamber for reactive magnetron sputtering. Two of four magnetrons are shown. The sample can be vertically moved for: presputtering, deposition, and transfer to the in-situ ESCA system, as well as for homogeneous layer deposition. The manipulator for the transfer is not shown.

experiments. A quartz-crystal monitor is installed which can be moved to the axis of the deposition position. A shutter protects the sample to be able to perform presputtering and to measure the deposition rate at the same time. Figure 4.8 shows a photograph of the deposition chamber. The motor for the sample motion, the process throttle valve with pumping stage and the Atmion pressure sensor can be seen. In the background of the picture an X-ray photoelectron spectroscopy (XPS) system is visible, also known as electron spectroscopy for chemical analysis (ESCA).

The deposition chamber has been designed to deposit samples up to 100 mm in diameter. To be able to deposit coloured multilayer films (see Section 3.6), a constant film thickness throughout the sample is a requisite. A few nanometres in thickness difference may change the coloured reflection already significantly. Since reflection colours of the interference filters depend strongly on a change of the absolute physical layer thickness, the relative layer homogeneity becomes with thicker layers more important. A slightly greater thickness of the spacer layer e.g. such as

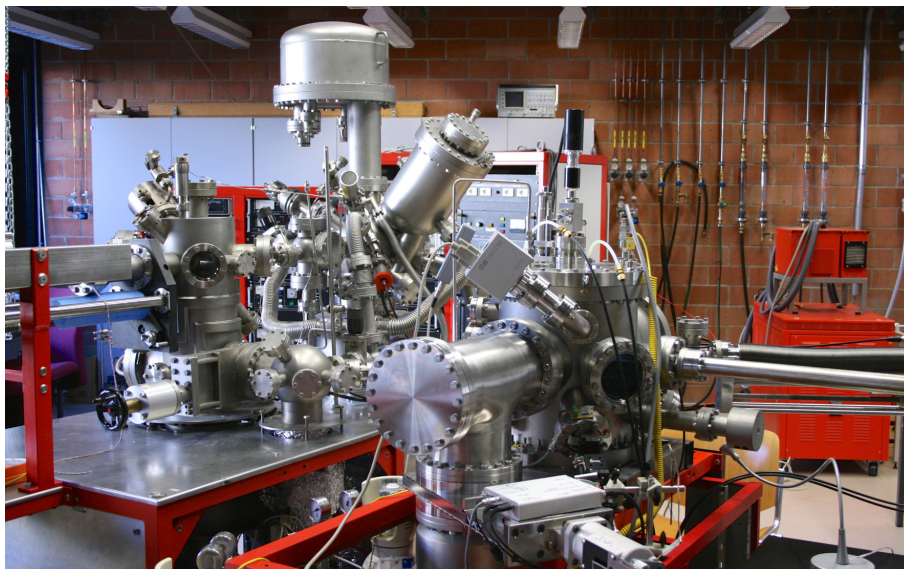**Figure 4.8:** Photograph of the new installed and custom-built UHV plasma-deposition chamber for magnetron sputtering with four sputtering sources. In the background of the picture the completely refurbished ESCA system is shown: with energy analyser, XPS source and monochromator for MXPS, UPS as well as preparation chamber and transfer system.

used in a typical QQR coatings design from Section 3.6.1, shifts the reflection peak towards longer wavelengths, whereas a smaller thickness shifts it to shorter. In addition to the geometry of the chamber, such as magnetron size and arrangement, the zone of homogeneity across the samples also depends on the sputtering parameters, such as target power, process pressure and gas flows, as well as the target–substrate distance. Figure 4.9 plots the thickness profiles – determined by spectroscopic ellipsometry (as described in Section 3.2.2) – of SiO_2 layers deposited at three different target–substrate distances with the same sputtering parameters (100 W RF driven Si target, 21 sccm Ar flow, 1 sccm O_2 flow and $2.3 \cdot 10^{-3}$ mbar process pressure). At the substrate–target distance of 65 mm (black curve in Figure 4.9) an excellent homogeneity for SiO_2 films has been achieved with a thickness deviation of less then 1% across a 4-inch wafer. At the same target–substrate distance (65 mm) the relative homogeneity of TiO_2 layers is in the order of 5–8%. TiO_2 is either sputtered in fully reactive mode from a Ti target driven by pulsed DC power, or from a sub-oxide TiO target operated with RF power. However, an uniform layer thickness is less critical for the TiO_2 reflectors in the coloured coating designs, since they are relatively thin
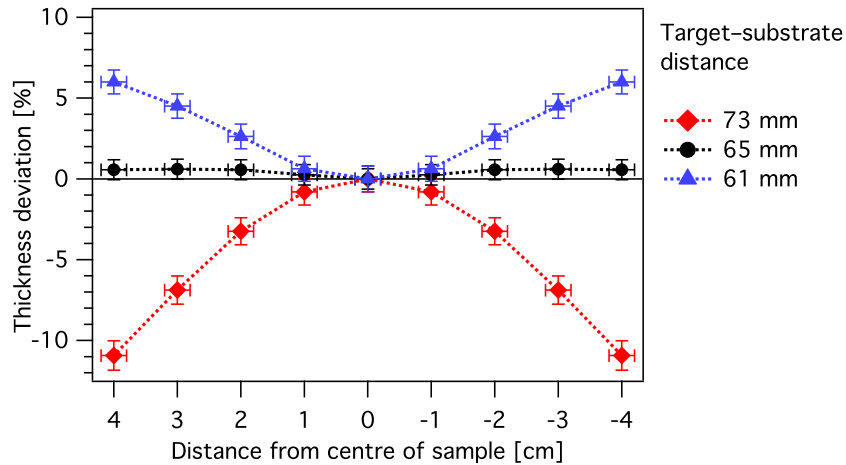
Figure 4.9: Thickness profiles of SiO_2 layers sputtered from an Si target. The layer with the red thickness profile (squares) was deposited at 73 mm target–substrate distance, and with the blue profile (triangles) at 61 mm. The black profile (circles) with an optimised target–substrate distance at 65 mm is in between, its relative film homogeneity is better the 1% across the substrate. All layers were deposited at 100 W RF target power and $2.3 \cdot 10^{-3}$ mbar process pressure. Ar flow was set to 21 sccm, O_2 flow to 1 sccm.

(< 20 nm). The absolute layer thickness homogeneity is still in the same order of ≤ 2 nm as for the thicker SiO_2 spacer layers. Table 4.1 summarise the deposition rates for TiO_2 and SiO_2 at different target powers, gas flows and target–substrate distances. Hereby, the deposition rate is determined by the deposition time and the film thickness in the centre of the substrate holder (centre position at 0 cm in Figure 4.9).

With these optimised deposition parameters and target–substrate distance, it was possible to deposit even films for coloured interference filters with a very homogeneous colour appearance (see Figure 4.10). Detailed results on the coloured coatings are discussed in the published results in Section 5.1.

Before deposition, the glass substrates were pre-treated. They were cleaned by an industrial dishwasher for glasses and ceramics. After the cleaning program, a rinsing program using demineralised water was used, followed by hot air drying. The glass substrates were cut with an industrial cutting tool before the cleaning process. The maximum used dimension for glass substrates is $70 \times 60 \times 4$ mm^3. The silicon wafers have been already factory clean. Before inserting the sample holder with the prepared sample in the chamber, dust particles were removed with pure dry nitrogen.

Material	Target	Power		Pressure	Ar	O_2	Distance	Rate
		[W]	mode	$[10^{-3}\,\text{mbar}]$	[sccm]	[sccm]	[mm]	[nm/min]
SiO_2	Si	100	r.RF	2.2	21	1	61	2.7
SiO_2	Si	100	r.RF	2.2	21	1	65	3.5
SiO_2	Si	100	r.RF	2.2	21	1	73	2.8
TiO_2	TiO	100	r.RF	2.3	21	1	61	0.3
TiO_2	Ti	120	r.p.DC	2.4	28	2.5	65	1.0
TiO_2	Ti	200	r.RF	2.2	9.7	1	65	0.7

Table 4.1: Deposition rate depending on the target–substrate distance, sputtering parameters and target nature, which were used for coating deposition. The sputtering modes are r.RF (reactive radio frequency at 13.56 MHz) and r.p.DC (reactive pulsed direct current).

The stoichiometry of thin-film coatings, as well as their electronic properties can be analysed with photoelectron spectroscopy (PES),[95,96] a powerful method to measure the atomic concentration and the chemical state of the elements of a film. Since the electron escape depth is only a few ångström (Å), which corresponds to several monolayers of atoms, PES is intrinsically surface sensitive. It is of great advantage to perform measurements on sputtered samples in-situ, without breaking the vacuum between deposition and analysis, as shown in several publications by Peter Oelhafen and his group.[97–99] Details about the PES principle can be found e. g. in HÜFNER.[100]

Figure 4.10: Homogenous coloured samples $6 \times 6\,\text{cm}^2$ with sputtered multilayer coatings on the reverse side of the glass. Front side is chemically etched for light defusing.

For this purpose a pre-owned ESCA system was moved in the framework of this doctoral work from the University of Basel to the LESO-PB and was completely refurbished. For the transport, the highly sensitive EA11 energy analyser from SPECS, Germany, was dismounted and shipped in a particular-built mechanical shock-damping transport box. After the transport the hemispheres have been re-aligned, and broken ceramic spacers replaced by new ones – in-house reproduced at the LESO-PB mechanical workshop. The EA11 housing as well as most vacuum parts have been mechanically cleaned with high-pressure micro bees. The photograph (Figure 4.8) shows the freshly refurbished ESCA system after re-calibration and first reference measurements after a second move to a newly constructed laboratory space on the EPFL campus. For further details and illustrations see Appendix D. Finally the deposition chamber and the PES have been joined to a large UHV system. Figure 4.11 shows the total arrangement of the sputtering-ESCA system. For this, an

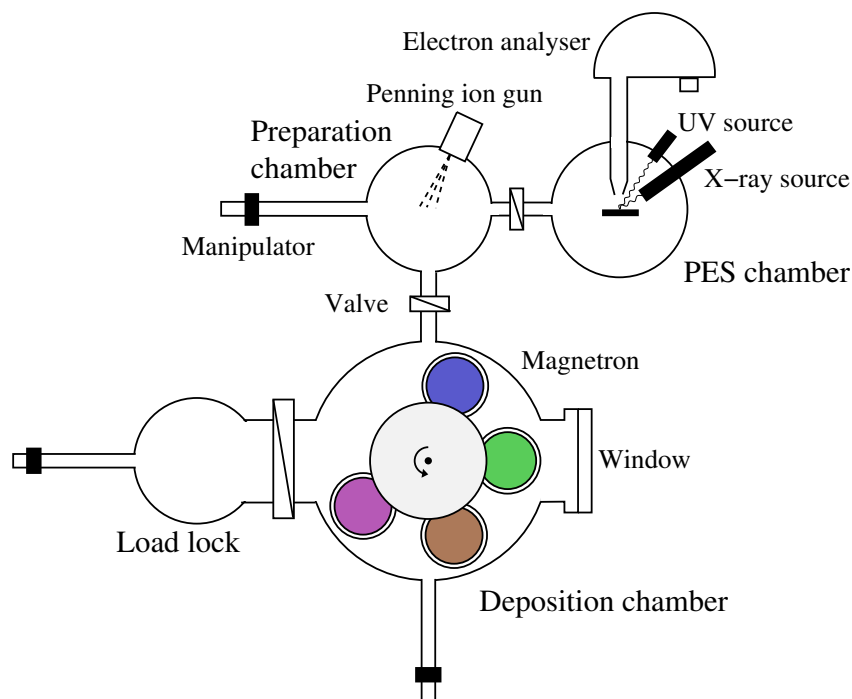**Figure 4.11:** Sputtering-ESCA system for multilayer coating development. The deposition chamber and the PES chamber are connected through a vacuum transfer system to avoid surface contaminations due to air exposure. The penning ion gun in the preparation chamber, which is situated between the deposition chamber and the PES recipient, can be used for cleaning ex-situ XPS samples or for depth-profiling measurements.

in-situ vacuum transfer system was planned and designed.

The photoelectron spectrometer is equipped with two X-ray sources for XPS (Mg K_α 1253.6 eV) and MXPS (Al K_α 1486.6 eV) and an UPS source (He I 21.2 eV and He II 40.8 eV). For the analysis of the coating materials the XPS source is used, which has been calibrated with a pure gold sample with Au $4f_{7/2}$ of 83.8 eV (binding energy). The layers to investigate are deposited on a silicon wafer and have a thickness of around 15 nm to avoid charging effects due to ejected photoelectrons. Since the escape depth of photoelectrons is much smaller than the penetration depth of the exiting X-ray photons, positive charges on the highly insulating ceramic and dielectric coatings can be therefore neutralised by an injection of a photoelectron from the conducting substrate.[97]

4.2.2   Reactively sputtered magnesium fluoride (MgF$_2$)

The deposition of MgF$_2$ films by reactive magnetron sputtering has been performed at the Department of Physics of the University of Basel. For the reactive plasma process a modular UHV deposition chamber is used. The background pressure of the chamber is in the range of 10^{-7} to 10^{-8} mbar, already without any bake-out. The substrates are mounted vertically on the sample holder, which can be rotated to face the different magnetron positions, as well as the sample transfer system. On the sample holder right above the sample, a quartz microbalance is installed (see Figure 4.12a). The holder can be displaced vertically to switch between deposition and quartz position. A shutter in front of the substrate allows pre-sputtering for target cleaning, process stabilisation and measuring of the deposition rate before starting the deposition. The reactive gases are diluted with the sputtering gas Ar before entering the process chamber. The whole gas system can be purged via a separate pumping stage. This guaranties that no reactive gas is entering the chamber in high concentration before the process is started. The process gas pressure is monitored with a MKS Baratron© manometer. The pumping speed can be reduced by a throttle valve. The magnetron used for the experiment with mounted Mg target is illustrated in Figure 4.12b. The target diameter is 22.8 mm. It can be driven with a power up to 100 W, which corresponds to around 25 W/cm^2.

For the film deposition pulsed DC and RF power were used. The target–substrate distance amounted to 104 mm. Glass and Si substrates were pre-treated before de-
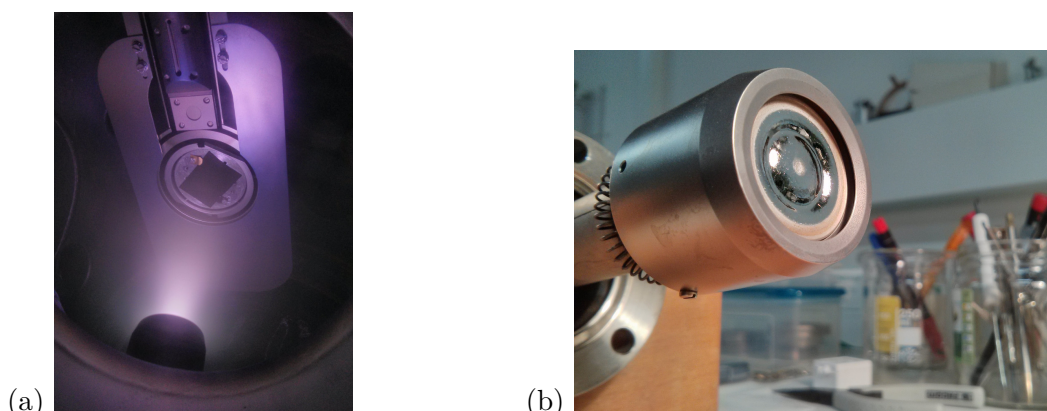
(a) (b)

Figure 4.12: (a) Photograph of the deposition process with ignited plasma. In the foreground the magnetron is visible, in the background the sample holder with shutter, quartz microbalance and Si substrate. (b) Photograph of the magnetron with the metallic Mg target used for reactively sputtered MgF_2. On the target (cathode) the racetrack is clearly visible. Furthermore, the magnetron shielding (anode) is shown.

position. They were cleaved with a diamond cutter to samples of $35 \times 25 \, \text{mm}^2$ before they were cleaned in an ultra-sonic bath for 10–15 min in both, first pure acetone and then pure ethanol. Right before loading the sample through the load lock, dust particles were removed with pure dry nitrogen.

When using two different reactive gases it is essential to understand the chemical reactions inside the plasma during the deposition. Therefore, a quadrupole mass spectrometer made by *Stanford Research System* has been installed especially for this experiment. It was mounted on the deposition chamber behind an orifice combined with an additional pumping stage to reduce the pressure for the mass spectrometer from 0.5 to $3 \cdot 10^{-2}$ mbar (process pressure) to $< 10^{-5}$ mbar (see Figure 4.13). With this arrangement it was possible to investigate qualitatively the chemical reactions during the plasma process by monitoring mass spectra without plasma discharge, directly after the plasma ignition, and under stabilised conditions (15–20 min after the ignition).

The deposition chamber is connected through a vacuum system to a photoelectron spectrometer to analyse the chemical composition of the deposited films. The samples were transferred after the deposition without breaking the vacuum, to avoid surface contaminations due to exposure to air. This is of great advantage since PES is a surface sensitive method. The configuration of the sample transfer system is
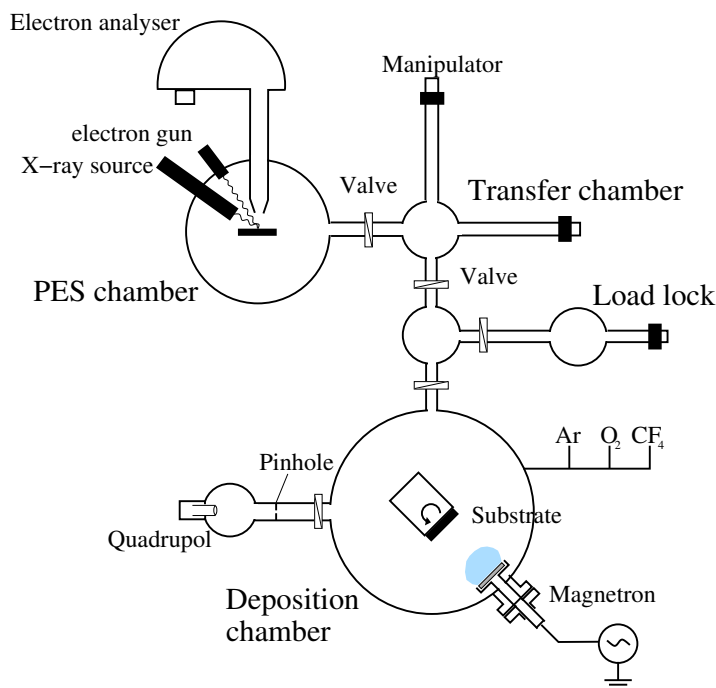
Figure 4.13: Simplified schematic drawing of the deposition chamber in the configuration for reactive magnetron sputtering. The chamber is attached through a vacuum system to a photoelectron spectrometer. The load lock in between can be also used to introduce samples for ex-situ XPS. A quadruple mass spectrometer is connected via an orifice and a differential pumping stage to analyse the process gas.

schematically shown in Figure 4.13. The spectrometer of the type VG ESCALAB 210 made by VG Scientific Ltd is equipped with a monochromatic X-ray source (Al K_α) with a photon energy of 1486.6 eV. The base pressure of the PES system is in the order of $1 \cdot 10^{-10}$ mbar. For narrow scans the resolution of the instrument is better than 0.6 eV. As reference for the binding energy the Au $4f_{7/2}$ electron state of a pure gold sample at 84 eV was used. To minimise the charging shift of the XPS spectra, the investigated films were deposited on silicon and have only a thickness of around 15 nm. Since the escape depth of photoelectrons is much smaller than the penetration depth of the exiting X-ray photons, positive charges on highly insulating coatings can then be neutralised by the injection of a photoelectron from the conducting substrate.[97] In addition, with the installed electron flood gun charges can be compensated during the XPS measurements. Furthermore, it is possible to partly etch the deposited films with a raster ion gun for depth profiling.

4.2.3 Co-sputtered Mg–F–Si–O nano-composite films

For the deposition of Mg−F−Si−O composite films on glass and silicon wafers an HV chamber at the LC was used, which has been dedicated to experiments which involve fluorine to avoid contaminations in other experiments. In addition, it fulfilled the prerequisites, such as large planar magnetrons that can be mounted at different sputtering angles and large sample sizes (up to $100\,\mathrm{mm}$ in diameter). The chamber has been rebuilt from scratch and adapted as best as possible to the needs of the experiments. Two AJA magnetrons with a target size of $2 \times 5.26\,\mathrm{inch}^2$ were installed in a co-sputtering arrangement of $90°$ to each other. The schematic configuration of the chamber is shown in Figure 4.14. With this setup it was possible to deposit composite films by co-sputtering with a spacial gradient of the atomic concentration in the film and consequently of its reactive index. Such a sputtering configuration is of great advantage for the research of novel coating materials, since on each sample multiple film compositions at the same sputtering conditions can be investigated and analysed. Figure 4.15 shows a photograph of the deposition chamber with two
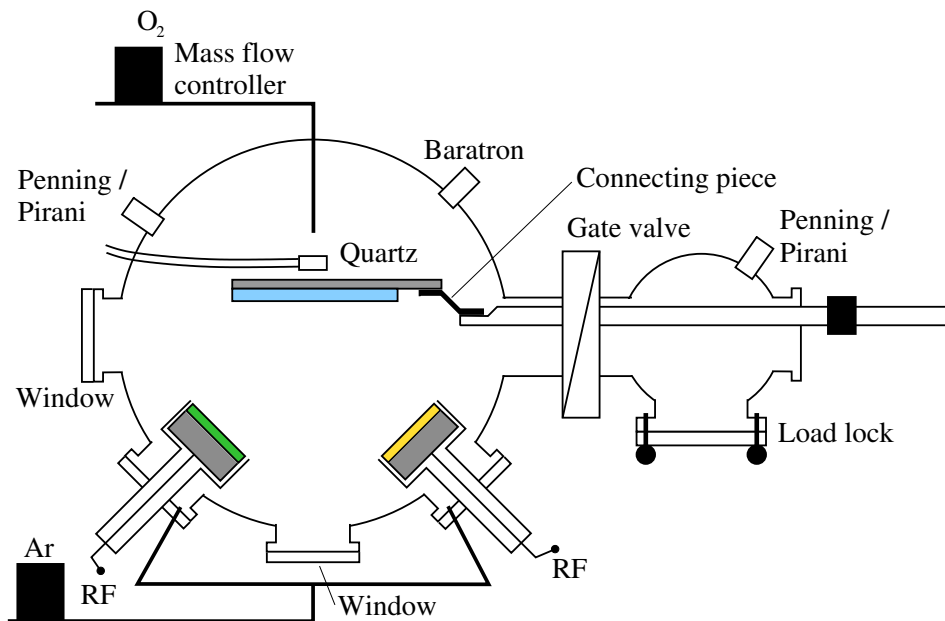

Figure 4.14: Schematic drawing of the deposition chamber for magnetron co-sputtering at the LC. The gate valve stays open during the deposition process, while the pumping speed at the load lock is reduced.

magnetrons and matchboxes installed. Through the window an ongoing plasma process of an SiO_2 deposition for calibration of deposition rate and stoichiometry is visible. During those calibration processes, the second magnetron with the MgF_2 target was covered with an aluminium foil to avoid cross sputtering. On the right-hand side of the picture the load lock can be seen. The base pressure of the chamber is in the range of $2 \cdot 10^{-6}$ to $5 \cdot 10^{-7}$ mbar.
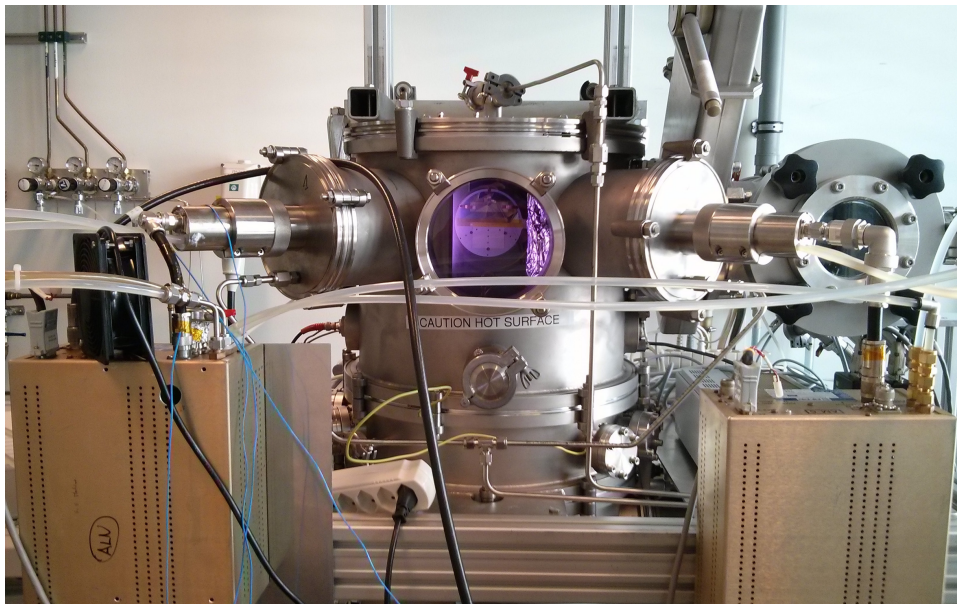
Figure 4.15: Photograph of the new installed and custom-built HV plasma-deposition chamber for magnetron sputtering with two sputtering sources for co-sputtering at LC. Through the window in the centre an ongoing SiO_2 sputtering process is visible. The MgF_2 target on the right side is protectd with aluminium.

The linear manipulator of the load lock also serves as substrate holder during the deposition process. For the deposition, the substrate is moved to the sputtering position, after the plasma discharge is stabilised. The idea of this configuration is to keep the experimental setup as simple as possible: neither a shutter is needed for the pre-sputtering process nor a complicated transfer system, where the substrate holder needs to be displaced from one manipulator to another. This configuration could be realised since the depositions were carried out at room temperature and no substrate bias was foreseen. Since the experimental setup was built from scratch within the time frame of less then six month, it has been necessary to reduce the planning and

construction time down to a minimum. As an additional benefit, the experimental design enables for future research the possibility to move the manipulator with a linear drive back and forth during the deposition, to simulate the co-sputtering process on an industrial in-line coater. A sample motion would also allow to deposit films with constant atomic concentration rather then with a gradient.

Another objective was to have the possibility of changing the samples without venting the main chamber. Therefore, a load lock has been installed. Due to this, the large volume of the main chamber remains under vacuum while loading the sample, and only the load lock with the small volume has to be pumped. This reduces the pumping time to reach 10^{-6} mbar from 24h down to only 1h. Since the sample holder is fixed to the manipulator through a connecting piece (see Figure 4.14), the setup is in addition very flexible to investigate different substrate positions during deposition. By changing the connecting piece, the target–substrate distance, as well as the deposition angle e.g. for off-axis sputtering can be varied. The basic idea of the different sputtering positions is illustrated in Figure 4.16.

As mentioned before, the whole experimental setup is designed to deposit gradient films of composite materials. For this purpose, the magnetrons are mounted with an angle of 45° relative to the substrate surface. Hereby, a decreased target–substrate

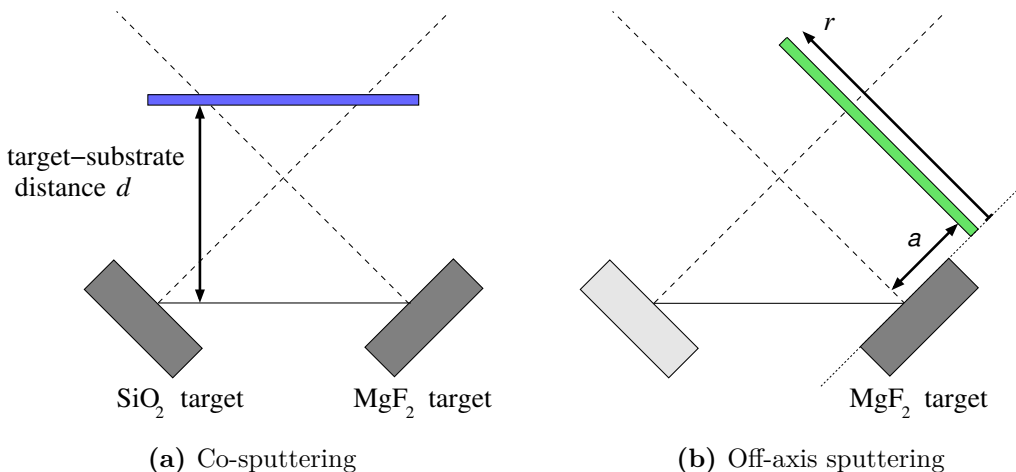**(a)** Co-sputtering   **(b)** Off-axis sputtering

Figure 4.16: Schematic drawing of the geometric sputtering arrangement in the deposition chamber for (a) Mg−F−Si−O co-sputtering with the target–substrate distance d and for (b) off-centre and off-axis MgF$_2$ sputtering with the target-axis distance a and the distance r perpendicular to the target surface.

distance d during deposition leads to more pronounced gradients (see thickness profiles in Figure 4.17). Another possibility to modify the thickness gradient is to vary the process pressure. Due to particle–particle scattering the sputtered materials are less focused at higher pressures, which reduces the gradient.
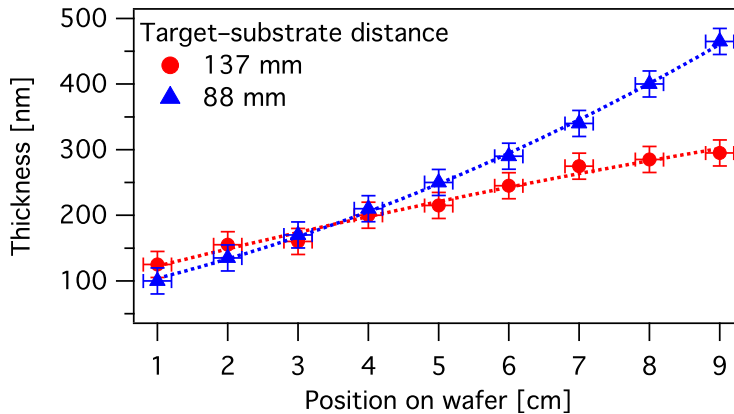

Figure 4.17: Spacial thickness profile of MgF_2 layers measured with the profilometer for two samples with identical deposition parameters, but at different target–substrate distances $d = 137\,\text{mm}$ (red, 60min deposition) and $d = 88\,\text{mm}$ (blue, 40min deposition). This shows that by increasing the target–substrate distance, the thickness gradient across the substrate becomes less pronounced.

The targets were driven with RF power up to $500\,\text{W}$. To be able to use this power, it has been necessary to replace the RF connectors and to minimise the cable length between matchbox and target. However, during the plasma process, cable and connectors remained additionally air cooled to prevent overheating. The gas line for the sputtering gas argon (Ar) enters the chamber behind the two magnetrons. The installation has been made in such a way that the gas enters with the same flow rate at both entrance inlets (see Figure 4.14). The Ar flow is controlled with a 100-sccm-mass-flow controller. As reactive gas oxygen is installed which enters the chamber in the centre of the chamber lid just above the substrate. It is regulated by a 20-sccm-mass-flow controller. The process pressure is measured with an MKS Baratron$^{\text{TM}}$ capacity pressure gauge. The process valve between pumping stage and the main chamber can be throttled to increase the working pressure during deposition, which is nevertheless limited to maximum $2 \cdot 10^{-2}\,\text{mbar}$. The reason for this is that the gate valve between sputtering chamber and load lock needs to stay open during the plasma process (related to the experimental setup, see Figure 4.14). To reduce the

influence of the turbo molecular pump of the load lock, its pumping speed has been reduced down to 66% of its nominal rotation frequency during deposition.

The deposition rates were monitored with a quartz-crystal microbalance. The crystal was installed below the deposition position of the sample at the target–substrate distance of 137 mm (see Figure 4.18). For calibration of the microbalance an Alpha Step 200 profilometer made by Tencor Instruments was used. By covering a part of the substrate with Kapton® tape, it was possible to measure the film thickness with the mechanical profilometer directly after film deposition. The Kapton® tape was removed with care parallel to the coated substrate to avoid a detachment and to minimise the lift up of the film. The measurements of the profilometer have an accuracy of 20 nm and were verified by scanning electron microscopy (SEM) cross sectional views. Figure 4.19 plots the MgF_2 sputtering rate versus the target power at 75 sccm Ar flow and $1.0 \cdot 10^{-2}$ mbar process pressure. The deposition rates were measured with the calibrated quartz microbalance. For the following depositions the quasi-linear area between 250 and 450 W RF power was chosen.
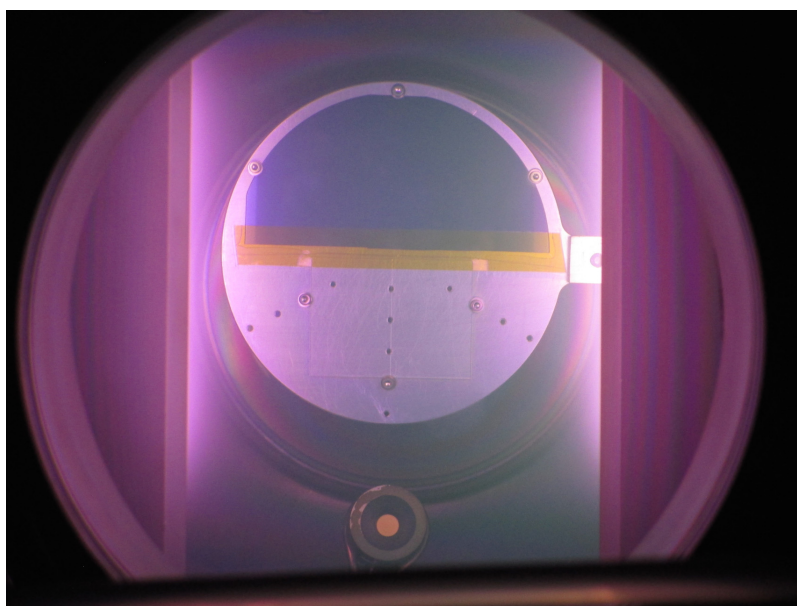

Figure 4.18: Co-sputtering from an SiO_2 (left side) and an MgF_2 target (right side). Argon is used as sputtering gas, which is enriched with a few sccm of oxygen. In the centre of the picture the samples (half of an Si wafer and two glass substrates) as well as the quartz-crystal microbalance are visible.
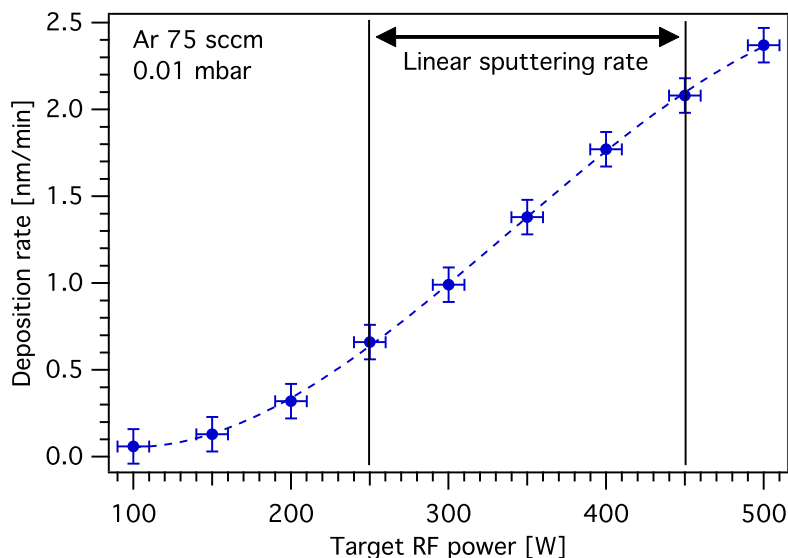
Figure 4.19: MgF_2 sputtering rate versus target power measured with the quartz microbalance. The quasi-linear area between 250 and 450 W was chosen for sample deposition.

The glass substrates were pre-treated before deposition. They were cleaved with a diamond cutter to samples of the size $35 \times 25\,mm^2$. In a next step they were cleaned in an ultra-sonic bath first in pure acetone and then in pure isopropanol about 10–15 min for each solvent. The Si wafers were cleaved in two half wafers, while taking care that they remain factory clean. Before installing the sample holder with the new samples in the load lock, dust particles were removed with pure dry nitrogen. The arrangement of the samples (Si half wafer on top, two glass substrates below) can be seen in the photograph of Figure 4.18. For a more precise investigation of the absorptance down to the UV range half wafers of 500-μm-thick fused silica were used instead of the extra-white glass substrates.

Since no supplementary fluorine gas is involved in the sputtering process the films tend to have fluorine deficiencies, which leads, as well known, to absorption in the films.[101,102] Therefore, the target–substrate distance and the process parameters (target power, pressure and gas flows) have been optimised to minimise the fluorine deficiencies. This was done in off-axis sputtering mode at a target-axis distance of $a = 74\,mm$ (see Figure 4.16b). Figure 4.20 plots the atomic concentration of the films measured by electron dispersive X-ray spectroscopy (EDX) in a Zeiss SEM
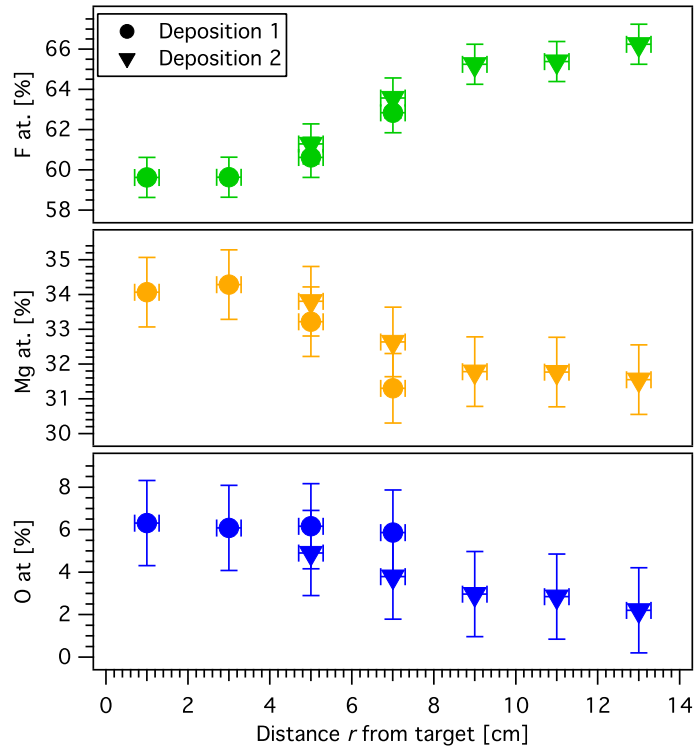
Figure 4.20: Atomic concentration measured with EDX of MgF_2 films versus the distance r (see Figure 4.16b). The substrate position is off-axis (perpendicular to target surface with a target-axis distance a = 74 mm). The target power is 450 W, the Ar flow is set to 75 sccm and the process pressure to $1.0 \cdot 10^{-2}$ mbar.

high-resolution microscope with 3 kV acceleration voltage. A typical measured EDX spectrum of an $Mg-F-Si-O$ film is shown in Figure 4.21. The low electron energy of 3 keV was chosen to reduce the penetration depth of the film while remaining high enough to detect all elements in the film. Besides the acceleration potential the electron penetration depth depends also on the material density in the film ($2.20\,g/cm^3$ for SiO_2[103] and 3.18–$3.19\,g/cm^3$ for MgF_2[104]). Corresponding to Figure 4.22, a film thickness greater 200 nm was chosen for the deposited coatings, to make sure that only the Si from the coatings but not from the Si substrate is detected.
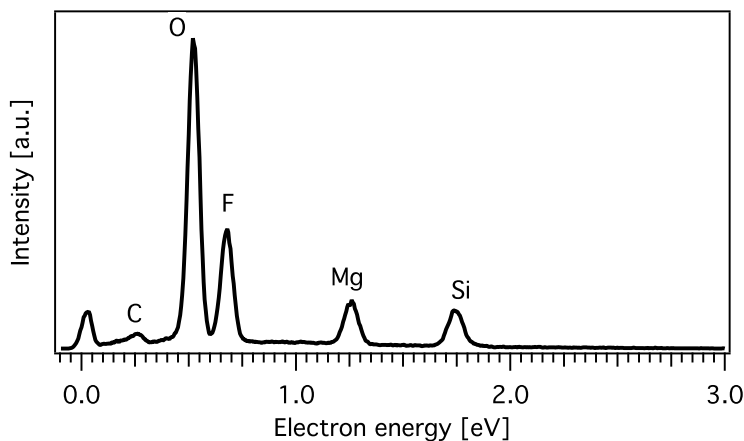
Figure 4.21: Typical measured EDX spectrum of an Mg−F−Si−O film. The small carbon peak which amounts to around 1–2 at.% is found on all ex-situ samples: its origin is mainly surface contamination due to air exposure of the films. The 3 keV electron energy is chosen to reduce the penetration depth while remaining at the same time high enough to detect all atomic elements (such as Si) in the coatings.
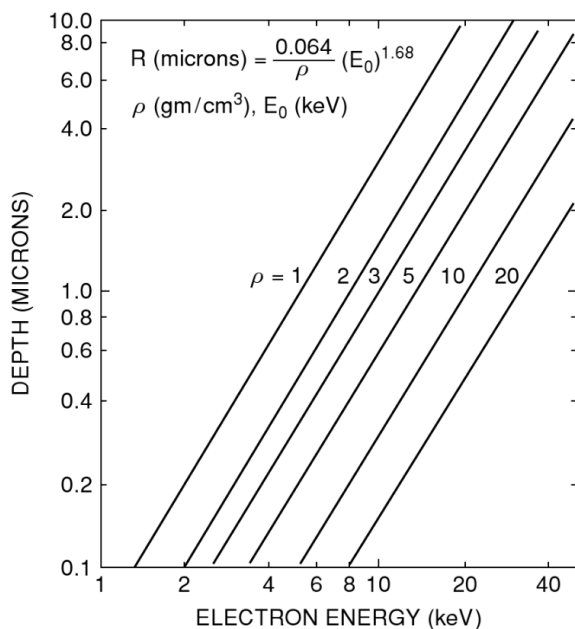
Figure 4.22: Electron penetration depth in EDX versus the incident electron energy for different material densities ρ. At 3 keV electron energy and $\rho = 2.20 \, \text{g/cm}^3$ for SiO_2 films the corresponding penetration depth amounts to approx. 200 nm. Source: ALFORD, FELDMAN, AND MAYER[105]

5 Results

This chapter is divided in four sections corresponding to four scientific paper manuscripts. Their current status is mentioned after each section title: which is either published, submitted for publication or still in preparation. Every section has a summary, where originality and novelty of the discussed research work is pointed out as well as the authors personal contribution to the specific research. Without exception the author of this thesis is primary author for all manuscripts, and they have been entirely written by him in person and have been revised by his supervisors.

There are three experimental research topics in the total scope and framework of this thesis research:

- Sputtered multilayer coatings for coloured solar collectors (Section 5.1, manuscript published in *Energy and Buildings* 68 (2014) 764–770)

- Reactively sputtered magnesium fluoride (MgF_2) (Section 5.2, submitted manuscript)

- Co-sputtered Mg–F–Si–O nano-composite films (Section 5.4, preliminary version of manuscript)

The research topics of Section 5.1 and Section 5.2 are linked through theoretic considerations about the coating design engineering which is presented in:

- Advanced coloured coating design with MgF_2 inter-layer (Section 5.3, submitted manuscript)

Each of the experimental research topics has been performed on specific experimental setups, which are described in detail in Chapter 4 (Deposition Methods and Tools).

5.1 Reactively Sputtered Coatings on Architectural Glazing for Coloured Active Solar Thermal Façades

5.1.1 Summary

Associating solar thermal collector glazing with a colour would grant architects complete freedom to integrate solar collectors into the building's envelope. First real-size prototypes of the coloured collectors were assembled at LESO-PB in collaboration with Glas Trösch AG, Switzerland to demonstrate the idea (see Figure 2.2). However, the energetic performance of the coatings was not optimised yet. For this purpose, new coating designs have been developed with a better visual and energetic performance on the basis of the numerical simulations described in Section 3.6. These new coating designs served as starting point for the deposition of new coloured multilayer coatings. The films consist of metal oxide layers and were deposited by reactive magnetron sputtering on silicon and glass substrates. The coloured glass samples exhibit a high solar transmittance $T_{\mathrm{sol}} > 87\%$ providing at the same time a complete opaque illusion to the human eye by their coloured reflection. Depending on the multilayer design and colour adjustment even values up to $T_{\mathrm{sol}} = 91\%$ have been reached.

Furthermore, a successful colour matching of the coloured interference filters to the colours of standard commercial architectural sun protection glasses (SPGs), a dark blue and a greenish-blue, have been demonstrated. This was achieved by following the so-called coating development cycle which is described in detail in Section 3.4.

In addition, a new large-scale prototype production in collaboration with Swiss-INSO SA, Switzerland has been launched. The new prototypes exhibit a homogeneous green reflection colour which is sufficiently stable for different viewing angles. The glazing has a high solar transmittance T_{sol} of 85.2% at normal incidence. Furthermore, the angular transmittance $T(\lambda, \vartheta)$, was measured with the Window Test Bench, as described in Section 3.2, and was compared to an uncoated glass panel.

This proves that the used technology is feasible on large-scale production for architectural glazing. The results are a promising step forward to the industrialisation of the LESO-PB coloured solar collectors.

This work has been carried out at LESO-PB under supervision of Andreas Schüler and is the follow-up research on former studies on the deposition of the coloured filters using the sol–gel technique or sputtering deposition in collaboration with the University of Basel.[21,23] In the framework of this doctoral research, a whole new deposition chamber for magnetron sputtering was sketched, developed, installed and calibrated to be able to investigate coloured coatings by magnetron sputtering at LESO-PB.

For the new experimental setup, the film homogeneity was optimised by the author and his colleagues by means of calibration samples to find the optimal target–substrate distance combined with suitable process parameters, such as working pressure, target power, gas flows, rotation speed, etc. for different materials. Hereby, the optimisation was performed for both, SiO_2 and TiO_2 depositions to ensure the possibility of precise multilayers as well as co-sputtered TiO_2-SiO_2 nano-composite films. For further details related to the optimisation of the target–substrate distance and the corresponding process parameters see Figure 4.9 and Table 4.1.

In addition, an entire pre-owned ESCA system was moved, installed, refurbished and calibrated with colleagues from EPFL to enhance the coating development by in-situ chemical analysis. The film fabrication, including in-situ ESCA analysis and optical characterisation, such as spectroscopic ellipsometry and spectrophotometry were performed in autonomy by the author himself. The characterisation of the commercial SPGs was performed by the collaborators of the Department of Physics of the University of Basel on the Windows Test Bench (see Section 3.2). The real-size prototype glazing was measured by the author with the same Window Test Bench, after he had moved it to LESO-PB, re-installed and re-calibrated it in collaboration with colleagues from LESO-PB and Basel.

The following manuscript was written entirely by the first author. It has been enriched with supplementary propositions concerning the angular-dependent measurements of the real-size prototype glazing by his colleagues. The manuscript has been finally refined through discussions with the author's supervisor.

Reactively Sputtered Coatings on Architectural Glazing for Coloured Active Solar Thermal Façades

Stefan Mertin[a], Virginie Hody-Le Caër[a], Martin Joly[a], Iris Mack[b], Peter Oelhafen[b], Jean-Louis Scartezzini[a], and Andreas Schüler[a]

[a]Solar Energy and Buildings Physics Laboratory, EPFL, Station 18, Bâtiment LE, 1015 Lausanne, Switzerland

[b]Department of Physics, University of Basel, Klingelbergstrasse 82, 4056 Basel, Switzerland

Abstract

Covering a standard solar thermal collector with a coloured glazing, which is opaque to the human eye but highly transparent to solar energy, permits a perfect architectural integration of solar panels into glazed building façades. The colours are based on interference in the thin-film coating on the reverse side of the glass.

Coloured thin-film filters with optimised energetic performance and angular stability in their coloured reflection were deposited by reactive magnetron sputtering. For substrates up to $100\,mm$ in diameter the geometric configuration of the deposition chamber and the process parameters were optimised.

The optical properties of the coatings were determined by spectroscopic ellipsometry and spectrophotometry. Furthermore, by means of a window test bench, the CIELAB colour coordinates of real-size glasses were determined as a function of the viewing angle. It was also demonstrated that the colour of solar collector glazing can be matched to colours of commercial windows.

In comparison to uncoated glass panels, the presented coloured samples for solar thermal panels have an energy loss of only 2.8–4.5 % at normal solar incidence. This difference reduces for higher angles of incidence. Thus, taking into account the angular distribution of solar radiation, the energetic losses are even lower.

Keywords: coloured collectors, solar coating, thin-film filters, reactive magnetron sputtering, spectroscopic ellipsometry, spectrophotometry, solar transmittance, photoelectron spectroscopy, façade integration

1 Introduction

A perfect architectural integration of common glazed or unglazed solar thermal collectors in a building is difficult to obtain. Perfect integration means that the collector is part of the building's envelope or an architectural design element and can therefore not be recognised immediately as solar collector.[7,8] Moreover, replacing conventional façade elements by solar collectors make the latter multifunctional which could save costs in comparison to solar systems, which are just added to the building.[106] Nowadays, most thermal collectors are installed on rooftops to produce domestic hot water or heat swimming pools. Façade integration is still rare for conventional solar collectors.[7] Main reasons for this are the black or dark blueish colour of the selective absorber and the visibility of corrugated metal sheets, welding traces and tubing. However, associating the glazing of the collector with a colour would grant architects complete freedom to integrate them perfectly into the building's envelope.[8,11] By using not only the roof but also the façade, a much larger surface will be available for active solar energy conversion. Moreover, since vertically mounted solar thermal panels offer a nearly constant energy gain for the solar thermal system from March till October, they could facilitate the planning and dimensioning of a solar thermal system for Central European latitudes.[7] At the Solar Energy and Building Physics Laboratory (LESO-PB) of the École Polytechnique Fédérale de Lausanne (EPFL), several coloured filters based on thin-film technology were developed.[17,37,65] Those filters combine a visible coloured reflection with a very high transmittance of solar radiation.

The feasibility of thin-film interference filters for coloured solar collectors was previously demonstrated as well by sol–gel techniques as by magnetron sputtering.[17,18,21,22] However, up-scaling of a thin-film process from laboratory to industrial size is usually a very difficult task. In industry, the technology of magnetron sputtering is wide-spread, and used for the deposition of a large variety of coatings including e.g. thin-film photovoltaic coatings and low-emissivity coatings on insulating windows. For large-area coating on architectural glazing it is the dominant technique.[26] It allows the production of large panes $(3.21 \times 6 \, \text{m}^2)$ with a sufficient reproducibility and at the same time a high production speed.

In this publication we focus on several aspects of the coating development, from the theoretical design of the multilayer stacks to the large-scale plasma deposition of

the coatings.

In the first part of the article we present optimised coating designs with coloured reflections from blue to yellowish-orange and their energetic solar performance. Then we describe the samples produced by reactive magnetron sputtering using those designs. In the second part we illustrate the possibility of matching the coloured reflection of the collector glazing to the colours of commercial products such as window glasses. Finally, we present a first greenish-blue prototype glazing, which is based on one of the described designs and was produced in collaboration with our industrial partner. We conclude with some remarks concerning the influence of an angular distribution of solar radiation.

2   Theory

2.1   Thin-Film Interference Filters

Optical thin-film filters are based on multi-layered coatings, where the thickness of each layer is smaller than the coherence length of a given reference wavelength. The optical properties of a multilayer stack are non-trivial, but can be calculated by taking into account the change of electric and magnetic field component at the interfaces.

For a single layer on a substrate this leads to:[33]

$$
\begin{pmatrix} E_a(\lambda) \\ H_a(\lambda) \end{pmatrix} = \begin{bmatrix} \cos(\delta) & \frac{i\sin(\delta)}{\eta_1} \\ i\eta_1\sin(\delta) & \cos(\delta) \end{bmatrix} \cdot \begin{pmatrix} E_b(\lambda) \\ H_b(\lambda) \end{pmatrix} \tag{5.1}
$$

with the characteristic matrix M, the electric and magnetic components, E and H, the tilted optical admittance $\eta = \frac{H}{E}$, the indices a and b indicating the two interfaces of the layer and the phase shift $\delta = 2\pi(n-ik)d\cos\vartheta/\lambda$, where d is the layer thickness, $(n-ik)$ the complex reflective index, and ϑ the corresponding complex angle.

A whole multilayer stack can be mathematically described by multiple multiplication of the characteristic matrices for each single layer:[33]

$$
\prod_{r=1}^{q} M_r = \prod_{r=1}^{q} \begin{bmatrix} \cos(\delta_r) & \frac{i\sin(\delta_r)}{\eta_r} \\ i\eta_r\sin(\delta_r) & \cos(\delta_r) \end{bmatrix} \tag{5.2}
$$

2.2   Colour Matching

The CIE 1931 colour space represents all existing colours in the xy chromaticity diagram, where x, y are colour values with keeping Y as the relative luminance of a specific colour.[66]

The more recently introduced standard CIELAB ($L^*a^*b^*$ colour space), with D_{65} as illuminant, is used to quantify the distance ΔE of two colours, as it represents better the linearity of the human colour vision.[67] The distance ΔE of two colours is defined as[66]

$$\Delta E = \sqrt{(\Delta L^*)^2 + (\Delta a^*)^2 + (\Delta b^*)^2} \tag{5.3}$$

with the a^*-axis corresponding to the colours from red to green and the b^*-axis to colours from yellow to blue and L^* to the lightness of a colour. Two different colours are in-distinguishable when ΔE becomes sufficient small. Reference[72] indicates a threshold of $\Delta E < 3$ to distinguish one colour from another for the human eye. To match the colour of thin-film filters with the colour of other objects, the ΔE of their colours is minimised by using a suitable search algorithm.

3   Experimental

3.1   Thin-Film Multilayer Deposition

For the development of thin-film interference filters, a modular deposition chamber was designed, constructed and installed in our laboratory. It can be equipped with up to five magnetrons, allowing the deposition of different materials as well as co-sputtering on substrates up to 100 mm in diameter. Already without any bake-out of the chamber, a background pressure in the range of 10^{-8} mbar is obtained. The geometry of the chamber and the process parameters were optimised in order to achieve a large zone of homogeneity across the substrates. The configuration of the chamber is schematically shown in Figure 5.1.

The ceramic materials used, such as silica, titania, and their composites, were sputtered in reactive mode from high-purity elementary targets or partially oxidised targets. Choosing a gas flow of 21 sccm for the sputtering gas (argon) a stable plasma was obtained with a RF power of 100 W at 13.56 MHz. The sputter process was driven
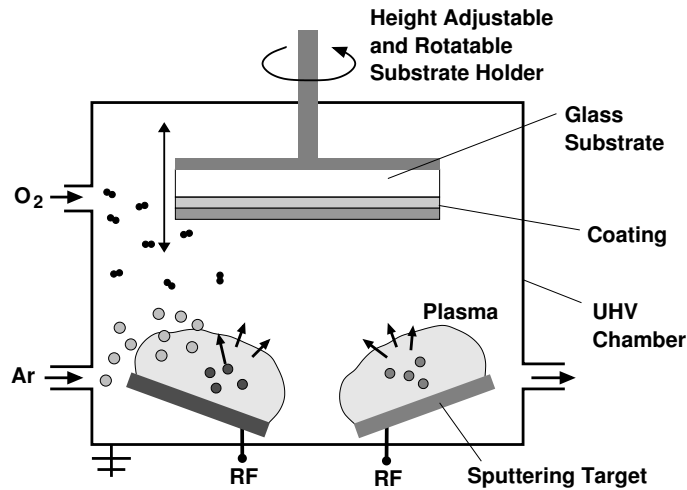
Figure 5.1: Simplified schematic drawing of the deposition chamber in the configuration for reactive magnetron sputtering. The target-substrate distance can be varied in order to maximise the zone of homogeneity of the deposited thin film.

with a reduced pumping speed and a working pressure of $2.3 \cdot 10^{-3}$ mbar. By using the hysteresis of the self-bias voltage for Si and TiO targets versus the $Ar:O_2$ ratio, we obtained a first indication for the argon-oxygen ratio suitable for the deposition of completely oxidised layers. To make sure that the correct stoichiometry of the oxides was obtained, the process was maintained in the stable reactive deposition regime of the hysteresis with an argon-oxygen ratio of 21:1. [107]

The stoichiometry of the coatings was checked by XPS measurements with an EA11 energy analyser from SPECS (see Figure 5.2) with a photon energy of 1253.6 eV ($Mg K_\alpha$). For measuring the survey a pass energy of 50.4 eV at the energy analyser was used, and for the peak measurements of the elements a pass energy of 30.0 eV. As reference a pure gold sample with $Au 4f_{7/2}$ of 83.8 eV (binding energy) was used. The investigated layers were deposited on a silicon wafer and had a thickness of around 10–15 nm to avoid charging effects on the sample due to ejected photoelectrons. Since the escape depth of photoelectrons is much smaller then the penetration depth of the exiting X-ray photons, positive charges on the highly insulating ceramic coatings can then be neutralised by an injection of a photoelectron from the conducting substrate. [97]
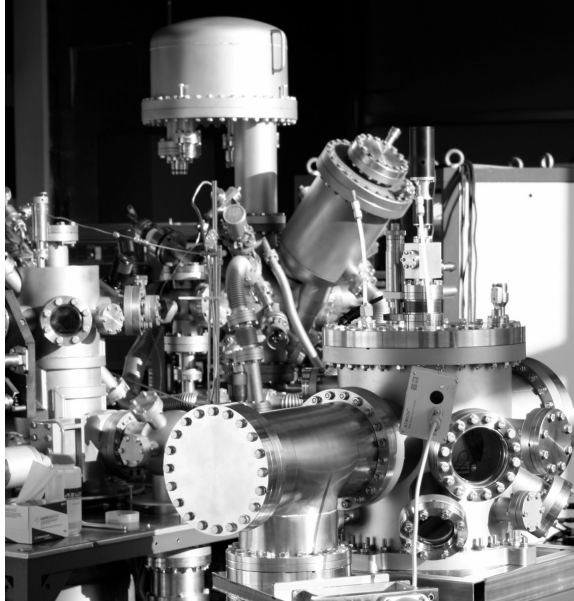
Figure 5.2: The high-vacuum plasma-deposition chamber for magnetron sputtering in the foreground and the ultra high-vacuum ESCA analysis system in the background, both installed at LESO-PB.

3.2 Characterisation Techniques

As substrates for the optical measurements, iron-poor extra-white float glass with a thickness of 4 mm was used. They have a solar transmittance of 91.8% and can therefore be considered as nearly non-absorbing. Furthermore, we also used extra-white float glass with a textured surface by a chemical etching process on the reverse side as glass substrates.

For spectral measurements a spectrophotometer is used, provided with a Multi-spec 77400 spectrometer from ORIEL for the visible wavelength range and for the near infrared wavelength range with an OL 730 detector combined with an OL 750-S monochromator from Optronic Laboratories. In order to measure not only the direct parts of the reflectance and transmittance, but also their diffuse parts, an Ulbricht sphere is installed. This allows to characterise also coloured samples with an etched reverse side.

The ellipsometric parameters ψ and Δ were measured with a spectroscopic ellipsometer GESP5 from Sopra in the spectral range 400–2000 nm at various reflection angles. From this data, the optical constants $n(\lambda)$ and $k(\lambda)$ were derived, as described

e. g. in RÖSELER.[71]

The angle-dependent reflectance $R(\lambda, \vartheta)$ and transmittance $T(\lambda, \vartheta)$ of glazings was measured with a window test bench. This equipment has been originally developed by the University of Basel to characterise the optical and thermal properties of real-size insulating glasses for different angles of light incidence.[70] It consists of a diffuse light source and a collimator. The selected light of one chosen direction is transmitted through a quartz fibre to two spectrometers from Zeiss (UV-VIS 180–1000 nm and NIR 880–2200 nm). In order to measure the angular dependency of the transmittance and reflectance the glasses can be turned from 0° to 75°. A limiting factor for this measurement set-up is that only specular reflectance and direct transmittance can be measured. Glasses having a diffuse surface, such as previously etched coloured panels, cannot be measured.

4 Results

4.1 Multilayer coating deposition

Multilayer systems for coloured solar thermal collectors were developed and produced by reactive magnetron sputtering. The interference filters, based on multilayers of nano-structured oxide materials, consist of amorphous silicon dioxide (SiO_{2-x}, with $x << 1$), crystalline titanium dioxide (TiO_2), and $Ti_xSi_{1-x}O_y$ compounds with y close to 2 and $0 < x < 1$.

Thickness profiles of several SiO_{2-x} layers were measured by spectroscopic ellipsometry across a 100-mm-large silicon wafer. The thickness deviation between the centre and a 40-mm off-centre point on a silicon wafer with a 300-nm-thick SiO_{2-x} single layer could be decreased down to 1%. The homogeneity of the samples was achieved by rotating the substrate during deposition and by optimising the target-substrate distance and the process parameters. The optimisation was repeated for TiO_2 using a TiO target. Using suitable sputtering parameters the same chamber geometry for TiO and Si targets could be used, which allowed deposition of homogeneous layer also by reactive co-sputtering.

With the ellipsometric parameters ψ and Δ the refractive index $n(\lambda)$ was determined for wavelengths between 400 nm and 2000 nm using the Cauchy dispersion model. The values of refractive index $n(\lambda)$ for SiO_{2-x}, TiO_2 and the used glass sub-

strates are illustrated in Figure 5.3. For the fit we made the initial assumption that for wavelengths in the range between 400 nm and 2000 nm the absorption in iron-poor glass and dielectrics is nearly zero and could therefore be neglected ($k(\lambda) = 0$); the absorption coefficient $k(\lambda)$ is therefore not shown.
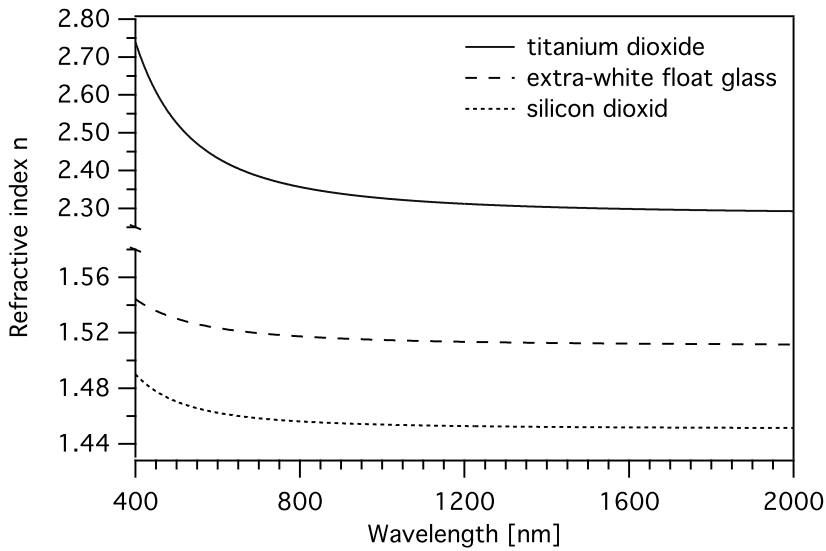
Figure 5.3: Refractive indices $n(\lambda)$ of used extra-white glass substrates, SiO_{2-x} and TiO_2, determined by spectroscopic ellipsometry; the absorption coefficient $k(\lambda)$ for glass and dielectric materials was assumed to be nearly zero in the wavelength range between 400 nm and 2000 nm and is therefore not shown.

The film thicknesses of the multilayers and the refractive indices $n(\lambda)$ of the nano-composite compounds might be subject of a patent application and can therefore not be described here.

Additional spectrophotometry measurements were performed to characterise the optical properties of the samples. With the optical data the layer thickness inside the multilayer stacks were checked by the matrix multiplication method using the optical constants $n(\lambda)$ and $k(\lambda)$ of single layers. For the determination of the colour coordinates the CIE standard illuminant D_{65} was used. Depending on their coloured reflection and their energetic performance the coatings consist of different multilayer stacks. The stacks were developed starting from the multilayer design types described by Schüler et al. [19,65] in 2005. Table 5.1 presents the CIELAB colour values and the energetic and optical performance of four new layer designs, which were energetically

Design	Colour coordinates L*	a*	b*	Approx. coloured reflection	normal incidence R_{vis} [%]	T_{sol} [%]	Δ_{sol} [%]	diffuse incidence $T_{sol,hh}$ [%]	$\Delta_{sol,hh}$ [%]
A *HL*	41.8	-10.7	12.9	green	12.4	91.4	0.4	71.8	0.0
B *HLH*	45.4	-8.0	-16.0	blue	14.8	88.9	2.9	70.2	1.6
C *HLH*	52.15	-14.5	13.06	green-blue	20.2	87.3	4.5	69.0	2.9
D *HLHL*	39.1	11.1	16.44	orange	10.8	89.0	2.8	70.1	1.7
uncoated				transparent		91.8		71.8	

Table 5.1: Simulations of different coloured multilayer designs for the interference thin-film filters. All designs are alternating high (H) and low (L) index material multilayer stacks. The total visible reflectance R_{vis} corresponds to the relative luminance and therefore the brightness of the colour. Besides the total solar transmittance T_{sol} at normal incidence, the total diffuse, bi-hemispherical solar transmittance $T_{sol,hh}$ is given (for details see this paper, Section 4.3). The corresponding solar losses Δ_{sol} and $\Delta_{sol,hh}$ are the differences in solar transmittance between the coated and an uncoated glass panel.

optimised for normal incidence of solar radiation. The energetic losses Δ_{sol} due to the coloured reflection could be limited to 4.5% and a direct solar transmittance greater than 87% was reached.

The spectral reflectance of reactively sputtered samples using these four designs is illustrated in Figure 5.4. Theoretic curves (black lines) and measured spectra (lines with symbols) are in good agreement. The accuracy of those measurements amounts to the order of 1%.
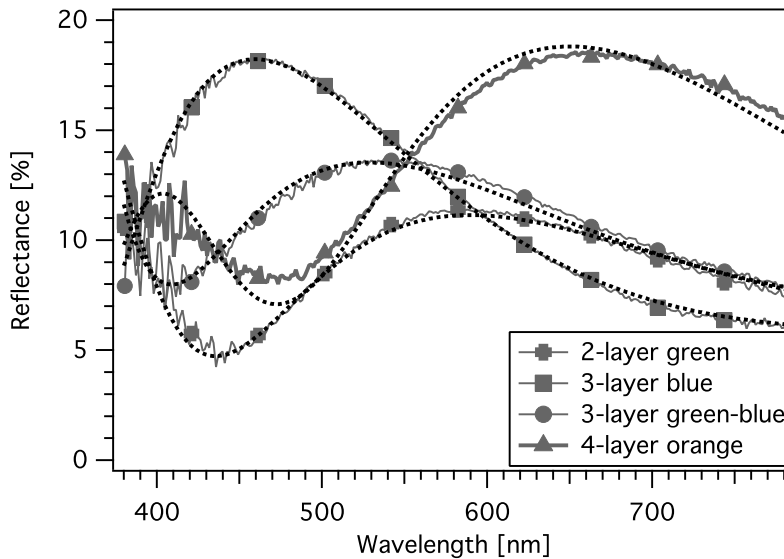
Figure 5.4: Spectral reflectance curves of multilayer coatings with different layer designs and colours. Theoretic curves (black lines) and measured spectra (lines with symbols) are in good agreement.

4.2   Colour matching

The good agreement of the measurements with the theory of optical thin-film filters and the sufficient reproducibility of the multilayer stacks opened the possibility of reproducing given colours. The coloured reflection of the interference filters were matched to colours of existing commercial glazing. Two standard sun protection glasses (SPGs) coming from building projects with a dark blue and a greenish-blue coloured reflection were chosen. By means of the window test bench the transmittance spectra of the glasses were measured for different angles of incidence from 0° to 75° as well as the reflectance spectra from 15° to 75°. From the measured spec-

tra the CIELAB colour coordinates were deduced using D_{65} as illuminant and the colour matching functions for a 10-degree field of view. The colour targets for the colour values of the reflection were chosen at the smallest angle $(15°)$ for reflectance measurements with the test bench. The resulting trajectories of the CIELAB colour coordinates in the a*b* plane are displayed in Figure 5.5. The lightness L* of the colours is not represented. For clarity the angles are noted by triangles every $15°$. For small angles of incidence $(\vartheta < 45°)$ the colours shift only little for both glasses, with a colour distance of $\Delta E < 3$ no significant colour change can be observed by the human eye.
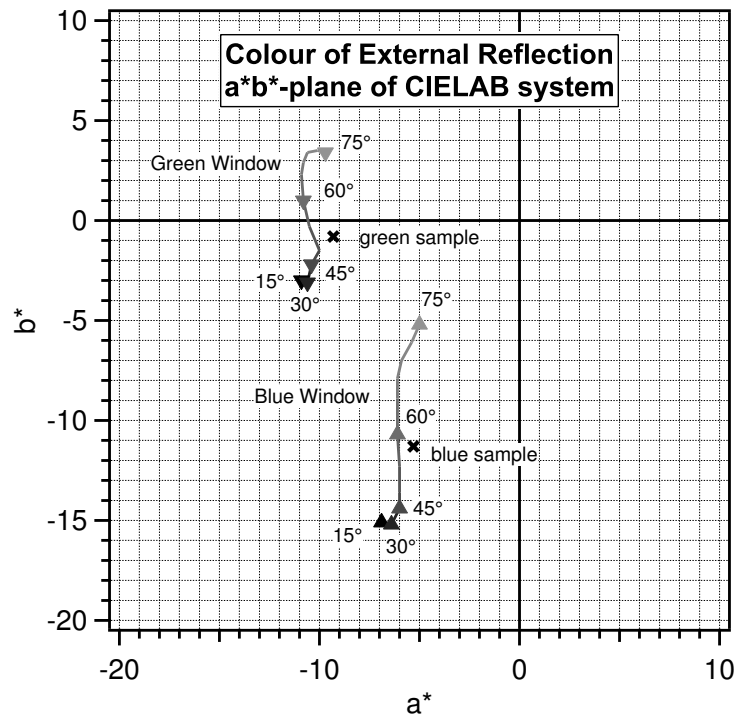
Figure 5.5: CIELAB colour coordinates of coloured samples (crosses) measured at near normal incidence; the triangles correspond to the two blue and green commercial insulating glazing for sun protection, measured for different angles of light incidence, from $15°$ (black) to $75°$ (grey).

The multilayer designs were refined to match the coloured reflection to the colour values of the SPGs using the matrix multiplication method. Thereafter, samples were produced by reactive magnetron sputtering on 4-mm-thick glass substrates, as

described in this paper, Section 3.1. The substrates are chemically etched on their reverse side. The CIELAB colour coordinates of the diffuse samples were determined for near normal incidence from the spectra measured by spectrophotometry using an Ulbricht sphere. Their colour values of the reflection are close to the trajectories of the colours of the corresponding SPGs (see Figure 5.5). For a quantification of the colour distance ΔE, the colours of the samples for near normal incidence were compared with the colours of the windows at 15° incidence. The colour distance in the a^*b^*-plane between the greenish-blue sample at near normal incidence and the greenish-blue SPG at 15° viewing angle is $\Delta E \approx 2.7$. For the blue sample the corresponding colour distance ΔE is approx. 4.1. The shortest colour distance of both samples to the trajectory of the respective SPGs is in the order of 1.

4.3   Characterisation of prototype glazing

Based on the multilayer Design C from Table 5.1 a new pilot production was effected by our industrial partner. An extra-white iron-poor float glass was used as substrate. The angle-dependent transmittance $T(\lambda, \vartheta)$ of a non-etched $30 \times 20\,\mathrm{m}^2$ sample of this greenish-blue prototype glazing was measured with the window test bench. The results are presented in Figure 5.6. The data accuracy amounts between 1% for normal incidence (0°) and 2% for 75° incidence.

For comparison, the solar spectrum AM 1.5 global is added to the graph (dotted curve). The dip in the transmittance spectrum of the prototype glazing corresponds to a reflectance peak producing the coloured appearance. For increasing angles of incidence this spectral feature shifts to shorter wavelengths, thereby implying a colour shift from green to blueish colour shades. In addition to the blue shift this spectral feature is less pronounced for larger angles of incidence.

Both aspects of the angle-dependent optical behaviour, the blue shift and the desaturation of the colours suggest that for large angles of incidence the energetic performance losses $\Delta_{\mathrm{sol}}(\vartheta)$ might become even smaller as for normal incidence.

A comparison of the total solar transmittance T_{sol} of a greenish-blue $30 \times 20\,\mathrm{m}^2$ prototype glazing and an uncoated extra-white iron-poor glass panel is shown in Figure 5.7 as a function of the incident angle ϑ of the solar radiation. The absolute error of the measurements is in the order of 1%. The distance between the two $T_{\mathrm{sol}}(\vartheta)$ curves corresponds to the energy loss Δ_{sol} of the coloured collector glazing
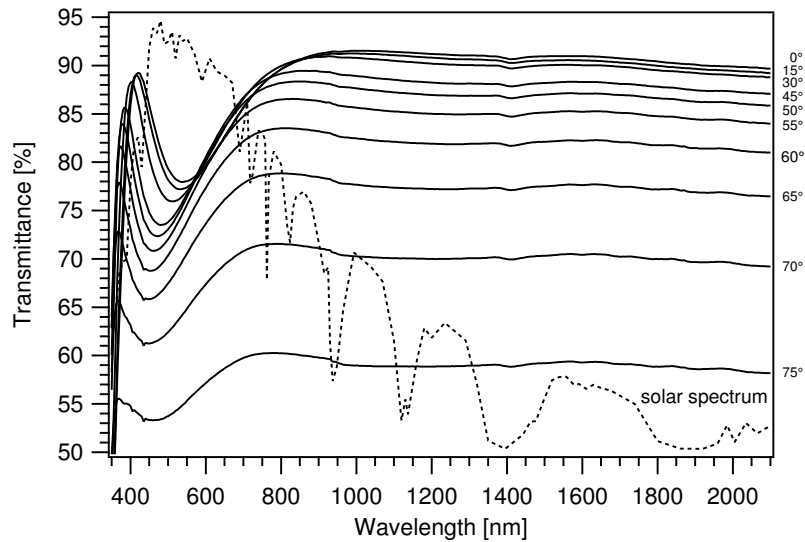
Figure 5.6: Measurements of the angle-dependent spectral transmittance of a greenish-blue prototype glazing between normal (0°) and 75° of solar incidence. For comparison the solar spectrum AM 1.5 global is shown (dotted curve). The dip in the transmittance shifts for larger angles from green to blue towards the UV edge of the solar spectrum.

Figure 5.7: Comparison of the angle-dependent total direct solar transmittance $T_{sol}(\vartheta)$ of a green prototype glazing and an uncoated extra-white glass substrate. The distance between the two curves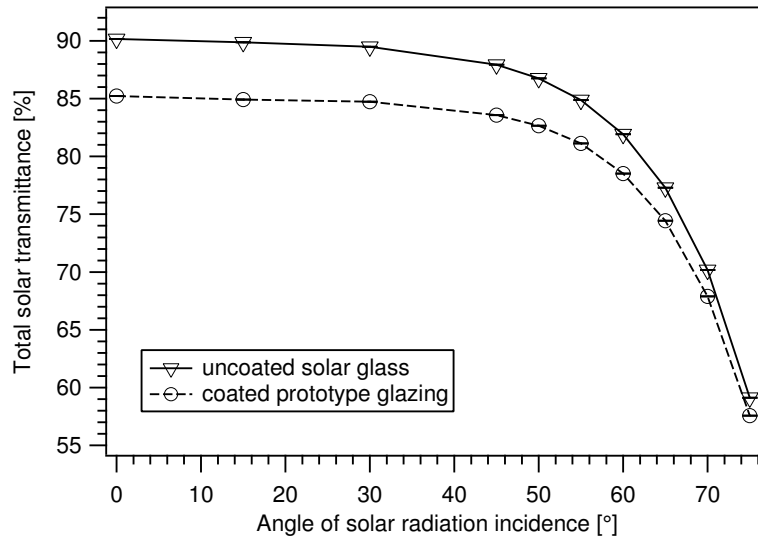 corresponds to the energy loss of the coloured collector in comparison to a collector with standard extra-white float glass.

with respect to an uncoated collector glass pane. For angles greater than 70° the difference becomes almost negligible.

The experimentally observed tendency was confirmed by simulations of the angle-dependent behaviour for the four coating Design A–D (absorption in the glass substrate was neglected). Table 5.1 shows a comparison of the total direct solar transmittance T_{sol} and the total diffuse or bi-hemispherical solar transmittance $T_{\mathrm{sol,hh}}$ for the selected coating design types and for an uncoated substrate. Hereby, T_{sol} corresponds to global solar radiation at normal incidence and $T_{\mathrm{sol,hh}}$ to a diffuse solar radiation, which is homogeneously distributed over the whole sky.

Applying the bi-hemispherical solar transmittance $T_{\mathrm{sol,hh}}$ the difference between the coated and the uncoated substrate decreases. This is valid for all our coloured filter designs. The corresponding losses will be further on referred to as bi-hemispherical losses $\Delta_{\mathrm{sol,hh}}$. For a 2-layer coating design with a green coloured reflection (see Table 5.1) even a bi-hemispherical zero-loss ($\Delta_{\mathrm{sol,hh}} = 0\%$) was achieved. Using designs with three and four layers for a larger choice in colour shades the losses $\Delta_{\mathrm{sol,hh}}$ could be limited between 1.6% and 2.9%.

5   Discussion

In the framework of a technology transfer – from laboratory samples to real-size glazing – of the coloured collector glazing to our industrial partner, energetically optimised designs for multilayer coatings were developed. Maximising the solar transmittance by maintaining a visible reflectance R_{vis} greater than 12% was the objective for the optimisation process. At normal incidence all presented designs exhibit a total solar transmittance T_{sol} greater than 87% (see Table 5.1).

For the glass and for the coating materials an absorption coefficient of $k = 0$ was assumed for wavelengths between 400 nm and 2000 nm. For thicker glass panes, where absorption in the substrate becomes more significant, and in the UV spectral range ($\lambda < 400$ nm) this approximation is no longer valid. However, within the visible range of the solar spectrum (380–780 nm) we could make this assumption for a 4-mm-thick substrate, since the theoretical measured spectra for the optical thin films are in good agreement with our experimental data (see Figure 5.4).

The reproducibility of the deposition in our chamber was sufficient for refinement.

The multilayer stacks could be fine-tuned to improve the energetic performance and the coloured appearance of the samples by slightly changing the layer thicknesses.

The presented multilayer designs were realised on 4-mm extra-white glass. To guarantee that the deposition process is driven in the stable reactive sputtering regime, the process parameters for the reactive sputtering with oxygen were chosen with a high oxygen content in the gas mixture. The advantage of this was to obtain coatings with the correct stoichiometry for completely oxidised films. However, high oxygen concentration in the sputtering gas reduces the deposition speed, which limits the flexibility of layer thickness. A lambda probe could be used to achieve a satisfying deposition speed also for fully oxidised films.

The 2-layer coating design with a green reflection has an excellent solar transmittance of 91.4% at normal incidence. These coatings exhibit a zone with anti-reflection for wavelengths around 440 nm. Furthermore, its coloured reflection is rather independent of the viewing angle. For certain colour shades more layers were needed to achieve a significant visible reflection while maintaining a high solar transmittance. For blueish and greenish colours based on a 3-layer design a solar transmittance higher than 87% could be reached, as well as for almost all colour shades in-between. However, orange-reddish colours, such as roof tiles, seem to be more demanding. Layer stacks with four and more layers were needed to obtain a sufficient energetic performance and simultaneously a sufficient bright and opaque colour reflection. The presented 4-layer coating design exhibits a solar transmittance T_{sol} of 89.0%, but remains slightly transparent at the normal viewing angle. Its colour is weak orange with a visible reflectance R_{vis} of only 10.8%. For larger angles the orange colour becomes brighter.

In general, the angular dependency of the colour of light which is reflected from the collector glazing must be improved. The spectral peak of the reflected colours tends to shift towards shorter wavelengths as the viewing angle becomes larger. The observed colours of the greenish and blueish samples are rather independent of the viewing angle, since blueish and greenish colours still remain blueish and greenish-blue for larger angles. The solar loss Δ_{sol}, which corresponds to the solar transmittance T_{sol}, indicates the efficiency reduction of the coloured solar collector. It is the difference between the solar transmittance of coloured coated and uncoated glass panes. At normal light incidence for most of the multilayer designs given in

Table 5.1 a solar loss Δ_{sol} between 2.8% and 4.5% is observed.

The reproducibility of the coloured films was sufficient to fine-tune the filters. The colours of the samples could be matched to the coloured appearance of commercial products. Blueish and greenish colours are widely used for glazing on façades. Therefore, we demonstrated it for dark blue and greenish-blue commercial sun protection glasses (SPGs). Using the colour matched solar collectors in combination with the SPGs could provide an uniform appearance on highly glazed façades of buildings. So far we matched the colours of the samples for near normal light incidence.

However, especially for larger viewing angles the effect of the etched outer surface of the coloured collector glazing becomes more and more significant. Collectors and windows might exhibit different colour desaturation at larger angles. This optical effect of the different surface is difficult to model. However, using daylight as natural light source for samples and SPGs, the visual impression of the colour-tuned samples and of the commercial glasses is already satisfying towards viewing angles of approx. 45° to 60°.

The angle-dependent solar transmittance $T_{\text{sol}}(\vartheta)$ of a first prototype glazing was measured. Its design is based on one of the new multilayer designs (Design C). At normal incidence a solar transmittance T_{sol} of 85.2% was measured. For a first industrial run this result is very promising.

A direct solar loss Δ_{sol} of approx. 5% is already acceptable. However, the solar loss could be even regarded as less significant for practical applications. Considering that in real solar thermal installations normal light incidence is very rare (i. e. sun moves along the ecliptic during a day, clouds and overcast sky, or vertical installations) an angular distribution should be taken into account. A comparison of the angle-dependent solar transmittance $T_{\text{sol}}(\vartheta)$ between an uncoated solar collector glazing and the greenish-blue prototype glazing illustrated that for greater angles the difference between the coated and the uncoated glasses decreases, and therewith the solar loss $\Delta_{\text{sol}}(\vartheta)$. For angles greater than 70° the $\Delta_{\text{sol}}(\vartheta)$ becomes almost negligible. From this follows that the angular distribution of solar radiation should be taken into account.

One extreme case, where the distribution of solar radiation is even, is respected by the total bi-hemispherical solar transmittance $T_{\text{sol,hh}}$. This approach might already give an idea of the behaviour at overcast sky conditions. In general, the transmitted

solar radiation through a collector glazing depends on the light path of the sun in the atmosphere. Simulations confirmed for a coated, coloured collector glass that its bi-hemispherical solar energy loss $\Delta_{\mathrm{sol,hh}}$ is approximately half of its direct solar loss Δ_{sol}, which means de facto a reduction by a factor of 2 ($\Delta_{\mathrm{sol,hh}} \approx 1.5\text{--}2\%$). The results illustrate that for a realistic characterisation of the energetic performance of a coloured solar thermal collector, in particular of vertically mounted collectors, a distribution of the solar radiation needs to be taken into account.

6 Conclusion

Energetically optimised coatings for solar thermal collector panels were produced by reactive magnetron sputtering. The samples exhibit a high solar transmittance $T_{\mathrm{sol}} > 87\%$ and are completely opaque to the human eye. Depending on layer design and colour shades even values with 91% of solar transmittance were reached. As well as for laboratory samples and for large-scale glazing, a homogeneous coloured appearance was achieved by depositing even films. The colours of the presented blueish and greenish samples are sufficiently stable for different viewing angles, whereas the angular dependency for orange-reddish colours needs to be reduced.

A successful example for colour matching was described. The coloured filters were adjusted to match the coloured appearance of standard commercial architectural glazing, a dark blue and a greenish-blue sun protection glass.

The presented coloured collector glasses exhibit a solar energy loss Δ_{sol} of 2.8–4.5% at normal incidence with a visible reflectance $R_{\mathrm{vis}} > 12\%$. In general, the solar radiance is not only normal and direct to the solar panel and therefore the real energy loss might be reduced up to a factor of 2 compared to its direct solar loss Δ_{sol}.

First prototype glazing was produced and characterised. It exhibits a solar transmittance T_{sol} of 85.2% for normal incidence. The used technology is feasible on large-scale production of architectural glazing. The results are promising and are a step forward to give architects more flexibility for the integration of solar thermal collectors into buildings.

Acknowledgements

5.2 Nanocrystalline Low-Refractive Magnesium Fluoride Films Deposited by Reactive Magnetron Sputtering: Optical and Structural Properties

Submitted manuscript.

5.2.1 Summary

Magnesium fluoride (MgF$_2$) is well known for its outstanding optical properties: very-low refractive index of 1.38 and high transparency over a wide spectral range (120 nm to 8 μm). However, it is rather difficult to deposit it by magnetron sputtering. Nevertheless, in order to be able to include MgF$_2$ in the development process of the coloured interference filters for solar collectors, it is mandatory to find a suitable sputtering process for the later industrial production (see Section 2.2.2).

In this result section, a novel method is presented to deposit MgF$_2$ via magnetron sputtering in reactive mode using a metallic magnesium (Mg) target and as reactive gases carbon tetrafluoride (CF$_4$) and oxygen (O$_2$) which are diluted with argon. The reaction path of the carbon from CF$_4$ to carbon dioxide (CO$_2$) has been confirmed qualitatively by mass spectrometry. The atomic concentration of oxygen and carbon in the MgF$_2$ films was measured by in-situ XPS and reaches a minimum for equal partial pressures of CF$_4$ and O$_2$. The fact to take advantage of a chemical reaction of two reactive gases during sputtering deposition to obtain a specific atom and to release the rest, is remarkable. The obtained refractive index n at 550 nm is 1.382 which is congruent with the one of the polycrystalline MgF$_2$ bulk ($n = 1.383$). It was possible to keep the absorption in the films on a weak level ($k = 0.001$ at 550 nm). A first MgF$_2$ single-layer anti-reflective coating was realised. It exhibits a reflectance minimum of 5.2% at 760 nm which is congruent with the theoretical limit of a quarter-wave MgF$_2$ anti-reflective coating. The resulting solar transmittance T_{sol} amounts to 93,4% which is 1.7% higher than for the uncoated glass substrate. By further optimising the layer thickness with respect to the maximum intensity of the solar spectrum, an increase in T_{sol} by 2% could be achieved.

The results are very promising towards sputtered MgF_2 films, which is a requisite for large-area coating and therefore for integrating MgF_2 in a multilayer coating design for coloured solar filters.

The work was planned, set up and performed by the first author in collaboration with the researchers at the Department of Physics of the University of Basel. The film fabrication, including in-situ ESCA analysis and optical characterisation, as well as X-ray diffraction (XRD) measurements were performed in autonomy by the author. For the SEM, transmission electron microscopy (TEM), and atomic force microscopy (AFM) measurements, he was supported by the co-authors from LC and the analysis of all data (XPS, optics, XRD and microscopy) was performed by himself. The manuscript was written entirely by the first author, it has been enriched with supplementary remarks for the XPS analysis from the co-authors from Basel and for the Microscopy measurements from EPFL. Finally, the manuscript was refined through discussions with the second author and the author's supervisor.

Nanocrystalline Low-Refractive Magnesium Fluoride Films Deposited by Reactive Magnetron Sputtering: Optical and Structural Properties

Stefan Mertin[a,b], Laurent Marot[c], Cosmin S. Sandu[b], Roland Steiner[c], Jean-Louis Scartezzini[a], and Paul Muralt[b]

[a]Solar Energy and Buildings Physics Laboratory, EPFL - ENAC - IIC LESO-PB, Station 18, Bâtiment LE, 1015 Lausanne, Switzerland
[b]Ceramics Laboratory, EPFL - STI - IMX LC, Station 12, Bâtiment MXC, 1015 Lausanne, Switzerland

[c]Department of Physics, University of Basel, Klingelbergstrasse 82, 4056 Basel, Switzerland

Abstract

In this work, we studied MgF_2 thin-film synthesis by reactive pulsed DC magnetron sputtering from a metallic magnesium target in a gas mixture of argon, oxygen and carbon tetrafluoride. Nanocrystalline films with excellent properties for optical application were achieved. They were deposited on silicon wafers and glass substrates. The plasma discharge was analysed with a differentially pumped mass spectrometer before and during the deposition process. Without breaking the vacuum, monochromatic photoelectron spectroscopy (XPS) was performed for in-situ determination of the atomic C and O concentration in the coating. Film nanostructure, topography and thickness were investigated by scanning electron microscopy (SEM), transmission electron microscopy (TEM) and atomic force microscopy (AFM). The optical constants n and k were measured by spectroscopic ellipsometry and spectrophotometry: a consistent parametric fit of the ellipsometric angles and spectral transmittance and reflectance based on three Lorentz-oscillators to determine n and k was achieved for a wide wavelength range (300–2300 nm). At 550 nm a refractive index n of 1.382 was obtained, which is in excellent agreement with $n = 1.383$ of polycrystalline bulk material. A significant decrease in reflection was measured on glass, congruent with the theoretical limit of polycrystalline MgF_2 films. The measured light transmission at 760 nm is enhanced by 3 % for a quarter-wave antireflective MgF_2 coating on glass compared to the uncoated glass substrate.

Keywords: magnesium fluoride, reactive magnetron sputtering, optical coating, low refractive index, nanocrystalline microstructure

1 Introduction

Magnesium fluoride (MgF_2) is well known for its outstanding optical properties: non-absorbing over a wide wavelength range from 120 nm to 8 μm,[108] and a refractive index of 1.38 at 550 nm,[32,33] which is the lowest known among inorganic dense coating materials. MgF_2 is mainly used for high-performance coatings on optical-precision glasses, filters, and laser applications reaching into the UV wavelength range.[46,109,110] It is also of great interest as anti-reflective coating for photovoltaics and solar devices.[111,112] Many techniques were investigated for growing MgF_2 thin films: ion-assisted evaporation,[113] plasma ion-assisted deposition (PIAD),[114] ion beam sputtering,[46] atomic layer deposition,[115] metalorganic chemical vapour deposition,[116] thermal evaporation,[110] electron beam evaporation,[46] and sol–gel deposition.[117] However, no method for large-area coating is available. Magnetron RF sputtering from an MgF_2 compound target – at first sight an obvious method – failed to produce stoichiometric thin films with near-zero absorption, a prerequisite for a high optical transmittance. The absorption was found to correlate with fluorine deficiency.[101,102,118,119] However, it is important to find a magnetron sputtering process, as this technique can be up-scaled to coat large glass panes (3.21×6 m^2) with a high production speed, combined with sufficient high reproducibility for commercial products on the large scale.[26]

To overcome the fluorine deficiency in the sputtered films obtained with MgF_2 targets, Martinu et al.[101] added carbon tetrafluoride (CF_4, also known as Freon 14) to the Ar sputtering gas in the ratio 60 CF_4 to 33 Ar. In addition, a small amount of oxygen (O_2, 7%) was added to reduce the carbon in the obtained film to decrease absorption in the UV range.[119] However, this approach failed: no stoichiometric films were reported. Alternatively, one could employ a metal target of magnesium (Mg) and use a fully reactive process. This approach was investigated by Iwahori et al.[102] in 2006 using with Ar diluted F_2 as reactive gas. They report a reactive index n of 1.42 and an extinction coefficient k of $0.5 \cdot 10^{-3}$ at the wavelength at 193 nm, which is less relevant for low-refractive-index applications in the visible (VIS) and near infrared (NIR) spectral range, such as anti-reflective coatings on glass. Moreover, the highly reactive F_2 gas is always a corrosion problem and severe safety concern.

In this publication we present a novel approach to grow nanocrystalline MgF_2 films. We studied their synthesis through reactive magnetron sputtering from a

metallic Mg target, operating the source with pulsed DC power. Instead of the highly reactive and dangerous F$_2$ we used a mixture of oxygen and carbon tetrafluoride as reactive gas diluted with argon. The basic idea for the reactive process is to obtain the reaction path

$$2\,\text{Mg(s)} + \text{CF}_4\text{(g)} + \text{O}_2\text{(g)} \longrightarrow 2\,\text{MgF}_2\text{(s)} + \text{CO}_2\text{(g)} \tag{5.4}$$

which requires ideally equal partial pressures of O$_2$ and CF$_4$ (s and g refer to solid and gas phase, respectively). Therefore, we focused in our study rather on the CF$_4$:O$_2$ ratio than on the ratio between argon and reactive gas and we define the ratio γ between the partial pressure of CF$_4$ and to the total partial pressure of O$_2$ and CF$_4$ as

$$\gamma = \frac{\text{P}_{\text{CF}_4}}{\text{P}_{\text{CF}_4} + \text{P}_{\text{O}_2}} \tag{5.5}$$

With the proposed method we obtained nanocrystalline and stoichiometric thin films with only a minor CO$_x$ contamination, showing a high optical performance, including low reflectance, high transmittance, and near-zero absorption in the investigated wavelength range 300–2300 nm, and a low refractive index close to the one of polycrystalline sintered MgF$_2$ bulk material.

2 Theoretical Background

MgF$_2$ is a tetragonal birefringent crystal which leads to two different speeds of light propagation and therefore two different refractive indices, n_o and n_e for the ordinary and extraordinary wave, respectively.[32] In hot pressed polycrystalline material however, the effective refractive index n_eff is an average of n_o and n_e corresponding to the formula:

$$n_\text{eff} = \frac{2n_\text{o} + n_\text{e}}{3} \tag{5.6}$$

Figure 5.8 plots n_o and n_e determined by Dodge[32], and the calculated n_eff for the wavelength range 300–2300 nm. In addition, the measured $n(\lambda)$ of hot pressed MgF$_2$ ceramics is shown (open circles).[104] In case of poly- or nanocrystalline thin films

the expected refractive index should be the one of ceramics. Therefore, to determine n by various angles spectroscopic ellipsometry, one single dispersion model can be applied simultaneously for all angles of light beam incidence.
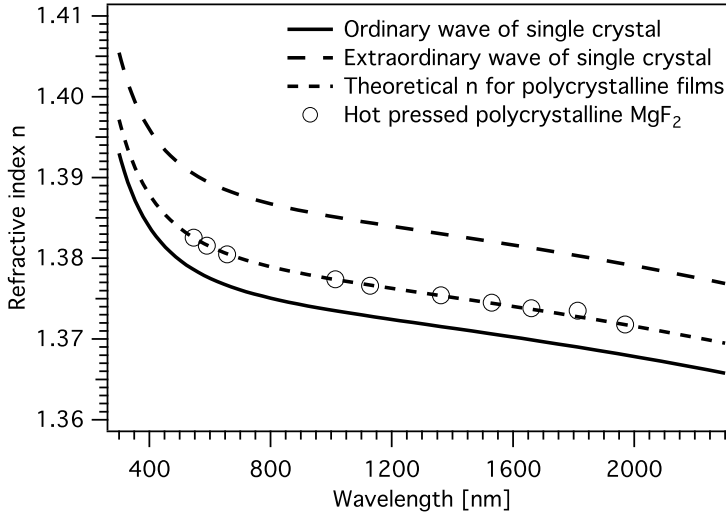

Figure 5.8: Refractive index n of MgF_2 in the spectral range 300–2300 nm. In single crystal n spits up in n_o and n_e for the ordinary and extraordinary wave, respectively. [32] The dashed line indicates the theoretical dispersion curve n_{eff} for an ideal homogeneous polycrystalline material or film, which is in good agreement of the measured n for hot pressed ceramic bulk material (circles). [104]

To further confirm the quality of the deposited films and its optical constants in application, we use the well-known anti-reflective property of a quarter-wave MgF_2 thin film on glass. A coating is named anti-reflective, when the wavelength-dependent reflectance of the coated surface at a given wavelength is less then the one of the uncoated surface of the same substrate. Transferring the concept of antireflection e. g. to solar energy, a coating has the property of being energetically anti-reflective, if the coated substrate reflects less solar radiation than the uncoated surface. An optical quarter-wave single layer represents the simplest form for anti-reflective coating. For antireflection the phase thickness of the layer is 90° at a given reference wavelength λ, the so-called quarter-wave optical thickness. [33]

The reflectance R for a coated surface is given by

$$R = \left(\frac{n_{air} - n_{coating}^2/n_{substrate}}{n_{air} + n_{coating}^2/n_{substrate}} \right)^2 \tag{5.7}$$

with the refractive index n of air, coating and substrate. For complete antireflection (zero reflectance) at a surface the derivative of the reflectance becomes zero. This is the case for a given substrate, when:

$$n_{\text{coating}} = \sqrt{n_{\text{air}} \cdot n_{\text{substrate}}} \tag{5.8}$$

In the case of glass substrate, the ideal refractive index for the coating amounts to $n_{\text{coating}} = 1.23$. At the reference wavelength $\lambda_{\text{ref}} = 550\,\text{nm}$ e. g. the physical thickness d computes to $d = 550\,\text{nm}/(4 \cdot 1.23) = 112\,\text{nm}$. However, as discussed in this paper, Section 1 among dense inorganic coating materials there is no lower n than 1.38.

3   Results and Discussion

3.1   Coating Deposition

To understand the influence of the O$_2$ and CF$_4$ in the reactive process, the gas composition was analysed before and during the deposition process. Figure 5.9a depicts the mass spectrum of the process gas ($\gamma = 0.51$) before plasma ignition. No CF_4^+ peak was observed. CF$_4$ is represented by CF_3^+, CF_2^+, and F_2^+. As shown in Figure 5.9b the magnetron plasma changes significantly the gas composition during the deposition process: the percentage of CO and CO$_2$ increases and the additional chemical compounds CFO and COF$_2$ are created in the plasma. As described by Martz et al.[120] CFO is an important intermediate molecule which is transformed into CO, CO$_2$ and COF$_2$ through different reaction mechanisms. The different reaction pathways are initiated by the dissociation and recombination reactions of CF$_4$ into CF$_3$ and CF$_2$. CF$_3$ may react with O to the stable COF$_2$ monomer and high-order polymers. Another path is the reaction of CF$_2$ with O to form CO, CO$_2$ and COF$_2$ by passing the intermediate COF.[120] During all the processes F and F$_2$ species occur which can react with the Mg from the target and the film. To find a reasonable deposition speed, a suitable chemical composition with optical properties close to pure MgF$_2$ several γ values were investigated. The dependency of the deposition rate from the γ-ratio is illustrated in Figure 5.9c. Using only CF$_4$ as reactive gas resulted in the highest deposition rate of 1.1 nm/min. However, at $\gamma = 0.67$ and above the plasma was unsteady and fluctuating during the process. A stable process
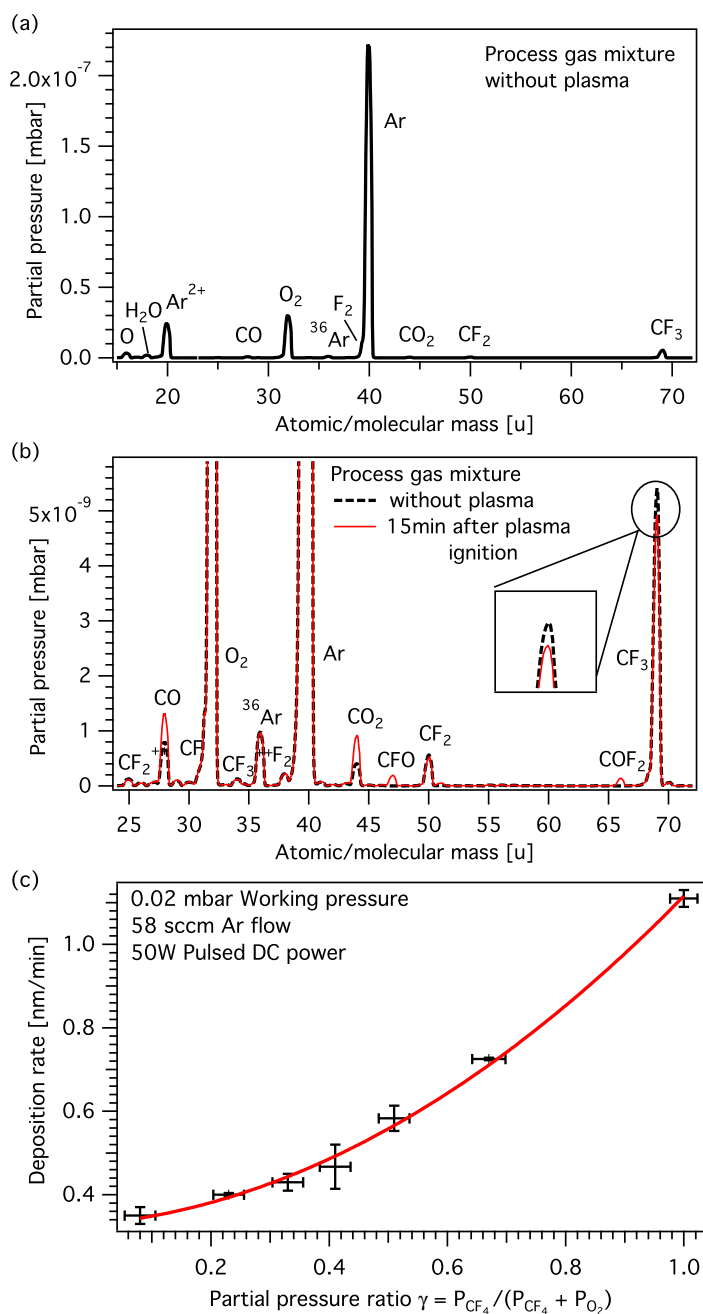
Figure 5.9: (a) In-situ mass spectrum (positive ions) of the process gas mixture without plasma discharge. (b) In-situ mass spectra of the process gas mixture without plasma and 15 min after the plasma ignition. With plasma the signal for the CF_4 derivates is smaller, whereas the signal of CO and CO_2 species is increased One finds also the intermediate products COF and COF_2. (c) Dependency of the deposition rate on the γ-ratio of the partial pressures of CF_4 and O_2, while the sum of their partial pressures is kept constant.

was achieved at γ-ratios of around 0.5 and below. At the same time, adding a small amount of O$_2$ decreased the deposition rate immediately and continued to drop when adding more O$_2$. $\gamma = 0.5$ was a good compromise between a stable process and high deposition rate.

3.2   In-situ XPS Analysis

By nature of the process used – with the CF$_4$ and O$_2$ reactive gases and the base pressure of the deposition chamber in the range of 10^{-7} to 10^{-8} mbar – the coatings contain a small amount of carbon and oxygen (see survey in Figure 5.10a). This is clearly visible in Figure 5.10b where the C and O atomic concentration is plotted versus the partial pressure ratio γ. In addition, at the end of the deposition the samples were some seconds in contact to the process gas and were partly contaminated before X-ray photoelectron spectroscopy (XPS) measurements. This led to a higher atomic concentration, especially for $\gamma = 1$, where after deposition and after removing few atomic layers by Ar sputtering the carbon concentration changes from 7 to 3 at.%, respectively. Whereas the oxygen concentration did not change. The same Ar sputtering was carried out for $\gamma = 0.51$ and 0.67 showing a rather small difference for the oxygen and carbon amount, which makes it rather impossible to distinguish, between a small coating degradation due to the sputter-cleaning and a very little surface contamination. By adding O$_2$ to the process the carbon content decreased down to 2 at.% for $\gamma = 0.1$ (red circles in Figure 5.10b), the oxygen amount, however, increased to 5.5 at.% (black triangles in Figure 5.10b). The C 1s and O 1s core level spectra were deconvolved in two components corresponding to graphite and carbon monoxide. Deconvolution of the Mg 2p and F 1s were possible with only one component i.e. no oxide or carbide component, which is in agreement with the carbon and oxygen spectra. Fitting of the core level lines was performed using Lorentzian and Gaussian line shapes for the individual peaks, with a Shirley background subtraction.[121] After this, the intensities were estimated by calculating the integral of the envelop function; the atomic concentrations were then derived using Scofield sensitivity factors.[122]

The measured binding energy E_b of the energy levels was charge shifted for all samples and could therefore not be used to determine the chemical shift of the elements inside the coating. However, the Auger parameter $\alpha' = E_b$(core level) $+$
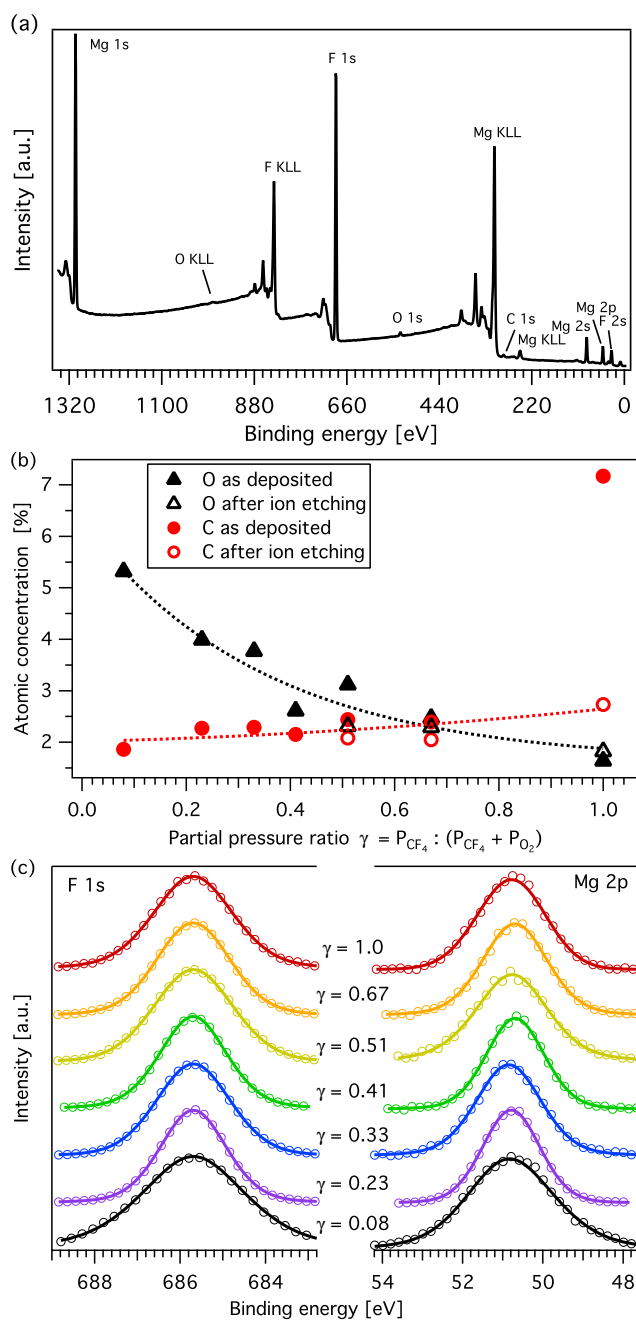
Figure 5.10: (a) In-Situ XPS wide scan of a 20-nm-thick magnesium-fluoride film. The small peaks of oxygen and carbon indicate a weak coating contamination. (b) Carbon and oxygen atomic concentration in the film versus the partial pressure ratio γ. The sum of the partial CF_4 and O_2 pressures was kept constant. A raster ion gun was used for removing partly the film by etching. (c) Measured core level spectra (open circles) and data fits (solid lines) of Mg 2p and F 1s for several γ-ratios. The spectra have been normalised for comparison.

E_k(Auger) is nearly charge independent, since the charging shift of the E_b of the electron core level and the shift of the kinetic energy E_k of the Auger lines are opposite in sign and therefore compensate each other. For the Mg Auger parameter we used the Mg states E_b(2p) and E_k(KLL). We obtained for all films α' values in the range 1228.8–1229.1 eV, which corresponds within 0.3 eV to the literature value of 1229.1 eV for MgF$_2$.[123] The C 1s core level spectrum, even though it was measured, was not chosen for calculating the charge shift due to its low intensity. Instead, the F 1s peak was used for charge correction since its high intensity and singlet state. Assuming MgF$_2$ bonding the F 1s binding energy was set to 685.7 eV. The charge corrected F 1s and Mg 2p core level spectra are plotted in Figure 5.10c as function of γ. The binding energy of the Mg 2p core level is in the range of 50.8–50.9 eV which is consistent with the literature value of 50.8 eV for MgF$_2$.[123] As function of γ the full width at half maximum values of the Mg 2p and F 1s peaks are similar, confirming the absence of oxide or carbide. For $\gamma = 0.08$ the electron flood gun was used at 12 V which led to the particular peak broadening. Peak symmetry and peak position however did not change. From Figure 5.10b the lowest carbon and oxygen concentration is found for $\gamma = 0.51$ and 0.67. However, as described above the plasma discharge was unstable for $\gamma = 0.67$. Therefore, to produce a 100–130 nm thick coating for optical characterisation the value of 0.51 was chosen for γ. It showed a dark blue colour on silicon and was nearly totally transparent on glass. It was chosen in the following for structural and optical analysis.

3.3   Structural and Topographical Characterisation

The film thickness was measured by non-tilted cross sectional SEM (scanning electron microscopy) view. It was determined to be 130 nm by averaging 10 thickness measurements. To also illustrate the topography the sample stage was tilted by 2° in Figure 5.11a. This SEM image reveals a typical columnar film growth for magnetron sputtering. The surface structure was imaged by AFM (atomic force microscopy) topography of the same sample in Figure 5.11b. The root mean square roughness values calculated over the entire image is 12 nm. The surface topography is non-isotropic in the nanometre scale. The pattern size is between a few nanometres and some 100 nm. This means that at wavelengths greater than the surface-pattern size (> 300 nm), however, the surface of the coating can be considered as optically flat. The columnar
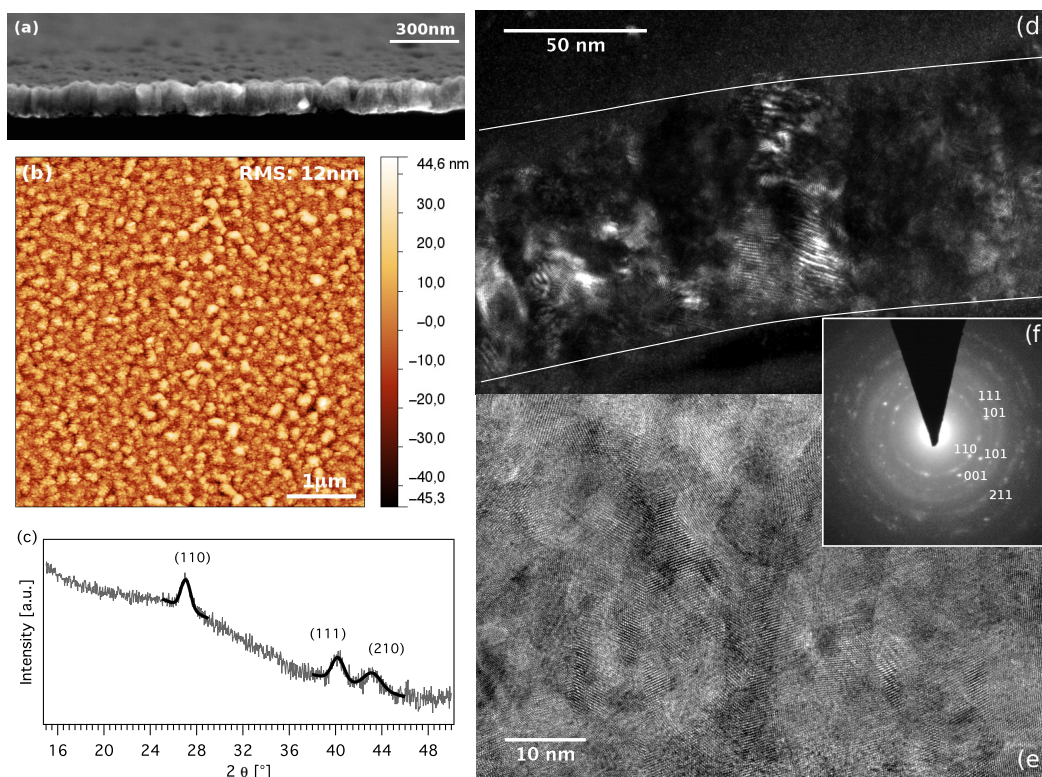
Figure 5.11: (a) SEM cross section of a 130 nm MgF$_2$ film. Columnar growth is visible. To give an impression of the topography of the film, the sample was tilted by 2° for this picture. (b) AFM image of the surface shows a micrometre-scale isotropy. However, it is highly inhomogenous in the nanometre scale. The RMS surface roughness is in the order of 12 nm. (c) XRD spectrum and data fits of the MgF$_2$ film on silicon measured at a grazing angle of 3°. TEM images of the MgF$_2$ coating. In the dark field (d) the atomic orientation of some crystal planes is visible as well as the columnar growth. The film was bended and detached from the substrate during sample preparation. The average crystallites size measured with high resolution TEM image (e) of the film is in the range of 5–30 nm. The diffraction pattern (f) reveals a polycrystalline nanostructure.

type was confirmed by TEM (transmission electron microscopy) dark field image in Figure 5.11d. The crystallite size measured in the high resolution TEM image in Figure 5.11e was in the range 5–30 nm. The selected area electron diffraction (SAED) diffraction rings in Figure 5.11f indicate the presence of a polycrystalline MgF$_2$ film with tetragonal phase (a = 0.462 nm and c = 0.305 nm[124]). Figure 5.11c shows the X-ray diffraction (XRD) measurement at grazing incidence of the same film. With the data fit of the XRD peaks the lattice parameters were calculated

to $a = 0.465$ nm and $c = 0.306$ nm which is in close agreement with the PDF card from reference.[124] The peaks at 27°, 40°, 44° corresponds to the crystal planes (110), (111) and (210), respectively. This confirms a tetragonal phase of MgF$_2$ in the coating.

3.4 Optical Characterisation

For optical characterisation the film was deposited simultaneously on silicon and glass substrates, which assured on both substrates the same material properties. A nominal film thickness of 130 nm has been chosen as reasonable compromise to determine the optical constants via spectroscopic ellipsometry and to produce an anti-reflective effect in the VIS range. The glass sample was measured by spectrophotometry and a reflection minimum was found at $\lambda_{ref} = 760$ nm. The measured transmittance and reflectance of the coated and uncoated substrate are illustrated in Figure 5.12a and Figure 5.12b, respectively. The accuracy of the data amounts to around 1%. A significant increase in transmittance is visible between 600 and 2500 nm with at maximum of 94.8% close to a reference wavelength $\lambda_{ref} = 760$ nm, where the reflectance exhibits a minimum of 5.2%, which is congruent with the theoretical limit of an MgF$_2$ quarter-wave coating. Figure 5.12c plots the spectral absorptance $A(\lambda)$ in the range 300–800 nm, which is derived by $A(\lambda) = 1 - T(\lambda) - R(\lambda)$ for near normal incidence. It is very weak over the whole spectral range and is mainly dominated by the glass substrate. For wavelengths below 500 nm, however, $A(\lambda)$ differs a little between coated and uncoated substrate. This weak UV-absorption in the MgF$_2$ films might be related to little remaining carbon impurities.[119]

The film on the silicon substrate was measured with spectroscopic ellipsometry at various angles (55–70°). The refractive index $n(\lambda)$ and the absorption coefficient $k(\lambda)$ were determined for wavelengths between 300–2300 nm from the measured ellipsometric angles ψ and Δ. In literature, the dispersion relation of crystalline MgF$_2$ is described by a three pole Sellmeier dispersion model,[32] which corresponds to an approximation of the Lorentz-oscillator dispersion model with a near-zero damping close to the oscillation frequencies.[125] Since the absorptance spectrum (Figure 5.12c) indicates a weak absorption in the films in the UV-VIS range, the Lorentz model for n and k with three oscillators appeared to be more appropriate. As first step, a data fit was performed at the oscillator energies corresponding to the Sellmeier poles for the
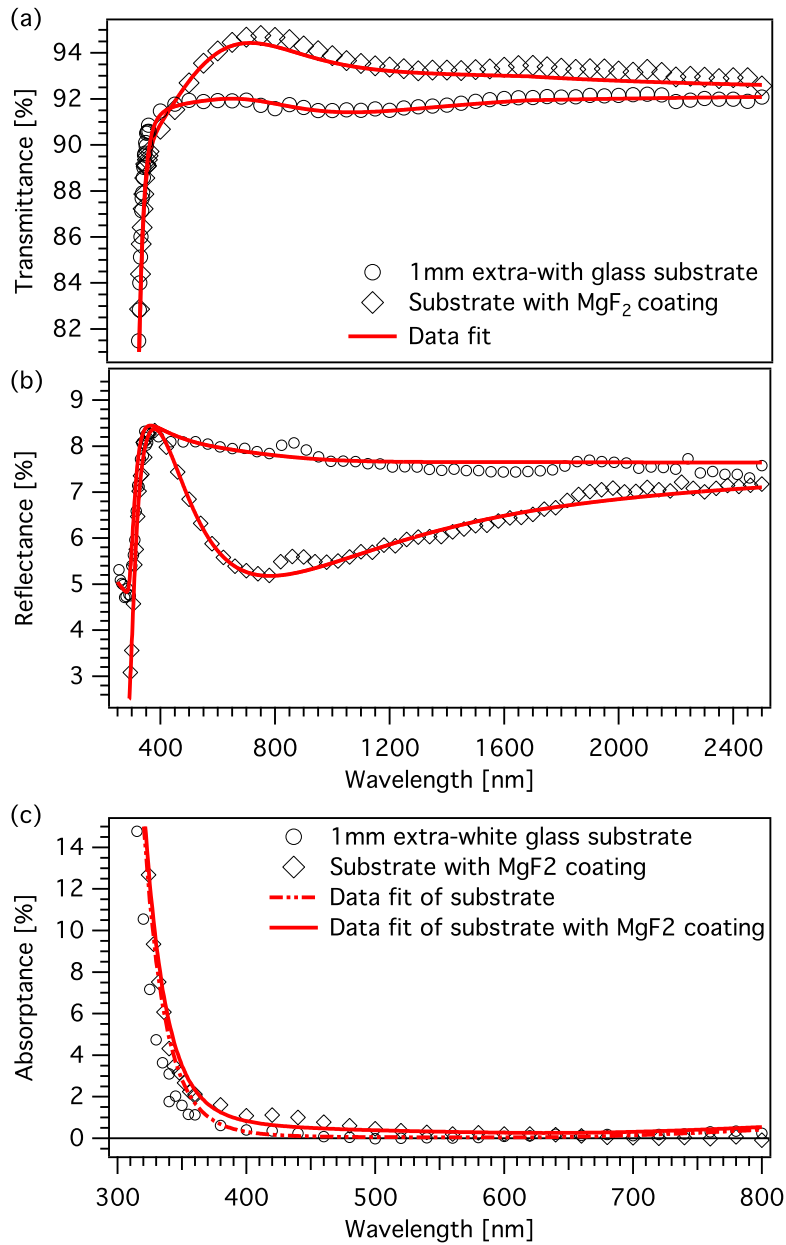
Figure 5.12: Measured transmittance (a) and reflectance (b) spectra of the optical sample with 135 nm MgF$_2$ coating and the uncoated glass substrate. The absorptance spectrum (c) is derived from (a) and (b) by energy conservation. Fit curves (solid lines) simulated with the beforehand determined optical constants and measured spectra (open circles) are in good agreement. The visible jump at the wavelength of 800 nm is due to a change of detector and grating wheel of the instrument.

ordinary beam of an MgF$_2$ single crystal,[32] which was then refined by allowing the oscillator frequencies to vary. In a second step damping factors were introduced to take into account a weak absorption. However, for thin and weak-absorbing coatings the determination of k by only ellipsometry is rather difficult.[69] Therefore, the spectral transmittance and reflectance curves were simulated using the optical constants from ellipsometry and then fitted to the data from spectrophotometry to refine $k(\lambda)$ by means of the matrix multiplication method for thin films.[33] The results were then used again as starting parameters for a new ellipsometric data fit. This process was iteratively repeated until both, $n(\lambda)$ and $k(\lambda)$ – determined by combined ellipsometry and spectrophotometry – were in good agreement. Figure 5.12 shows the results of the fit curves (red, solid lines) for the spectral data after several iterations. The simulated transmittance and reflectance fit curves are in good agreement with the data with a root mean squared error (RMSE) of 0.12. The absorptance is derived from the transmittance and reflectance data and fit curves, respectively.

The results of the measured ellipsometric angles ψ and Δ and the corresponding data fits are shown in Figure 5.13. They have a good correlation (RMSE of 0.93) between 300 nm and 2300 nm. The refined values of $n(\lambda)$ and $k(\lambda)$ are illustrated in
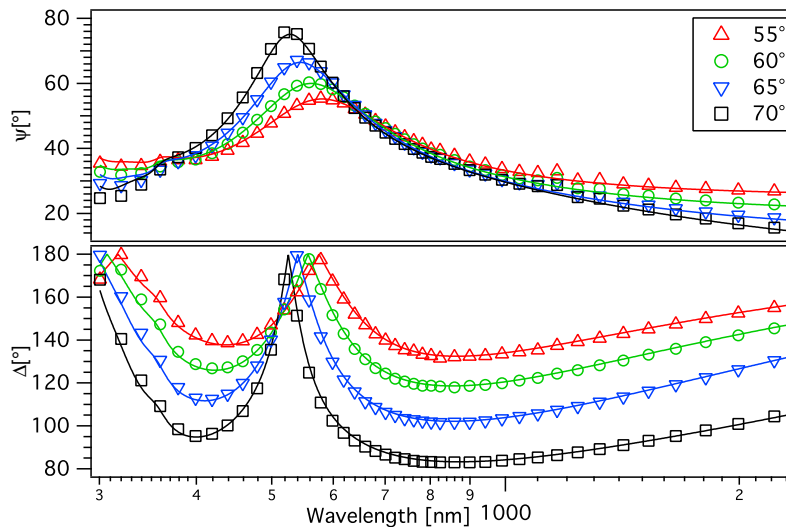

Figure 5.13: Measured ellipsometric angles ψ and Δ to determine the optical constants n and k of the MgF$_2$ coating. The open symbols represent the measurement points, the solid lines the fit curves. For better readability the wavelength axis is plotted in logarithmic scale and the number of data points reduced.
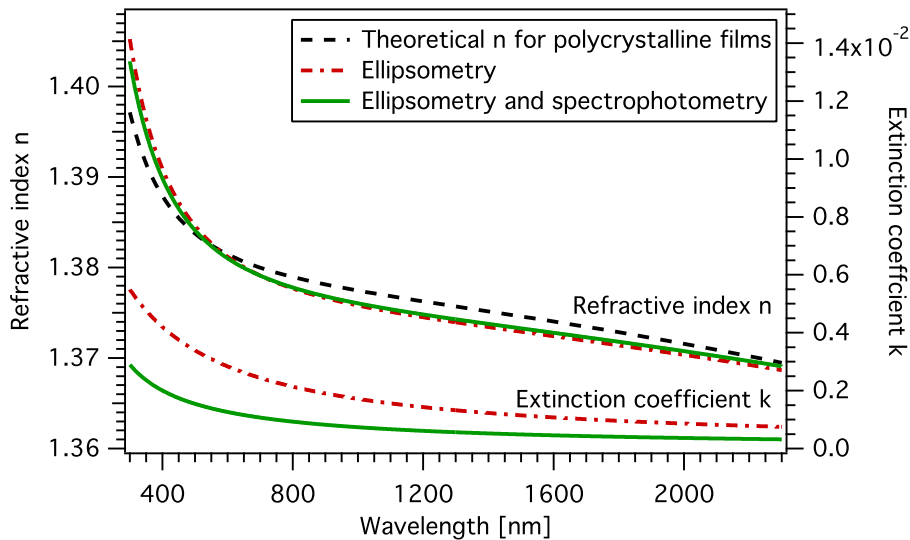
Figure 5.14: Refractive index $n(\lambda)$ and extinction coefficient $k(\lambda)$ of the deposited MgF_2 coating: the green (solid) curves are determined from the ellipsometry data only, the red (dashed) curves with a combined ellipsometry-spectrophotometry analysis.

Figure 5.14 (green, solid curves).

The films are slightly absorbing with $k = 10^{-4}$ to 10^{-3}, which is similar to MgF_2 deposited by evaporation or PIAD,[114] while $n = 1.382$ at $550\,nm$ is close to the literature value of a pure polycrystalline MgF_2 bulk material.[104] For comparison the dispersion relations for $n(\lambda)$ and $k(\lambda)$ from only ellipsometry analysis are included in the Figure 5.14 (red, dashed curves). The combined method, using spectroscopic ellipsometry and spectrophotometry permitted to determine the optical constants of the MgF_2 coating very precisely. Using only ellipsometry, the extinction coefficient k of the film was overestimated by a factor of 2–3, while the refractive index n changed only a little. The film thickness of the coating of the glass substrate was calculated to $138\,nm$ by means of the matrix multiplication method from the optical spectra in Figure 5.12 using the beforehand determined optical constants n and k. On the silicon substrate the film thickness was mathematically derived to $129\,nm$ using the data fit of ellipsometric data from Figure 5.13, which is in excellent agreement with thickness of $130\,nm$ obtained by SEM cross section view. The explanation for the different thickness values on the Si and glass samples, is the slightly different deposition rate between the two sample positions, which was taken into account for

the optical data analysis. The grown MgF$_2$ film exhibit the very-low refractive index as predicted by the theoretical curve for poly- or nanocrystalline MgF$_2$ films over the whole investigate spectral range ($n = 1.382$ nm at 550 nm and $n = 1.370$ nm at 2000 nm, see Figure 5.8).

4   Conclusion

In this work the authors present a novel method to deposit nanocrystalline MgF$_2$ films via magnetron sputtering in reactive mode using a metallic magnesium target and carbon tetrafluoride and oxygen as reactive gases diluted with argon. The reaction path of the carbon from CF$_4$ to CO$_2$ was confirmed qualitatively by mass spectrometry. The atomic concentrations of oxygen and carbon in the film were minimal when the partial pressures of CF$_4$ and oxygen were equal, as stipulated by the simple chemical reaction model (see Equation (5.4)) for contamination free MgF$_2$ films. The obtained optical constant n at 550 nm was obtained as 1.382, which is in excellent agreement to the one of polycrystalline MgF$_2$ bulk material (1.383). The absorption could be kept weak (0.001 at 550 nm). A first realisation of an anti-reflective coating confirms the quality and the optical properties of the film. It exhibits a reflectance minimum of 5.2% at 760 nm which corresponds to the theoretical limit of an MgF$_2$ quarter-wave anti-reflective coating. Applying such a coating e. g. on a solar energy device would result in an increase of the solar transmittance to $T_\text{sol} = 93,4\%$ which is 1.7% higher than for the uncoated substrate. By further optimisation of the layer thickness with respect to the solar spectrum, an increase in T_sol of 2% could be achieved. These results and the novel invented deposition process are very promising towards magnesium fluoride films as sputtered large-area low-refractive coatings.

Experimental Section

The films were deposited by reactive magnetron sputtering from a pure metallic Mg target driven by pulsed DC power (50 W, 1056 ns pulse width, 50kHz) in a high vacuum chamber (10^{-7} to 10^{-8} mbar). The target used had a diameter of 22.8 mm and were mounted with a target–substrate distance of 104 mm. Ar was used as main sputtering gas at a constant flow of 58 sccm ($1.6 \cdot 10^{-2}$ mbar). The reactive gases of

O_2 and CF_4 were added whereby the sum of their partial pressures was kept constant ($3.9 \cdot 10^{-2}$ mbar). The total gas pressure was set constant ($2.0 \cdot 10^{-2}$ mbar) while the γ-ratio was varied. A capacitance manometer was used to measure the individual gas pressures. The process gas before and during the sputtering process was analysed with a quadruple mass spectrometer differentially pumped through an orifice. The coatings were deposited simultaneously on two different substrates: $20 \times 20\,\text{mm}^2$ extra-white glasses (1 mm thick) and $20 \times 15\,\text{mm}^2$ single-side polished silicon wafers ($500\,\mu\text{m}$ thick). XPS measurements were performed in-situ after the coating process (to avoid surface contamination due to air exposure) using a VG ESCALAB 210 made by VG Scientific Ltd to analyse the chemical film composition. The spectrometer is equipped with a monochromatic X-ray source (Al $K_\alpha = 1486.6$ eV). The acquisition mode was set to CAE (constant analyser energy) with a 100 eV and 20 eV pass energy for wide and narrow scans, respectively. For narrow scans the energy resolution is better than 0.6 eV. A pure gold sample with Au $4f_{7/2}$ electron state of 84.0 eV binding energy was used as reference. The investigated layers were deposited on a silicon wafer and have a thickness of 15–20 nm to minimise charging effects on the sample due to ejected photoelectrons.[126] A low-energy electron flood gun (12 V) was used to suppress major charging of the samples and to allow reproducible measurements over time. XPS measurements were also performed after removing partly the film by etching with Ar^+ ions (2 keV). The total hemispherical transmittance $T(\lambda)$ and reflectance $R(\lambda)$ of the glass samples were measured with a Varian Cary 5 spectrophotometer equipped with a 110-mm-diameter integrating sphere in the spectral range 250–2500 nm. The samples are mounted under near-normal incidence ($3°$) with the coating facing the incident beam. A diffuse reflectance standard was used for calibration. The $T(\lambda)$ and $R(\lambda)$measurements are calibrated with a fused silica standard. The ellipsometric angles ψ and Δ were measured with a Sentech SE 850 spectroscopic ellipsometer in the spectral range 300–2300 nm at various reflection angles (55–70$°$). The wavelength-dependent optical constants $n(\lambda)$ and $k(\lambda)$ were derived by means of a Levenberg–Marquardt algorithm for minimising the RMSE between the simulated curves and the measured data, as described e.g. in RÖSELER.[71] The homogeneity of the layer thickness on the ellipsometer measuring spot was verified with a FilMetrics F20-UV reflectometer (200–1100nm) with a spot size of 1.5 mm. The morphology of the films was investigated by SEM on a high

resolution Zeiss microscope of the type Merlin (3 kV and 1.0 nA) by top and cross sectional views. For higher topographic contrast the HE-SE2 detector was used. The surface structure of the MgF$_2$ films was further investigated by a *Dimension* FastScan$^{\text{TM}}$ AFM made by Bruker (3 Hz lateral speed). The AFM was used in the PeakForce Tapping mode. The micro- and nanostructure of the films was examined in cross-section by TEM on a FEI Tecnai Osiris high resolution microscope (200 kV accelerating voltage). The cross section TEM specimens were prepared following the conventional method: mechanical cutting, gluing face to face, mechanical thinning and polishing and finally ion milling in a PIPS$^{\text{TM}}$ (precision ion polishing system) installation. SAED patterns were used to measures the crystal structure. The film was further investigated with an XRD system of the type Bruker D8 Discover at grazing angle (3°) in detector scanning mode. Its X-ray source is equipped with a germanium double bounce monochromator (Cu K$_\alpha$ = 8047.7 eV).

Acknowledgements

5.3 Advanced Coloured Coating Designs with Colour-Invariant Solar Transmittance by Means of a Magnesium Fluoride Inter-Layer

Submitted manuscript.

5.3.1 Summary

It is essential to keep in mind that the whole idea of the coloured collector coatings is about bringing an aesthetic aspect to solar collectors. Therefore, a huge variety of different colour shades is one of the keys for a market success of these coatings. Changing, adapting and matching the coloured reflection, while keeping the solar transmittance high, is a repetitive and mandatory task for every different colour hue. Therefore, the steps from the designing phase of new interference thin films up to their prototype production should be kept as simple as possible. Moreover, providing a single coating design, suitable for a whole palette of different colours, with a colour-invariant high energetic performance, could shorten the coating development cycle enormously.

In this result section, two novel coloured coating design types are presented, energetically and colour-wise optimised by numerical simulations. A three-layer interference filter, described in generalised form as a narrowband filter, was energetically optimised for the coating materials TiO$_2$ and SiO$_2$. Furthermore, the design has been simplified through the elimination of design parameters. Only the design reference wavelength λ_{ref} at the maximum of the coloured reflection remains as variable parameter.

A second advanced coloured coating design type was investigated. It is a derivative of the before discussed band pass where a supplementary inter-layer was added exhibiting a very-low refractive index, such as MgF$_2$. This new introduced inter-layer acts as a colour-tuning layer. By only varying the inter-layer thickness the colour changes while the thicknesses of the TiO$_2$ and SiO$_2$ layer are kept constant. Therefore, only one single layer has to be adjusted during the colour fine-tuning process. In addition, this design has the outstanding property of a reflection-colour-invariant

solar transmittance of 85–85.7%. This would allow to offer a whole colour palette for solar thermal collectors with the same energetic performance.

Both design types presented in this section simplify the development process of the coloured collector coatings significantly: in both cases only one remaining design parameter needs to be adapted. The second design with the MgF_2 colour-tuning layer reduces in addition also the amount of layers which need be tuned during the deposition. Furthermore, it separates the aesthetic of the collector from its energetic performance which would grant architects and solar engineers all freedom in choice of the colour for the solar thermal collector, completely independent from the dimensioning of the components of the solar thermal systems.

All simulations including the idea of the colour-tuning layer were developed and performed in autonomy by the first author. He implemented a whole new simulation framework in Mathematica[TM] for coloured solar thin films, which had major influence on the outcome and results of this publication. The manuscript was written entirely by the first author and has been finally refined through discussions with the author's supervisors.

Advanced Coloured Coating Designs with Colour-Invariant Solar Transmittance by Means of a Magnesium Fluoride Inter-Layer

Stefan Mertin[a], Paul Muralt[b], and Jean-Louis Scartezzini[a]

[a]Solar Energy and Buildings Physics Laboratory (LESO-PB), Ecole Polytechnique Fédérale de Lausanne, 1015 Lausanne, Switzerland

[b]Ceramics Laboratory (LC), Ecole Polytechnique Fédérale de Lausanne, 1015 Lausanne, Switzerland

Abstract

Improving the aesthetic of solar thermal collectors would grant architects a huge potential to integrate them into buildings. This can be achieved by interference thin-film filters producing colours that could be even matched to other architectural components. An important boundary condition for the coloured filters is however, to provide a high solar transmittance. For this reason, an optimal concept is needed to obtain the desired colours without reducing the thermal collector efficiency. One drawback for the architectural design integration of such collectors is up to now that each new colour requires additional research and development efforts for the coating design engineering, as well as new prototypes, since it is necessary to modify the thickness of all layers in the multilayer filters.

In this paper the authors present novel multilayer stacks for coloured solar coatings. The new design models reduce the number of parameters to be adjusted during the coating development process: this will shorten the prototyping time on industrial coaters significantly, as well as the whole product development cycle. Furthermore, by introducing a supplementary magnesium fluoride (MgF_2) inter-layer, the colour could be varied by only changing the thickness of this inter-layer. Thus, with a whole colour palette with invariant $T_{sol} = 85$–85.7% for solar collectors, it becomes feasible to produce colour matched collector panels on demand.

The proposed novel approach for coloured coatings separates aesthetic and functionality of solar collectors, which could simplify the planning and use of building integrated coloured collectors in solar thermal installations.

Keywords: solar coloured collectors, solar coating, magnesium fluoride, thin-film multilayers, colour-invariant solar transmittance, optical coating design

1 Introduction

Solar thermal collectors are well-established worldwide as a technology converting solar radiation into heat. Most of them are used for domestic hot water (DHW), or to heat swimming pools. The majority is installed on the rooftop, and one rarely finds façade-mounted collectors.[7] Nevertheless, in European latitudes, the mounting of solar collectors on façades could be advantageous, because their energy output is almost constant from spring to autumn for 90° facing south mounted solar collectors.[7,8] A constant energy output would make the sizing of solar heating systems and their integration as heat producers into building services easier.[1] The high visibility of the often black or dark blueish absorber, including welding traces, tubing and corrugated metal sheets, however, makes it rather difficult to integrate them from an aesthetic point of view into the building's façade.[4,9] Matching the exposed part of solar thermal collectors with a façade colour or design element would grant architects complete freedom for their building integration.[8] An even more important aspect is that an aesthetically satisfying integration might have a greater impact on the solar market than price or performance improvement.[7]

Thin-films interference coatings on the reverse side of the cover glass of the collector making it opaque to the human eye while remaining highly transparent for solar radiation, is a promising approach for façade and building integration proposed by the Solar Energy and Building Physics Laboratory (LESO-PB) of the École Polytechnique Fédérale de Lausanne (EPFL).[11,17,21–23] These coatings based on coloured interference filters consist of alternating layers of high- and low-refractive-index materials. The principle and several coating designs were already presented in various publications.[19,20,65,73]

In this work, the authors present two novel coating designs for coloured solar thermal collector glazing. Due to the requirement of quasi-nil absorption dielectric films turned out to be the most promising coating materials, as their extinction coefficient k is nearly zero in the whole solar spectral range.[17] The first design model (Design A, Figure 5.15) is based on standard thin-film narrowband filters using silicon dioxide (SiO$_2$, $n = 1.45$) as spacer layer and titanium oxide (TiO$_2$, $n = 2.4$) as reflectors. It is a simplified and generalised model of a three-layer design type described by Schüler et al.[19] The second design model (Design B, Figure 5.15) is a modified narrowband filter based on a four-layer stack of SiO$_2$, TiO$_2$ and a supplementary magnesium flu-
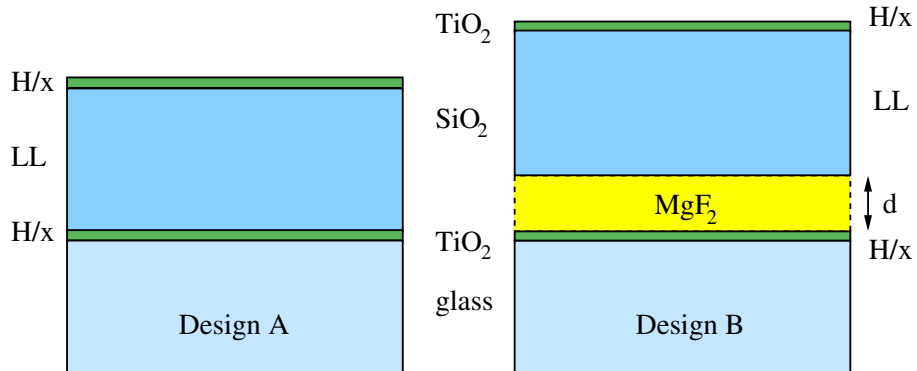
Figure 5.15: Left: Coloured filter design of the type glass$\|\frac{\text{H}}{\text{x}}\text{LL}\frac{\text{H}}{\text{x}}\|$air (Design A), where $x > 1$; H and L represent the corresponding quarter-wave thickness of the high-index and low-index material, respectively. Right: Advanced coloured filter design with MgF$_2$ inter-layer (Design B).

oride (MgF$_2$, $n = 1.38$) inter-layer. With this novel three-material four-layer model it is possible to achieve an almost colour-invariant high solar transmittance of $T_{\text{sol}} = 85\text{–}85.7\%$. This would simplify the planning and configuration of solar DHW and/or space heating plants with coloured collectors, since the aesthetic of the collectors and their energy performance are no longer influenced by each other.

2 Numerical simulations

2.1 Solar performance of coloured interference filters

In general, the optical properties of thin-film filters can be computed by numerical simulations using the method of the complex matrix multiplication, where each layer is represented by its own characteristic matrix. A detailed description of the method can be found e. g. in MACLEOD.[33] The assembly of a multilayer stack on a substrate can be described as

$$\begin{bmatrix} B \\ C \end{bmatrix} = \prod_{r=1}^{q} M_r \cdot \begin{bmatrix} 1 \\ \eta_{\text{sub}}(\lambda) \end{bmatrix} \tag{5.9}$$

where Equation (5.9) is called matrix of the assembly. The optical admittance of the parallel components of the incident electromagnetic wave at the surface of the outermost layer is given by $Y(\lambda) = H(\lambda)/E(\lambda) = C/B$. M_r is the characteristic

matrix of each layer, $\eta_{\mathrm{sub}}(\lambda)$ is the optical admittance of the substrate and q the number of layers in the stack. Zero absorptance is assumed for all simulations, which is consistent with the quasi-nil-absorptance requirement and with the used dielectric coating materials. The reflectance is then given by

$$R(\lambda) = \left(\frac{\eta_0(\lambda) - Y(\lambda)}{\eta_0(\lambda) + Y(\lambda)} \right)^2 \tag{5.10}$$

and the transmittance by

$$T(\lambda) = \frac{4 \cdot \eta_0(\lambda)Y(\lambda)}{(\eta_0(\lambda) + Y(\lambda))^2} \tag{5.11}$$

where $\eta_0(\lambda) = 1$ (incident medium air). For non-absorbing media the energy conservation equation is simply:

$$1 = R + T \tag{5.12}$$

Equation (5.12) is very general, and valid for spectral values as well as for the integrated quantities, such as solar transmittance T_{sol} and visible reflectance R_{vis}. T_{sol} is defined as ratio between incident and transmitted solar radiation, where R_{vis} is defined as ratio between incident and reflected daylight (CIE D_{65}) weighted by the photopic luminous efficiency function $V(\lambda)$ of the human eye.[127] In order to be able to improve the energetic performance of the coloured filters, all relevant quantities, such as T_{sol}, R_{vis}, colour coordinates, etc., should be taken into account for the numerical simulations. However, practice has shown this is not trivial. Most software packages for thin-film simulations compute the optical spectra as well as their colour coordinates, but nevertheless, for the most relevant quantity for solar thermal applications – T_{sol} – one searches in vain. This fact makes it rather difficult to optimise coloured solar coatings on both aspects: energy and visual wise.

To assess the performance of a coloured solar coating, a direct access to the resulting T_{sol} and R_{vis} values of the computed transmittance and reflectance spectra is fundamental. For this purpose, a new thin-film simulation framework for optical solar coatings was written on the basis of Wolfram Mathematica$^{\mathrm{TM}}$. The latter is divided into several packages for computing $T(\lambda)$, $R(\lambda)$ and $A(\lambda)$ of the coating, their corresponding integrated solar and visible values (T_{sol}, R_{sol}, A_{sol} and T_{vis}, R_{vis},

A_{vis}, respectively), as well as the colour coordinates of the spectra in CIE 1931 and CIELAB colour space (details to CIE colour spaces see e. g. SCHANDA[66]). The developed framework is very flexible and can be easily adapted to the needs of the corresponding application. The simulation variables include physical and optical thickness as well as the overall design scheme of the multi-layer stack (order and number of layers). Options can be easily adjusted with standard Wolfram commands e. g. switching from physical to optical thickness. For the optical constants, such as n and k, single or tabulated values can be used as well as mathematical dispersion relations. The number of layers and materials is only limited by computational time. For sake of simplicity all simulations carried out in this work were performed using a single value for the refractive indices at 550 nm, as it is common practice.

2.2 Colour refinement and development cycle for coloured solar thin-film coatings

By the nature of the architectural application of coloured solar collectors, the achievement of a precise reflection colour is extremely important, especially when matching the coloured reflection to commercial products.[73] The spectral curves of the thin-film interference filters depend on both, the optical constants n and k of the coating materials, as well as the thickness of each layer. In practice, however, n and k are usually pre-defined by the established deposition processes.[74,75] Therefore, in general, the thickness of the layers is tuned to adjust the spectral properties of the filters. The refinement of the different layer thicknesses is performed by following the so-called coating development cycle, which is shown in Figure 5.16. After measuring the optical properties of the produced coating, the individual layer thickness is determined with the characteristic matrix method described in this paper, Section 2.1. In the following step the deposition parameters are adapted to refine the layer thicknesses of the interference multilayer stack; the coating is then re-deposited. This procedure needs to be iteratively repeated, until the required coloured reflection combined with a sufficiently high T_{sol} value is achieved. Hereby, it is important to keep in mind that complicated coating-design models with multiple unknown parameters, such as layer thickness and/or n and k, increase the number of the iteration steps until the colour targets and the T_{sol} target of the filter are reached. A coating design-model with only a small number of parameters, which has to be tuned and adjusted during
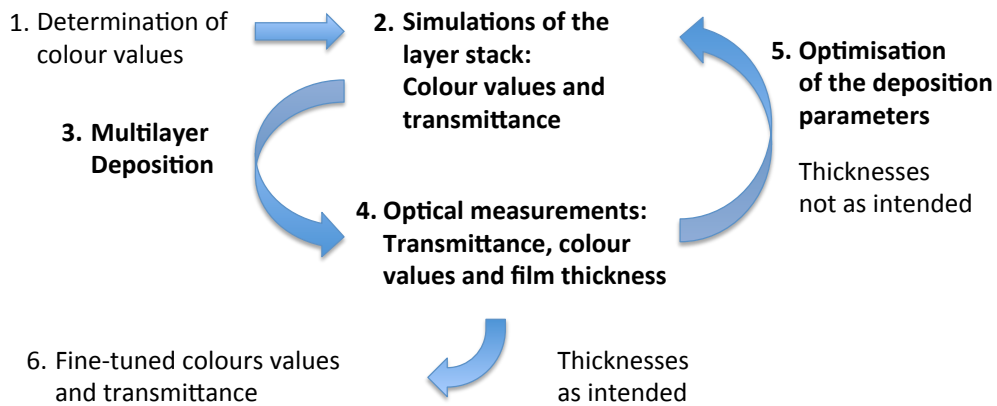
Figure 5.16: Coating development cycle for coloured solar collector coatings. Steps 2–5 need to be repeated until the required coloured reflection and solar transmittance is reached.

the film deposition and the iterative fine tuning – as described above – is the key for successful coloured solar coating development.

3   Results

A generalised model (Design A) of a three-layer design for solar thermal collectors is presented in this section; in addition a novel four-layer stack (Design B) involving two different low-refractive-index materials, where the first one (L) refers to SiO_2 and the second one is named simply by its material MgF_2, is discussed as a novel approach for coloured solar coatings.

3.1   Design A: Three-layer coloured narrowband filter

The coating Design A consists of alternating high- and low-index layers, similar to a narrowband filter. For a given number of layers the reflectance is maximised, if a high-index material makes-up the outermost layer. Therefore, the design is made of two high-index reflectors (however, thinner than the optical quarter-wave thickness in standard narrowband filters), separated by a half-wave low-index spacer layer (LL). The design scheme can be expressed as glass$\|\frac{H}{x}LL\frac{H}{x}\|$air with $x > 1$ whereas x defines the intensity of the coloured reflection and the reference wavelength λ_{ref} the location

of the reflection peak, and consequently the spectral colour. The peak shape does not vary significantly, when λ_{ref} is modified. For TiO$_2$ as high-index and SiO$_2$ as low-index material, $x = 4$ was found to be a suitable value for a bright and saturated coloured reflection combined with a high T_{sol} value. For $x = 4$ the reflectance and transmittance are plotted in Figure 5.17 for different wavelengths. The reflectance peak, and hence the coloured reflection, shifts for increasing λ_{ref} from blue-green to reddish colour hues, while the peak is slightly broadening.
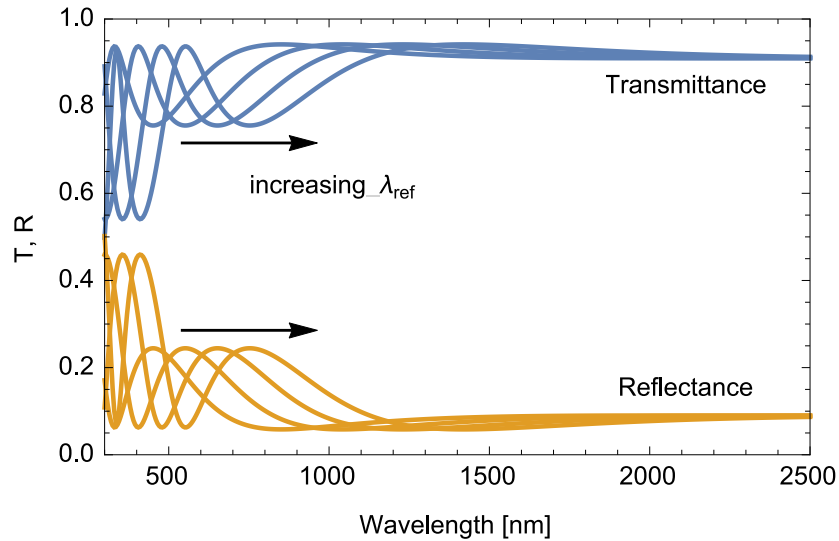

Figure 5.17: Simulated transmittance and reflectance spectra for $\lambda_{\text{ref}} = 450, 550, 650$, and $750\,\text{nm}$ of the coloured filter Design A of the type glass$\|\frac{\text{H}}{4}\text{LL}\frac{\text{H}}{4}\|$air, where H and L represent corresponding quarter-wave thickness of the high-index and low-index material, respectively. Increasing λ_{ref} shifts the reflection peak to longer wavelength, while its amplitude remains unchanged.

3.2 Design B: Coloured filter with MgF$_2$ inter-layer

Starting from Design A a supplementary layer was added between the SiO$_2$ and the innermost TiO$_2$ reflector layer. The refractive index of this inter-layer needs to be lower than the one of the spacer SiO$_2$ layer (n = 1.45) from the original narrowband filter. Therefore, MgF$_2$ has been chosen. The design reference wavelength λ_{ref} is maintained fixed (the thickness of SiO$_2$ and TiO$_2$ layers therefore do not change) while the thickness of the MgF$_2$ inter-layer is varied. The design can be expressed

in the form glass$\|\frac{H}{x}LL(MgF_2)\frac{H}{x}\|$air; for the simulations $\lambda_{ref} = 400\,nm$ and $x = 2.8$ were chosen. Increasing the MgF_2 layer thickness shifts the reflection peak towards longer wavelengths, while its reflection intensity decreases slightly (see Figure 5.18).
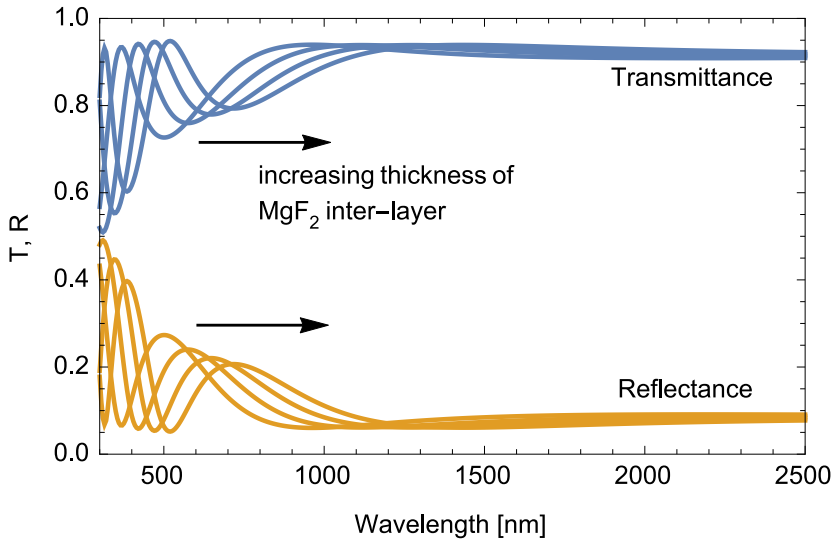

Figure 5.18: Simulated transmittance and reflectance spectra of the coloured filter Design B of the type glass$\|\frac{H}{2.8}LL(MgF_2)\frac{H}{2.8}\|$air ($\lambda_{ref} = 400\,nm$), where H and L represent corresponding quarter-wave thickness of the high-index and low-index material, respectively. By increasing the layer thickness of the MgF_2 inter-layer (28.8, 57.6, 86.3, and 115.1 nm), the reflectance peak shifts to longer wavelength, while its amplitude slightly decreases.

3.3   Solar performance and colour matching

In Figure 5.19 the simulated T_{sol} and R_{vis} values are plotted for both designs. For Design A, T_{sol} decreases from 88% at blue-greenish to 83% at reddish-purple coloured reflections (increasing λ_{ref}), while for Design B, T_{sol} remains almost constant (85–85.7%) and invariant of the reflected colour (increasing thickness of the MgF_2 inter-layer). R_{vis} reaches 12–22% with a maximum at green-yellowish wavelengths for Design A, and to 10–24% for Design B with a maximum in the blue-greenish range. Choosing the suitable values for λ_{ref} and x (400 nm and 2.8, respectively) it was possible to match congruently the trajectory of the coloured reflection of Design B (while changing only the thickness of the MgF_2 inter-layer), to the colour trajectory
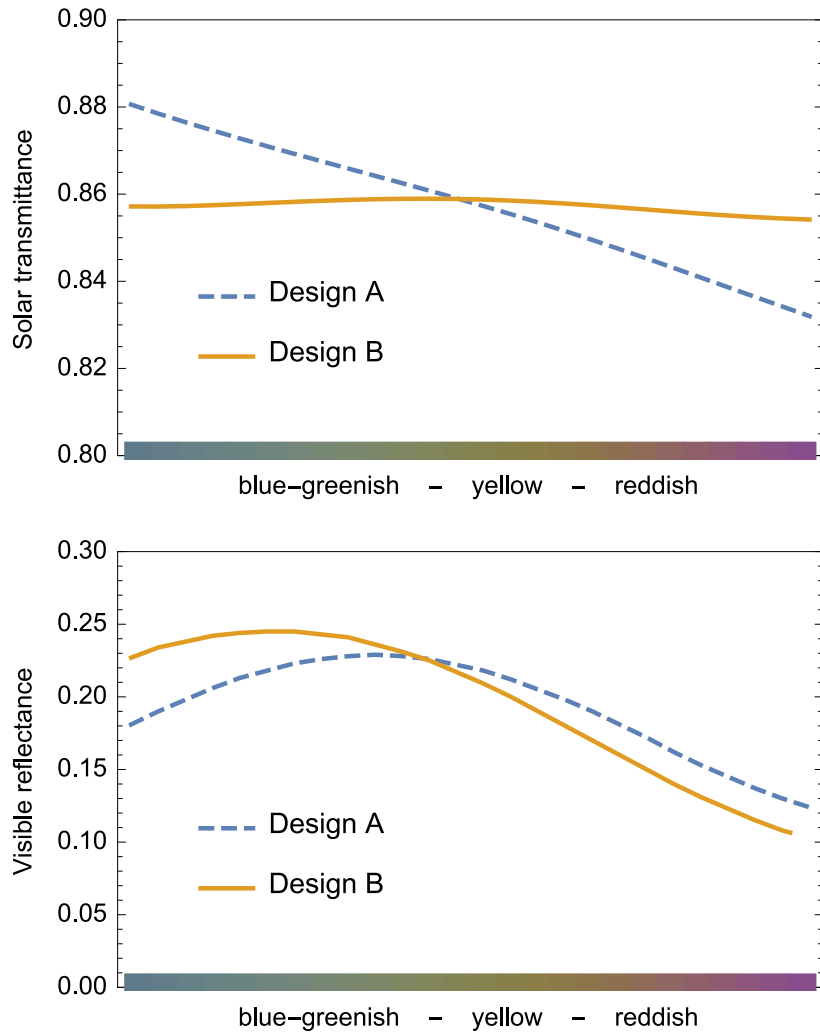
Figure 5.19: Simulated solar transmittance and visible reflectance of Design A and B. The reflection colour of both design types follow the same trajectory in the a^*b^*-plane, which is indicated on the x-axis in form of calculated colours in the CIELAB system.

of Design A (where λ_{ref} is changed and therefore all three thicknesses of the SiO$_2$ and TiO$_2$ layers). The trajectories of the two designs are plotted in Figure 5.20 in the a^*b^*-plane of the CIELAB colour system. For a suitable plot the lightness L^* in the graph was set to 50, which corresponds well to the brightness of the blueish and greenish coloured reflection. The orange and reddish coloured reflection have, however, smaller L^* values of around 35–45.
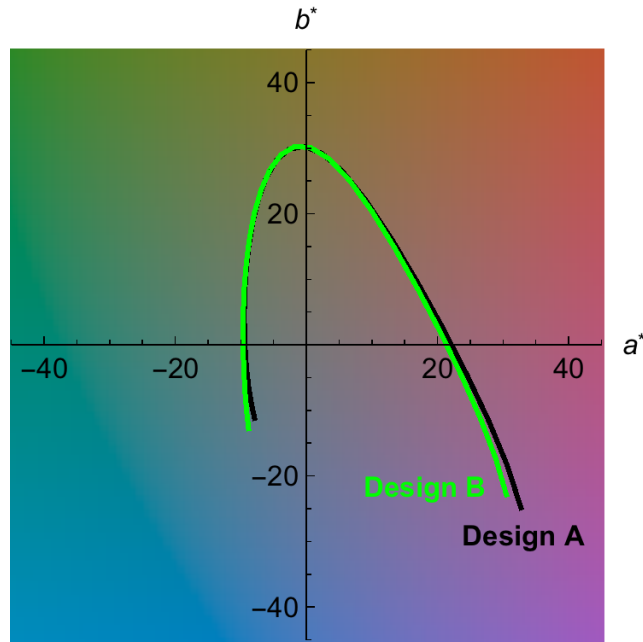
Figure 5.20: CIELAB colour trajectories of the Design A and B in the CIELAB a^*b^* colour plane. They are almost congruent. In the colour chart the lightness is set to $L^* = 50$.

4   Discussion

The two investigated designs for coloured solar thermal collectors were kept on purpose as simple as possible i. e. the design parameters were reduced to a minimal configuration; the aim was to reduce the coating development cycles (see this paper, Section 2.2). Both designs exhibit a high solar transmittance above 85% for blue to yellow colours, which remains within the T_{sol} acceptance limit of a few percent in comparison to the uncoated substrate ($T_{sol} = 91.8\%$).[19,20] Design A is described as a standard three-layer narrowband filter with a SiO_2 half-wave spacer and two TiO_2 reflectors layers. Only standard materials are used: TiO_2 (high refractive index) and SiO_2 (low refractive index) layers are widely used for optical coating.[128] The intensity of the reflection peak depends on the difference between the refractive index n of the two reflectors and the spacer. The optical thickness of the reflectors was optimised in such a way that for $450\,\mathrm{nm} \leq \lambda_{ref} \leq 650\,\mathrm{nm}$ the solar transmittance T_{sol} remained above 84% and the visible reflectance above 15%. A quarter was found as a suitable fraction of the optical quarter-wave thickness of the reflec-

tors. By varying the only design parameter – the design reference wavelength λ_{ref} – the reflection colour of the coating can be tuned from blue-green to orange-reddish. For deep red and purple colours however, T_{sol} decreases below the defined limit of 84%. This decrease of T_{sol} for red reflection colours is a general phenomenon of the coloured filter principle, and explains why coatings with orange or reddish reflection colours are difficult to realise.[73] For greenish and blueish reflections, however, Design A shows an excellent solar energy and visual performance ($T_{\text{sol}} > 86\%$ and $R_{\text{vis}} > 18\%$). To produce coloured coatings with Design A on an industrial in-line vacuum coater, however, three physical thicknesses, the one of the SiO$_2$ layer and the two of the TiO$_2$ layers, need to be re-adjusted each time a different colour hue is demanded. Therefore, the question remains whether a possibility exists to minimise the number of layers to tune during the coating deposition, and with it the number of development cycles.

One possible solution is proposed in form of Design B. It requires a supplementary very-low-refractive-index inter-layer. Magnesium fluoride (MgF$_2$) was chosen as coating material, being the one exhibiting the lowest known refractive index among inorganic dense coating materials.[32,33] By modifying only the layer thickness of this MgF$_2$ inter-layer, while keeping the thickness of all other layers constant, the coloured reflection of the coating can be varied. At the same time, increasing the MgF$_2$ layer thickness, Design B exhibits a constant and colour-invariant solar transmittance T_{sol}. The advantage of coatings based on this design is that for different colour hues, which shall be produced on demand, only the thickness of one single layer has to be re-adjusted during the deposition, making colour production and tuning easier.

A stumbling block to use MgF$_2$ as low-refractive-index material has been the difficulties to deposit it by magnetron sputtering, the dominant technology for large-area coating on glass.[26] However, this drawback one might overcome with the novel deposition process for nano-crystalline MgF$_2$ films deposited by reactive magnetron sputtering and showing excellent optical properties ($n = 1.382$ and $k < 0.001$ at 550 nm), which has been recently discovered: this novel MgF$_2$ deposition process will be published elsewhere.

When comparing the coloured reflection R_{vis} of Design A and B, both show similar visible colour brightness in the yellowish colour range. Between blue and green the R_{vis} curve flattens and the brightness for Design B is slightly higher; it is reversed

for the orange and reddish hues. Since building façades shine often in bright greenish and blueish colour hues, which goes well with natural colours of sky and flora, the lack of visible reflection intensity for orange and red might be even advantageous. While saturated orange colour shades are of interest for roof installations, soft orange tones, such as terracotta might also be for façades.

One feature of Design B that stands out among the others is the quasi-constant T_{sol} value remaining in the range 85–85.7%. The slight deficit for blue and green reflection colours, where the solar energy performance of Design A is a little bit higher, could turn out to be a real benefit. According to the best knowledge of the authors, there is no other way to colour solar thermal collectors exhibiting energy-invariant colour properties. In other words, this design would provide a whole colour palette of cover glasses while the solar thermal absorbers behind so-coated glasses are exposed all to the same solar energy input. Thus, the planning of a solar thermal system becomes independent of the reflection colour of the collector cover glass. This outstanding feature would grant architects more freedom for their colour choice. Even different colours on each façade elements might be an interesting architectural option.

5   Conclusion

Energetically and colour-wise optimised designs for solar thermal collectors were developed by advanced numerical simulations. A three-layer filter design (Design A), expressed in generalised form as a narrowband filter, was optimised from the energy point of view for the coating materials TiO_2 and SiO_2. Through the reduction of the variable and free design parameters to only one – the reference wavelength λ_{ref} – it simplifies the first phase of the coloured coating development cycle: to find a suiting multilayer stack for a specific colour, combined with a sufficient high solar transmittance.

In addition, a novel approach for advanced coloured solar coatings (Design B) was investigated. This design is a derivative of the before discussed coloured filter where a supplementary inter-layer with a very-low refractive index, such as MgF_2, is added. This design has the advantage that only the thickness of one layer, needs to be adjusted during the coating deposition in order to tune the coloured reflection, whereas when using Design A there are still three layers to be adjusted. Therefore,

not only the coating-designing phase, but also the prototype-production phase on an vacuum coater could be shortened. The proposed novel approach is a step forward to on-demand production of coloured coatings for solar collectors. Moreover, this design has in addition the outstanding property of a reflection-colour-invariant solar transmittance of 85–85.7%. Aesthetic and functionality of solar thermal collectors are now separated, granting architects and solar system engineers with a full freedom in their colour choice for the solar thermal collectors, independently of the required energy performance or dimensioning of the building services.

6 Acknowledgements

5.4 Combinatorial Study of Low-Refractive Mg−F−Si−O Nano-Composites Deposited by Magnetron Co-Sputtering from Compound Targets

Preliminary version of manuscript.

5.4.1 Summary

The possibility to choose any arbitrary refractive index would be advantageous when designing an ideal coating for a specific application. In reality, coating development is often limited by the accessibility of coating materials with suitable optical properties. One approach to achieve a huge variety of different refractive indices is to mix two or more materials to obtain a nano-composite material with novel optical properties, such as $TiO_2−SiO_2$ which is e. g. used in glass industry.[44] A second interesting point for coating development is to have a material with a refractive index lower than SiO_2 ($n = 1.46$). This would open new possibilities in general for more flexibility in the coating design and in particular for larger spectral antireflection features. Among inorganic dense coating materials MgF_2 exhibits the lowest n with 1.38.[32,33] A combination of both, an arbitrarily choosable and at the same time low refractive index, could be achieved by composites made of SiO_2 and MgF_2. In a co-authored publication it was demonstrated that it is possible to mix MgF_2 and SiO_2 using the sol–gel method to deposit Mg−F−Si−O composite films. This material exhibits excellent optical properties with a very-low refractive index and a close to zero absorptance.[129] Investigations by TEM revealed the consistence of MgF_2-rich nano-crystallites embedded in an SiO_2-rich matrix.

Since the properties of the described nano-composites would be advantageous for thin-film coatings, but the deposition method (sol–gel) is incompatible with the dominating method in large-area production (in-line magnetron sputtering), it is of great interest to develop a novel magnetron sputtering process for such composites.

This combinatorial study, performed at the LC, reports on novel co-sputtered Mg−F−Si−O nano-composite films from ceramic and quartz glass targets. Depositing MgF_2 from ceramic targets, without additional fluorine in the process, leads to

fluorine deficiency in the film which results, as well known, in an increase of the absorption.[102,119] For this reason, the process parameters such as working pressure, target power, and target–substrate distance have been optimised for MgF_2 films before starting the co-sputtering research on the $Mg-F-Si-O$ films. By decreasing the RF power, or by increasing the target–substrate distance or the process pressure, the fluorine deficiency could be minimised. A possible explanation might be that energetic F^- ions have a negative influence on the film formation. Lower power, larger distance or higher pressure reduces the impact energy of those ions on the substrate by increased inelastic particle scattering which might be beneficial for the MgF_2 forming process. The atomic concentration, analysed by EDX measurements, indicates this mechanism.

First $Mg-F-Si-O$ composite materials were produced and the influence of several process parameters on the film composition, such as target power, process pressure, target–substrate distance, and varying oxygen partial pressure were investigated. When supplying a small amount of O_2 as reactive gas to the process, the films get highly transparent which was confirmed by spectrophotometry measurements. The first results are very promising towards sputtered optical $Mg-F-Si-O$ composite films. Non-absorbing films with with $n = 1.424$ were achieved, which is well below sputtered SiO_2. TEM dark field images and SAED diffraction rings reveal an MgF_2-rich nanocrystalline and an SiO_2-rich amorphous phase. Further investigations and process optimisations are necessary to fully analyse the composite films and to better understand the different processes during film formation. This will allow to selecting a specific formation processes and consequently the microstructure and optical properties of the films.

The experiment was planned, set up, installed and performed in autonomy by the first author. For the coating deposition and optical measurements he was assisted by a master student (second author) in material science in the framework of semester and inter-semestral projects. In addition, a bachelor semester project was included in some preliminary studies to determine MgF_2 deposition rates and linearity of thickness profiles. For the SEM, TEM and EDX measurements, the first author was supported by his co-authors from the LC. The analysis of all data (EDX, optics, and microscopy) was performed by himself. The manuscript has been written entirely by him and will be enriched with recent results from the ongoing research.

Combinatorial Study of Low-Refractive Mg−F−Si−O Nano-Composites Deposited by Magnetron Co-Sputtering from Compound Targets

Stefan Mertin[a,b], Tony Länzlinger[b], Cosmin S. Sandu[b], Jean-Louis Scartezzini[a], and Paul Muralt[b]

[a]Solar Energy and Buildings Physics Laboratory, EPFL - ENAC - IIC LESO-PB, Station 18, Bâtiment LE, 1015 Lausanne, Switzerland

[b]Ceramics Laboratory, EPFL - STI - IMX LC, Station 12, Bâtiment MXC, 1015 Lausanne, Switzerland

Abstract

The deposition of nano-composite Mg−F−Si−O films by magnetron co-sputtering from magnesium fluoride (MgF_2) and fused silica (SiO_2) targets is studied. The basic idea is to obtain a stable and reliable sputtering process for optical coatings exhibiting a lower refractive index than 1.46 without adding gaseous fluorine to the process. The here described process only needs a small amount of additional oxygen. The two magnetrons were installed $45°$ off-axis with respect to the static substrate, thus creating a gradient in the thin-film composition. The deposited Mg−F−Si−O coatings were analysed by electron dispersive X-ray spectroscopy (EDX), transmission electron microscopy (TEM) and scanning electron microscopy (SEM). These investigations reveal that the films contain MgF_2 nanocrystals embedded in a SiO_2-rich amorphous matrix. Spectroscopic ellipsometry and spectrophotometry measurements show that they are highly transparent exhibiting a very-low extinction coefficient k and a refractive index n between MgF_2 and SiO_2. Films with $n = 1.424$ to 1.438 and $k < 3.0 \cdot 10^{-4}$ at $550\,nm$ were produced. Since the UV absorption edge of the coatings is located at smaller wavelengths then the edge of an extra-white glass, all presented films can be considered as non-absorbing for optical applications.

The results are very promising towards sputtered Mg−F−Si−O nano-composite films. Further experiments will help to understand the complex film forming mechanism and to control it to be able to selectively choose the composition of the composite films and with it their structural and optical properties.

Keywords: magnesium fluoride, silicon dioxide, thin-film deposition, magnetron co-sputtering, nano-composite, composite target

1 Introduction

Low-refractive-index materials are of special interest for optical coatings to reduce the reflection at dielectric interfaces. [112,130] Having the possibility to apply coatings with a refractive index lower than silica (SiO$_2$, refractive index $n = 1.46$) would allow to obtain e. g. a larger spectral antireflection than with coating materials with the same or higher refractive index. However, materials with a suitable refractive index lower than silica are very limited. One of them is MgF$_2$, well known for its outstanding properties: a refractive index of 1.38 at 550 nm and non-absorbing in the spectral range from 120 nm to 8 μm. [32,33,108] Non-reactively sputtered MgF$_2$ from ceramic targets is found to be always linked with a fluorine deficiency and absorption in the film. [101,102,118,119] Nevertheless, adding fluorine gas to the process is a corrosion and severe safety concern. A novel process to deposit MgF$_2$ by reactive magnetron sputtering without using the highly reactive F$_2$ gas will be published by the authors elsewhere.

Another way to reduce the refractive index below the one of SiO$_2$ is to mix it with MgF$_2$. Creating films with a specific n by mixing two materials is widely used for Si$-$Ti$-$O composites. They are deposited either by sol–gel [21] or by co-sputtering. [79–81] The advantage of co-sputtering is that by varying the applied power, and with it the deposition rate of each material, the refractive index can be tuned. The combination of SiO$_2$ with MgF$_2$ by sol–gel deposition is investigated by Hody-Le Caër et al. [129] showing a tuneable low refractive index which is lower than the 1.46 of silica and which exhibits at a mixing ratio of 50:50 even a lower refractive index than the one of MgF$_2$ (n = 1.38). The films posses a nano-composite microstructure, with MgF$_2$ crystallites embedded in an SiO$_2$ matrix. Sol–gel deposited films however, tend to be porous, which is confirmed by Ishizawa et al. [131]

In this work the authors study the deposition nano-composite thin films on the basis of MgF$_2$ and SiO$_2$ by RF (radio frequency) magnetron co-sputtering from ceramic, respectively quartz glass targets. The aim is to find a stable and reliable sputtering process for optical coatings with a lower refractive index than $n = 1.46$. For SiO$_2$ targets there exists an established RF sputtering process. A small amount of oxygen is added to the process to compensate the oxygen loss during deposition. [132] For the co-sputtered Mg$-$F$-$Si$-$O films presented in this work, also a small amount of oxygen – however no fluorine – is added to the process which can react with the

involved Si as well as with Mg, and F atoms.

The films presented show that it is possible to deposit non-absorbing $Mg-F-Si-O$ composite films by magnetron co-sputtering. Absorption-free films with the lowest refractive index $n = 1.424$ at $550\,nm$ exhibit an index well in between the reactive indices of sputtered SiO_2 and MgF_2, $n = 1.460$ and $n = 1.382$, respectively.

2 Experimental

2.1 Thin-Film Deposition

The films are deposited by co-sputtering from a ceramic MgF_2 and a glass SiO_2 target. Two planar magnetrons with a target size of $2 \times 5.26\,inch^2$ are used. They are installed at an angle of $90°$ to each other, facing the static substrate at $45°$ (see Figure 5.21). This setup was chosen to deposit films with a spacial gradient in their composition i. e. with a gradient of atomic concentration (at.%) and therefore a changing refractive index across the substrate with up to $100\,mm$ in diameter. The targets are driven with RF ($13.56\,MHz$) power of $350\,W$ on the MgF_2 target and of 200 or $250\,W$ on the SiO_2 target.

The base pressure of the chamber is in the range of $2 \cdot 10^{-6}$ to $5 \cdot 10^{-7}\,mbar$. As sputtering gas argon (Ar) at a mass flow of $100\,sccm$ is used. By throttling the process valve between pumping stage and the main chamber the process pressure can be increased up to $2.0 \cdot 10^{-2}\,mbar$. It is measured with a MKS Baratron^{TM} capacity pressure gauge. In parallel, the pumping volume of the load-lock pumping stage is reduced, since the gate valve to the main chamber has to remain open during deposition. The working pressure during the process is set to $1.5 \cdot 10^{-2}\,mbar$. No sample shutter is needed, since the sample is transferred to the deposition position when the plasma discharge is stabilised (after 10–$15\,min$). The substrate is electrically grounded.

A linear manipulator is used to load the samples through the load lock. The substrate holder is designed very flexible to be able to investigate different substrate positions (target–substrate distances combined with different deposition angles). It remains on the manipulator during the deposition. The target–substrate distance has been optimised for both small thickness gradients of the films deposited from only one source, as well as for a minimised F deficiency in pure MgF_2 films. A
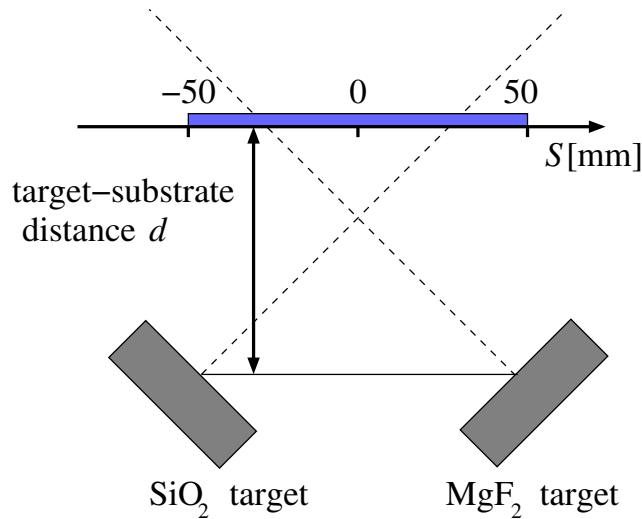
Figure 5.21: Schematic drawing of the magnetron arrangement for co-sputtering deposition. The standard sputtering position for the substrate is in the centre of the two magnetrons, the distance d to the targets can be varied. The film position on a 100-mm wafer is given by the distance S wheres 0 corresponds to the substrate centre, -50 mm the edge close to the SiO_2, and 50 mm close to the MgF_2 target.

small oxygen flow (0.5–1 sccm) is added to the process as reactive gas to compensate oxygen losses during the sputtering process. The optimised target–substrate distance of $d = 167$ mm is used for the here described coatings.

The depositions are carried out simultaneously on a half disk of a 100-mm-silicon wafer and extra-white glass substrates (35×25 mm^2). To investigate also the optical properties in the UV range with wavelengths below the UV-absorption edge of glass, fused-silica-half-disk wafers are used instead of the glass. The glasses are cleaned in an ultra-sonic bath for 10–15 min, first in pure acetone and then in pure isopropanol. The wafers are factory cleaned and are not additionally pre-treated.

The deposition rate is measured with a quartz microbalance which has been calibrated by scanning electron microscopy (SEM) cross sectional views. The deposition parameters for selected films are summarised in Table 5.2.

2.2   Chemical and Structural Characterisation

The morphology of the films is investigated by SEM on a high resolution Zeiss microscope of the type Merlin (3 kV and 1.0 nA) by top and cross sectional views. For

Film	Flow ratio Ar:O_2	RF power [W] SiO$_2$	MgF$_2$	Rate [nm/min]	Distance S [mm]
A	100:1	250	350	1.29	-40
B	100:1	250	350	1.21	-20
C	100:0.5	250	350	1.68	-40
D	100:0.5	250	350	1.47	-20
E	100:1	200	350	0.89	-40
F	100:0.5	200	350	0.94	-40

Table 5.2: Process parameters of coating depositions for absorption-free Mg−F−Si−O films in the spectral range 300–2500 nm. The target–substrate distance d is set for all deposition to 167 mm and the process pressure to 0.015 mbar.

higher topographic contrast the HE-SE2 detector is used. For chemical analysis the microscope is equipped with an Oxford X-Max 80 mm^2 EDX (energy-dispersive X-ray spectroscopy) detector. The same electron acceleration voltage of 3 kV and probe current of 1.0 nA as for the SEM investigations are used for the EDX measurements. By the nature of ex-situ chemical analysis a few percent of carbon surface contamination is always measured. Since the deposition process involves no carbon, the C contamination is assumed to be only on the film surfaces and is therefore not taken into account (set to zero in the EDX analysis). The Mg and F concentrations are calibrated with an MgF$_2$ single crystal.

The micro- and nanostructure of the films is examined in cross-section by transmission electron microscopy (TEM) on a FEI Tecnai Osiris high resolution microscope (200 kV accelerating voltage). The cross section TEM specimens are prepared following the conventional method: mechanical cutting, glueing face to face, mechanical thinning and polishing. In a last step they are ion milled in a PIPS^{TM} (precision ion polishing system) installation. Selected area electron diffraction (SAED) patterns are used to investigate the presence of a nanocrystalline phase in the films.

2.3 Optical Characterisation Techniques

Spectroscopic ellipsometry at various angles (55–70°) is used to determine the optical properties – refractive index $n(\lambda)$ and extinction coefficient $k(\lambda)$ – of the films. The

ellipsometric angles ψ and Δ were measured with a Sopra GES 5E spectroscopic ellipsometer equipped with a spectrograph (CCD detector for 190–990 nm and linear detector for 990–1700 nm). The advantage of the spectrograph and the linear detector is the relative short measuring time. In addition, the ellipsometer is equipped with an automatic sample stage which allows to map a whole wafer in one measurement run (approx. 1h). This is of great advantage when investigating the spacial gradient of samples, although the resolution is smaller than with a high resolution spectrometer. From ψ and Δ the wavelength-dependent optical constants $n(\lambda)$ and $k(\lambda)$ are derived in the spectral range 300–1100 nm by means of a Levenberg–Marquardt algorithm for minimising the RMSE (root mean square error) between the simulated fit curves with a suitable dispersion model and the measured data, as described e. g. in RÖSELER[71]. The spectral transmittance $T(\lambda)$ of the coatings on glass and fused silica are measured with a double beam Brechbrühler V-670 spectrophotometer (187–2700 nm) equipped with a monochromator and two detectors for UV-VIS and NIR. The spectral reflectance $R(\lambda)$ is measured with a FilMetrics F20-UV reflectometer (200–1100 nm). The absolute error of the spectral measurements amounts to around 1%. A fused silica standard (SiO_2) is used to calibrate the instruments for $T(\lambda)$ and $R(\lambda)$. Therefore the accuracy of the measurements is reduced to the reproducibility of the spectra (around 0.5%). The spectral absorption $A(\lambda)$ is derived via energy conservation ($A = 1 - T - R$).

3 Results and Discussions

3.1 Chemical and Structural Analysis

Several composite samples with a spacial gradient in the atomic concentration were produced. Figure 5.22 shows the atomic concentration of Mg, Si, F, and O in the films measured by EDX. The measured carbon concentration of around 1–1.5 at.% was found to be only related to surface contaminations and is therefore not included in the evaluation. As expected, it can be seen that for all films close to the MgF_2 target the Mg and F concentration is maximised, where Si and O have the highest concentration close to the SiO_2 target. The absolute values, however depend on target power and Ar:O_2 ratio.
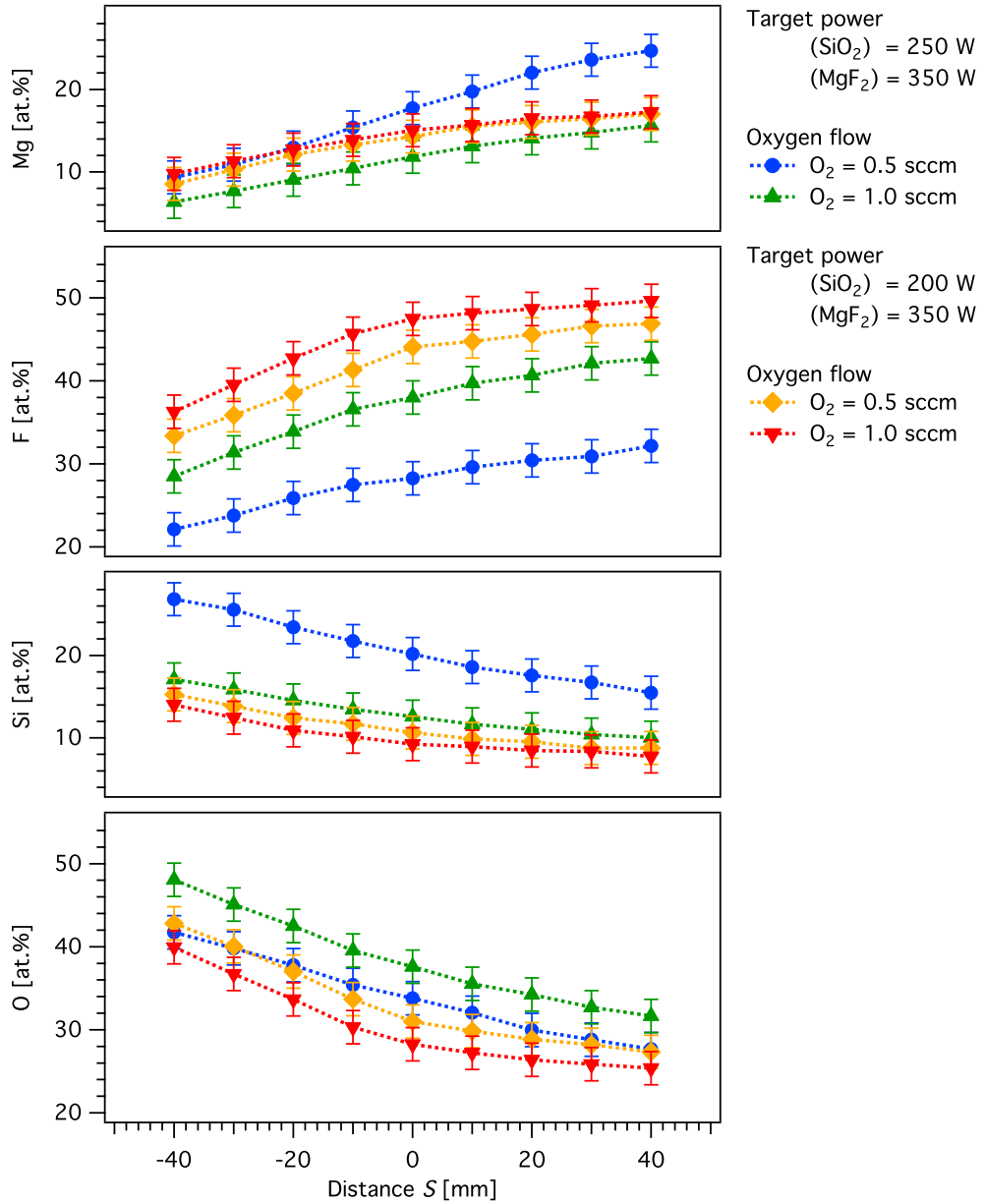
Figure 5.22: Atomic concentration measured by EDX of Mg-F-Si-O films deposited with different oxygen flow. The SiO_2 target was powered by 200 W or 250 W RF, whereas MgF_2 always by 350 W RF. The process pressure was set to 0.015 mbar and the Ar flow to 100 sccm. The O_2 flow was either set to 0.5 sccm or 1 sccm for the different depositions. The target-substrate distance d for all films was 167 mm. The distance $S = 0$ mm on the substrate corresponds to the wafer centre, whereas $S = -50$ mm is located close to the SiO_2, and $S = 50$ mm to the MgF_2 target (see Figure 5.21).

All films have a thickness of 400–600 nm. With this thickness there is no EDX signal from the Si substrate visible, since the electron penetration depth at the used electron acceleration energy of 3 keV is around 200 nm for SiO_2 films and 150 nm for MgF_2 films.[105]

For the process parameters 250 W for SiO_2, 350 W for MgF_2, 100 sccm Ar and 0.5 sccm O_2 flow, the Mg concentration increases strongly on the right hand side of the sample ($0 < S < 50$ mm) whereas the F concentration almost stagnates. The resulting metallic Mg excess leads to absorption in the coatings. At distance $S = 40$ mm the film has a composition of the form $(MgF_2)_{16}(SiO_2)_{14}Mg_9Si$. Increasing the oxygen flow to 1.0 sccm increased the F and O content while the Mg and Si concentrations decreased. The resulting mixture of the film at $S = 40$ mm is now $(MgF_2)_{16}(SiO_2)_{10}F_{11}O_{12}$, with no metallic excess in the coating, all metallic atoms seem to be ionically bound. However, the coating remains absorbing.

As discuss below in this paper, Section 3.2 the film compositions at a distance -40 mm $\leq S \leq -20$ mm seem to be most interesting because they are only weak or non-absorbing. Table 5.3 summarises the atomic concentrations of six films in this deposition zone. As it can be seen for the same power and gas flow at $S = -40$ mm (Film A) all metallic atoms are also ionically bonded: $(MgF_2)_6(SiO_2)_{17}F_{15}O_{14}$. However, now the film becomes non-absorbing.

| Film | At $\lambda = 550$ nm | | d [nm] | Atomic concentr. [%] | | | |
	n	k		Mg	F	Si	O
A	1.424	$< 10^{-9}$	551	6.4	28.5	17.1	48.1
B	1.436	$9.4 \cdot 10^{-5}$	512	9.1	33.9	14.6	42.5
C	1.435	$2.2 \cdot 10^{-5}$	543	9.3	22.1	26.8	41.7
D	1.438	$5.4 \cdot 10^{-5}$	511	13.0	25.9	23.4	37.8
E	1.437	$2.9 \cdot 10^{-4}$	431	9.8	36.3	14.0	40.0
F	1.428	$1.8 \cdot 10^{-4}$	390	8.6	33.4	15.3	42.8

Table 5.3: Optical constants n and k of different Mg−F−Si−O films (A–F) at $\lambda = 550$ nm and their thickness d are given. Furthermore, the atomic concentration determined by EDX is indicated. For all depositions the process pressure was set to 0.015 mbar, whereas the other process parameters were as shown in Table 5.2.

The microstructure of the films was investigated by TEM measurements to understand the mechanism of the film absorption. The TEM dark field image indicates the presents of nanocrystals in the film (white spots in Figure 5.23a). MgF_2 nanocrystallites embedded in an SiO_2-rich amorphous matrix are reported by Hody-Le Caër et al. [129] for Mg−F−Si−O films deposited by sol–gel. They describe similar white spots in the TEM dark field image. The SAED diffraction rings in Figure 5.23b confirme the presence of a nanocrystalline tetragonal phase of MgF_2 (a = 0.462 nm and c = 0.305 nm). [124] The crystallite size measured in the high resolution TEM image in Figure 5.23c is in the range 3–8 nm. Since SiO_2 tends to form amorphous structures it can be concluded that co-sputtered films also exhibit an MgF_2-rich crystalline and an SiO_2-rich amorphous phase containing the excess ions. In the case of a high absorption metallic Mg excess atoms are embedded in the matrix. Respectively, for no or weak absorption F and/or O excess ions could be located in the amorphous phase. However, MgF_2-rich composites does not automatically imply weak-absorbing and
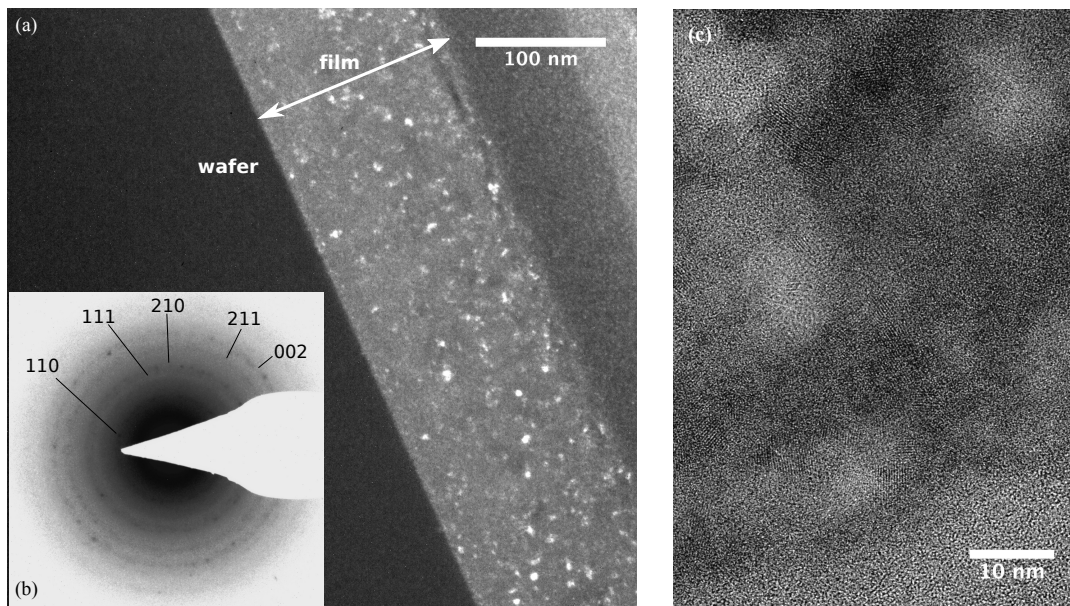

Figure 5.23: TEM images of a sputtered Mg−F−Si−O film. In the dark field image (a) the white spots reveal the existence of nanocrystals. The inverse coloured diffraction pattern (b) confirms the presents of MgF_2 nanocrystallites. The rings of the MgF_2 crystal planes (110), (111), (210), (211) and (002) could be identified. The average crystal size measured by the high resolution TEM image (c) is in the order of 3–8 nm.

low-refracting films. It seems to play an important role how the Mg^{2+} and F^- ions are implanted in the coating during the film formation process. A possible explanation for a high k of MgF_2-rich films could be that close to the MgF_2 target ($S = 40\,mm$) energetic F^- ions from the target have a negative effect on the film formation process, consequently on its microstructure, leading to a higher n and k. At greater distance to the MgF_2 target ($S < -20\,mm$) the F^- ions can loose already a significant part of their kinetic through inelastic particle–particle scattering. This could explain why MgF_2-rich films, formed at $S > 0\,mm$ (close to MgF_2 target), exhibit a significant higher excitation coefficient than those films at $S < 0\,mm$ (close to SiO_2 target), even though both films seem to have a similar atomic concentration.

Figure 5.24 shows a SEM cross sectional view of a film similar to Film C. It can be seen that the film exhibits a microscopic planar surface, which is a prerequisite for the optical measurements described below. The image does not resolve the microstructure, however, the film appears to be compact and dense, as confirmed by TEM (see Figure 5.23a).
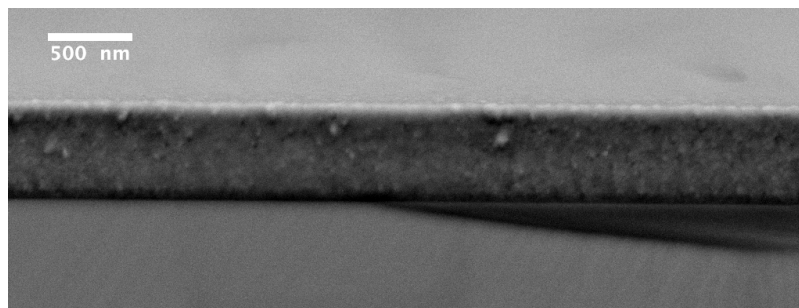

Figure 5.24: SEM cross sectional view of similar film to Film C with 568 nm film thickness, measured with 3 keV and 1 nA probe current. The film appears compact and with a smooth plane surface.

3.2 Optical Characterisation

The coated fused silica substrates were analysed by spectrophotometry for the four different process parameter pairs from Table 5.2 and at the EDX measuring points given in Figure 5.22 (Film A–F).

The spectral transmittance curves of the films are shown in Figure 5.25 for the UV range (200–400 nm) in comparison to an uncoated fused silica substrate ($500\,\mu m$
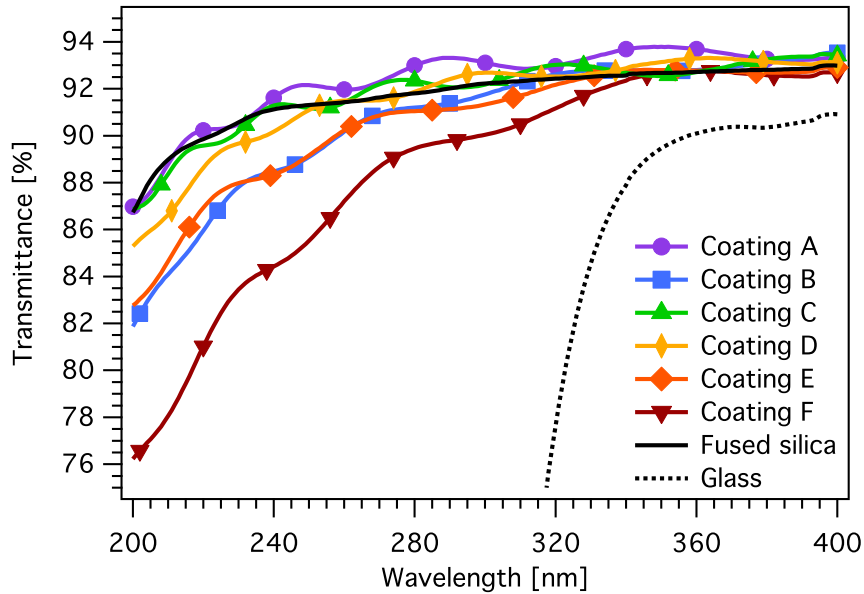
Figure 5.25: Transmittance spectra of Film A–F in the UV range. It can be seen that for all coatings the absorptance increases at wavelengths smaller than the absorptance edge of the extra white glass. Therefore these coatings are non-absorbing for optical applications on glass.

thick), as well as to an uncoated extra–white glass (1 mm thickness). Film A is quasi nil-absorbing, where as Film B–F are absorbing in the UV range (from only weakly to significantly). However, for all presented films the absorption increases at wavelengths beyond the absorption edge of extra–white glass (shorter approx. 300 nm). Therefore, all of these coatings can be considered as non-absorbing for optical coating applications on glass.

The optical properties of the films were fully analysed by a combined method of ellipsometry (on Si wafers) and spectrophotometry (on fused silica wafers). For the ellipsometric data fit a Lorentz-oszillator dispersion model with four oscillators was used. In the first step the damping factors were set to zero. For the oscillator energies, the corresponding energies of SiO_2 and MgF_2 coatings were used. The optical constants were then refined by performing a data fit to the measured spectral data using the characteristic matrix model for thin films.[33] This process was iteratively repeated until both, $n(\lambda)$ and $k(\lambda)$ – determined by ellipsometry and spectrophotometry – were in good agreement.

Table 5.3 summarises the determined optical constants n and k at 550 nm, as well as the film thickness of the selected Mg−F−Si−O coatings (A–F) determined by ellipsometry on the Si wafer and verified by SEM cross sectional views. Film A exhibits the lowest n and is quasi nil-absorbing in the invested spectral range between 300 nm (the UV absorption edge region of glass) and 1100 nm (NIR limit of the used reflectometer). Film C has a comparable n to the other four coatings, but it exhibits the second lowest absorption. Therefore, Film A and C were chosen as the best adapted coatings for optical applications (prerequisite near-zero absorption) and the results of their optical analysis are presented in detail below.

Figure 5.26 plots the data fit curves of the measured $\psi(\lambda)$ and $\Delta(\lambda)$ of Film A at various angles (55–70°), after several iterations of the former describe combined ellipsometric and spectrophotometric analysis. The data is in good agreement with the fit curves (RMSE = 3.2), which is reasonable for an ellipsometer with a spectrograph (see this paper, Section 2.3). The refractive indices of Film A and C in the spectral range (300–1100 nm) are presented in Figure 5.27. For comparison the indices of RF
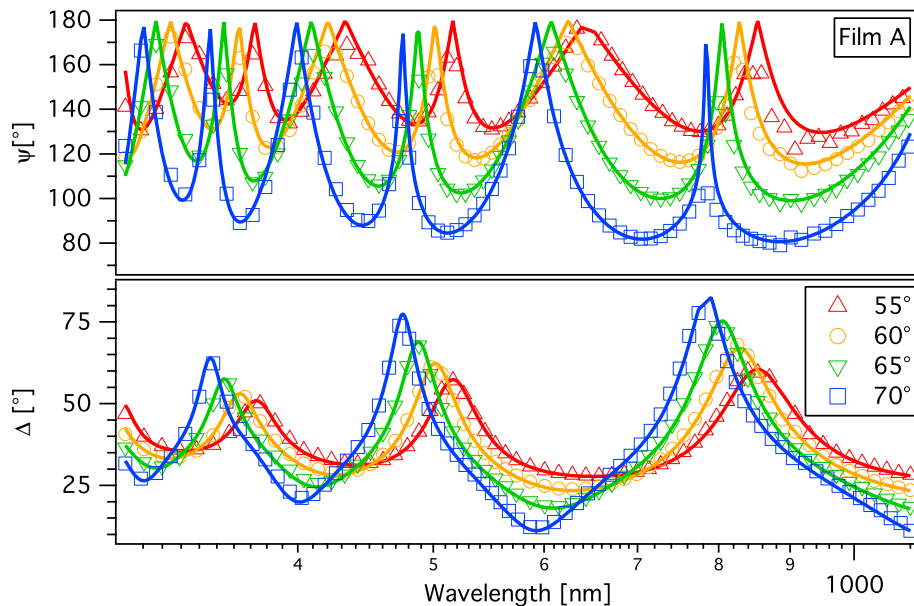

Figure 5.26: Measured ellipsometric angles ψ and Δ in the range 300–1100 nm to determine the optical constants n and k of the composite Film A. The open symbols represent the measured data, whereas the solid lines the fit curves. For better readability the shown amount of data points is reduced and the wavelength axis is plotted in logarithmic scale.

sputtered SiO_2 and pulsed DC sputtered MgF_2 films are shown. For the latter we recently developed a novel process for reactive magnetron sputtering which will be published elsewhere. Film A exhibit the lowest produced refractive index of 1.424 at 550 nm which is well in the centre between the indices of SiO_2 (n=1.460) and MgF_2 (n=1.382).
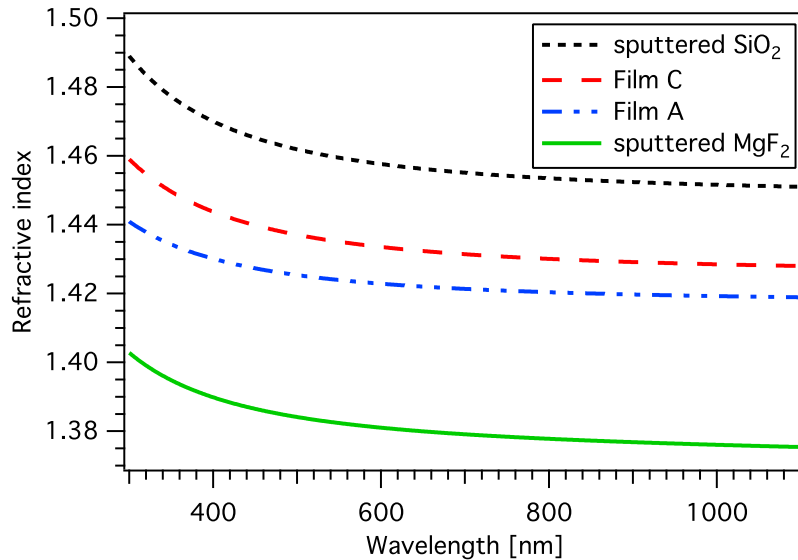

Figure 5.27: Refractive indices of Mg−F−Si−O composite Film A and C at different process parameters in comparison to pure sputtered SiO_2 and MgF_2 films.

Figure 5.28a and Figure 5.28b show the results of the simulated fit curves (red, solid lines) for the spectral transmittance and reflectance using the determined optical constants n and k. The simulated fit curves are in excellent agreement with the data giving a RMSE of 0.14 and 0.13 for Film A and C, respectively. The absorptance is derived from the transmittance and reflectance data and the corresponding fit curves. It is close to zero and therefore not shown in the graph as it is not distinguishable from the substrate. For comparison, $T(\lambda)$ and $R(\lambda)$ of the uncoated fused silica substrate is added in Figure 5.28. On can easily see that the transmittance of both coated substrates is always higher then the uncoated, touching each other tangential in their interference minimum, while for the reflectance it is the opposite, both coated substrates remain below the reflectance of the uncoated one.
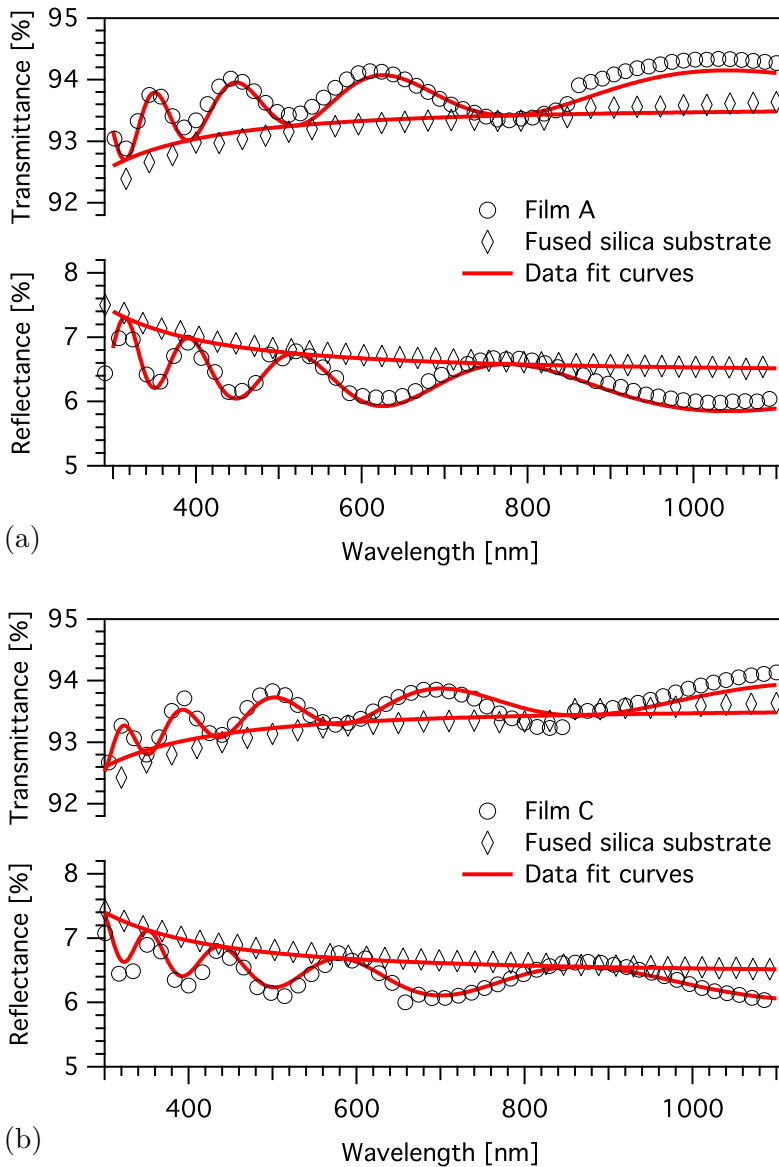
Figure 5.28: Transmittance $T(\lambda)$ and reflectance $R(\lambda)$ spectra of Film A (a) and Film C (b). Both films exhibit a near-zero absorptance in the measured spectral range (300–1100 nm). The data fit curves are modelled by the method of the characteristic matrix for thin films using the former determined optical constants n and k. For comparison, $T(\lambda)$ and $R(\lambda)$ of the uncoated fused silica substrate is added.

4 Conclusions and Outlook

This combinatorial study shows that co-sputtering from SiO_2 and MgF_2 compound targets allows the synthesis of absorption-free dielectric thin films with a refractive index of $n = 1.424$. The microstructure is driven by MgF_2 nanocrystal formation. SiO_2 which is much more prone to form amorphous phases, forms the main constituent of the amorphous matrix around these MgF_2-rich nanocrystals. Excess ions tend to be localised in the SiO_2-rich matrix. Coatings with an excess of Mg ions exhibit a strong absorption, whereas weakly or non-absorbing films can contain F and O excess ions in the amorphous matrix. The MgF_2 nanocyrstalline part has an effect to reduce the refractive index. However, it cannot be excluded that the amorphous matrix has a lower density than SiO_2, and might also contribute to the lowering of n. Nevertheless, compositions with a higher percentage of MgF_2 do not show a lower refractive index, meaning that an amorphous phase containing more MgF_2 does not lower the refractive index. It seems that there is a correlation of the proximity of the substrate to the MgF_2 target and a high absorption coefficient k. A possible explanation is that energetic F^- ions from the target have a negative impact on the film formation process and therefore on the microstructure and optical properties of the film.

Further experiments will help to better understand the complex film forming mechanisms and to control it to be able to choose the composition of the films, their microstructure and with it their optical properties.

6 Conclusions

6.1   Final evaluation

The basic objective of this thesis was to improve and optimise the interference filters for the coloured solar thermal collectors, developed at the Solar Energy and Building Physics Laboratory (LESO-PB) and to support the industrialisation process of the coloured collector glazing. Hereby, the main focus was on novel, energetically optimised coloured interference filters and on the research on new coating materials for those filters, especially on materials exhibiting a low refractive index, such as magnesium fluoride (MgF_2) and MgF_2 containing composites.

In addition to the energetic optimisation, the aesthetic aspect of visual appearance plays an important role. For this purpose, a study to match the colours of the collector cover panels to existing architectural glazing was carried out. A prerequisite to ensure the later industrial production of the coatings was to use the industrial dominating technology for glass coating – magnetron sputtering – for the coating development. In addition to the produced coloured samples on laboratory scale ($60 \times 70 \, \mathrm{mm}^2$), a new real-size prototype production was initiated for an energetically optimised green interference filter in collaboration with the industrial partner SwissINSO SA, Switzerland.

The investigated improvements and achieved results of this thesis research are analysed in the following paragraphs in detail.

New coloured interference filters

Energetically and colour-wise optimised designs for solar thermal collectors were developed by means of numerical simulations. The energetic performance, indicated through a figure of merit, has been increased. The colours of the presented blueish

and greenish designs are sufficiently stable for different viewing angles, whereas the angular dependency for the presented orange-reddish coloured coatings still needs to be improved. Alternatively, an angular-dependent colour variation could also serve as unique selling point for special design elements in particular buildings.

Coloured laboratory samples on glass

The new and improved colour filters described above were deposited by reactive magnetron sputtering on the reverse side of extra-white glass substrates. The samples exhibit a solar transmittance $T_{sol} > 87\%$ and are completely opaque to the human eye by means of a chemical fine-structured (etched) surface finish on the front side of the glass. For some multilayer design types with greenish colour hues, even transmittance values of $T_{sol} = 91\%$ were reached. The target–substrate distance for the deposition process has been optimised in combination with the suitable process pressure and oxygen flow to deposit flat and even films. This led to an extraordinary homogeneous coloured appearance for samples of laboratory size ($60 \times 70 \, mm^2$). Furthermore, the colours of the presented blueish and greenish samples are sufficiently stable for different viewing angles. In contrast, the angular behaviour of orange-reddish coatings still needs to be improved. This angular-dependent colour variation is in good agreement with the thin-film simulations of the coloured filters.

Industrial prototype glazing

A first industrial prototype production of a new and energetically optimised green collector glazing was initialised in cooperation with SwissINSO SA. The glazing exhibits a T_{sol} of 85.2% at normal light incidence. This proves the feasibility to produce the investigated and developed coatings on large-scale architectural glazing. The real-size prototype (some square metres) provides a homogeneous coloured appearance from different viewing angles which was confirmed by angular-dependent transmittance and reflectance measurements on the Window Test Bench.

Colour matched solar collectors

It has been shown that by means of the coating development cycle for coloured interference coatings the design of the filters could be successfully adapted and fine-tuned to match their coloured reflection with the colours of commercial sun protection

glasses (SPGs). Colour-matched samples fitting to a blue and a greenish-blue SPG were successfully produced.

Sputtered low-refractive-index materials

MgF_2 films were deposited via magnetron sputtering in a reactive mode using a metallic magnesium target and as reactive gases carbon tetrafluoride (CF_4) and oxygen (O_2) diluted with argon. The experiments were carried out in collaboration with and at the Department of Physics of the University of Basel. The obtained refractive index at 550 nm is $n = 1.382$ which is congruent with $n = 1.383$ of polycrystalline MgF_2. The films are only weakly absorbing ($k = 0.001$ at 550 nm). The novelty of this process is the usage of the chemical reaction path from CF_4 to carbon dioxide (CO_2) during the sputtering deposition. This is qualitatively confirmed by in-situ mass spectrometry during the plasma process as well as by the analysis of the atomic concentrations in the deposited films by in-situ XPS measurements. As predicted by the chemical reaction path the C and O contamination in the films is minimised for equal partial pressures of O_2 and CF_4 in the reactive gas mixture.

A first anti-reflective coating was realised exhibiting a reflectance minimum of 5.2% at 760 nm which is congruent to the theoretical limit for MgF_2 anti-reflective coatings. The resulting T_{sol} of the coated sample amounts to 93.4% which is 1.7% higher then for the uncoated glass substrate. By optimisation of the layer thickness with respect to the solar spectrum, a T_{sol} increase of 2% could be achieved.

Reduction of design parameters

It is important to simplify both, the coating-designing and the prototype-production phase to have the possibility to offer a huge variety of colours on demand for solar thermal collectors. These two phases are influenced by the number of variable parameters, such as coating materials, quantity of individual layers, and number of different layer thicknesses. A generalised model for a three-layer filter, based on the narrowband-pass filter theory, has been energetically optimised by means of numerical simulations for the coating materials titanium dioxide (TiO_2) and silicon dioxide (SiO_2). The number of variable simulation parameters could be reduced down to only one: the design wavelength λ_{ref}. This simplifies the first phase of the coloured coating development cycle – finding a suitable multilayer design which

exhibits the desired colour in combination with a sufficiently high solar transmittance T_{sol}. Furthermore, as an additional improvement step, a single colour-tuning layer was introduced. This novel advanced coating design is a derivate of the former described three-layer band pass where a supplementary inter-layer with a very-low refractive index, such as MgF_2, is inserted. Only the thickness of this colour-tuning layer needs to be modified to change the coloured reflection, while the thickness of the other three layers remains the same. This reduces the number of layers to tune during the second development phase – the prototype phase on a vacuum coater – down to one. In addition, this novel design has an outstanding property: it separates the aesthetic aspect and the functionality by exhibiting a T_{sol} of 85–85.7% which is nearly invariant from the reflection colour.

Co-sputtered composite materials with low refractive index

A tuneable refractive index would further increase the flexibility for optical coating development. A promising approach are nano-composite materials. In this combinatorial study the deposition of $Mg-F-Si-O$ films by magnetron co-sputtering from compound targets was investigated. Absorption-free dielectric thin films with a refractive index of $n = 1.424$ were achieved. The microstructure of the films consists of MgF_2-rich nanocrystals embedded in an SiO_2-rich amorphous matrix. Even though the MgF_2 nanocrystallites lower the refractive index, it cannot be excluded that the amorphous matrix has a lower density than SiO_2, and might also contribute to the lowering of n. These results are very promising towards composite films with a low refractive index by magnetron co-sputtering. Further research is needed for a better understanding of the complex film forming mechanism and to control it to selectively choose the film composition, its microstructure and with it its optical properties.

6.2   Summary and outlook

The presented results of this doctoral research bring the façade integration of solar thermal collectors several steps forward, which will support the spread of solar thermal energy to the building sector. New coloured filters were simulated and afterwards successfully deposited by reactive magnetron sputtering. Hereby, the filter design has been simplified while the solar energy and visual performance was increased. The

new filters exhibit a high solar transmittance T_{sol} between 86% and 91% depending on the filter design used and the desired colour hue. Glazings with green and blue reflections are sufficient stable in their coloured appearance at changing viewing angles whereas the angular behaviour of orange and reddish coatings still needs to be improved. However, a changing colour hue at various viewing angles could also be integrated in modern architectural design. First new green real-size prototypes were produced. They exhibit an angle-invariant and homogenous coloured reflection and a $T_{\text{sol}} = 85.2\%$ at normal solar incidence. These results are very promising and a great step towards active solar energy façades by means of coloured collector integration.

In addition, a novel reactive sputtering process for stoichiometric MgF_2 films has been invented. The films exhibit a refractive index $n = 1.382$ at $550\,\text{nm}$ and a near nil-absorption in the spectral wavelength range 300–$2300\,\text{nm}$. The possibility to sputter MgF_2 as low-refractive-index coating material opens new paths to improve existing coating designs e. g. by combining the colour-reflection peak with an anti-reflective region in the UV or VIS, or to develop completely novel filter design types. For the latter using a second low-index layer as inter-layer, with a refractive index well below the index of SiO_2 ($n = 1.46$), is a promising approach. In the proposed design, by changing only the thickness of the introduced MgF_2 inter-layer the reflection colour of the filter can be tuned: the MgF_2 layer acts as colour-tuning layer. Moreover, a whole colour palette of different hues with a colour-invariant solar energy performance could be realised. These coatings could grant architects and solar engineers full freedom in their colour choice for the solar thermal collectors. The decision on architectural design and aesthetic appearance becomes independent of the required energy performance and of the dimensioning of the building services. Last but not least, the first results on co-sputtered $Mg{-}F{-}Si{-}O$ composite films are very promising for novel optical low-refractive coating materials deposited by magnetron sputtering, a prerequisite for industrial large-scale production. Absorption-free films with $n = 1.424$ at $550\,\text{nm}$ were realised, which is well in between the one of sputtered SiO_2 ($n = 1.460$) and MgF_2 ($n = 1.382$).

In summary, several new coloured coatings were produced on the basis of common coating materials and new engineered coating designs. In addition, the filter designs were extended with a second low-refractive-index material. Therefore, two novel sputtering processes for MgF_2-containing low-refractive films were developed.

Originated in the obtained results described in this thesis, new scientific questions and ideas for applications come up. Some of these are discussed in the following paragraphs.

The theoretical concept of a colour-tuning layer should be proven experimentally. This could be done by deposition and afterwards investigation of these advanced colour filters. In addition, the variety for further improvements and different layer combination for the coloured coating designs by including MgF_2 and/or $Mg-F-Si-O$ layers in the filter design is enormous. Another completely new approach could be e. g. the combination of three materials having the differences of their refractive index equally spaced, such as the combination of TiO_2 with $n = 2.4$, Si_3N_4 with $n = 1.9$ and MgF_2 with $n = 1.38$.

The number of possibilities to optimise the novel sputtering process for MgF_2 is huge. One interesting point would be to vary the ratio between sputtering- and reactive-gas to increase the deposition rate. This could also further reduce the carbon and oxygen contamination in the films and improve their microstructure with the goal to minimise the extinction coefficient k of the films, especially in the UV range. A next step would be to also increase the target size to deposit larger samples with up to $100\,mm$ in diameter i. e. 4-inch wafers.

To improve the homogeneity of such large samples, the installation of a lateral substrate motion during deposition could be investigated. Such a sample motion would also be of interest for the $Mg-F-Si-O$ composite films deposited from compound targets by co-sputtering. Furthermore, also the influence of the target–substrate distance and the total process pressure on the microstructure of the nano-composite films and with it on their optical properties is of great interest and provides a huge potential for future improvements.

A Spectral Quantities and Colorimetry

A.1   Definition of optical and solar quantities

The total solar transmittance T_sol and the total solar reflectance R_sol describe the amount of solar radiation transmitted or reflected, respectively, relative to the impinging solar radiation. They can be mathematically described by integration of the spectral quantities over the solar spectrum I_sol:[127]

$$T_\mathrm{sol} = \frac{\int\limits_{300\mathrm{nm}}^{2500\mathrm{nm}} T(\lambda)I_\mathrm{sol}(\lambda)d\lambda}{\int\limits_{300\mathrm{nm}}^{2500\mathrm{nm}} I_\mathrm{sol}(\lambda)d\lambda} \tag{A.1}$$

$$\tag{A.2}$$

$$R_\mathrm{sol} = \frac{\int\limits_{300\mathrm{nm}}^{2500\mathrm{nm}} R(\lambda)I_\mathrm{sol}(\lambda)d\lambda}{\int\limits_{300\mathrm{nm}}^{2500\mathrm{nm}} I_\mathrm{sol}(\lambda)d\lambda} \tag{A.3}$$

Energy conservation leads to the fundamental radiation equation, through which the solar absorption α_sol can be simply calculated by:

$$A_\mathrm{sol} = 1 - R_\mathrm{sol} - T_\mathrm{sol} \tag{A.4}$$

In case of negligible absorption the radiation equation simplifies to:

$$1 = R_\mathrm{sol} + T_\mathrm{sol} \tag{A.5}$$

The colour impression seen by the human eye is directly related to the visible

part of the spectral reflectance $R(\lambda)$. By integrating $R(\lambda)$ over the visible spectrum, weighted by the CIE standard illumination of natural daylight D_{65} and the photopic luminous efficiency function $V(\lambda)$ of the human eye, visible reflectance derives to:[127]

$$R_{\text{vis}} = \frac{\int\limits_{380\text{nm}}^{780\text{nm}} R(\lambda) \cdot D_{65}(\lambda) \cdot V(\lambda) d\lambda}{\int\limits_{380\text{nm}}^{780\text{nm}} D_{65}(\lambda) \cdot V(\lambda) d\lambda} \tag{A.6}$$

The visible reflectance corresponds to the relative luminance Y from the CIE 1931 chromaticity diagram with D_{65} as illuminant.[66] Since the values $D_{65}(\lambda)$, $V(\lambda)$, $T(\lambda)$ and $I_{\text{sol}}(\lambda)$ are all measured quantities and therefore not continuous functions, the integration needs to be mathematically performed by numerical summation, where the wavelength interval $\Delta\lambda$ should not be larger than $5\,\text{nm}$.

$$T_{\text{sol}} = \frac{\sum\limits_{300}^{2500} T(\lambda) \cdot I_{\text{sol}}(\lambda)\Delta\lambda}{\sum\limits_{300}^{2500} I_{\text{sol}}(\lambda)\Delta\lambda}$$

$$R_{\text{sol}} = \frac{\sum\limits_{300}^{2500} R(\lambda) \cdot I_{\text{sol}}(\lambda)\Delta\lambda}{\sum\limits_{300}^{2500} I_{\text{sol}}(\lambda)\Delta\lambda}$$

$$R_{\text{vis}} = \frac{\sum\limits_{380\text{nm}}^{780\text{nm}} R(\lambda) \cdot D_{65}(\lambda) \cdot V(\lambda)\Delta\lambda}{\sum\limits_{380\text{nm}}^{780\text{nm}} D_{65}(\lambda) \cdot V(\lambda)\Delta\lambda} \tag{A.7}$$

A.2   Colorimetry

A.2.1   CIE 1931 colour-matching functions and CIE xyY chromaticity diagram

Colours can be mathematically described by the CIE 1931 colour system of the International Commission on Illumination (Commission Internationale de l´Eclairage, CIE). It defines the colours through the colour-matching functions (CMFs) $\bar{x}(\lambda)$, $\bar{y}(\lambda)$, and $\bar{z}(\lambda)$ (see Figure A.1), which correspond to the sensitivity of the photoreceptors in the human eye. The CMFs of the CIE 1931 standard colorimetric observer are used (2° visual field). Each colour can be described by a combination of the three tristimulus values X, Y, and Z, which are derived from $\bar{x}(\lambda)$, $\bar{y}(\lambda)$, and $\bar{z}$ via[66]

$$X = k \int\limits_{380\text{nm}}^{780\text{nm}} \Phi(\lambda)\bar{x}(\lambda)d\lambda \tag{A.8}$$
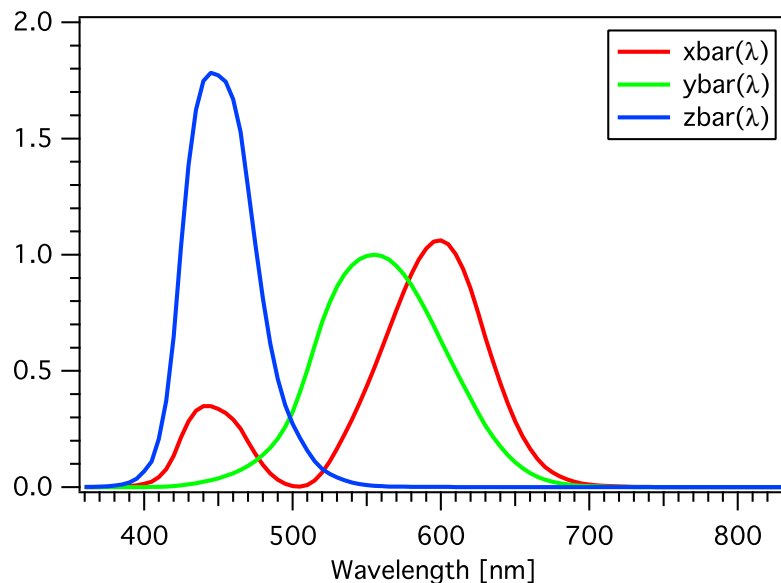
Figure A.1: Colour-matching functions with a visual field of 2° of the CIE standard observer.

$$Y = k \int\limits_{380\text{nm}}^{780\text{nm}} \Phi(\lambda)\bar{y}(\lambda)d\lambda \tag{A.9}$$

$$Z = k \int\limits_{380\text{nm}}^{780\text{nm}} \Phi(\lambda)\bar{z}(\lambda)d\lambda \tag{A.10}$$

where k is a constant, $\Phi = R(\lambda) \cdot I_{\text{spec}}$ the relative stimulus function of the reflected light and $\bar{y}(\lambda)$ is equal to the photopic luminous efficiency function $V(\lambda)$ of the human eye. According to CIE recommendations the integration can be carried out by numerical summation at wavelength intervals $\Delta\lambda$ equal to $1\,$nm:[66]

$$X = k \sum_{380\text{nm}}^{780\text{nm}} \Phi(\lambda)\bar{x}(\lambda)\Delta\lambda \tag{A.11}$$

$$Y = k \sum_{380\text{nm}}^{780\text{nm}} \Phi(\lambda)\bar{y}(\lambda)\Delta\lambda \tag{A.12}$$

$$Z = k \sum_{380\text{nm}}^{780\text{nm}} \Phi(\lambda)\bar{z}(\lambda)\Delta\lambda \tag{A.13}$$

$$\tag{A.14}$$

The constant k is chosen in such a way that Y is 100 for the objects with $R(\lambda) = 100\%$ for all wavelength. Therefore, k derives to:

$$k = \frac{100}{\sum\limits_{380\text{nm}}^{780\text{nm}} I_{\text{spec}}(\lambda)\bar{y}(\lambda)\Delta\lambda} \tag{A.15}$$

For the CIE 1931 chromaticity diagram representing all natural colours in a 2-dimensional chart, the two normalised colour values x and y are used:

$$x = \frac{X}{X + Y + Z} \tag{A.16}$$

$$y = \frac{Y}{X + Y + Z} \tag{A.17}$$

The colour space specified by x, y, and Y, the relative luminance of the colour, is known as the CIE xyY or CIE 1931 colour space. The plot of the colour values x and y is given in Figure A.2. All pure spectral colours are located on a horseshoe shape curve (380–780\,nm). Due to its shape it is sometimes also named *horseshoe*

diagram. The line between the red (780 nm monochromatic radiation) and the blue (380 nm) corner is called the line of purples.
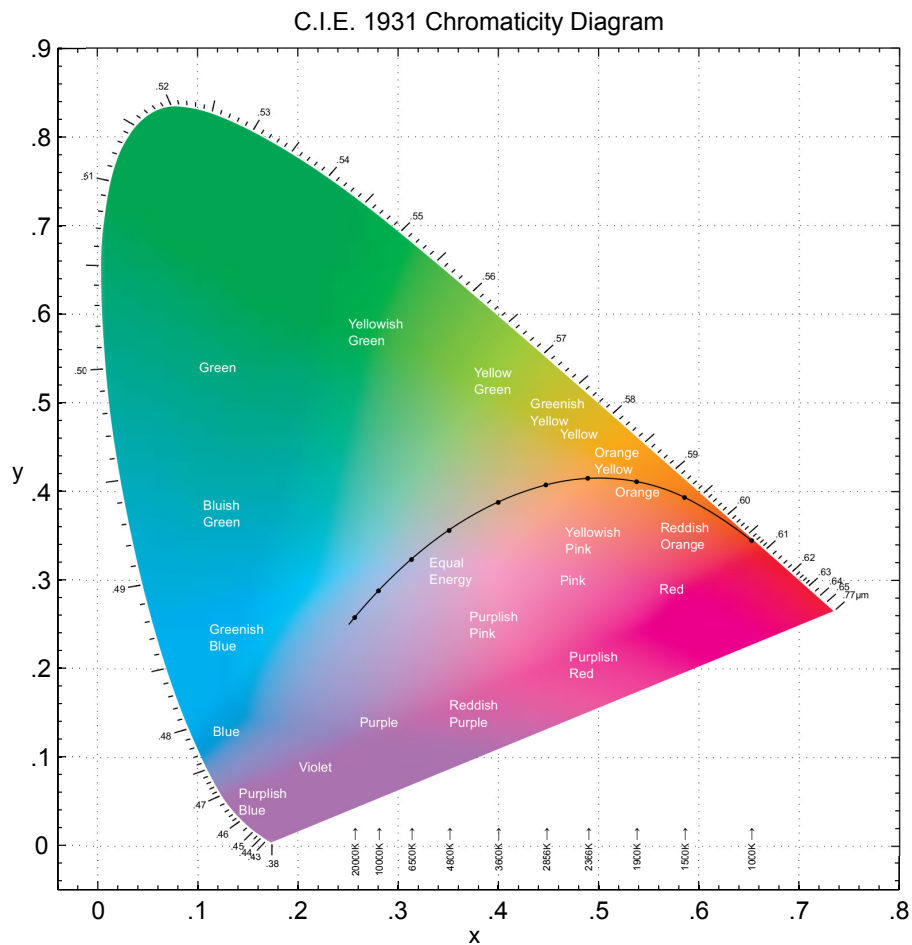

Figure A.2: CIE 1931 chromaticity diagram, also known as the *xyY* or CIE 1931 colour chart. All natural spectral colours (380–780 nm) are located on the horseshoe like curve. The bottom line located in between 380 nm and 780 nm is called *line of purples*. For a perfect white illuminant the white point is at $x = 0.33$ and $y = 0.33$. Depending of the colour temperature (indicated at the bottom of the graph) the white point move along the black-body curve (black curve). Natural daylight (CIE D$_{65}$) is close to the 6500 K white point. [133]

A.2.2 Uniform CIELAB colour space and colour distance

The more recent standard CIELAB ($L^*a^*b^*$ colour space) with D$_{65}$ as illuminant is more suitable for describing colour differences[67]. In the CIELAB system the a^*-axis describes the colours red to green and the b^*-axis the colours yellow to blue. Whereas L^* denotes the lightness of a colour. The values for L^*, a^* and b^* are derived mathematically from the tristimulus values X, Y, and Z using the CMFs of the CIE photometric observer having $10°$ visual field:[66]

$$L^* = 116 \cdot f\left(\frac{Y}{Y_N}\right) - 16 \tag{A.18}$$

$$a^* = 500 \cdot \left[f\left(\frac{X}{X_N}\right) - f\left(\frac{Y}{Y_N}\right)\right] \tag{A.19}$$

$$b^* = 200 \cdot \left[f\left(\frac{Y}{Y_N}\right) - f\left(\frac{Z}{Z_N}\right)\right] \tag{A.20}$$

where X, Y and Z are the colour tristimulus of the object colour and X_n, Y_n and Z_n are the tristimulus values of a perfect white diffuser illuminated with the same illuminant as the object. As in the CIE 1931 colour space Y_n is normalised to 100. The functions f are hereby calculated via

$$f(u) = u^{\frac{1}{3}} \quad \text{if} \quad u > \left(\frac{24}{116}\right)^3 \tag{A.21}$$

$$f(u) = \frac{841}{108}u + \frac{16}{116} \quad \text{if} \quad u \leq \left(\frac{24}{116}\right)^3 \tag{A.22}$$

where the argument u needs to be replaced by $\frac{X}{X_n}$, $\frac{Y}{Y_n}$, and $\frac{Z}{Z_n}$, respectively.

Figure A.3 plots the CIELAB colour charts for different lightness values L^*. It can be seen that the colour hue for the same colour coordinates a^* and b^* changes slightly with different L^*. However, for colours with small lightness difference $\Delta L^* < 10$, the a^*b^*-plane with a fix L^* remains close enough for a suitable colour representation. The colour distance between to colours in the CIELAB system is defined as[66]

$$\Delta E = \sqrt{(\Delta L^*)^2 + (\Delta a^*)^2 + (\Delta b^*)^2} \tag{A.23}$$

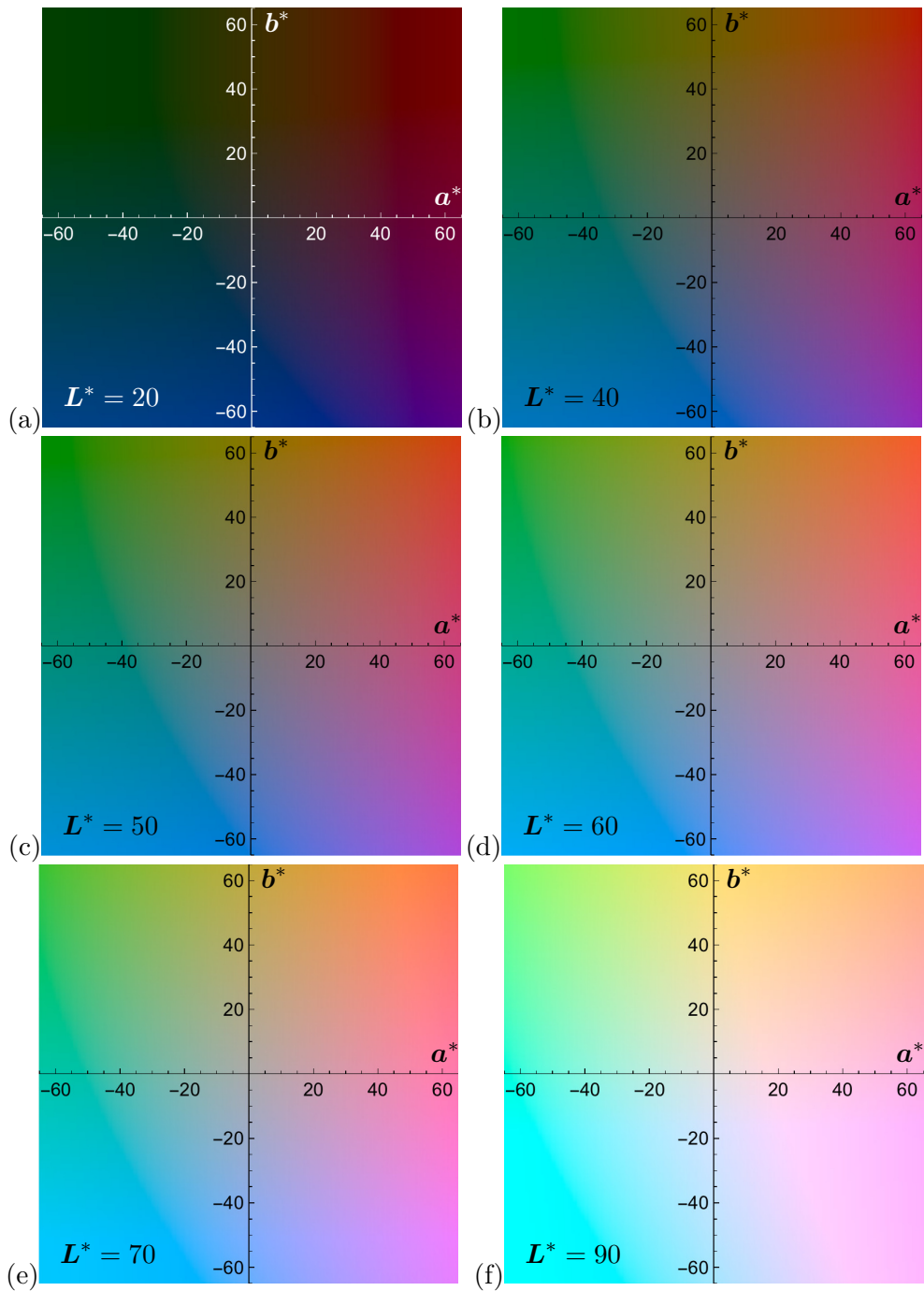which describes well how colour differences are observed by the human eye.

Figure A.3: Colour charts in the CIELAB (L^*, a^*, b^*) colour space for different lightness values L^*. The colour hue for the same coordinates in a^* and b^* changes slightly with L^*. However, for colours with $\Delta L^* < 10$ it remains close enough for a suitable colour representation in the a^*b^*-plane with a fix L^*.

B Interaction of Electromagnetic Waves with Matter

B.1 Maxwell equations

The Maxwell equations for a isotropic medium are:

$$
\begin{aligned}
\text{rot } \vec{H} &= \frac{d\vec{D}}{dt} + \vec{j} \\
\text{rot } \vec{E} &= -\frac{d\vec{B}}{dt} \\
\text{div } \vec{B} &= 0 \\
\text{div } \vec{D} &= \varrho
\end{aligned}
$$

with the material equations

$$
\begin{aligned}
\vec{D} &= \varepsilon\varepsilon_0 \vec{E} \\
\vec{B} &= \mu\mu_0 \vec{H} \\
\vec{j} &= \sigma\vec{E}
\end{aligned}
$$

with the electrical vector $\vec{E}$, the magnetic induction $\vec{B}$, the electrical displacement $\vec{D}$, the magnetic vector $\vec{H}$, the electrical current density $\vec{j}$, the electric charge density ϱ and the electrical conductivity σ. Using the material equations the first Maxwell equation can also be written as:

$$
\text{rot } \vec{H} = \varepsilon\varepsilon_0 \frac{d\vec{E}}{dt} + \sigma\vec{E} \tag{B.1}
$$

The electrical vector of a wave in general is:

$$\vec{E} = \vec{E_0} \exp i(\omega t - kx)$$

The derivative $\frac{d}{dt}$ of the electrical wave vector is:

$$\frac{d\vec{E}}{dt} = i\omega \vec{E}$$

By replacing $\vec{E}$ through this relation, the first Maxwell equation (B.1) it simplifies to:

$$\mathrm{rot}\ \vec{H} \quad = \quad \left(\varepsilon \varepsilon_0 + \frac{\sigma}{i\omega} \right) \frac{d\vec{E}}{dt}$$

If one compares this Maxwell equation with the one for insulators, it becomes clear that the only difference is, that the dielectric constant is complex. Therefore, the complex dielectric constant $\hat{\varepsilon}$ can be written as

$$\hat{\varepsilon} = \varepsilon' + i\varepsilon'' = \varepsilon - i\frac{\sigma}{\varepsilon_0 \omega} = (n - ik)^2 = N^2 \tag{B.2}$$

where n is the real refractive index and k the extinction coefficient.

B.2   Lorentz-oscillator model

The interaction between electromagnetic waves and insulating or dielectric materials can be described semi-classical by free oscillating electrons around static not moving atomic cores: the Lorentz oscillator model.[134] Hereby, the dielectric function is written as a sum of Lorentz oscillators:

$$\hat{\varepsilon} = 1 + \sum_{j=1}^{M} \frac{\tilde{f}_j}{\tilde{\omega}_{0j}^2 - \omega^2 - 2i\omega\Gamma_j} \tag{B.3}$$

By expanding the fraction and using the binomial function $(a - b) \cdot (a + b) = a^2 - b^2$ the above equation becomes:

$$\hat{\varepsilon} = 1 + \sum_{j=1}^{M} \frac{\tilde{f}_j \cdot (\tilde{\omega}_{0j}^2 - \omega^2 - 2i\omega\Gamma_j)}{(\tilde{\omega}_{0j}^2 - \omega^2)^2 + 4\omega^2\Gamma_j^2} \tag{B.4}$$

This can be separated in a real and an imaginary part:

$$\varepsilon = \varepsilon' = \operatorname{Re}\hat{\varepsilon} \;=\; (1 + \sum_{j=1}^{M} \frac{\tilde{f}_j \cdot (\tilde{\omega}_{0j}^2 - \omega^2)}{(\tilde{\omega}_{0j}^2 - \omega^2)^2 + 4\omega^2\Gamma_j^2} \tag{B.5}$$

$$\varepsilon'' = \operatorname{Im}\hat{\varepsilon} \;=\; \sum_{j=1}^{M} \frac{\tilde{f}_j \cdot 2\omega\Gamma_j}{(\tilde{\omega}_{0j}^2 - \omega^2)^2 + 4\omega^2\Gamma_j^2} \tag{B.6}$$

B.3   Sellmeier's and Cauchy's formluae

There are spectral regions where the dielectric function is almost real (see Figure B.1). This is the case when:[125]

$$(\omega_{0j} - \omega)^2 \gg \Gamma_j^2 \qquad \forall j \tag{B.7}$$

At this condition the Equation (B.3) can be simplified to

$$\varepsilon = \operatorname{Re}\hat{\varepsilon} \;\approx\; 1 + \sum_{j=1}^{M} \frac{\tilde{f}_j}{\tilde{\omega}_{0j}^2 - \omega^2} \tag{B.8}$$

$$\operatorname{Im}\hat{\varepsilon} \;=\; 0 \tag{B.9}$$

Using the relation

$$\omega = 2\pi \frac{c}{\lambda} \tag{B.10}$$

Equation (B.9) may be written as:

$$\varepsilon \;=\; 1 + \sum_{j=1}^{M} \frac{\tilde{f}_j}{4\pi^2 c^2} \cdot \frac{\lambda^2 \tilde{\lambda}_{j0}^2}{\lambda^2 - \tilde{\lambda}_{j0}^2} \tag{B.11}$$

Using

$$\frac{\lambda^2}{\lambda^2 - \tilde{\lambda}_{j0}^2} \equiv 1 + \frac{\tilde{\lambda}_{j0}^2}{\lambda^2 - \tilde{\lambda}_{j0}^2} \tag{B.12}$$

Equation (B.11) becomes:

$$\varepsilon = 1 + \sum_{j=1}^{M} \frac{\tilde{f}_j \tilde{\lambda}_{j0}^2}{4\pi^2 c^2} \cdot \left(1 + \frac{\tilde{\lambda}_{j0}^2}{\lambda^2 - \tilde{\lambda}_{j0}^2}\right) \tag{B.13}$$

$$= 1 + \underbrace{\sum_{j=1}^{M} \frac{\tilde{f}_j \tilde{\lambda}_{j0}^2}{4\pi^2 c^2}}_{=a} + \sum_{j=1}^{M} \underbrace{\frac{\tilde{f}_j \tilde{\lambda}_{j0}^4}{4\pi^2 c^2}}_{b_j} \cdot \frac{1}{\lambda^2 - \tilde{\lambda}_{j0}^2} \tag{B.14}$$

$$\varepsilon = 1 + a + \sum_{j=1}^{M} \frac{b_j}{\lambda^2 - \tilde{\lambda}_{j0}^2} \tag{B.15}$$

$$\tag{B.16}$$

This may also be written as

$$\varepsilon - 1 = n^2 - 1 = a + \sum_{j=1}^{M} \frac{b_j}{\lambda^2 - \tilde{\lambda}_{j0}^2} \tag{B.17}$$

which is known as Sellmeier's dispersion formula.
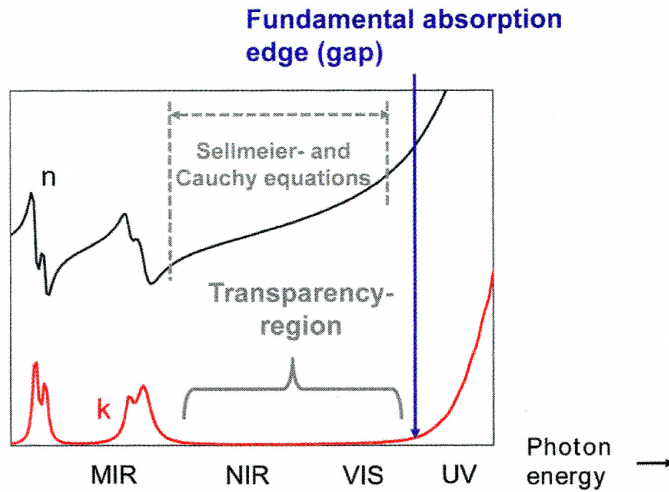
Figure B.1: Principle scheme of refractive index $n(\lambda)$ and the extinction coefficient $k(\lambda)$ versus the wavelength (photon energy) for insulating materials described by a multi-oscillator model. Furthermore the graph indicates the spectral region where Sellmeier and Cauchy equations can be applied. Source: STENZEL [135]

Another approach is to expand Sellmeier's dispersion formula (Equation (B.17)) by a power series

$$n^2(\lambda) = 1 + a - \sum_{\tilde{\lambda}_{0j} > \lambda} \frac{b_j}{\tilde{\lambda}_{j0}^2 - \lambda^2} + \sum_{\tilde{\lambda}_{0j} < \lambda} \frac{b_j}{\lambda^2 - \tilde{\lambda}_{j0}^2} \tag{B.18}$$

where the long-wavelength resonances are covered by the first sum and the short-wavelength ones by the second one. The two sums are now expanded into a power series of $(\lambda/\tilde{\lambda}_{0j})^2$ for the first and of $(\lambda/\tilde{\lambda}_{0j})^{-2}$ for the second, by the means of:

$$\frac{1}{1-x} = 1 + x + x^2 + x^3 + \cdots \tag{B.19}$$

For this the sums are rewrite as follows:

$$n^2(\lambda) = 1 + a - \sum_{\tilde{\lambda}_{0j} > \lambda} \frac{b_j \cdot \tilde{\lambda}_{0j}^{-2}}{1 - \frac{\lambda^2}{\tilde{\lambda}_{j0}^2}} + \sum_{\tilde{\lambda}_{0j} < \lambda} \frac{b_j \cdot \lambda^{-2}}{1 - \frac{\tilde{\lambda}_{j0}^2}{\lambda^2}} \tag{B.20}$$

The power series for the first sum of Equation (B.20) is

$$\sum_{\tilde{\lambda}_{0j} > \lambda} \frac{b_j \cdot \tilde{\lambda}_{0j}^{-2}}{1 - \frac{\lambda^2}{\tilde{\lambda}_{j0}^2}} = \sum_{\tilde{\lambda}_{0j} > \lambda} b_j \cdot \tilde{\lambda}_{0j}^{-2} \cdot \left(1 + \frac{\lambda^2}{\tilde{\lambda}_{j0}^2} + \left(\frac{\lambda^2}{\tilde{\lambda}_{j0}^2}\right)^2 + \left(\frac{\lambda^2}{\tilde{\lambda}_{j0}^2}\right)^3 + \cdots\right)$$

$$= \sum_{\tilde{\lambda}_{0j} > \lambda} (a_j + b_j\lambda^2 + c_j\lambda^4 + d_j\lambda^6 + \cdots) \tag{B.21}$$

and for the second sum:

$$\sum_{\tilde{\lambda}_{0j} < \lambda} \frac{b_j \cdot \lambda^{-2}}{1 - \frac{\tilde{\lambda}_{j0}^2}{\lambda^2}} = \sum_{\tilde{\lambda}_{0j} < \lambda} b_j \cdot \lambda^{-2} \left(1 + \left(\frac{\lambda}{\tilde{\lambda}_{0i}}\right)^{-2} + \left(\frac{\lambda}{\tilde{\lambda}_{0i}}\right)^{-4} + \left(\frac{\lambda}{\tilde{\lambda}_{0i}}\right)^{-6} + \cdots\right)$$

$$= \sum_{\tilde{\lambda}_{0j} < \lambda} (b'_j\lambda^{-2} + c'_j\lambda^{-4} + d'_j\lambda^{-6} + \cdots) \tag{B.22}$$

By replacing the sums by the just determined power series, Equation (B.20) becomes

$$n^2(\lambda) = A + B\lambda^{-2} + C\lambda^{-4} + \cdots - B'\lambda^2 - C'\lambda^4 - \cdots \tag{B.23}$$

where A, B, C, ... are new constants. This is called Cauchy's dispersion formula.

C Window Test Bench for Angular-Dependent Measurements

The Window Test Bench was developed by the University of Basel to characterise the optical properties of real-size insulating windows for different angles of light incidence.[70] In contrast to a conventional spectrophotometer with an Ulbrichts sphere, the light path is reversed: A diffuse light source produces a homogeneous radiation from all possible directions (from normal until close to 90°) of which one single light path (normal to light source) is selected by the collimator on the detector side. Figure C.1 shows a photograph from the inside of the light source showing the halogen light bulbs and one of the light-diffusing glass panels, which are both duplicated multiple times by aluminium mirrors.

In the framework of this doctoral thesis the equipment was moved from Basel to LESO-PB at EPFL. For the move, the relatively large system had to be dismounted. Therefore, an entire re-alignment of the optical system was necessary after the re-installation and a new calibration of the diffuse light source. Figure C.2 plots the relative light intensity of the source versus the horizontal position on the source for different wavelengths. In the 30-cm-centre area the source intensity variation is less then 4 % for VIS–NIR range and for the UV range better then 10 %.

The photograph in Figure C.3 shows the Window Test Bench setup at EPFL after fully re-aligning and calibrating the system. In the background of the picture the light source is visible behind a mounted sun protection glass (SPG). On the screen in the foreground the measured transmittance of the SPG is plotted for 0° to 75° light incidence.
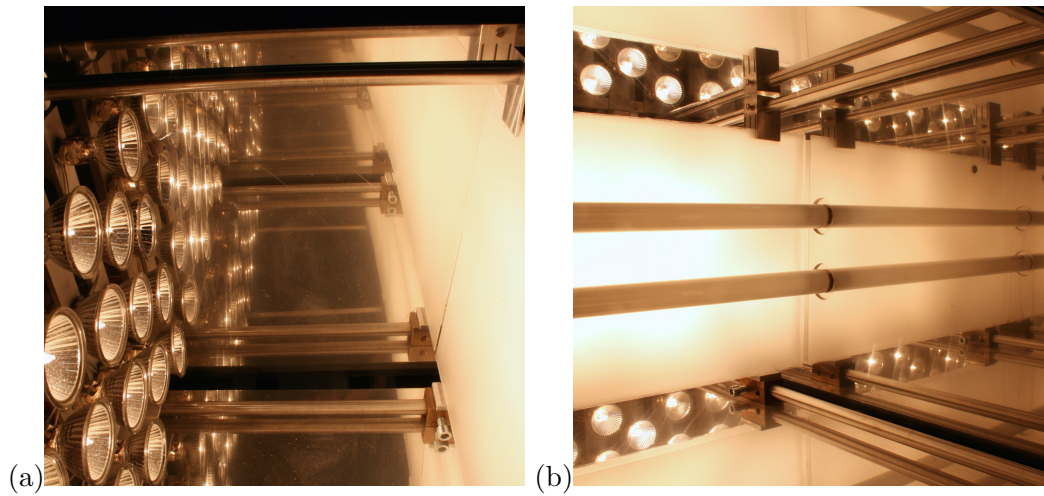
Figure C.1: (a) View to the inside of the diffuse light source of the Window Test Bench. Aluminium mirrors extend the source to quasi infinity. Double-side etched glass panels (on the right sight of the photograph) diffuse the radiation from the halogen bulbs. (b) In front of the first diffusing panel two fluorescent tubes providing UV radiation are installed followed by another two light diffusers (not shown in the picture).
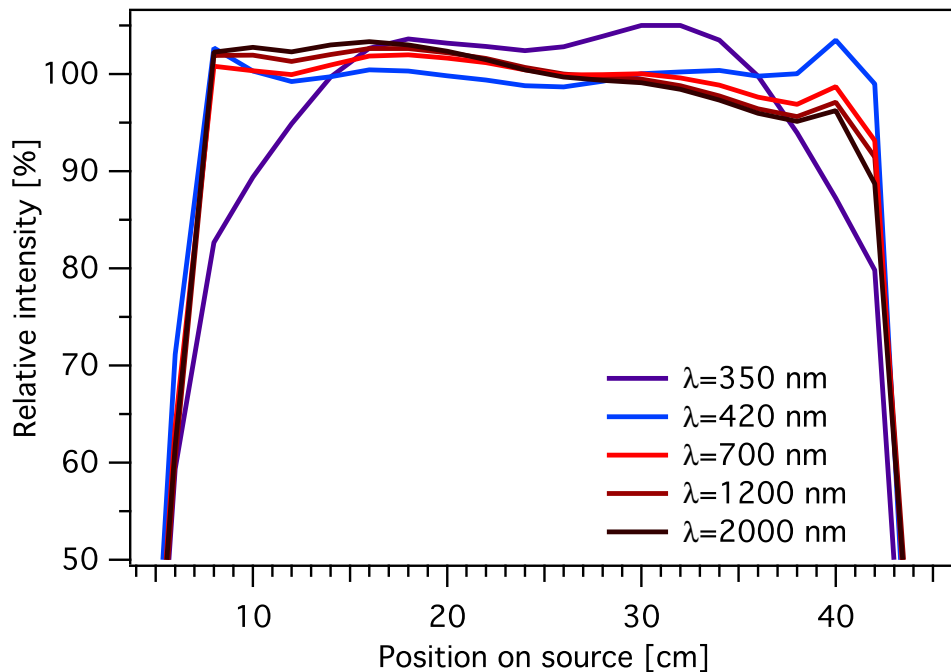

Figure C.2: Relative light intensity of the diffuse light source measured at collimator distance. The difference of intensity between the position 10 and 40 cm is better then 4% for VIS–NIR and better then 10% for the UV.
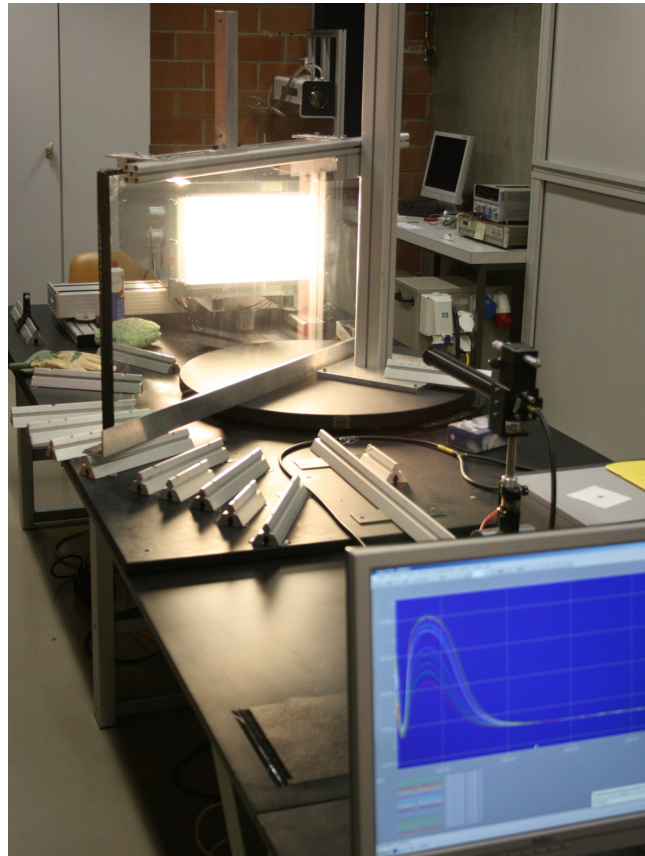
Figure C.3: Photograph of the Window Test Bench for angular-dependent transmittance and reflectance measurements of real-size glazing after being moved to EPFL and re-calibrated.
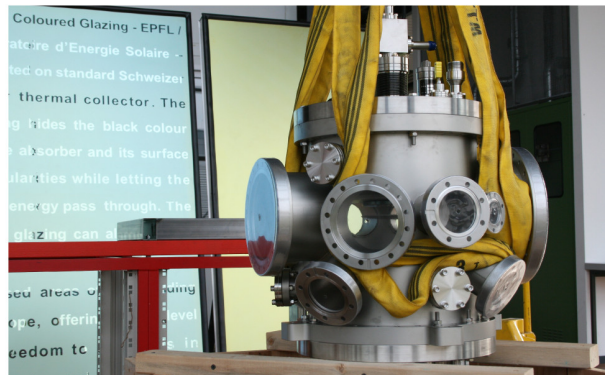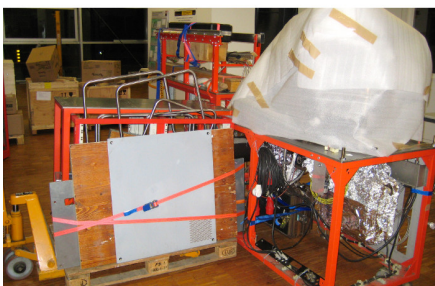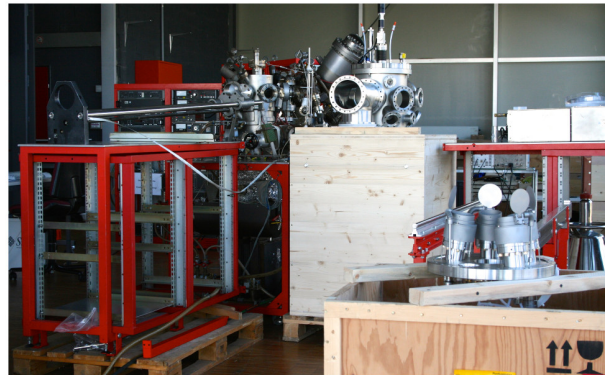
D An Unexpected (Long) Journey of an ESCA

ESCA moves and refurbishment (November 2009 to September 2011).
1. From the Department of Physics of the University of Basel to the LESO-PB, EPFL
2. From LESO-PB, EPFL to GC A, EPFL
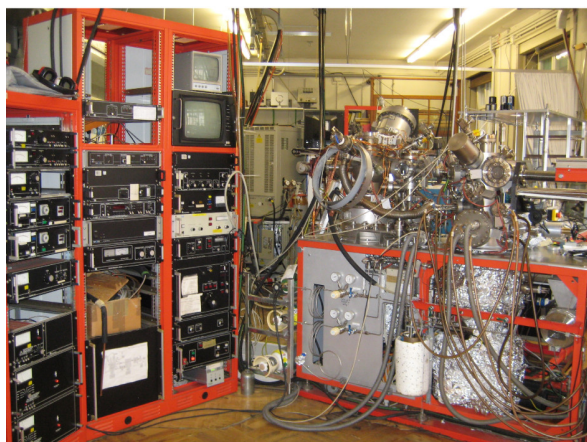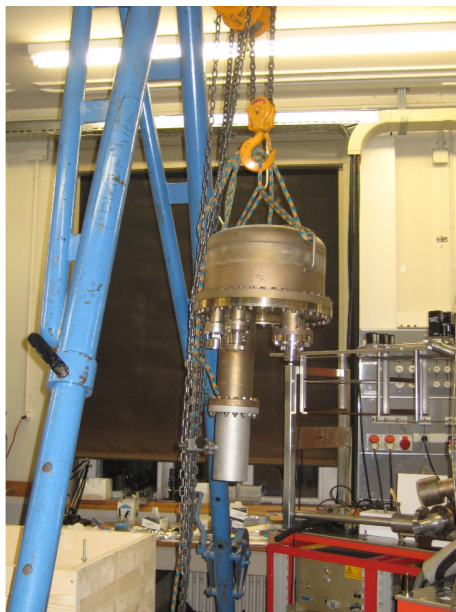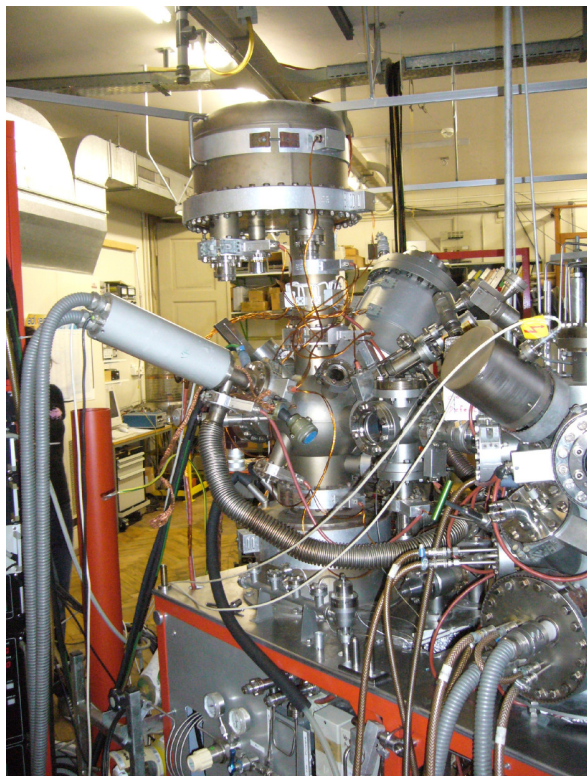
Preparing of ESCA move (Basel–Lausanne, November and December 2009) and separate transport of the sensitive energy analyser.

ESCA move (Basel–Lausanne, December 2009), including unpacking (January to February 2010) and assembling of sputtering chamber (March to May 2010).
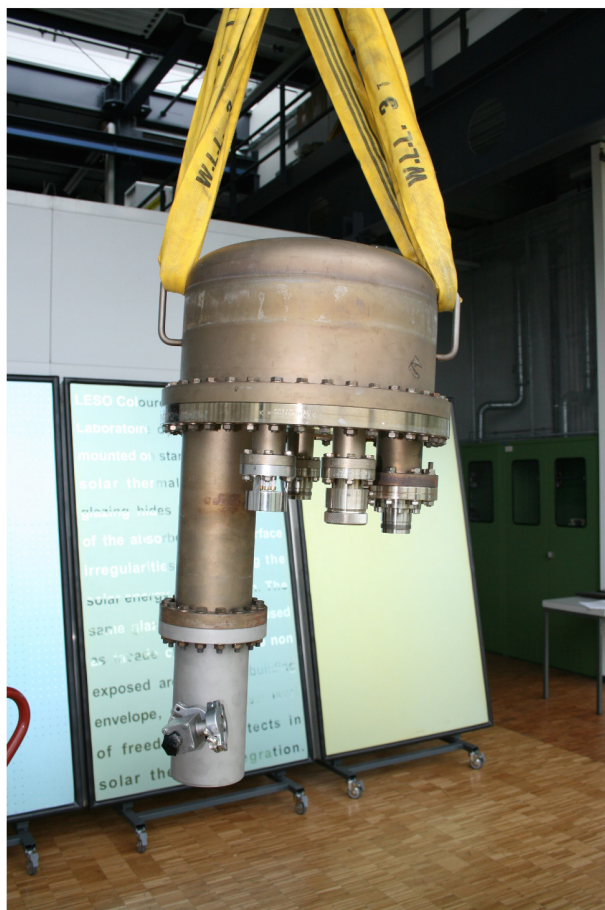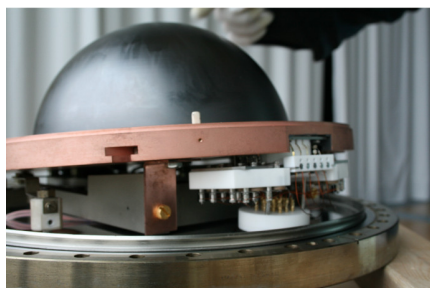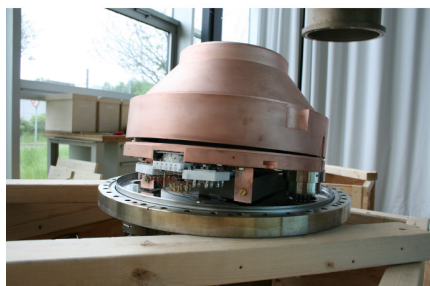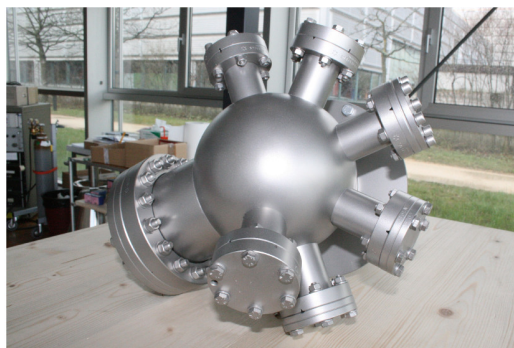
ESCA refurbishment and re-alignment of photoelectron energy analyser at LESO-PB (March to May 2010).

ESCA refurbishment at LESO-PB, re-installing the aligned energy analyser, and first reference spectrum before christmas (May to December 2010).
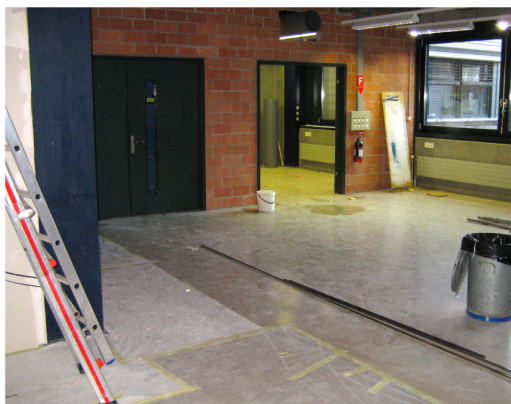
Construction of new laboratory and preparing of 2nd ESCA move from EPFL LESO-PB to EPFL GC A (Februar to September 2011).
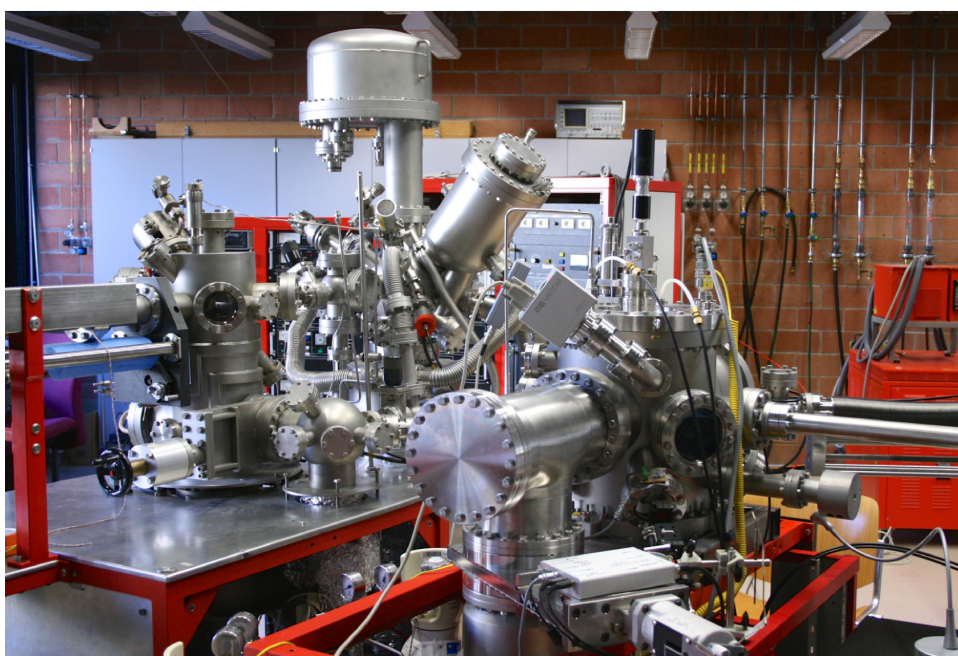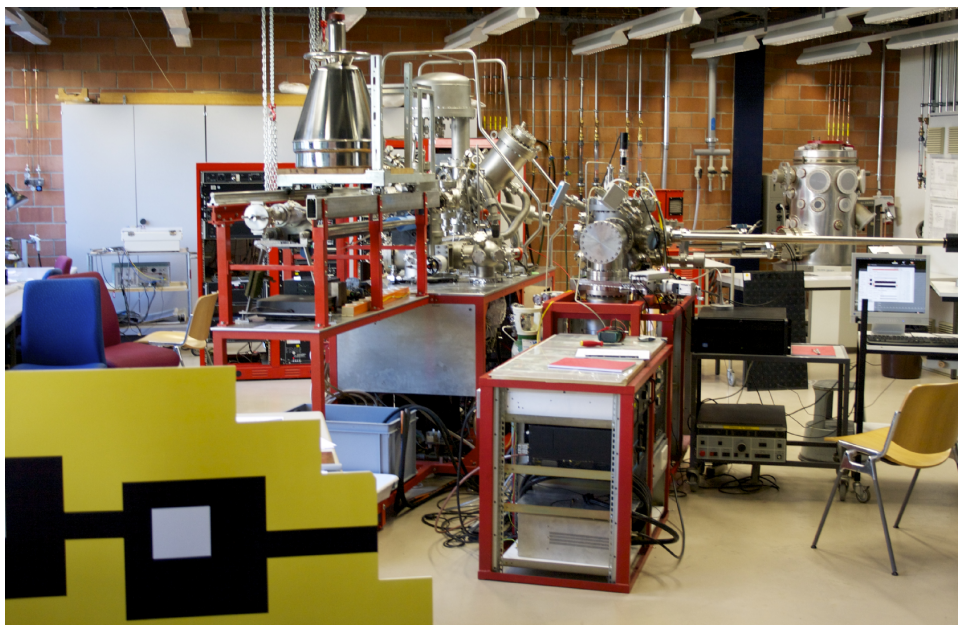
Inauguration of ESCA and new laboratory at EPFL GC A (September 2011).

Bibliography

[1] John A. Duffie and William A. Beckmann, editors. *Solar Engineering of Thermal Processes.* John Wiley & Sons, Hoboken, 4th editio edition, 2013.

[2] S. A. Kalogirou. Solar thermal collectors and applications. *Prog. Energy Combust. Sci.*, 30(3):231–295, 2004.

[3] Martin A. Green, Keith Emery, Yoshihiro Hishikawa, Wilhelm Warta, and Ewan D. Dunlop. Solar cell efficiency tables (version 39). *Prog. Photovoltaics Res. Appl.*, 20:12–20, 2012.

[4] A. G. Hestnes. Building Integration Of Solar Energy Systems. *Sol. Energy*, 67 (4-6):181–187, 1999.

[5] Hans-Martin Henning, editor. *Solar-Assisted Air-Conditioning in Buildings.* Springer-Verlag Wien New York, Wien, 2nd revise edition, 2007.

[6] Rémi Charron and Andreas Athienitis. Design and Optimization of Net Zero Energy Solar Homes. *ASHRAE Trans.*, 112(2):285–296, 2006.

[7] Werner Weiss, editor. *Solar heating systems for houses: a design handbook for solar combisystems.* James & James (Science Publisher) Ltd, London, 2003.

[8] M. C. Munari Probst and C. Roecker. *Architectural Integration and Design of Solar Thermal Systems.* EPFL Press, Lausanne, 2011.

[9] Roland Krippner and Thomas Herzog. Architectural Aspects of Solar Techniques. Studies on the Integration of Solar Energy Systems into the Building Skin. In *Eurosun 2000. Visions New Millenn. 3th ISES-Europe Sol. Congr.*, Copenhagen, 2000. International Solar Energy Society.

[10] Martin Joly. *Développement et optimisation de revêtements minces nanostructurés pour capteurs solaires thermiques et modules photovoltaïques*. PhD thesis, École Polytechnique Fédérale de Lausanne, 2012.

[11] M. C. Munari Probst and C. Roecker. Towards an improved architectural quality of building integrated solar thermal systems (BIST). *Sol. Energy*, 81 (9):1104–1116, September 2007.

[12] S. Kalogirou, Y. Tripanagnostopoulos, and M. Souliotis. Performance of solar systems employing collectors with colored absorber. *Energy Build.*, 37(8):824–835, August 2005.

[13] Y. Tripanagnostopoulos, M. Souliotis, and Th. Nousia. Solar collectors with colored absorbers. *Sol. Energy*, 68(4):343–356, 2000.

[14] Z. Crnjak Orel, M. Klanjšek Gunde, and M. G. Hutchins. Spectrally selective solar absorbers in different non-black colours. *Sol. Energy Mater. Sol. Cells*, 85:41–50, June 2004.

[15] Anca Duta, Luminita Isac, Andrea Milea, Elena Ienei, and Dana Perniu. Coloured Solar-thermal Absorbers – A Comparative Analysis of Cermet Structures. *Energy Procedia*, 48:543–553, 2014.

[16] Dechun Zhu and Shuxi Zhao. Chromaticity and optical properties of colored and black solar–thermal absorbing coatings. *Sol. Energy Mater. Sol. Cells*, 94 (10):1630–1635, October 2010.

[17] A. Schüler, C. Roecker, J.-L. Scartezzini, J. Boudaden, I. R. Videnovic, R. S.-C. Ho, and P. Oelhafen. On the feasibility of colored glazed thermal solar collectors based on thin film interference filters. *Sol. Energy Mater. Sol. Cells*, 84(1-4):241–254, October 2004.

[18] J. Boudaden. *Multilayer Films for Coloured Glazed Solar Collectors*. Phd thesis, University of Basel, 2009.

[19] A. Schüler, C. Roecker, J. Boudaden, P. Oelhafen, and J.-L. Scartezzini. Potential of quarterwave interference stacks for colored thermal solar collectors. *Sol. Energy*, 79(2):122–130, August 2005.

[20] C. Roecker, M. C. Munari Probst, E. de Chambrier, A. Schüler, and J.-L. Scartezzini. Façade Integration of Solar Thermal Collectors : A Breakthrough. In *Proc. ISES World Congr. 2007 (Vol. I – Vol. V)*, pages 337–341, 2009.

[21] A. Schüler, D. Dutta, E. de Chambrier, C. Roecker, G. De Temmerman, P. Oelhafen, and J.-L. Scartezzini. Sol-gel deposition and optical characterization of multilayered SiO2/Ti1-xSixO2 coatings on solar collector glasses. *Sol. Energy Mater. Sol. Cells*, 90(17):2894–2907, November 2006.

[22] J. Boudaden, R. S.-C. Ho, P. Oelhafen, A. Schüler, C. Roecker, and J.-L. Scartezzini. Towards coloured glazed thermal solar collectors. *Sol. Energy Mater. Sol. Cells*, 84(1-4):225–239, October 2004.

[23] J. Boudaden, P. Oelhafen, A. Schüler, C. Roecker, and J.-L. Scartezzini. Multi-layered Al2O3/SiO2 and TiO2/SiO2 coatings for glazed colored solar thermal collectors. *Sol. Energy Mater. Sol. Cells*, 89(2-3):209–218, November 2005.

[24] H. K. Pulker. Characterization of optical thin films. *Appl. Opt.*, 18(12):1969–77, June 1979.

[25] G. Bräuer, J. Szczyrbowski, and G. Teschner. New approaches for reactive sputtering of dielectric materials on large scale substrates. *J. Non. Cryst. Solids*, 218:19–24, September 1997.

[26] N. Kaiser and H. Pulker, editors. *Optical Interference Coatings*. Springer, Berlin, 2003.

[27] S. M. Edlou, A. Smajkiewicz, and G. A. Al-Jumaily. Optical properties and environmental stability of oxide coatings deposited by reactive sputtering. *Appl. Opt.*, 32(28):5601–5, October 1993.

[28] J. M. Ngaruiya, S. Venkataraj, R. Drese, O. Kappertz, T. P. Leervad Pedersen, and M. Wuttig. Preparation and characterization of tantalum oxide films produced by reactive DC magnetron sputtering. *Phys. Status Solidi*, 198(1): 99–110, July 2003.

[29] H. Szymanowski, O. Zabeida, J. E. Klemberg-Sapieha, and L. Martinu. Optical properties and microstructure of plasma deposited Ta2O5 and Nb2O5 films. *J. Vac. Sci. Technol. A Vacuum, Surfaces, Film.*, 23(2):241, 2005.

[30] Jessica Gene Sandland. *Sputtered Silicon Oxynitride for Microphotonics: A Materials Study*. PhD thesis, Massachusetts Institute of Technology, 2005.

[31] Vivekanand Bhatt and Sudhir Chandra. Silicon Nitride Films Deposited by RF Sputtering for Microstructure Fabrication in MEMS. *J. Electron. Mater.*, 38(9):1979–1989, June 2009.

[32] M. J. Dodge. Refractive properties of magnesium fluoride. *Appl. Opt.*, 23(12): 1980, June 1984.

[33] H. Agnus Macleod. *Thin-Film Optical Filters*. Institute of Physics Publishing, Bristol and Philadelphia, London, 3. edition edition, 2001.

[34] Irving H. Malitson. A Redetermination of Some Optical Properties of Calcium Fluoride. *Appl. Opt.*, 2(11):1103–1107, 1963.

[35] E. Ritter. Optical film materials and their applications. *Appl. Opt.*, 15(10): 2318–27, October 1976.

[36] D.-H. Kuo and K.-H. Tzeng. Characterization and properties of r.f.-sputtered thin films of the alumina-titania system. *Thin Solid Films*, 460(1-2):327–334, July 2004.

[37] P. Oelhafen and A. Schüler. Nanostructured materials for solar energy conversion. *Sol. Energy*, 79(2):110–121, August 2005.

[38] R. Rabady and I. Avrutsky. Titania, silicon dioxide, and tantalum pentoxide waveguides and optical resonant filters prepared with radio-frequency magnetron sputtering and annealing. *Appl. Opt.*, 55(3):378–383, 2005.

[39] E. de Chambrier, D. Dutta, C. Roecker, M. C. Munari Probst, J.-L. Scartezzini, and A. Schüler. Nanostructured Coatings on Glazing for Active Solar Façades. In *CISBAT 2007*, pages 527–532, 2007.

[40] L. Liljeholm, T. Nyberg, T. Kubart, A. Roos, and S. Berg. Reactive sputtering of SiO2–TiO2 thin film from composite Six/TiO2 targets. *Vacuum*, 85(2): 317–321, August 2010.

[41] Suman Singh, Rajinder Singh Deol, M.L. Singla, and D.V.S. Jain. Light harvesting efficiency of hybrid nano-composite for photovoltaic application. *Sol. Energy Mater. Sol. Cells*, 128:231–239, September 2014.

[42] Georg Hass and Elmar Ritter. Optical Film Materials and Their Applications. *J. Vac. Sci. Technol.*, 4(2):71, March 1967.

[43] K. Lau, J. Weber, H. Bartzsch, and P. Frach. Reactive pulse magnetron sputtered SiOxNy coatings on polymers. *Thin Solid Films*, 517(10):3110–3114, March 2009.

[44] R. Laird and A. Belkind. Cosputtered films of mixed TiO2/SiO2. *J. Vac. Sci. Technol. A Vacuum, Surfaces, Film.*, 10(4):1908, July 1992.

[45] Dan Leng, Lili Wu, Hongchao Jiang, Yu Zhao, Jingquan Zhang, Wei Li, and Lianghuan Feng. Preparation and Properties of SnO2 Film Deposited by Magnetron Sputtering. *Int. J. Photoenergy*, 2012:1–6, 2012.

[46] Detlev Ristau, Winfried Arens, Salvador Bosch, Angela Duparre, Enrico Masetti, Damien Jacob, George Kiriakidis, Francesca Peiro, Etienne Quesnel, and Alexander V. Tikhonravov. UV-Optical and Microstructural Properties of MgF2-Coatings Deposited by IBS and PVD Processes. In Claude Amra and H. Angus Macleod, editors, *SPIE 3738, Adv. Opt. Interf. Coatings*, number May, pages 436–445, September 1999.

[47] Hannes Krüger, Erhard Kemnitz, Andreas Hertwig, and Uwe Beck. Transparent MgF2-films by sol–gel coating: Synthesis and optical properties. *Thin Solid Films*, 516(12):4175–4177, April 2008.

[48] Shinobu Fujihara, Yasuhiro Kadota, and Toshio Kimura. Role of Organic Additives in the Sol-Gel Synthesis of Porous CaF2 Anti-Reflective Coatings. *J. Sol-Gel Sci. Technol.*, 24(2):147–154, 2002.

[49] Tero Pilvi, Kai Arstila, Markku Leskelä, and Mikko Ritala. Novel ALD process for depositing CaF2 thin films. *Chem. Mater.*, 19(9):3387–3392, 2007.

[50] J. T. Cox, G. Hass, and A. Thelen. Triple-Layer Antireflection Coatings on Glass for the Visible and Near Infrared. *J. Opt. Soc. Am.*, 52(9):965, 1962.

[51] Chunrong Xue, Kui Yi, Chaoyang Wei, Jianda Shao, and Zhengxiu Fan. Determination of optical constants in the VUV range for fluoride thin films. In *SPIE 3283, 4th Int. Symp. Adv. Opt. Manuf. Test. Technol. Opt. Test Meas. Technol. Equip.*, volume 7283, pages 72831E1–8, 2009.

[52] I. Porqueras and E. Bertran. Electrochromic behaviour of nickel oxide thin films deposited by thermal evaporation. *Thin Solid Films*, 399:41–44, 2001.

[53] J. E. Klemberg-Sapieha, J. Oberste-Berghaus, L. Martinu, R. Blacker, I. Stevenson, G. Sadkhin, D. Morton, S. McEldowney, R. Klinger, P. J. Martin, N. Court, S. Dligatch, M. Gross, and R. P. Netterfield. Mechanical characteristics of optical coatings prepared by various techniques: a comparative study. *Appl. Opt.*, 43(13):2670–9, May 2004.

[54] A. Billard and C. Frantz. Recent Results on Reactive Magnetron Sputtering for High-Rate Deposition of Ceramic Compound Films. *Mater. Sci. Forum*, 288:107–117, 1998.

[55] Z. S. Khalifa, H. Lin, and S. Ismat Shah. Structural and electrochromic properties of TiO2 thin films prepared by metallorganic chemical vapor deposition. *Thin Solid Films*, 518(19):5457–5462, July 2010.

[56] W. Que, Z. Sun, Y. Zhou, Y. L. Lam, Y. C. Chan, and C. H. Kam. Optical and mechanical properties of TiO2/SiO2/organically modified silane composite films prepared by sol-gel processing. *Thin Solid Films*, 359:177–183, 2000.

[57] M. List, C. Melde, J. Strümpfel, and C. Illgen. Fully automated inline sputtering for optical coatings. *Proc. SPIE*, 5250:414–422, 2004.

[58] Alan E. Delahoy, Liangfan Chen, Masud Akhtar, Baosheng Sang, and Sheyu Guo. New technologies for CIGS photovoltaics. *Sol. Energy*, 77(6):785–793, December 2004.

[59] Hans Joachim Gläser. *Dünnfilmtechnologie auf Flachglas*. Verlag Karl Hofmann, Schorndorf, 1999.

[60] G. Bräuer, B. Szyszka, M. Vergöhl, and R. Bandorf. Magnetron sputtering – Milestones of 30 years. *Vacuum*, 84(12):1354–1359, June 2010.

[61] C. Blawert and B.L. Mordike. Industrial applications of plasma immersion ion implantation. *Surf. Coatings Technol.*, 93(2-3):274–279, September 1997.

[62] S. Matthews, W. Debosscher, A. Blondeel, J. Vanholsbeke, and H. Delrue. New target materials for innovative applications on glass. *Vacuum*, 83(3):518–521, October 2008.

[63] Walter Greulich, editor. *Lexikon der Phyik in sechs Bänden: Band 2*. Spektrum Akademischer Verlag GmbH Heidelberg, Heidelberg, Berlin, 1999.

[64] John David Jackson. *Classical Electrodynamics*. John Wiley & Sons, third edition, 1999.

[65] A. Schüler, J. Boudaden, P. Oelhafen, E. de Chambrier, C. Roecker, and J.-L. Scartezzini. Thin film multilayer design types for colored glazed thermal solar collectors. *Sol. Energy Mater. Sol. Cells*, 89(2-3):219–231, November 2005.

[66] János Schanda, editor. *COLORIMETRY, Understanding the CIE System*. John Wiley & Sons, 2007.

[67] A. E. Yakuninskaya and M. M. Seredenko. Using colorimetric characteristics in developing colored optical glasses. II. Diffusely reflecting neutral glasses. *J. Opt. Technol.*, 66:608–613, 1999.

[68] Iris Mack. *Development of Innovative Coatings for Sun Protection Glasses Based on the Theory of the Optimal Spectral Transmittance*. PhD thesis, University of Basel, 2008.

[69] P. A. van Nijnatten. Optical analysis of coatings by variable angle spectrophotometry. *Thin Solid Films*, 516:4553–4557, 2008.

[70] R. Steiner, P. Oelhafen, G. Reber, and A. Romanyuk. Experimental Determination of Spectral and Angular Dependent Optical Properties of Insulating Glasses. In *CISBAT 2005*, pages 441 – 446, 2005.

[71] A. Röseler. *Infrared Spectroscopic Ellipsometry*. Akademie-Verlag, Berlin, 1990.

[72] Ch.-H. Chou and T.-L. Wu. Embedding color watermarks in color images. In *2001 IEEE Fourth Work. Multimed. Signal Process. (Cat. No.01TH8564)*, pages 327–332. IEEE, 2001.

[73] Stefan Mertin, Virginie Hody-Le Caër, Martin Joly, Iris Mack, Peter Oelhafen, Jean Louis Scartezzini, and Andreas Schüler. Reactively sputtered coatings on architectural glazing for coloured active solar thermal façades. *Energy Build.*, 68:764–770, 2014.

[74] G. Bräuer. Large area glass coating. *Surf. Coatings Technol.*, 112:358–365, 1999.

[75] J. Szczyrbowski, G. Bräuer, G. Teschner, and A. Zmelty. Large-scale antireflective coatings on glass produced by reactive magnetron sputtering. *Surf. Coatings Technol.*, 98:1460–1466, 1998.

[76] G. A. Niklasson, C. G. Granqvist, and O. Hunderi. Effective medium models for the optical properties of inhomogeneous materials. *Appl. Opt.*, 20(1):26–30, January 1981.

[77] Ping Sheng. Theory for the Dielectric Function of Granular Composite Media. *Phys. Rev. Lett.*, 45(1):60–63, 1980.

[78] André Anders. Plasma and ion sources in large area coating: A review. *Surf. Coatings Technol.*, 200(5-6):1893–1906, November 2005.

[79] W. Robert Sinclair and F. G. Peters. Method for Controlled Multicomponent Sputtering. *Rev. Sci. Instrum.*, 33(7):744, 1962.

[80] Michael A. Russak, Christopher V. Jahnes, and Eric P. Katz. Reactive magnetron sputtered zirconium oxide and zirconium silicon oxide thin films. *J. Vac. Sci. Technol. A Vacuum, Surfaces, Film.*, 7(3):1248, May 1989.

[81] Stefan Bruns, Michael Vergöhl, Oliver Werner, and Till Wallendorf. High rate deposition of mixed oxides by controlled reactive magnetron-sputtering from metallic targets. *Thin Solid Films*, 520(12):4122–4126, April 2012.

[82] Brian Chapman. *Glow Discharge Processes*. John Wiley & Sons, New York, Chichester, Brisbane, Toronto, Singapore, 1980.

[83] Marcel Goossens. *An Introduction to Plasma Astrophysics and Magnetohydrodynamics.* Kluwer Academic Publishers, Dordrecht, Boston, London, 2003.

[84] S. M. Rossnagel. Thin film deposition with physical vapor deposition and related technologies. *J. Vac. Sci. Technol. A Vacuum, Surfaces, Film.*, 21(5): S74–S87, 2003.

[85] John A. Thornton. Substrate heating in cylindrical magnetron sputtering sources. *Thin Solid Films*, 54(1):23–31, October 1978.

[86] O. Almén and G. Bruce. Collection and sputtering experiments with noble gas ions. *Nucl. Instruments Methods*, 11:257–278, January 1961.

[87] Nils Laegreid and G. K. Wehner. Sputtering Yields of Metals for Ar+ and Ne+ Ions with Energies from 50 to 600 eV. *J. Appl. Phys.*, 32(3):365–369, 1961.

[88] J. H. Keller and R. G. Simmons. Sputtering Process Model of Deposition Rate. *IBM J. Res. Dev.*, 23(1):24–32, January 1979.

[89] Alain Billard and Frédéric Perry. Pulvérisation cathodique magnétron, 2005.

[90] Robert K. Waits. Planar magnetron sputtering. *J. Vac. Sci. Technol.*, 15(2): 179–187, March 1978.

[91] Ronald A. Powell and Stephen M. Rossnagel. *PVD for Microelectronics: Sputter Deposition Applied to Semiconductor Manufacturing.* Academic Press, San Diego, 1999.

[92] T. Kubart, O. Kappertz, T. Nyberg, and S. Berg. Dynamic behaviour of the reactive sputtering process. *Thin Solid Films*, 515(2):421–424, October 2006.

[93] D. C. Carter, R. L. Arent, and D. J. Christie. Sputter Process Enhancement through Pulsed-dc Power. In *50th Annu. Tech. Conf. Proc.*, pages 210–215. Society of Vacuum Coaters, 2007.

[94] A. Billard and C. Frantz. Low-frequency modulation of pulsed d.c. or r.f. discharges for controlling the reactive magnetron sputtering process. *Surf. Coatings Technol.*, 87:722–727, 1996.

[95] D. Guerin and S. Ismat Shah. Reactive-sputtering of titanium oxide thin films. *J. Vac. Sci. Technol. A Vacuum, Surfaces, Film.*, 15(3):712, May 1997.

[96] H. Tomaszewski, H. Poelman, D. Depla, D. Poelman, R. De Gryse, G. Heynderickx, and G. B. Marin. TiO2 films prepared by DC magnetron sputtering from ceramic targets. *Vacuum*, 68(1):31–38, October 2002.

[97] A. Schüler and P. Oelhafen. In situ core-level and valence-band photoelectron spectroscopy of reactively sputtered titanium aluminum nitride films. *Phys. Rev. B*, 63(11):1–8, March 2001.

[98] A. Romanyuk and P. Oelhafen. Oxidation of vanadium with reactive oxygen plasma: A photoelectron spectroscopy study of the initial stages of the oxide growth process. *Thin Solid Films*, 515(16):6544–6547, June 2007.

[99] A. Romanyuk, R. Steiner, I. Mack, P. Oelhafen, and D. Mathys. Growth of thin silver films on silicon oxide pretreated by low temperature argon plasma. *Surf. Sci.*, 601(4):1026–1030, February 2007.

[100] Stefan Hüfner. *Photoelectron Spectroscopy: priciples and applications.* Springer, Berlin, 1996.

[101] L. Martinu, H. Biederman, and L. Holland. Thin films prepared by sputtering MgF2 in an rf planar magnetron. *Vacuum*, 35(12):531–535, 1985.

[102] Koichiro Iwahori, Masahiro Furuta, Yusuke Taki, Tomoyuki Yamamura, and Akira Tanaka. Optical properties of fluoride thin films deposited by RF magnetron sputtering. *Appl. Opt.*, 45(19):4598–602, July 2006.

[103] Bernard H. W. S. De Jong, Ruud G. C. Beerkens, and Peter A. van Nijnatten. Glass. In *Ullmann's Encycl. Ind. Chem.* Wiley-VCH Verlag GmbH & Co. KGaA, 2005.

[104] Dean A. Buckner, Harold C. Hafner, and Norbert J. Kreidl. Hot-Pressing Magnesium Fluoride. *J. Am. Ceram. Soc.*, 45(9):435–438, 1962.

[105] Terry L. Alford, Leonard. C. Feldman, and James W. Mayer. *Fundamentals of Nanoscale Film Analysis.* Springer Science+Business Media, Inc., New York, 2007.

[106] H.-Y. Chan, J. Zhu, and S. Riffat. Solar facade for space cooling. *Energy Build.*, 54:307–319, November 2012.

[107] S. Berg and T. Nyberg. Fundamental understanding and modeling of reactive sputtering processes. *Thin Solid Films*, 476(2):215–230, April 2005.

[108] Edward D. Palik, editor. *Handbook of Optical Constants of Solids II*. Academic Press, 1998.

[109] Garima Kedawat, Subodh Srivastava, Vipin Kumar Jain, Pawan Kumar, Vanjula Kataria, Yogyata Agrawal, Bipin Kumar Gupta, and Yogesh K. Vijay. Fabrication of Artificially Stacked Ultrathin ZnS/MgF2 Multilayer Dielectric Optical Filters. *Appl. Mater. Interfaces*, 5:4872–4877, 2013.

[110] F. Perales, J.M. Herrero, D. Jaque, and C. de las Heras. Improvement of MgF2 thin coating films for laser applications. *Opt. Mater. (Amst).*, 29(7):783–787, March 2007.

[111] S. E. Lee, S. W. Choi, and J. Yi. Double-layer anti-reflection coating using MgF2 and CeO2 films on a crystalline silicon substrate. *Thin Solid Films*, 376 (1-2):208–213, November 2000.

[112] Suresh Kumar Dhungel, Jinsu Yoo, Kyunghae Kim, Sungwook Jung, Somnath Ghosh, and Junsin Yi. Double-Layer Antireflection Coating of MgF2/SiNx for Crystalline Silicon Solar Cells. *J. Korean Phys. Soc.*, 49(3):885–889, 2006.

[113] M. Kennedy, D. Ristau, and H. S. Niederwald. Ion beam-assisted deposition of MgF2 and YbF3 films. *Thin Solid Films*, 333(1-2):191–195, November 1998.

[114] Seouk-hoon Woo, Sung-hwa Kim, and Chang Kwon Hwangbo. Optical and Structural Properties of TiO2 and MgF2 Thin Films by Plasma Ion-Assisted Deposition. *J. Korean Phys. Soc.*, 45(1):99–107, 2004.

[115] Tero Pilvi, Timo Hatanpää, Esa Puukilainen, Kai Arstila, Martin Bischoff, Ute Kaiser, Norbert Kaiser, Markku Leskelä, and Mikko Ritala. Study of a novel ALD process for depositing MgF2 thin films. *J. Mater. Chem.*, 17(48):5077, 2007.

[116] Maria E. Fragala, Roberta G. Toro, Patrizia Rossi, Paolo Dapporto, and Graziella Malandrino. Synthesis, Characterization, and Mass Transport Properties of a Self-Generating Single-Source Magnesium Precursor for MOCVD of MgF2 Films. *Chem. Mater.*, 21(c):2062–2069, 2009.

[117] J. Krishna Murthy, Udo Groß, Stephan Rüdiger, Erhard Kemnitz, and John M. Winfield. Sol–gel-fluorination synthesis of amorphous magnesium fluoride. *J. Solid State Chem.*, 179(3):739–746, March 2006.

[118] K. Kawamata, T. Shouzu, and N. Mitamura. K-M-S (keep-molecules sputtering) deposition of optical MgF2 thin films. *Vacuum*, 51(4):559–564, December 1998.

[119] E. Quesnel, L. Dumas, D. Jacob, and F. Peiro. Optical and microstructural properties of MgF2 UV coatings grown by ion beam sputtering process. *J. Vac. Sci. Technol. A*, 18(6):2869–2876, 2000.

[120] J. C. Martz, D. W. Hess, and W. E. Anderson. A mass spectrometric analysis of CF4/O2 plasmas: Effect of oxygen concentration and plasma power. *Plasma Chem. Plasma Process.*, 10(2):261–275, June 1990.

[121] D. A. Shirley. High-resolution x-ray photoemission spectrum of the valence bands of gold. *Phys. Rev. B*, 5(100):4709–4714, 1972.

[122] J.H. Scofield. Hartree-Slater subshell photoionization cross-sections at 1254 and 1487 eV. *J. Electron Spectros. Relat. Phenomena*, 8:129–137, 1976.

[123] Giuliano Moretti. Auger parameter and Wagner plot in the characterization of chemical states by X-ray photoelectron spectroscopy: a review. *J. Electron Spectros. Relat. Phenomena*, 95(2-3):95–144, October 1998.

[124] Powder Diffraction File, Card 00-041-1443. *Int. Cent. Diffr. Data*, 2008.

[125] Olaf Stenzel. *The Physics of Thin Film Optical Spectra - An Introduction.* Springer-Verlag Berlin Heidelberg, Berlin, Heidelberg, 2005.

[126] P. Oelhafen, D. Ugolini, S. Schelz, and J. Eitle. *Diamond and Diamond-like Films and Coatings.* Plenum, New York, 1991.

[127] Glass in building - Determination of luminous and solar characteristics of glaz-
      ing; German version of DIN EN 410:1998-12, 1998.

[128] Olaf Stenzel. Basic Coating Materials for UV/VIS Applications. In *Opt. Coat-
      ings - Mater. Asp. Theory Pract.*, pages 187–239. Springer-Verlag Berlin Hei-
      delberg, Heidelberg New York Dordrecht London, first edition, 2014.

[129] V. Hody-Le Caër, E. De Chambrier, S. Mertin, M. Joly, M. Schaer, J.-L.
      Scartezzini, and A. Schüler. Optical and morphological characterisation of
      low refractive index materials for coatings on solar collector glazing. *Renew.
      Energy*, 53:27–34, May 2013.

[130] Sameer Chhajed, Martin F. Schubert, Jong Kyu Kim, and E. Fred Schubert.
      Nanostructured multilayer graded-index antireflection coating for Si solar cells
      with broadband and omnidirectional characteristics. *Appl. Phys. Lett.*, 93
      (2008):15–18, 2008.

[131] H. Ishizawa, S. Niisaka, T. Murata, and A. Tanaka. Preparation of MgF2-SiO2
      thin films with a low refractive index by a solgel process. *Appl. Opt.*, 47(13):
      C200–5, May 2008.

[132] S.-H. Jeong, J.-K. Kim, B.-S. Kim, S.-H. Shim, and B.-T. Lee. Characteriza-
      tion of SiO2 and TiO2 films prepared using rf magnetron sputtering and their
      application to anti-reflection coating. *Vacuum*, 76(4):507–515, November 2004.

[133] Wikipedia. CIE 1931 color space — Wikipedia, the free encyclo-
      pedia. `http://en.wikipedia.org/w/index.php?title=CIE_1931_color_
      space&oldid=625197184`, 2014. [Online; accessed 26-December-2014].

[134] Mark Fox. *Optical Properties of Solids*. Oxford University Press, Oxford, New
      York, 2001.

[135] Olaf Stenzel. *Optical Coatings: Material Aspects in Theory and Practice.*
      Springer-Verlag Berlin Heidelberg, Berlin Heidelberg, 1. edition, 2014.

Acknowledgements

Making a thesis is always a huge step in life, which would never be possible without the help of many people for which I would like to thank them all.

- First of all I want to thank Professor Jean-Louis Scartezzini, my thesis director, for the opportunity to do my thesis at the Solar Energy and Building Physics Laboratory (LESO-PB) of the EPFL. Furthermore, I want to thank him for his support during the last years.

- Next, I would like to thank Professor Paul Muralt for co-supervising my thesis, for the welcome in his group at the Ceramics Laboratory (LC) of the EPFL, for his interest in my work, for his support, and especially for his encouragement during the last period of my thesis.

- Furthermore, I thank Dr Andreas Schüler for the good collaboration during the first years of my thesis.

- I would like to express my gratitude to my thesis jury, Prof. Katrin Beyer, Prof. Jean-Louis Scartezzini, Prof. Paul Muralt, Dr Andriy Romanyuk, Dr Virginie Hody-Le Caër, and Dr Rosendo Sanjines.

- Dr Laurent Marot, Roland Steiner, and Prof. Ernst Meyer at the Department of Physics of the University of Basel, I would like to thank for their welcome, for giving me the possibility to perform my research on reactively sputtered MgF_2 in their laboratories, and for the excellent and pleasant collaboration.

- Furthermore, I grant my special thanks to Pierre Loesch from the LESO-PB, for his highly professional support, technical advise and machining skills during the moving, refurbishing and re-installing of the ESCA as well as his help designing the UHV deposition chamber at the LESO-PB. Furthermore, for his

great support during re-building the HV deposition chamber at the LC, and last but not least for his regular last-minute help.

- Michel Teuscher and his collaborators from the Civil Engineering mechanical workshop I thank for professional support and help when refurbishing the ESCA and machining vacuum parts for the UHV deposition chamber at the LESO-PB.

- Lino Olivetta from the LC and Pierre-André Despont, Werner Bronnimann, Adrien Grisendi, and all other collaborators from the ATMX workshop I would like to thank for their professional work and just-in-time help during re-building and adjusting the HV chamber at the LC.

- For the possibility to use their scientific equipment I am very thankful to Prof. Holger Frauenrath of the Laboratory of Macromolecular and Organic Materials and Prof. Harm-Anton Klok of the Polymers Laboratory.

- Dr Andriy Romanyuk and Sarah Leuthold from the Glas Trösch AG I would like to thank for their help with the precise determination of the extinction coefficient of glass substrates.

- For the financial support of my research, I would like to thank the SwissINSO SA, Switzerland, and the EPFL School of Architecture, Civil and Environmental Engineering.

- I am very grateful to Marie Ligier, Chantal Strickler and Professor Michel Bierlaire for their advice and support during eventful times.

- Then I want to thank all Lézards, namely all my colleagues and former colleagues from LESO-PB, for the unique friendly and collegial atmosphere at the LESO, especially Virginie Hody-Le Caër and Martin Joly for the good common project work, André Kostro for being a long time my office mate – we had a lot of good scientific and non-scientific discussions, Antonio Paone for his help and advice with the evaporator, Nicolas Jolissaint for helping to re-align the Window Test Bench, and Mario Geiger for his great programming support.

- As well as I would like to thank all my colleagues at the LC, especially Cosmin S. Sandu for his help with SEM, TEM and EDX measurments, Kaushik

Vaideeswaran and Nachiappan Chidambaram for advice with the XRD system, Andrea Mazzalai, Ludwig Feigl, Mahmoud Hadad, Ramin Matloub, Davide Balma, Robin Nigon and Emilie Trioux for the nice collegial atmosphere.

- Special thanks go to Suzanne L'Eplattenier, Barbara Smith, Yuko Kagata Spitteler and Sarah Duplan, who always helped independent of the problem you addressed them with.

- Professor Peter Oelhafen I would like to thank for the welcome in his laboratory, for the always good collaboration, his support, as well as for his understanding and helpful advices.

- My two students, Maude Maréchal and Tony Länzlinger I thank for the results they obtained during their semester projects and the nice working atmosphere we had together. And Tony especially, for his enthusiasm to enrich the results during following projects.

- My special thanks goes to Carolin Pröstler, Ingo Ramsteiner and Martin Tacke, for reading the manuscript of this thesis critically and finding the errors and the imprecisions.

Last but not least, I would like to thank

- My very best colleague and friend Nikos, for his friendship, advise and always open ear to all kind of topics.

- My best friend Jan, for his close friendship no matter how close (geographically) we currently are.

- My family: first of all my mother Ingrid and my father Eberhard, for supporting me my whole life, no matter what way, and of course my brother Michael, who was there in the right moments to take off and me out of the daily business, for changing ideas.

- Most of all, my wonderful girlfriend Iris, for being always there for me. For all her support, great help and most important, her understanding during the eventful and sometimes difficult last years.

Curriculum Vitae

Stefan Mertin

Diplom-Physiker (University of Heidelberg, Germany)
Dr ès sciences (EPFL)
Nationality: German
Born on January 27$^{\text{th}}$, 1977 in Munich, Germany

chemin du Parc-de-Valency 11
CH-1004 Lausanne

stefan.mertin@gmx.ch

Professional experience

11.2009 – present	**PhD Thesis** at the Solar Energy and Building Physics Laboratory, EPFL, Lausanne, Switzerland, entitled: *Reactively Sputtered Nano-Structured Multilayer Coatings on Architectural Glazing for Active Solar Energy Façades*
02.2009 – 10.2009	**Scientist** at the Solar Energy and Building Physics Laboratory, EPFL, Lausanne, Switzerland, on the SFOE Project *Coloured solar collectors* of the Swiss Federal Office of Energy
10.2004 – 01.2009	**Web and system developer**, IMM Reiseservice KG, Leonberg, Germany
07.2004 – 09.2004	**Scientist** at the Max-Planck-Institute for Astronomy, Heidelberg, Germany, follow up experiments of Diplom Thesis

Education

10.1999 – 06.2004	**Academic studies in physics**, at the University of Heidelberg, Germany
01.2003 – 04.2004	**Diplom Thesis**, at the Max Planck Institute for Astronomy, Heidelberg, Germany, entitled: *Untersuchungen an Komponenten für Filter- und Gitterräder gekühlter Infrarot-Instrumente des James-Webb-Space-Telescopes*
June 2004	**Diplom in Physics**
10.1998 – 09.1999	Interruption for military service
10.1996 – 09.1998	**Academic studies in physics**, at the University of Stuttgart, Germany
08.1987 – 06.1996	Eberhard-Ludwigs-Gymnasium, Stuttgart, Germany
June 1996	**Abitur** (university entrance diploma)

Trainings and qualifications

Cleanroom training	Thin-film deposition and characterisation in cleanroom (ISO 5, class 100), Center for MicroNanoTechnology, EPFL
Languages	German, mother tongue
	English, business fluent
	French, fluent (level B1/B2)
Computer skills	**Operating system administration**: Apple Mac OSX, Linux, Unix, Windows
	Office applications: Word, Excel, Power Point, LaTeX, combit Relationship Manager (CRM)
	Scientific applications: Agilent VEE, Igor Pro, TFCalc, Origin, Film Wizard
	Programming: Mathematica, IDL, C, HTML, PHP, bash
	Data bases: Basic knowledge in MySQL and PostgreSQL
Ancient languages	Greek (Graecum), Latin (Großes Latinum)

Teaching experience

09.2011 – 07.2014	**Teaching assistant** for the course *Building Physics for Architects* at the EPFL, Lausanne, Switzerland
10.1997 – 04.1998	**Instructor** of an Unix introductory course for first year students, University of Stuttgart, Germany

Military service

10.1998 – 12.1998	Marineoperationsschule of the German Navy, Bremerhaven, Germany
01.1999 – 09.1999	Navy ship *Fregatte Brandenburg*, Wilhelmshaven, Germany

Hobbies and free time

09.2012 – 9.2014	Committee member of the LUC Voile (Lausanne university sailing club), former Club de voile de l'EPFL, founding committee member of the LUC Voile (2014)
	Dinghy and keelboat regatta sailing
	Skiing

Lausanne, December 26$^{\text{th}}$ 2014